DEVELOPMENT OF TWO DIMENSIONAL MATERIALS IN PHOTOCATALYSIS

Zizhen Li

Thesis submitted to the University of Ottawa

in partial Fulfillment of the requirements for the

Doctorate in Philosophy degree in Chemical Engineering

uOttawa

Department of Chemical and Biological Engineering

Faculty of Engineering

University of Ottawa

Abstract

Photocatalysis is a process to convert light energy into chemical energies. This advanced process has been extensively applied in different areas, such as water splitting to evolve hydrogen, organic/ inorganic pollutants decomposition, artificial photosynthesis (CO_2 reduction), disinfection, heavy metal recovery, organic synthesis and nitrogen fixation (reduction). The difficulty for photocatalysis applied in practical is primarily due to the low quantum yield as for the high recombination of photogenerated charge carriers. Various strategies have been implemented to overcome these challenges. As recently developed advanced materials, two dimensional materials have attracted lots of attentions as for their superiorities such as large specific surface area and high conductivity. These advantages for two dimensional materials make them be promising cocatalysts in enhance catalytic activity. In this thesis, various two dimensional materials (such as MoS_2, SnS, BN as well as C_3N_4) other than graphene were prepared and investigated in the promotion of photocatalytic activity. Specifically, the focus of present work is on two dimensional materials enhanced photocatalysis in environmental remediation, including organic pollutants detoxification as well as bacteria inactivation. It was found that two dimensional materials, including MoS_2, SnS, BN, may be excellent candidates as cocatalysts to enhanced visible-light-driven photocatalytic activity. And g-C_3N_4 as an effective photocatalyst exhibited excellent photocatalytic oxidation activity, and its activity can be further enhanced with surface modification by hydroxyl functional groups (a modification method reported in the thesis). Suggestions for future work were also proposed in this thesis.

Resúmé

La photocatalyse est un processus de conversion de l'énergie lumineuse en énergies chimiques. Ce processus avancé a été largement appliqué dans différents domaines, tels que le fractionnement de l'eau afin d'en dégager de l'hydrogène, la décomposition des polluants organiques / inorganiques, la photosynthèse artificielle (réduction du CO_2), la désinfection, la récupération des métaux lourds, la synthèse organique et la fixation de l'azote (réduction). La difficulté de la photocatalyse appliquée dans la pratique est principalement due au faible rendement quantique quant à la forte recombinaison des porteurs de charge photogénérés. Diverses stratégies ont été mises en œuvre pour surmonter ces défis. Comme matériaux avancés récemment développés, les matériaux bidimensionnels ont attiré beaucoup d'attention quant à leurs supériorités telles qu'une grande surface spécifique et une conductivité élevée. Ces avantages pour les matériaux bidimensionnels en font des cocatalyseurs prometteurs pour améliorer l'activité catalytique. Dans cette thèse, divers matériaux à deux dimensions (tels que MoS_2, SnS, BN ainsi que C_3N_4) autres que le graphène ont été préparés et étudiés pour la promotion de l'activité photocatalytique. Le présent travail se concentre particulièrement sur la photocatalyse améliorée à base de matériaux à deux dimensions pour la dépollution de l'environnement, y compris la détoxification des polluants organiques et l'inactivation des bactéries. Il a été établi que les matériaux bidimensionnels, y compris MoS_2, SnS, BN, peuvent être d'excellents candidats comme cocatalyseurs afin d'améliorer l'activité photocatalytique induite par la lumière visible. De plus, le g-C_3N_4 considéré comme un efficace photocatalyseur présentait une excellente activité d'oxydation photocatalytique, et son activité peut être encore améliorée avec la modification de surface par des groupes

fonctionnels hydroxyle (une méthode de modification rapportée dans la thèse). Des suggestions de travaux futurs ont également été proposées dans cette thèse.

Copyright Statement

All material contained in this thesis that has previously been published has been published in journals that allow their use in graduate theses. Full references for the original publication are provided where required.

Statement of Contributions of Collaborators

I hereby declare that everything presented in this document is original and entirely the product of the author's work, with exception of the contribution made by co-authors, details of which are listed below. All of the material used for the purpose of this thesis with co-authors' full knowledge and consent, and in accordance with the rules established by University of Ottawa.

Chapter	Collaborator(s) and affiliation	Details
3	X. Meng, University of Ottawa	X. M. provided guidance contribution.
4	X. Meng, University of Ottawa	X. M. provided guidance contribution, and conducted the adsorption tests.
5	X. Meng, University of Ottawa	X. M. provided guidance contribution, and conducted DFT simulations, XRD tests as well as electrochemical analysis.
6	X. Meng, University of Ottawa	X. M. provided guidance contribution, and conducted DFT simulations, XRD tests as well as electrochemical analysis.
7	X. Meng, University of Ottawa	X. M. conducted DFT simulation and made editorial contributions to the written work presented.
8	X. Meng, University of Ottawa	X. M. conducted DFT simulations.
9	X. Meng, University of Ottawa	X. M. provided guidance, conducted DFT simulation and made editorial contributions to the written work presented.

Acknowledgements

I would first like to acknowledge my supervisor, Prof. Jason Zhang, for his guidance, support, and mentorship during my doctoral studies.

I would also like to acknowledge the Natural Science and Engineering Research Council of Canada (NSERC), the China Scholarship Council (CSC) and University of Ottawa for financial support.

I am also grateful to technicians at the Center for Catalysis Research and Innovation (CCRI) at the University of Ottawa: Dr. Yun Liu (SEM&TEM), Dr. Alexander Mommers (XPS), Dr. Yong Yang (BET), Dr. Bulat Gabidullin (PXRD), and Dr. Rebeca Rondon Belandria (Raman). I would also like to express my gratitude to technicians in CHG and CVG for their technical support. Thanks are also extended to Scott Proulx and Fahad Chowdhury for their assistance in English language editing of the document.

I also want to extend my thanks to all of my friends and my current and former group mates who provided me with both research insights and encourage during my doctoral studies, especially Zhiliang Yang, Yu Qiao and Yuxuan Ren.

Finally, I would like to thank my warm family, the selfless help of my parents and my beloved husband (Xiangchao Meng). Without whom, none of this would have been possible.

To my family

Table of Contents

List of Figures

List of Tables

Nomenclature, Abbreviations and symbols

Nomenclature and Abbreviation

2D	Two dimensional
3D	Three dimensional
AFM	Atomic force microscopy
AOP	Advanced oxidation process
BBS	Bismuth-based semiconductor(s)
BET	Brunauer, Emmett and Teller
BJH	Barrett-Joyner-Halenda
CB	Conduction band
CBM	Conduction band minimum
c-BN	Cubic BN
CFU	Colony forming units
CVD	Chemical vapor deposition
CZTS	Cu_2ZnSnS_4
DBPs	Disinfection by-products
DDW	Deionized distilled water
DFT	Density functional theory
DMAc	Anhydrous *N, N*-dimethylacetamide
DOS	Density of states
D-R	Dubinin-Radushkevich
DRS	Diffuse reflectance spectra

e^-	Electron
E. Coli	*Escherichia coli*
EDS	Energy-dispersive X-ray spectroscopy
EIS	Electrochemical impedance spectroscopy
FT-IR	Fourier transform infrared spectrometer
g-C_3N_4	Graphitic C_3N_4
GGA	Generalized gradient approximation
h^+	Hole
h-BN	Hexagonal BN
HER	Hydrogen evolution reaction
HPLC	High-performance liquid chromatograph
IPA	Isopropanol
ITO	Indium-tin oxide
MB	Methylene blue
MO	Methyl orange
M-S	Mott-Schottky
NDIR	Non-dispersive Infra-Red
NHE	Normal hydrogen electrode
NIR	Near-infrared
NMP	N-methyl-pyrrolidinone
NOM	Natural organic matter
NRs	Nanorods
NSs	Nanospheres

NTs	Nanotubes
NVP	N-vinyl-pyrrolidinone
NWF	Non-woven fiber
PANI	Polyaniline
PAW	Projector augmented wave
PBE	Perdew, Burke, and Ernzerhof
pCBA	*p*-chlorobenzoic acid
PEC	Photoelectrocatalysis
PL	Photoluminescence
rGO	Reduced graphene oxide
RhB	Rhodamine B
ROS	Reactive oxidative species
SCE	Standard calomel electrode
SEM	Scanning electron microscopy
SL	Single-layer
SPR	Surface Plasmon Resonance
SSCN	Self-sensitized carbon nitride
TBO	Triazine-based oligomer
TEM	Transmission electron microscopy
TEOA	Triethanolamine
TMD	Transition metal dichalcogenide
TOC	Total organic carbon
UV	Ultraviolet

VASP	Vienna *ab initio* simulation package
VB	Valence band
VBM	Valence band maximum
VLR	Visible light-responsive
XPS	X-ray photoelectron spectroscopy
XRD	X-ray diffraction

Symbols

A_T	Temkin isotherm equilibrium binding constant (L/g)
b	Langmuir adsorption constant (L/mg)
B	Constant related to heat of adsorption
b_T	Temkin isotherm constant (J/mol)
C	Semiconductor space charge layer capacitance (cm^4/F^2)
C_0	Initial pollutant concentration (mg/L)
C_{dosage}	Initial adsorbent dosage (g/L)
C_e	Equilibrium concentration of adsorbate in liquid-phase (mg/L)
C_t	Pollutant concentration at time t (mg/L)
d_p	Pore size (nm)
E	Applied potential (V)
E_{ads}	Adsorption energy (eV)
$E_{adsorbate}$	Total energies of the isolated adsorbate molecules (eV)
E_{CB}	Bottom position of the conduction band (eV)

E^e	Energy of free electrons on the hydrogen scale (~ 4.5 eV)
E_f	Fermi energy (V)
E_{FB}	Flat-band potential (eV)
E_g	Band gap energy (eV)
E_{photon}	Energy of photons (eV)
E_{slab}	Total energies of the slab (eV)
$E_{slab+adsorbate}$	Total energies of the system (eV)
E_{vac}	Vacuum energy (V)
E_{VB}	Top position of the valence band (eV)
h	Planck constant (6.626x10-34 J s)
$\hbar$	Reduced Planck constant
k'	Pseudo first-order reaction constant (s^{-1})
k_1	Rate constant of the pseudo first-order adsorption (min^{-1})
k_2	Rate constant of the pseudo second-order model (g/mg/min)
k_{ip}	Intra-particle diffusion rate constant ($mg/g/min^{1/2}$)
λ	Wavelength (nm)
m^*	Effective mass
N_D	Donor density (cm^{-3})
Q_0	Maximum monolayer coverage capacity of adsorbent (mg/g)
q_e	Equilibrium concentration of adsorbate in solid phase (mg/g)
q_{photon}	Wave vector of the assisted photon
q_s	Theoretical isotherm saturation capacity (mg/g)
R	Universal gas constant (8.314 J/mol/K)

R^2	Regression coefficient
R_{ct}	Resistance to electron transfer (Ω)
T	Temperature (K)
ν	Frequency (s^{-1})
V	Volume (m^3)
W	Weight of adsorbent (g)
β	D-R isotherm constant with a dimension of energy
γ	Surface tension (mJ/m^2)
ε	Polanyi potential
ε_0	Vacuum permittivity (8.85×10^{-14} F/cm)
ε_r	Dielectric constant of the semiconductor
κ	Boltzmann constant (8.617×10^{-5} eV/K)
τ	Lifetime of injected electrons (ns)
Φ	Work function (V)
χ_p	Electronegativity of the semiconductor (eV)

SECTION I: INTRODUCTION

Chapter 1 Introduction

With the rapid increase of population, energy shortage and environmental pollution have become two primary problems facing us today. With the use up of fossil fuels, it is urgent to pursue alternative energy source. Solar energy has been considered a promising candidate to alternate fossil fuels. To date, the primary strategies for solar energy conversion are solar-to-heat, solar-to-electricity and solar-to-chemical energy. Among them, solar-to-chemical energy is a process to directly store solar energy into useful chemicals. One of the approaches is photocatalysis. Heterogeneous photocatalysis has become a hot research field, and has been implemented in various areas such as water splitting to evolve hydrogen, artificial photosynthesis (CO_2 reduction), disinfection, heavy metals recovery, organic synthesis and N_2 fixation (reduction). These applications are attributed to the fields of energy storage and environmental remediation, which suggest that photocatalysis may be a useful approach to overcome the problems faced by mankind today.

The bottleneck for photocatalysis in practical use is the low quantum yield as for the low charge carriers' separation. The effective approaches can be divided into two aspects: modifications of semiconductors and preparation of highly photoactive materials. Our research group, in recent years, has focused on bismuth-based semiconductors (BBS) applied in photocatalysis. As a group of promising photoactive materials, BBS exhibited excellent visible-light-driven photocatalytic activity. However, the activity of BBS can be further improved through modifications. In this work,

various two dimensional materials were tried to combine with BBS, as co-catalysts to improve the photocatalytic activity. This document is divided into ten chapters. Chapter 1 provides an introduction to this document. Chapter 2 provides in-depth literature review of the relevant fields. Chapters 3-7 discuss work performed to improve the photocatalytic activities of bismuth-based photocatalysts through combination with different dimensional materials. Specifically, Chapter 3 comprehensively reviews MoS_2 enhanced photocatalysis in literature. Chapter 4 studies the adsorption properties of MoS_2 with different morphology prepared with different sulfur precursors. And Chapter 5 gives a case study on the MoS_2 enhanced photocatalytic activity of Bi_2MoO_6. Chapters 6 and 7 introduce the SnS and BN, respectively, applied as a cocatalyst to improve the photocatalytic activity of BBS. Chapters 8 and 9 are focused on g-C_3N_4 with hydroxyl surface modification. Chapter 10 provides the conclusions, outlooks and scholarly contributions.

Chapter 2 Background and Literature Review

2.1 Mechanism of photocatalysis

In the photocatalytic process, semiconductor acts as a photocatalyst for light harvesting. When the semiconductor is activated by a photon (hv) with the energy equal or larger than the bandgap energy (E_g), a free electron (e^-) can be promoted from the valence band (VB) into the conduction band (CB), producing a hole (h^+) in the valence band (Figure 2.1). When the photogenerated charge carriers transfer to the surface of semiconductor, they can directly degrade organic pollutants adsorbed on the surface or a series of redox reactions may occur to generate reactive oxidative species (*e.g.* •OH, $•O_2^-$, and $•HO_2$), which are capable of oxidizing pollutants. The possible redox reactions are proposed as follows [1]:

$$Photocatalysts + hv \rightarrow h^+ + e^- \quad (1)$$

$$H_2O + h^+ \rightarrow \bullet OH + H^+ \quad (2)$$

$$h^+ + \text{Pollutant} \rightarrow \text{Pollutant}^* \quad (3)$$

$$\bullet OH + \text{ Pollutant} \rightarrow CO_2 + H_2O \quad (4)$$

$$O_2 + e^- \rightarrow \bullet O_2^- \quad (5)$$

$$H^+ + O_2 + e^- \rightarrow \bullet HO_2 \,/\, H_2O_2 \quad (6)$$

However, the photon-induced electrons and holes can recombine within a magnitude of few nanoseconds in the absence of suitable charge scavengers, leading to a low activity of photocatalysis [2, 3]. In this regard, many efforts have been made to improve photocatalytic activity, such as doping, modulating morphology of semiconductor materials, and establishing heterostructures. Among these, the formation of heterostructure is a simple and effective method to promote charge separation and photocatalytic activity [4].

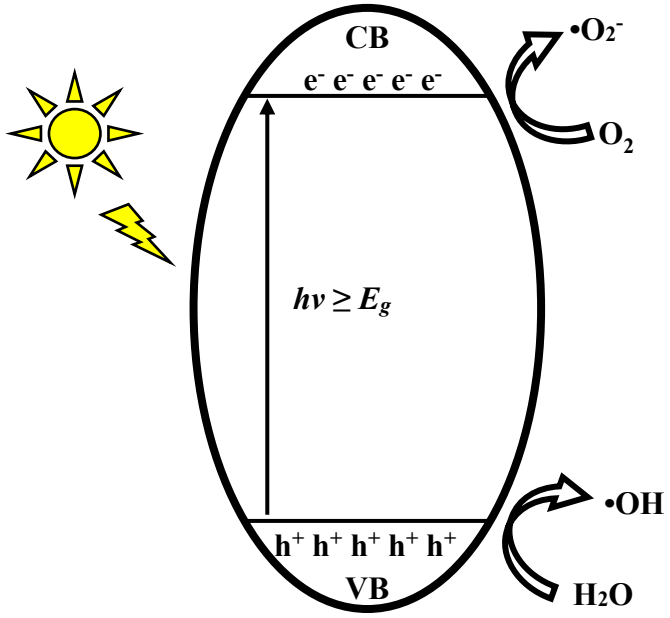

Figure 2.1. Scheme of a heterogeneous photocatalytic process.

2.2 Two-dimensional materials in photocatalysis

Since the emergence of mono-layered graphene, a typical 2D material, many other 2D layered materials have been discovered and implemented in the field of photocatalysis, chemical and biological sensors, optoelectronics, energy storage, *etc.* [5]. Compared to their 3D counterparts, 2D layered materials possess several unique features, beneficial to photocatalysis. For example, 2D layered materials generally have high specific areas; thus, abundant surface active sites and

good photocatalytic activity can be expected [6]. Secondly, some of them have high electric conductivity due to the π-conjugated structure, providing an excellent electron transport platform for charge separation [7]. Thirdly, the ultrathin nature of 2D layered material could shorten the diffusion length of photogenerated charge carriers from the inside to the material surface. As a result, the probability of charge recombination could be significantly reduced and more electrons and holes could reach the surface to react with the target pollutants [8]. Besides, the 2D layered materials could serve as a flexible catalyst support due to their layered features, thus contributing to the dispersion of co-catalyst and charge transfer at the interface of composites [3]. To date, more than two dozen 2D materials have been explored for photocatalysis, including metal oxide nanosheets (*e.g.* WO_3, titanoniocate, and perovskite oxides), layered transition metal dichalcogenides (TMDs), metal-free nanosheets (*e.g.* graphene or graphene oxide, C_3N_4, and h-BN) and many more [3, 7]. The rapid progress in the development of 2D layered materials has triggered a variety of reviews focusing on the properties, synthesis methods, and applications [9-11]. Typical 2D materials were selected for study in this work, and these materials were introduced below.

2.2.1 MoS_2

MoS_2 is an earth-abundant material that naturally occurs as mineral molybdenite. Due to the intrinsic layered structure, the exfoliation of bulk MoS_2 into mono- or few-layer level is straightforward through a variety of methods such as mechanical exfoliation, chemical exfoliation and liquid phase ultrasonic exfoliation [12, 13]. Each layer is connected by weak van der Waals force and made up of plane of Mo atoms sandwiched between two planes of S atoms [6]. Depending on the atomic coordination between a central Mo atom and surrounding S atoms, the MoS_2 can be semiconducting or metallic. In addition, the optical and electronic properties of MoS_2

can be varied by band gap adjustment. It is reported that bulk MoS_2 has an indirect bandgap of 1.29 eV, which is insufficient for photocatalytic reactions and charge separation [5]. In contrast, when the size of MoS_2 is reduced to the 2-dimentional scale (mono- or few-layers), the indirect bandgap transfers to a direct bandgap of ~1.9 eV [14]. Therefore, the low-dimensional MoS_2 is regarded as a competitive candidate for visible-light driven photocatalytic reactions. More detailed information about properties and structures, problems along with possible approaches, and applications of MoS_2 are discussed in Chapter 3.

2.2.2 SnS

Tin sulfides with different oxidation states of Sn can be divided into two chemical compositions: SnS and SnS_2. Compared to the bulk counterparts, the structural distortions of layered tin sulfides contribute to the increasing density of states at the valence band edge, which can facilitate the light harvesting capacity and mobility of photogenerated charge carriers [7, 15]. It is reported that SnS was more efficient than SnS_2 for photocatalytic hydrogen production, due to the low electron affinity and small ionization potential [16]. Additionally, lower cost, less toxic nature, and earth abundant feature of SnS have opened new horizons for the solar cell [17], lithium ion battery [18], photodetectors[19], and photocatalysis [20]. The energy band gap of SnS has exhibited both direct and indirect transition of around 1.07~1.3 eV, which is suitable for light absorption in the visible-light region and near-infrared region [20, 21]. As a result, synthesis of SnS-based heterostructure with matched band alignments can not only improve charge separation but also broaden the light adsorption spectra of prepared composites. For example, Hu *et al.* synthesized SnS/SnS_2 heterostructure through a facile pyrolysis method [22]. The band alignment of prepared composites belongs to the type-I heterostructure, which could suppress the photogenerated charge recombination, compared to pure SnS and SnS_2. The pristine SnS nanoflakes exhibited negligibly

photocatalytic degradation efficiency under simulative sunlight, while almost 90% of RhB could be removed after 120 min in the presence of SnS/SnS_2 heterostructure. Yao *et al.* further explored the effect of Sn^{4+} content on the photocatalytic activity of urchinlike SnS/SnS_2 heterostructures [23]. It was reported that the optimum content of Sn^{4+} was 40 wt% and the excessive content of Sn^{4+} resulted in the decreasing photocatalytic activity of methyl orange (MO) degradation. This is because the large content of Sn^{4+} may reduce the visible-light absorption capacity of the heterostructures due to the wide bandgap property of SnS_2. Our group fabricated a novel Z-scheme heterostructure by combing n-type SnS with hierarchical n-type Bi_2WO_6 [21]. The formation of Z-scheme heterostructure could efficiently facilitate the separation of charge carriers without compromising their redox potentials. More results and discussions are furnished in Chapter 6. Besides, SnS is also known as a p-type semiconductor and integrated with other n-type semiconductors to form the p-n heterostructures [23, 24]. A 3D porous ZnO-SnS p-n heterostructure is established by Wang's group through a novel two-step solution approach [25]. These composites synergistically integrated the large surface area and high redox potential of n-type ZnO with visible-light absorption capacity of p-type SnS, which gives rise to carrier transfer and more reactive sites.

2.2.3 BN

Boron nitride (BN) is a metalloid compound, chemically composed of equal number of boron (B) and nitrogen (N) atoms. BN is a synthetic product, not found in nature at early years. And BN is isostructural to carbon (C) with various crystalline forms as shown in Figure 2.2. Among these forms, cubic BN (c-BN) and hexagonal BN (h-BN) are relatively stable [26, 27]; h-BN was more thermodynamically stable compared to c-BN at standard conditions, as BN synthesis usually resulted in the formation of h-BN. It can be found that the crystal structure of h-BN is similar to

graphite with layered sp^2-bonded hexagonally packed sheets. And h-BN can also be exfoliated to form 2D BN nanosheets; BN nanosheets were also called 'white-graphene'. However, 2D BN and graphene exhibit different properties as the different chemical compositions. It was well-known that in graphite, valence electrons set in a conjugated system make it an excellent electron conductor, whereas, BN exhibited insulating properties for the quite different electronegativity between these two atoms (*i.e.* B and N) in BN [28, 29]. In addition, BN was found with a wide band gap, which make it an attractive candidate in various areas such as ultraviolet photoluminescence and photocatalysis [30]. BN applied in photocatalysis usually acted as a cocatalyst to improve the photocatalytic activity of the substrate [31]. BN in photocatalyst systems can provide high surface area, form heterostructures as well as act as charge carriers accepters. All these properties are in favor of enhancing photocatalytic activity. BN nanosheets can be formed by mechanical exfoliation technique such as ball milling, as reported by Lee *et al.* [32], and liquid exfoliation method as reported by Coleman *et al.* [33] And the latter method is very promising, as it is insensitive to air and water and can potentially be scaled up to large quantities of exfoliated material, which was also adopted to 2D BN nanosheets in this work. And as-prepared BN was chemically combined with bismuth-based semiconductor, to explore the possibility of improving the visible-light-induced photocatalytic activity.

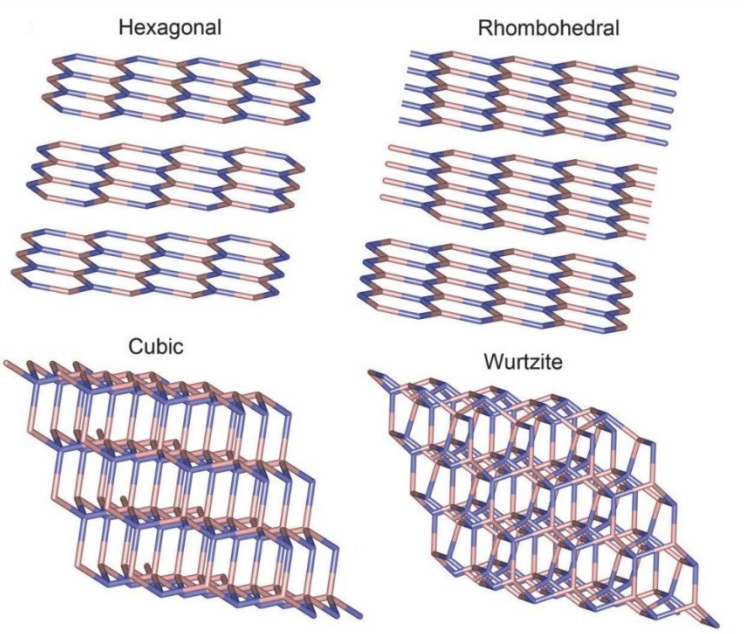

Figure 2.2. Crystal structures for BN (adapted from [26])

2.2.4 C_3N_4

Carbon nitride, as a metal-free compound, has attracted significant attention in recent years, since the first report about photocatalytic water splitting using C_3N_4 by Wang *et al.* in 2008 [34]. The applications of C_3N_4 were extended from water splitting to other energy conversion and storage technologies such as fuel cells, metal-air batteries and environmental remediation [35, 36]. Various crystalline structures for C_3N_4 were predicted and reported, primarily including *β-, α-,* g-, defect zincblende- and cubic-C_3N_4 [37]. Graphitic C_3N_4 (g-C_3N_4) with similar crystal structure to graphene has been regarded as the most attractive crystalline form, when applied as a photocatalyst. In contrast to the pure carbon constituent of graphene, g-C_3N_4 is composed of carbon (C) and nitrogen (N), with some impurity of Hydrogen (H). And similar to BN, C_3N_4 is a semiconductor with a narrower band gap (compared to BN) of ~2.7 eV, which determines its responsiveness to visible light photons [38]. As a photocatalyst, C_3N_4 exhibits advantages such as being non-toxic, abundant, easy-to-synthesize and low cost [39]. And g-C_3N_4 is easy to prepare by thermal

polymerization of abundant nitrogen-rich precursors, such as urea, melamine, dicyandiamide, cyanamide, thiourea, and ammonium thiocyanate. C_3N_4 with a suitable band gap is usually applied as a photocatalytic substrate. However, for the low electrical conductivity and high recombination of photogenerated charge carriers, modifications on g-C_3N_4 are required to improve its photocatalytic activity. These modification methods were comprehensively reviewed, such as Ag modified C_3N_4 [40], formation of heterostructure [41] and morphology control [42, 43]. Further modification methods are required to improve the photocatalytic activity and make it possible to be applied in practice.

2.3 Conclusions

Two dimensional materials have become more and more popular, for their excellent performance in various areas including photocatalysis. General properties of typical 2D materials were introduced in this chapter, and more details would be discussed and reviewed in the Introduction part of each chapter.

References

[1] Z. Li, X. Meng, Z. Zhang, Few-layer MoS_2 nanosheets-deposited on Bi_2MoO_6 microspheres: A Z-scheme visible-light photocatalyst with enhanced activity, Catal. Today, 315 (2018) 67-78.

[2] M.R. Hoffmann, S.T. Martin, W. Choi, D.W. Bahnemann, Environmental Applications of Semiconductor Photocatalysis, Chem Rev, 95 (1995) 69-96.

[3] B. Luo, G. Liu, L. Wang, Recent advances in 2D materials for photocatalysis, Nanoscale, 8 (2016) 6904-6920.

[4] H. Wang, L. Zhang, Z. Chen, J. Hu, S. Li, Z. Wang, J. Liu, X. Wang, Semiconductor

heterojunction photocatalysts: design, construction, and photocatalytic performances, Chem. Soc. Rev., 43 (2014) 5234-5244.

[5] M. Xu, T. Liang, M. Shi, H. Chen, Graphene-Like Two-Dimensional Materials, Chem Rev, 113 (2013) 3766-3798.

[6] J. Low, S. Cao, J. Yu, S. Wageh, Two-dimensional layered composite photocatalysts, Chem Commun, 50 (2014) 10768-10777.

[7] D. Deng, K.S. Novoselov, Q. Fu, N. Zheng, Z. Tian, X. Bao, Catalysis with two-dimensional materials and their heterostructures, Nature Nanotechnology, 11 (2016) 218.

[8] J. Di, J. Xia, H. Li, Z. Liu, Freestanding atomically-thin two-dimensional materials beyond graphene meeting photocatalysis: Opportunities and challenges, Nano Energy, 35 (2017) 79-91.

[9] L. Wang, T. Sasaki, Titanium Oxide Nanosheets: Graphene Analogues with Versatile Functionalities, Chem. Rev., 114 (2014) 9455-9486.

[10] H. Zhang, Ultrathin Two-Dimensional Nanomaterials, ACS Nano, 9 (2015) 9451-9469.

[11] S.Z. Butler, S.M. Hollen, L. Cao, Y. Cui, J.A. Gupta, H.R. Gutiérrez, T.F. Heinz, S.S. Hong, J. Huang, A.F. Ismach, E. Johnston-Halperin, M. Kuno, V.V. Plashnitsa, R.D. Robinson, R.S. Ruoff, S. Salahuddin, J. Shan, L. Shi, M.G. Spencer, M. Terrones, W. Windl, J.E. Goldberger, Progress, Challenges, and Opportunities in Two-Dimensional Materials Beyond Graphene, ACS Nano, 7 (2013) 2898-2926.

[12] M. Chhowalla, H.S. Shin, G. Eda, L.-J. Li, K.P. Loh, H. Zhang, The chemistry of two-dimensional layered transition metal dichalcogenide nanosheets, Nature Chemistry, 5 (2013) 263.

[13] X. Huang, Z. Zeng, H. Zhang, Metal dichalcogenide nanosheets: preparation, properties and applications, Chem. Soc. Rev., 42 (2013) 1934-1946.

[14] Y.-J. Yuan, H.-W. Lu, Z.-T. Yu, Z.-G. Zou, Noble-Metal-Free Molybdenum Disulfide Cocatalyst for Photocatalytic Hydrogen Production, Chemsuschem, 8 (2015) 4113-4127.

[15] J. Deng, H. Li, J. Xiao, Y. Tu, D. Deng, H. Yang, H. Tian, J. Li, P. Ren, X. Bao, Triggering the electrocatalytic hydrogen evolution activity of the inert two-dimensional MoS_2 surface via single-atom metal doping, Energy & Environmental Science, 8 (2015) 1594-1601.

[16] Y. Shiga, N. Umezawa, N. Srinivasan, S. Koyasu, E. Sakai, M. Miyauchi, A metal sulfide photocatalyst composed of ubiquitous elements for solar hydrogen production, Chem. Commun., 52 (2016) 7470-7473.

[17] H. Noguchi, A. Setiyadi, H. Tanamura, T. Nagatomo, O. Omoto, Characterization of vacuum-evaporated tin sulfide film for solar cell materials, Sol. Energy Mater. Sol. Cells, 35 (1994) 325-331.

[18] A.M. Tripathi, S. Mitra, Tin sulfide (SnS) nanorods: structural, optical and lithium storage property study, RSC Advances, 4 (2014) 10358-10366.

[19] J. Chao, Z. Wang, X. Xu, Q. Xiang, W. Song, G. Chen, J. Hu, D. Chen, Tin sulfide nanoribbons as high performance photoelectrochemical cells, flexible photodetectors and visible-light-driven photocatalysts, RSC Advances, 3 (2013) 2746-2753.

[20] A.J. Biacchi, D.D. Vaughn, R.E. Schaak, Synthesis and Crystallographic Analysis of Shape-Controlled SnS Nanocrystal Photocatalysts: Evidence for a Pseudotetragonal Structural Modification, J. Am. Chem. Soc., 135 (2013) 11634-11644.

[21] Z. Li, X. Meng, Z. Zhang, Hexagonal SnS nanoplates assembled onto hierarchical Bi_2WO_6 with enhanced photocatalytic activity in detoxification and disinfection, J Colloid Interf Sci, 537 (2019) 345-357.

[22] X. Hu, G. Song, W. Li, Y. Peng, L. Jiang, Y. Xue, Q. Liu, Z. Chen, J. Hu, Phase-controlled synthesis and photocatalytic properties of SnS, SnS_2 and SnS/SnS_2 heterostructure nanocrystals, Mater. Res. Bull., 48 (2013) 2325-2332.

[23] K. Yao, J. Li, S. Shan, Q. Jia, One-step synthesis of urchinlike SnS/SnS_2 heterostructures with superior visible-light photocatalytic performance, Catal. Commun., 101 (2017) 51-56.

[24] S. Jayswal, R.S. Moirangthem, Construction of a solar spectrum active SnS/ZnO p–n heterojunction as a highly efficient photocatalyst: the effect of the sensitization process on its performance, New J. Chem., 42 (2018) 13689-13701.

[25] L. Wang, H. Zhai, G. Jin, X. Li, C. Dong, H. Zhang, B. Yang, H. Xie, H. Sun, 3D porous ZnO-SnS p-n heterojunction for visible light driven photocatalysis, PCCP, 19 (2017) 16576-16585.

[26] A. Pakdel, Y. Bando, D. Golberg, Nano boron nitride flatland, Chem Soc Rev, 43 (2014) 934-959.

[27] V. Guerra, C. Wan, T. McNally, Thermal conductivity of 2D nano-structured boron nitride (BN) and its composites with polymers, Prog Mater Sci, 100 (2019) 170-186.

[28] M.S.R.N. Kiran, K. Raidongia, U. Ramamurty, C.N.R. Rao, Improved mechanical properties of polymer nanocomposites incorporating graphene-like BN: Dependence on the number of BN layers, Scripta Mater, 64 (2011) 592-595.

[29] S. Kemaloglu, G. Ozkoc, A. Aytac, Properties of thermally conductive micro and nano size boron nitride reinforced silicon rubber composites, Thermochim Acta, 499 (2010) 40-47.

[30] W. Lei, D. Portehault, D. Liu, S. Qin, Y. Chen, Porous boron nitride nanosheets for effective water cleaning, Nature Communications, 4 (2013) 1777.

[31] C. Zhou, C. Lai, C. Zhang, G. Zeng, D. Huang, M. Cheng, L. Hu, W. Xiong, M. Chen, J.

Wang, Y. Yang, L. Jiang, Semiconductor/boron nitride composites: Synthesis, properties, and photocatalysis applications, Applied Catalysis B: Environmental, 238 (2018) 6-18.

[32] D. Lee, B. Lee, K.H. Park, H.J. Ryu, S. Jeon, S.H. Hong, Scalable Exfoliation Process for Highly Soluble Boron Nitride Nanoplatelets by Hydroxide-Assisted Ball Milling, Nano Lett, 15 (2015) 1238-1244.

[33] J.N. Coleman, M. Lotya, A. O'Neill, S.D. Bergin, P.J. King, U. Khan, K. Young, A. Gaucher, S. De, R.J. Smith, I.V. Shvets, S.K. Arora, G. Stanton, H.-Y. Kim, K. Lee, G.T. Kim, G.S. Duesberg, T. Hallam, J.J. Boland, J.J. Wang, J.F. Donegan, J.C. Grunlan, G. Moriarty, A. Shmeliov, R.J. Nicholls, J.M. Perkins, E.M. Grieveson, K. Theuwissen, D.W. McComb, P.D. Nellist, V. Nicolosi, Two-Dimensional Nanosheets Produced by Liquid Exfoliation of Layered Materials, Science, 331 (2011) 568-571.

[34] X. Wang, K. Maeda, A. Thomas, K. Takanabe, G. Xin, J.M. Carlsson, K. Domen, M. Antonietti, A metal-free polymeric photocatalyst for hydrogen production from water under visible light, Nat Mater, 8 (2008) 76.

[35] X. Dong, F. Cheng, Recent development in exfoliated two-dimensional g-C3N4 nanosheets for photocatalytic applications, Journal of Materials Chemistry A, 3 (2015) 23642-23652.

[36] W. Niu, Y. Yang, Graphitic Carbon Nitride for Electrochemical Energy Conversion and Storage, ACS Energy Letters, 3 (2018) 2796-2815.

[37] M. Inagaki, T. Tsumura, T. Kinumoto, M. Toyoda, Graphitic carbon nitrides (g-C3N4) with comparative discussion to carbon materials, Carbon, 141 (2019) 580-607.

[38] D. Masih, Y. Ma, S. Rohani, Graphitic C_3N_4 based noble-metal-free photocatalyst systems: A review, Applied Catalysis B: Environmental, 206 (2017) 556-588.

[39] B. Xu, M.B. Ahmed, J.L. Zhou, A. Altaee, G. Xu, M. Wu, Graphitic carbon nitride based nanocomposites for the photocatalysis of organic contaminants under visible irradiation: Progress, limitations and future directions, Sci Total Environ, 633 (2018) 546-559.

[40] S. Patnaik, D.P. Sahoo, K. Parida, An overview on Ag modified g-C3N4 based nanostructured materials for energy and environmental applications, Renewable and Sustainable Energy Reviews, 82 (2018) 1297-1312.

[41] J. Fu, J. Yu, C. Jiang, B. Cheng, g-C3N4-Based Heterostructured Photocatalysts, Advanced Energy Materials, 8 (2018) 1701503.

[42] W. Jiang, H. Wang, X. Zhang, Y. Zhu, Y. Xie, Two-dimensional polymeric carbon nitride: structural engineering for optimizing photocatalysis, Sci. China Chem., 61 (2018) 1205-1213.

[43] Z. Zhao, Y. Sun, F. Dong, Graphitic carbon nitride based nanocomposites: a review, Nanoscale, 7 (2015) 15-37.

SECTION II: MoS_2 ENHANCED PHOTOCATALYSIS

Chapter 3 Recent Development on MoS_2-based Photocatalysis: a Review

Zizhen Li, Xiangchao Meng and Zisheng Zhang

Journal of Photochemistry & Photobiology C: Photochemistry Reviews *35*, 39-55 (2018)

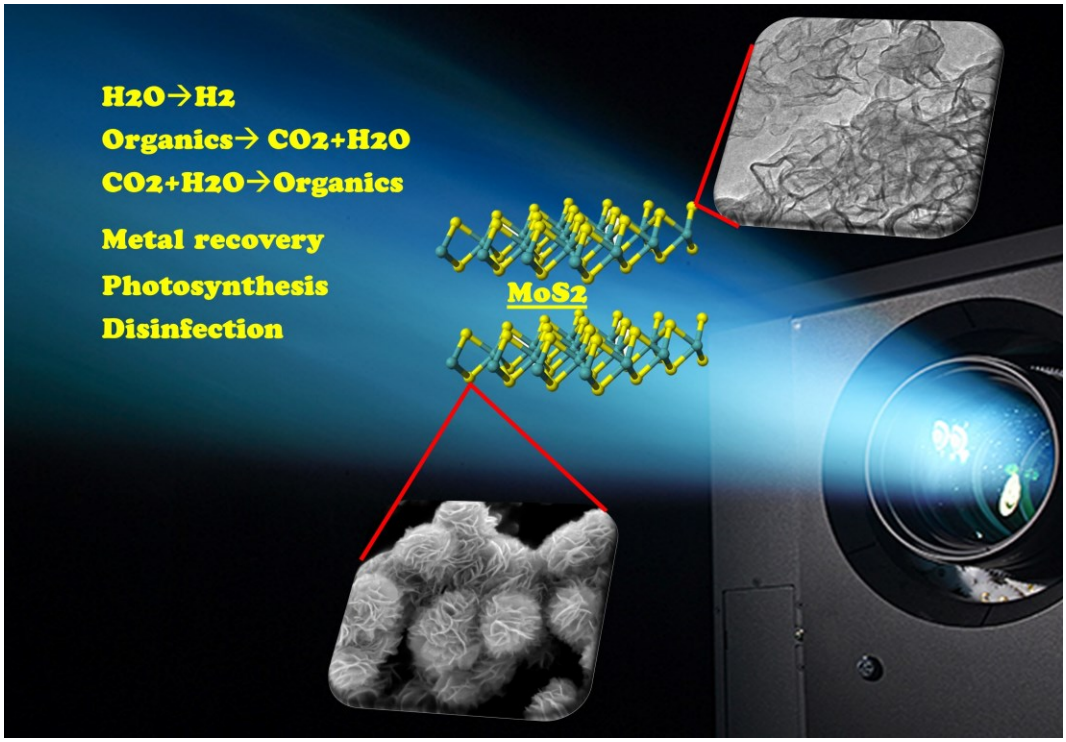

Abstract

MoS_2-based photocatalysts attract wide attention as they possess a suitable band gap for visible-light harvesting, making it a promising earth-abundant photocatalyst for hydrogen production, environmental remediation, and photosynthesis. However, the rapid recombination of photogenerated electron-hole pairs, limited quantity of active edge sites, and difficult photocatalyst separation and recycling hinder the practical application of this

material. In this review, recent development of MoS_2-based photocatalysts in various photocatalytic applications is summarized. In addition, possible approaches to enhance photocatalytic activity and separate photocatalysts from reaction media are discussed to provide a future direction in highly efficient photocatalyst design.

3.1 Introduction

Photocatalysis, as one of the advanced oxidation processes (AOPs), has been extensively studied since 1972 [1]. Applications of this advanced technique were developed from hydrogen evolution to environmental application as well as photosynthesis. Various semiconductors were also explored as a photocatalytic material. It is well known that even though TiO_2 is the original material for photocatalysis and is mostly applicable in commercial processes [2, 3], hindrances are still apparent. One of the intrinsic hindrances is the band gap of TiO_2 (~ 3.2 eV for anatase and brookite, ~ 3.0 eV for rutile), which determines that the excitation wavelength is in the UV region. It means only 5% of solar flux incident in the spectral regime can be utilized by TiO_2-mediate photocatalytic system. To overcome this problem, one of the approaches is to tune the band gap of TiO_2 via surface modification, doping *etc.* [4, 5]. Another effective method is to prepare novel visible light-responsive photocatalysts with suitable band gaps.

Among recently developed photocatalytic materials, noble-metal-free MoS_2 has attracted attention and various results were reported, due to its high mobility of charge carriers and excellent optical absorption property [6-8]. Bulk MoS_2 is an excellent catalyst for hydrodesulfurization, but not for photocatalysis due to its edge activity. That is because the S-Mo-S coordination in the crystal lattice generates unsaturated Mo and S atoms at the

edge, leading to the activity sites existing at the edges [7]. To overcome this problem to improve the photocatalytic activity of MoS_2, several studies were reported and implemented in various applications.

In this review, MoS_2-based photocatalysis applied in various fields would be comprehensively summarized. Moreover, the emerged problems as well as possible approaches would be mentioned and suggested. Future development of MoS_2-based photocatalysis would be proposed.

3.2 Properties and structures

Bulk MoS_2 has a layered structure stacked by weak van der Waals forces as shown in Figure 3.1 [9]. Each layer consists of a plane of Mo atoms sandwiched between two planes of S atoms [10]. According to the stacking sequence of MoS_2-layers and atomic coordination between a central Mo atom and surrounding S atoms, the MoS_2 crystal structure can be classified into 4 types: 1H, 1T, 2H and 3R (Figure 3.1) [11]. The 1H polytype is the most stable phase with hexagonally packed Mo atom coordinated by six S atoms. The tetragonal polytype layered crystals (1T) has Mo atoms coordinated by six S atoms in an octahedral arrangement. The hexagonal polytype layered crystals (2H) is the most common phase and can be transformed from semiconductor into the metallic 1T phase by phase engineering [12]. Rhombohedral polytype layered crystals (3R) has three layers per unit cell and each Mo atom is surrounded by six S atoms in a trigonal prismatic arrangement. Among them, the 1T and 3R structures are metastable [13]. The electronic and optical properties of MoS_2 can be varied by band gap adjustment due to the quantum confinement effect [7]. The bulk MoS_2 has a small indirect bandgap (1.3eV), which in not

sufficient to induce photocatalytic reactions and not beneficial for the separation of charge carriers. However when the size of MoS_2 is reduced to the 2-dimentional scale (*e.g.* MoS_2 nanosheets), the indirect bandgap transfers to a direct bandgap of 1.9 eV [7]. Thus, the low-dimensional MoS_2 is considered as a promising visible light-responsive photocatalyst. The fabrication methods of two-dimensional (2D) MoS_2 can be classified into mechanical exfoliation, chemical exfoliation and bottom-up approaches, such as chemical vapor deposition (CVD), physical vapor transport and wet chemical approaches. [11, 14]. The first emergence of monolayer MoS_2 is reported in 2005 using the mechanical cleavage strategy [15]. Various synthesis methods have their own advantages and intrinsic limitation. Among them, chemical exfoliation is capable of producing large quantities of mono- or few-layered MoS_2 nanosheets with relatively high carrier mobility compared with mechanically exfoliated method. As a result, it may be potentially applied to a scaled-up fabrication of two-dimensional (2D) MoS_2 [16, 17]. It is reported that the quality and quantity of prepared MoS_2 nanosheets via chemical exfoliation is highly dependent on the solvent surface tension [17, 18]. When the surface tension (γ) of solvent is about 40 mJ/m^2, the required exfoliation energy was minimized, leading to a mass of stable nanosheets. As a result, solvent with suitable surface tension is regarded as "good" solvent, such as N-methyl-pyrrolidinone (NMP) and N-vinyl-pyrrolidinone (NVP). While the most commonly used solvent, H_2O, is not suitable for MoS_2 exfoliation by itself due to a relatively high value of surface tension (72 mJ/m^2) and regarded as a "bad" solvent [16]. This modeling also demonstrated an easy way to fabricate a range of hybrid dispersions of 2D materials via adding different raw materials in a suitable solvent, whose surface tension is within well-defined ranges for both 2D materials. Compared with the inactive bulk,

nanosized MoS_2 is also in favor of increasing the specific edge sites. Recent studies have shown that the photocatalytic activity depends on the quantity of edge sites of MoS_2. Specifically, Hinnemann *et al.* observed that approximately 25 percent of edge sites are active for photocatalytic reaction [19].

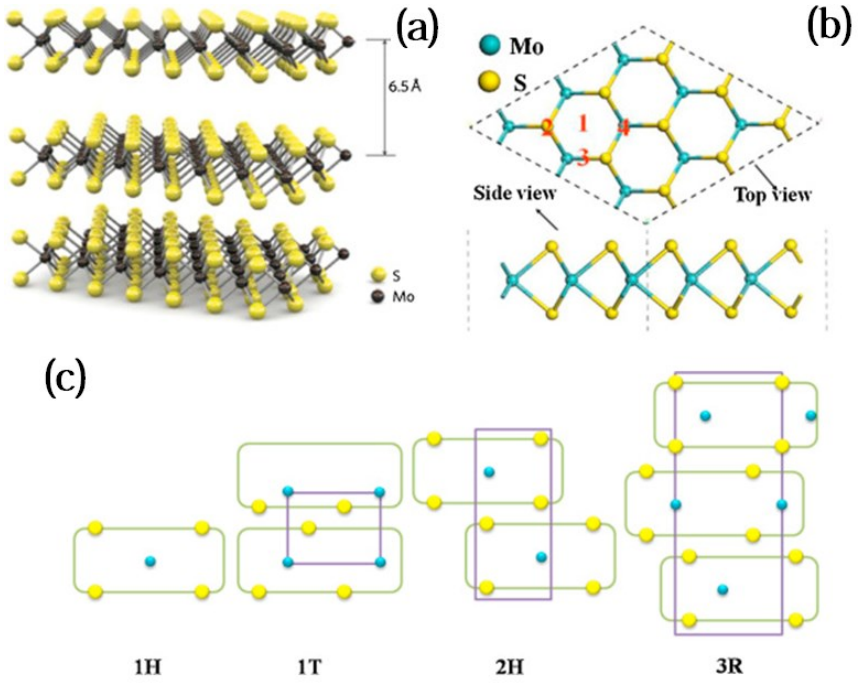

Figure 3.1. (a) Three-dimensional representation of the structure of MoS_2 (b) Active adsorption sites of MoS_2 monolayer with optimal structure (c) Schematic structure of the 1H, 1T, 2H, 3R polytypes of MoS_2. (Adapted from [20] and [11])

3.3 Applications

3.3.1 Photocatalytic hydrogen production

The increasing consumption of fossil fuel has triggered the global energy crisis and global warming. As a result, exploring a renewable and sustainable alternative to fossil fuel has become an important research area. Hydrogen has been considered as a clean energy resource that can be easily stored and used without producing any greenhouse gases. Since

the emergence of photocatalytic water splitting in 1972 [21], hydrogen evolution reaction (HER) via photocatalysis has raised enormous attention because it only requires water and solar energy. However, producing the conventional photocatalyst involves the utilization of noble metals or alloys (*e.g.* Pt) which hindered their large-scale application [22]. Thus, the development of competitive alternatives to noble metals is pursued. MoS_2 has recently been regarded as a promising candidate of noble-metal-free co-catalyst as it is an earth-abundant and visible light-responsive photocatalyst with unique physical and chemical properties [9, 23].

As a naturally layered material, the layer number of MoS_2 plays an important role of HER activity. Chang *et al.* [24] systematically investigated the relationship between MoS_2 layer number and photocatalytic hydrogen generation activity. In their study MoS_2 loaded CdS (MoS_2/CdS) with MoS_2 layer numbers varying from 1 to 112 are prepared. The corresponding hydrogen production activity in Na_2S-Na_2SO_3 and lactic acid solutions are explored respectively. It is demonstrated that the photocatalytic activity is increasing with decreasing MoS_2 layer number and the highest H_2 production rate is achieved when the MoS_2/CdS has a single-layer (SL) MoS_2. This layer-number-dependent photocatalytic activity is contributed to three major reasons. Firstly, it is well known that the unsaturated S atoms of the exposed edge sites are the active sites of hydrogen generation. With the decrease of MoS_2 layer number, more active S atoms are exposed compared to the bulk material. Therefore, the SL MoS_2 has the highest photocatalytic activity. Secondly, the transient photocurrent experiment indicates that reducing the MoS_2 layer number is beneficial to charge carriers' separation. It is likely due to the strong binding force between SL MoS_2 and CdS. Therefore, it is easier for electrons to transport from CdS to SL MoS_2

than the bulk material. Finally, the conduction band minimum (CBM) of SL MoS_2 is not only more negative than H^+/H_2 potential but also negative versus the CBM of bulk form, thereby more electrons in the conduction band can reduce H^+ to H_2.

It has been noted that the H_2 production rate of SL MoS_2/CdS in lactic acid solution (2.59 mmol h^{-1}) is higher than that in the Na_2S-Na_2SO_3 solution (2.01 mmol h^{-1}) and even higher than the production rate of Pt/CdS in lactic acid solution(0.44 mmol h^{-1}). This is because the lactic acid solution is more abundant of H^+ ions than Na_2S-Na_2SO_3 solution, facilitating H^+ absorption on active sites and H_2 generation. Moreover, the -CO form generated from the degradation process in the lactic acid solution may poison the Pt catalyst and lead to the lower H_2 production rate of Pt/CdS in lactic acid solution [25].

Very recently, Ha *et al.* reported a Cu_2ZnSnS_4 (CZTS)/MoS_2-reduced graphene oxide (rGO) heterostructure as the alternative of noble metals to produce H_2 under visible light irradiation (Figure 3.2) [26]. The photocatalytic H_2 generation rate of this ternary hybrid exhibited not only 320% higher than that of bare CZTS, but also much higher than that of Au or Pt decorated CZTS. The synergetic effect of superior conductive rGO and MoS_2 with large number of active site lead to the high photocatalytic activity of CZTS/MoS_2-rGO. On the other hand, the epitaxial growth induced formation of nanoscale interfacial contact between CZTS nanoparticles and MoS_2-rGO substrates also facilitates the transportation of photogenerated electrons. This close contact is easier for electrons to transfer from the CZTS to MoS_2 directly or indirectly via rGO achieving the electron-hole pairs' separation.

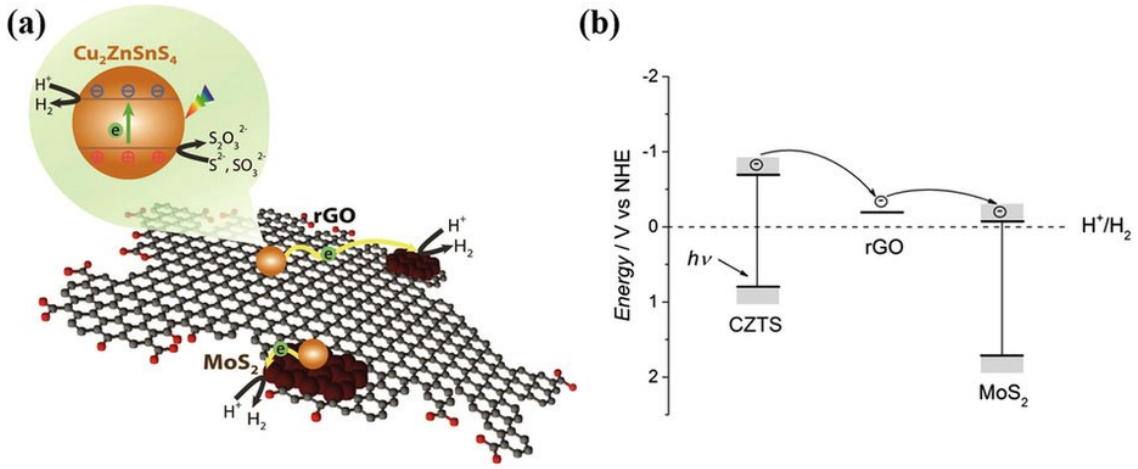

Figure 3.2. (a)Schematic illustration of charge transfer and band energy diagram in CZTS/MoS_2-rGO nanocomposites (b) Illustration of band energy diagram in CZTS/MoS_2-rGO nanocomposites (Adapted from [26])

3.3.2 Environmental remediation

With the global economic growth in recent times, the treatment of tremendous pollutants has become a global priority. Therefore, a variety of methods have been made to develop pollutant removal or pollutant degradation technologies, such as adsorption [27], biodegradation [28] and photocatalytic oxidation [29]. Compared with other technologies, the major merits of photocatalysis include the facile reaction conditions, its eco-friendly performance due to the utilization of solar energy and its lack of toxic by-products. MoS_2 has also extensively implemented in photocatalytic oxidation of pollutants. In photocatalytic oxidation process, photogenerated holes on the valence band play a significant role. The valence band edge potentials for bulk MoS_2 and monolayer MoS_2 were estimated to be 1.40 eV and 1.78 eV respectively, which are not oxidative enough to generate free radicals (*e.g.* •OH) and directly decompose pollutants [30]. However, MoS_2 may serve as a co-catalyst to improve the photocatalytic activity of the support via suppressing the recombination of photogenerated charge carriers.

3.3.2.1 Organic pollutants decomposition

To date, MoS_2-based photocatalyst has been used in many areas, such as dye degradation in water treatment, degradation of toluene in the gas phase [31]，Photocatalytic oxidative desulfurization of gasoline [32], and other decomposition of refractory pollutants [33].

In order to enhance the photocatalytic performance, the construction of unique structures to improve the charge carriers' separation and photocatalytic stability has been widely used in the design of photocatalysts. Shao *et al.* synthesized a novel ternary photocatalyst ($Ag_3PO_4/TiO_2@MoS_2$) and optimized the content of $TiO_2@MoS_2$ in the $Ag_3PO_4/TiO_2@MoS_2$ nanocomposite [34]. When the mass fraction of $TiO_2@MoS_2$ is 3.5%, almost all the methyl orange (MO) and methylene blue (MB) can be degraded within 12 and 5 min, respectively. Due to the excellent electronic conductivity of MoS_2, the TiO_2 nanofibers vertically coated with MoS_2 layer could act as a 'wire' to transfer photogenerated electrons from Ag_3PO_4 into the solution quickly. Accompanied by the photogenerated carriers' separation, the photocorrosion of Ag^+ is also effectively inhibited. As a result, the degradation rate of oxyteracycline in the presence of the $Ag_3PO_4/TiO_2@MoS_2$ only reduced by 10% after 10 cycling runs. The following XPS test further confirmed that no obvious metallic Ag is formed during the photocatalytic reaction. The inhibition effect of MoS_2 on the metal loss during photocatalytic process is also reported in another study [35]. The excellent photogenerated carriers' separation and anti-photocorrosion ability makes the MoS_2-based photocatalyst as a promising candidate in the practical applications.

The near-infrared (NIR) light accounts for 46% of the solar light. Therefore, it is important to develop NIR responsive photocatalysts for effective sunlight harvesting. A commonly

used method is combining the photocatalytic semiconductors with upconversion materials [36, 37]. For instance, Chatti *et al.* synthesized nanocomposites for Rhodamine B decomposition [36]. The degradation rate of MoS_2-$NaYF_4$:Yb^{3+}/Er^{3+} is much higher than that of $NaYF_4$:Yb^{3+}/Er^{3+} because of the layered structure of MoS_2 and the compact interface between MoS_2 and $NaYF_4$:Yb^{3+}/Er^{3+}. In addition, the degradation rate of MoS_2-$NaYF_4$:Yb^{3+}/Er^{3+} is almost three times higher than that of the mechanical mixture of $NaYF_4$:Yb^{3+}/Er^{3+} nanocrystals and MoS_2 which reveals that the close contact at the interface is the key for the transmission of photon energy and further influence the NIR photocatalytic activity. Although the NIR responsive photocatalyst provides an approach for sunlight harvesting, it still suffers from the low photocatalytic efficiency compared with other visible light-responsive photocatalysts [38, 39]. Thereby, the NIR responsive photocatalyst still needs further development before it can be deemed practical.

3.3.2.2 Inorganic pollutants treatment

The diverse inorganic pollutants discharged into the environment have generated increasing ecological concerns. Nowadays, MoS_2-based photocatalysts have been widely used in the treatment of heavy metals [35, 40, 41] and nitric oxide (NO) removal [42, 43].

Chromium (VI) is a typical carcinogenic heavy metal that widely existed in wastewater due to its extensive use in the field of leather tanning, wood preservation, mineral extraction and so on [44, 45]. Therefore, the development of advanced technologies for efficient Cr(VI) removal has become a hot spot for research. Presently, a lot of researchers have focused on the adsorption and photocatalytic reduction of Cr(VI) using MoS_2-based photocatalysts [35, 40, 46]. Gao and coworkers have investigated the efficiency of a novel organic-inorganic hybrid, Polyaniline (PANI) modified MoS_2, as the

adsorbent/photocatalyst for Cr(VI) removal [40]. Based on their results, the Cr(VI) adsorption feature is highly pH dependent. At low pH values (pH:1.5-4.0), the protonated amine groups of PANI is favourable to attract negatively charged Cr(VI) anions, such as $HCrO_4^-$ and $HCr_2O_7^{2-}$ leading to a higher removal efficiency. The acidic condition also facilitates the photocatalytic reduction of Cr(VI), because the reduction product ($Cr(OH)_3$ under alkaline conditions can precipitate on the surface of PANI@MoS_2. Therefore, the active sites can be covered and photocatalytic activity will be inhibited. Compared with bare PANI and MoS_2, PANI@MoS_2 possessed the highest Cr(VI) removal rate with or without UV irradiation due to the good adsorption capacity of PANI and the flower-like MoS_2 that provides a large surface area and active binding sites. In addition, this new adsorbent/photocatalyst also has better Cr(VI) removal ability than that of other adsorbents [44, 47]. The effects of ionic strength and reusability of the PANI@MoS_2 were also tested. The photocatalytic reductive adsorption features of Cr(VI) is shown in Figure 3.3. This work implies that the adsorption capacity of MoS_2-based materials targeting heavy metal ions may not be negligible and the pH value of the wastewater should be considered when a MoS_2-based material is used for Cr(VI) removal. This conclusion may also be applied to other applications of MoS_2-based materials, such as photocatalytic degradation of organic pollutants. Wang *et al.* reported a ternary nanocomposite composed of Fe^0, graphitic carbon nitride (g-C_3N_4) and MoS_2 (GCNFM) for the long-term application of Cr(VI) reduction [35]. Upon an excitation of visible light, the photogenerated electrons could transfer to the CB of MoS_2 and doped Fe^0 particles due to the suitable band alignment. This promoted the separation of charge carriers leading to an enhanced Cr(VI) reduction efficiency compared with g-C_3N_4 (GCN), MoS_2-modified GCN and Fe^0 doped GCN. Moreover, the Fe^{2+}/ Fe^0

redox potential (E_0 = -0.44 V *vs* NHE) is more negative than $Cr_2O_7^{2-}$/Cr(III) (E_0 = 1.35 V *vs* NHE). Therefore, Fe^0 particles could also participate in the reaction of Cr(VI) reduction and be consumed with a prolonged reaction. However, the recycle experiment indicates a good reusability of this nanocomposite. There is no obvious decrease in Cr(VI) reduction efficiency after five repeated cycles. This is attributed to the fact that the Fe^0 could be regenerated by the reduction of photogenerated electrons. As a result, this work provides an approach to a recyclable photocatalyst design.

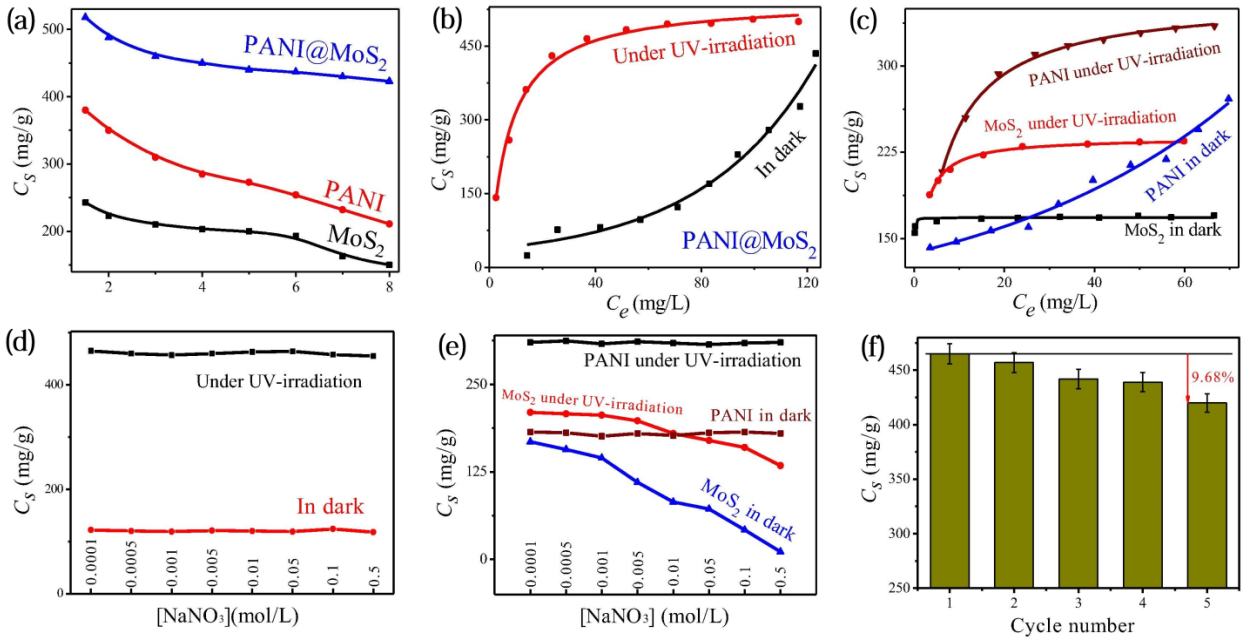

Figure 3.3. (a) The effect of pH on Cr(VI) adsorption in the presence of different materials under UV irradiation (I=0.01 M $NaNO_3$ and T=293K); (b) and (c) Adsorption isotherms of Cr(VI) on different materials with or without UV irradiation (pH=3.0 ±0.1, I=0.01 M $NaNO_3$ and T=293K); (d) and (e) The effect of ionic strength on Cr(VI) adsorption in the presence of different materials with or without UV irradiation (pH=3.0 ±0.1); (f) Reusability of PANI@MoS_2 for Cr(VI) removal. (Adapted from [40])

Nowadays, MoS_2-based photocatalysts have also been used for air purification, especially for NO removal [42, 43]. A novel Z-scheme structure, $(BiO)_2CO_3/MoS_2$, is reported by

Xiong *et al.* for NO removal in gas phase [43]. The content of the MoS_2 nanocomponent in the structure can affect the efficiency of NO removal. An enhanced efficiency in NO removal is observed when the MoS_2 content is increased from 1% to 5%. However, further increasing content of MoS_2 leads to a decrease in NO removal efficiency. The possible reason for the negative effect of excessive content could be the blocking of incident light by MoS_2 [48]. Although $(BiO)_2CO_3$ and MoS_2 are n-type and p-type semiconductors, respectively, the p-n junction is not formed in this photocatalyst system. This is confirmed by the electron spin resonance trapping experiment which revealed that holes and $\bullet O_2^-$ were the main reactive oxidization species. Instead, a novel Z-scheme photocatalyst was obtained. This structure can effectively separate photogenerated electrons and holes without compromising the redox ability of the charge carriers. Accompanied by the porous and hierarchical structures, the performance of $(BiO)_2CO_3/MoS_2$ is better than that of pure $(BiO)_2CO_3$ and MoS_2. However, the activity loss caused by MoS_2 oxidation/corrosion should be considered, which might hinder the practical application of this type of material [48]. Wen *et al.* synthesized MoS_2-g-C_3N_4 nanocomposites by a simple ultrasonic dispersion method and tested their photocatalytic activity by NO removal [42]. The influence of MoS_2 content on the photocatalytic activity of MoS_2-g-C_3N_4 nanocomposites exhibited a similar trend of that in $(BiO)_2CO_3/MoS_2$. A slight increase of MoS_2 content is beneficial to the photocatalytic activity. However, further increase of MoS_2 content could inhibit light absorption and the increasing intermediates (HNO_2 and HNO_3) loaded on the photocatalytic surface may also block the activity. The highest photocatalytic activity was obtained when the weight content of MoS_2 was 1.5 wt%. The resulting NO removal efficiency is enhanced by 65% when compared with bare g-C_3N_4.

3.3.2.3 Photocatalytic disinfection

Extensive research has been conducted for the photocatalytic inactivation of microbial pollutants due to the superior inactivation ability of photocatalytic semiconductors compared with conventional disinfection methods [49-51]. Chlorination is a typical conventional disinfection method, which suffers from many problems. For example, chlorine can react with natural organic matter (NOM) to form some undesirable disinfection by-products (DBPs) and it is not effective for some pathogens, such as protozoa which are zoonotic pathogens [52]. Even some advanced disinfection methods such as ozonation also have their own hazardous disinfection by-products and lack of disinfection residuals [49]. In contrast, photocatalytic disinfection is a reusable and eco-friendly process that does not form DBPs due to its relatively inert chemical and biological features.

The major mechanism of photocatalytic disinfection involves the reactive oxygen species [51]. They can trigger the breakdown of cell membranes and then promote the internalization of the semiconductor photocatalyst, ultimately leading to cell death [53, 54]. Therefore, improving the separation of photogenerated electrons and holes is in favor of photocatalytic disinfection efficiency.

Due to its excellent conductivity and unique layered structure, MoS_2 can be used to combine with other semiconductors to enhance the separation of photogenerated charge carriers resulting in promoted ability of photocatalytic disinfection. Awasthi *et al.* attached flower-like ZnO on the surface of layered MoS_2 via the hydrothermal method [55]. An enhanced antibacterial activity was observed by using gram negative *E. coli* bacteria in comparison with pristine ZnO and MoS_2. It is not only attributed to the efficient separation

rate of electron and hole pairs in the ZnO/MoS_2 nanocomposite, but also the increased surface area induced by the layered MoS_2. According to the SEM and TEM images, the introduction of MoS_2 could lead to a larger surface area with reduced particle size compared with pristine ZnO. The smaller size could facilitate the administration of nanoparticles, thus resulting in better disinfection ability [56]. Liu *et al.* prepared a ternary photocatalyst (carbon nanotubes(CNTs)-MoS_2-Ag) and discovered its antibacterial activity against the *Staphylococcus aureus* and *Escherichia coli* [57]. It is reported that the antibacterial mechanism of this material not only includes the microorganism killing effect of Ag particles, but also relies on light absorption. The CNTs-MoS_2-Ag nanocomposites showed good antibacterial activity both in dark and visible light. However, the antibacterial activity of CNTs-Ag only enhanced slightly under illumination compared with that in the dark. Herein, the ultra-thin MoS_2 could improve the photo-absorption and catalytic activity.

3.3.3 Photosynthesis

Excited by the incident photons, photocatalytic can generate a series of redox species for the photoreduction or photooxidation process with adsorbed organic or inorganic substrates to produce targeted substances. To date, various types of photosynthesis processes have been explored such as photoreduction of carbon dioxide for solar fuel generation [58], photoreduction of nitrogen for ammonia production [59, 60] and photosynthetic production of organics [61].

Photosynthetic production of organics has been considered as a promising alternative to the conventional route of organic production due to its mild conditions and environmentally friendly process. Conventional route of organic production usually requires a large excess amount of strong redox chemicals and hazardous heavy metal

catalyst [61, 62]. In comparison, the photocatalytic organic synthesis utilizes sustainable solar light as the energy source and nontoxic photocatalysts which are chemically stable and reusable with the negligible loss of catalytic ability [61]. Wang *et al.* developed a visible light-driven photocatalyst, TiO_2 nanoparticle modified MoS_2 layer, for aerobic thiocyanation of indoles at room temperature [62]. The optimal isolated yield (93%) was achieved when the molar ratio of TiO_2 to MoS_2 is 10. A possible mechanism for the photocatalytic thiocyanation of indoles is shown in Figure 3.4. MoS_2 served as photosensitizer and synergistically worked with TiO_2 to boost the photocatalytic activity. Based on the recycling test, this TiO_2/MoS_2 nanocomposite exhibited good recyclability with no substantial loss of activity in eight repeated cycles. Thus, this work provided a competitive facile, simple work-up and eco-friendly route for thiocyanation of indoles.

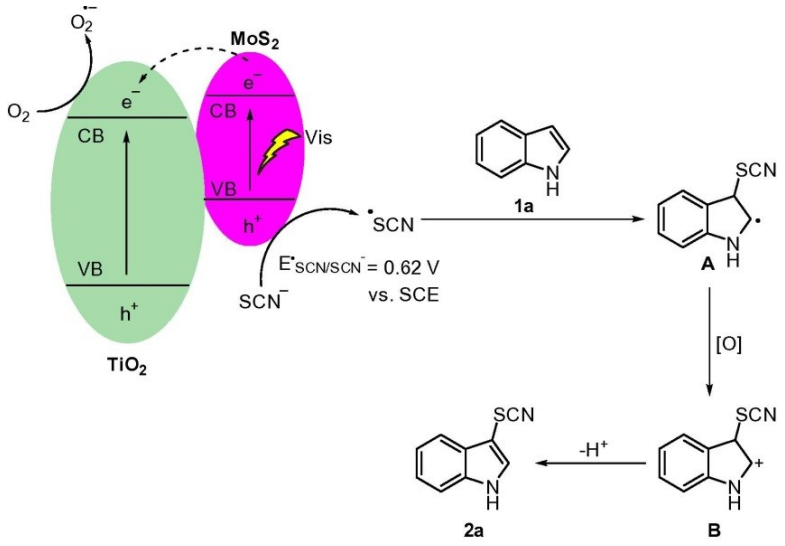

Figure 3.4. Possible mechanism for photocatalytic thiocyanation of indoles. (Adapted from [62])

N_2 reduction for ammonia production plays an important role in the industrial and biological fields [63]. Traditional Haber-Bosch process requires a lot of energy and the total annual CO_2 emission could reach 300 million metric tons in this process [64]. As a

result, great efforts have been adopted in order to economically and environmentally improve the ammonia production process [59, 65, 66]. Sun *et al.* took advantage of ultrathin MoS_2 to generate tightly bound excitons to capture additional electrons for the multi-electron reduction process of N_2 [67]. This electron-rich system can reduce the thermodynamic barrier for the reaction of N_2 reduction and avoid the formation of high-energy intermediates, such as N_2H and N_2H_2. Although the highest photocatalytic ammonia synthesis rate (0.5 mg/L) still cannot meet the practical demand, this pioneering work provides a possibility of applying electron-rich semiconductor photocatalysts (*e.g.* n-type semiconductor) to the multi-electron reduction process.

3.3.4 Bifunctional photocatalysis

Nowadays, extensive efforts have been dedicated to the study of bifunctional photocatalysis [35, 68-70]. Due to the natural properties of semiconductor photocatalysts, they can generate both reductive and oxidative species simultaneously under an illumination [71]. Thereby, a bifunctional photocatalyst generally contains an active wide band gap semiconductor as the substrate that can be ideally involved in a variety of photocatalytic reduction and oxidation reactions for different applications. For example, Rong *et al.* developed a new visible light-responsive nanocomposite, Er^{3+}:$Y_3Al_5O_{12}$/MoS_2-$NaTaO_3$-PdS, for photocatalytic degradation and hydrogen production [33]. In their system, Er^{3+}:$Y_3Al_5O_{12}$ converts the visible light into ultraviolet light, which is capable of exciting the $NaTaO_3$ to generate the electron-hole pairs. After that, the photo-induced electrons and holes can be effectively separated by transfer to the MoS_2 co-catalyst and PdS co-catalyst, respectively. Subsequently, the separated charge carriers can degrade refractory pollutants and produce hydrogen. The band energy of Er^{3+}:$Y_3Al_5O_{12}$/MoS_2-$NaTaO_3$-PdS

nanocomposite photocatalyst is shown in Figure 3.5. This nanocomposite also retained good photocatalytic performance after three repetitive cycles. The excellent stability of this new material makes it a promising candidate for bifunctional photocatalyst.

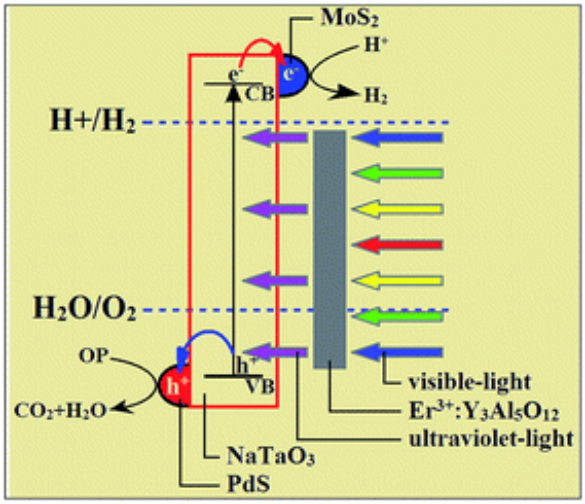

Figure 3.5. The band energy of Er^{3+}:$Y_3Al_5O_{12}$/MoS_2-$NaTaO_3$-PdS nanocomposite photocatalyst (Adapted from [33]).

Briefly, bifunctional MoS_2-based photocatalysts can be classified into four groups according to their applications: organic pollutant decomposition and photocatalytic reduction of Cr(VI) [35], organic pollutant decomposition and photocatalytic hydrogen production [68], organic pollutant decomposition and photocatalytic disinfection [55], and organic pollutant decomposition and metal ion sensor [72]. The detailed bifunctional photocatalysts and their applications are summarized in Table 2.1.

Although promising in principle, bifunctional photocatalysts still suffer from many challenges before they can be used in a wide range of practical applications. Firstly, the photocatalytic activity of a bifunctional photocatalyst is generally lower than that of a monofunctional photocatalyst [69, 73]. In addition, performing two different photocatalytic

processes simultaneously cannot be reached currently due to the different reaction conditions of these processes and the lack of reactor designing [33].

Table 2.1. Summarized bifunctional photocatalysis

Application of photocatalyst	**Photocatalyst**	**Description**	**Ref.**
Organic pollutant decomposition and photocatalytic reduction of Cr(VI)	n-$BiVO_4$@p-MoS_2	Photocatalytic degradation of Crystal violet and photocatalytic reduction of Cr(VI) under visible light	[41]
	Fe^0 doped g-C_3N_4/MoS_2	Photocatalytic degradation of rhodamine B (RhB) and photocatalytic reduction of Cr(VI) under visible light	[35]
Organic pollutant decomposition and photocatalytic hydrogen production	TiO_2/MoS_2/TiO_2	Photocatalytic degradation of MO and photocatalytic hydrogen production under visible light	[74]
	g-C_3N_4/Ag/MoS_2	Photocatalytic degradation of RhB and photocatalytic hydrogen production under visible light	[75]
	TiO_2@MoS_2	Photocatalytic degradation of RhB and photocatalytic hydrogen production under irradiation with wavelength in the range of 280-700nm	[76]
	TiO_2-MoS_2	Photocatalytic degradation of RhB and photocatalytic hydrogen production under UV irradiation ($\lambda < 400$ nm)	[77]
	MoS_2/TiO_2	Photocatalytic degradation of MO under visible light and photocatalytic hydrogen production under simulated solar light	[68]
	N-TiO_{2-x}@MoS_2	Photocatalytic degradation of MO under visible light and photocatalytic hydrogen production under irradiation from a solar simulator	[69]
	$ZnIn_2S_4$/ MoS_2	Photocatalytic degradation of MO and photocatalytic hydrogen production under visible light	[78]
	Er^{3+}:$Y_3Al_5O_{12}$/MoS_2–$NaTaO_3$–PdS	Photocatalytic degradation of amaranth and photocatalytic hydrogen production under visible light	[33]
Organic pollutant decomposition and photocatalytic disinfection	MoS_2/ ZnO	Photocatalytic degradation of phenol red and photocatalytic disinfection under UV lamp and natural sun light	[55]
	MoS_2-Bi_2WO_6	Photocatalytic degradation of RhB and photocatalytic disinfection under visible light	[70]
Organic pollutant decomposition and metal ion sensor	MoS_2/C_3N_4	Photocatalytic degradation of MO under visible light and photoelectrochemical selective sensing of Cu^{2+}	[72]

3.4 Problems along with possible approaches

3.4.1 Morphology control

Morphology of MoS_2 influenced its photocatalytic performance to some extent. Hu *et al.* has explored the effect of MoS_2 morphology and particle size on its photocatalytic properties [79]. They have prepared MoS_2 with two-type morphologies, namely, nano-ball and nano-slice. It was found that for bulk MoS_2, owing to its large size and the narrow band gap, no hydroxyl free radicals were produced. When the size decreased to nanosize range, the photocatalytic activity of MoS_2 in the degradation of organic pollutants in water was greatly improved, and the nano-ball MoS_2 performed better that the nano-slice MoS_2, which was due to the curvature effect of the curved basal surface. Tan *et al.* have reported the fabrication of MoS_2-ZnO nano-heterostructure with MoS_2 of different morphology and explored its effect on the photocatalytic activity [80]. Four different precursors, including $(NH_4)_2S$, C_2H_5NS, CH_4N_2S and Na_2S, were used in preparing MoS_2 with four different morphologies. When the morphology of MoS_2 changed from bulk to layered, the photocatalytic activity was significantly influenced. As calculated by Kuc *et al.* [81], band gap of MoS_2 was greatly influenced by the number of MoS_2 layers. With decreases in the number of layers from 8 to 1, the band gap was increased from 1.2 eV to 1.9 eV, and the band transition was changed from indirect to direct transition. The change in the band gap values as well as the transition type is in favor of supressing the recombination rate of photogenerated charge carriers, so as to improve the photocatalytic activity of MoS_2 [76] (*e.g.* improving the hydrogen evolution rate [82, 83]). Controlling the morphology of MoS_2, by means of adjusting the preparation conditions or reducing the number of layers, is an effective approach to improve its photocatalytic performance.

3.4.2 Modulation of energy band by doping

In order to achieve an enhanced photocatalytic activity, decorating the band gap energy of semiconductor photocatalysts by chemical dopants is extensively used. The impurity level generated by dopants could trap photogenerated charge carriers [39] and enhance the visible light absorption of the photocatalyst [69, 84]. With respect to MoS_2-based photocatalysts, the commonly used metallic dopants include Co [85], Ni [85], Ag [39], Fe [35] and Ti^{3+} [69, 86], while the non-metallic dopants include N [87-89] and P [90].

Liu *et al.* reported that the mid gap level generated by N dopant could reduce the bandgap energy of MoS_2, improving the visible light adsorption and the degradation activity of RhB [88]. Moreover, N-doped MoS_2 has a larger surface area with more exposed active sites in comparison with bare MoS_2. The large surface area of N-doped MoS_2 increases the surface adsorption ability of the reactants, thus enhancing the degradation activity of RhB. However, the photocatalytic activity of this N-doped MoS_2 is still very low (rate constant for the photocatalytic degradation of RhB: 0.06928 min^{-1}) due to the intrinsic narrow band gap of MoS_2. Therefore, combining MoS_2, dopants and another photocatalyst is an effective way to improve the photocatalytic activity. For example, MoS_2 has been combined with N-doped graphene for improved photocatalytic activity [87, 89]. By doping with nitrogen, a reduced graphene (rGO) can change from a passive support for charge transport to an active n-type semiconductor photocatalyst for enhanced charge transport and generation [89]. The integration of n-type N-doped rGO and p-type MoS_2 can form multiple nanoscale p-n junction composites which can both facilitate the generation of photoinduced charge carriers and inhibit charge recombination. Additionally, the novel p-n junction composites indicated a wide spectral response, from UV irradiation to the near-

infrared light, for photocatalytic hydrogen generation [89]. Carraro *et al.* combined N-doped crumpled graphene and MoS_2 as p-n nanojunctions by a novel one-pot aerosol process [87]. The as prepared p-n nanojunctions displayed a photocatalytic efficiency that is 7-fold higher than pure MoS_2 due to the enhanced charge transfer and separation ability provided by the local p-n junction. The existence of C-N-Mo bonds also indicated that the doped N atoms can serve as an anchoring center for the assembly of MoS_2 nanoparticles [87]. Liu developed a core-shell nanostructure consisting of N and Ti^{3+} co-doped TiO_2 core and MoS_2 shell for both photocatalytic degradation and hydrogen production [69]. N doping and Ti^{3+} self-doping created new mid gap stages above the valance band and at the bottom of the conduction band of TiO_2, respectively. These generated new mid gap states narrow the band gap of TiO_2 to increase visible light adsorption. The introduction of a MoS_2 shell further improved the photocatalytic activity due to the effective charge separation capacity supplied by the core-shell heterojunction structure and the abundant active sites provided by the MoS_2 shell.

Some studies also revealed that transition metal ion (*e.g.* Co^{2+} and Ni^{2+}) doped MoS_2 can expose more unsaturated sulfur atoms for hydrogen production and reduce the HER over potential, thus enhancing the photocatalytic activity of MoS_2-based hybrid photocatalysts [85]. In some cases, doped transition metal ions could also capture the photogenerated electrons to promote charge separation [35]. With the help of a rationally designed band alignment, partial transition metal ions can be regenerated, highlighting their potential ability for long-term practical applications [91].

3.4.3 Band alignment via forming heterojunction

Besides doping, formation of heterojunctions between MoS_2 and other semiconductors is another ingenious method to improve the photocatalytic activity of MoS_2-based photocatalysts [91-94]. Generally, MoS_2-based heterostructure is formed by the *in situ* growth of MoS_2 precursor on the surface of another semiconductor, followed by MoS_2 nucleation and growth [25, 95]. Based on the band alignments, conventional heterojunction photocatalysts can be divided into three groups (see Figure 3.6) [96]. As illustrated in Figure 3.6c, the band alignments of type III is not in favor of charge separation because the bandgaps of two semiconductors are not overlapped. In contrast, type I and type II heterojunction photocatalysts can facilitate the charge separation by different mechanisms. Take the CdS/MoS_2, a type I heterojunction photocatalyst, as an example [91]: photogenerated electrons in the conduction band of CdS nanosheets can transfer to the conduction band of MoS_2 nanosheets because MoS_2 possesses a more positive conduction band than CdS (see Figure 3.6a). As a result, the photogenerated electron-hole pairs in CdS can be separated to further enhance the photocatalytic activity. However, the photogenerated holes in valence band of CdS could transfer to the valence band of MoS_2 due to the more negative valence band of MoS_2, leading to the accumulation of both electrons and holes in the MoS_2 semiconductor. Therefore, charge carriers may not be effectively separated in type I CdS/MoS_2 heterojunction photocatalyst. For type II heterojunction photocatalysts, the pathway for charge transfer is shown in Figure 3.6b (MoS_2/g-C_3N_4 as an example) [97]. After activated by visible light, photogenerated electrons can transfer from the conduction band of g-C_3N_4 to the conduction band of MoS_2 while holes move oppositely. Consequently, electrons and holes are accumulated in MoS_2

and g-C_3N_4, respectively. The spatial separation of charge carriers can significantly reduce the charge recombination and achieve high photocatalytic activity.

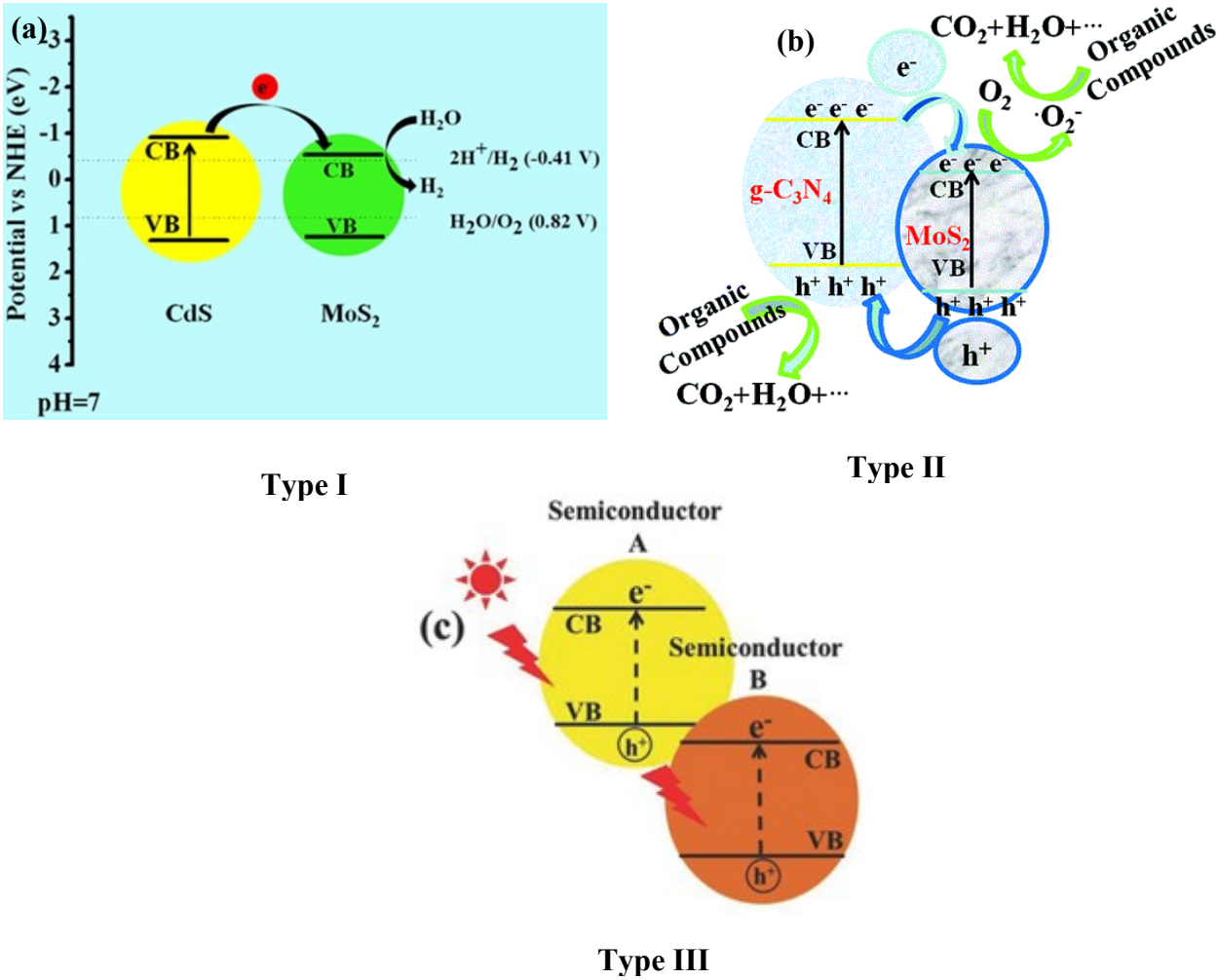

Figure 3.6. different types of conventional heterojunction photocatalysts and their corresponding charge transfer pathways: (a) type I (Adapted from [91]), (b) type II (Adapted from [97]), and (c) type III (Adapted from [98]).

Another interesting heterojunction, p-n heterojunction, is able to considerably improve charge separation compared to type II heterojunction due to the formation of an inner electric field [98-102]. For example, our group reported a novel p-n heterojunction photocatalyst, p-MoS_2 / n-Bi_2WO_6, via a simple bath sonication method (see Figure 3.7a)

[70]. At the interface of Bi_2WO_6 and MoS_2, electrons on the n-Bi_2WO_6 tend to diffuse into the p-MoS_2. Simultaneously, holes on the p-MoS_2 tend to diffuse to the opposite direction. Therefore, a built-in electric field is formed at the p-n interface. Under illumination, the electrons and holes can be rapidly separated by the synergetic effect between the built-in electric field and the band alignments. As a result, the fast charge recombination can be efficiently inhibited. These heterojunction photocatalysts all exhibit good separation efficiency of photogenerated electron-hole pairs, though the electrons and holes all eventually accumulate at the conduction band or valence band with lower redox potentials. In order to achieve good charge separation efficiency without compromising the redox ability of the charge carriers, the Z-scheme heterojunction photocatalysts have been applied. Xiong *et al.* reported a Z-scheme heterojunction system, $(BiO)_2CO_3/MoS_2$, for NO removal [43]. Under visible light irradiation, both $(BiO)_2CO_3$ and MoS_2 can be excited to generate electron-hole pairs. Subsequently, the photogenerated electrons in the conduction band of $(BiO)_2CO_3$ could migrate and combine with the holes in the valence band of MoS_2. As a result, photogenerated electrons and holes are spatially separated and eventually accumulated at the conduction band of MoS_2 and the valence band of $(BiO)_2CO_3$, respectively (see Figure 3.7b). Moreover, ternary heterojunctions have been reported as an effective architecture to further improve the photocatalytic activity of binary structures. Zhang and co-workers reported a ternary nanocomposite, $TiO_2/g\text{-}C_3N_4/MoS_2$, which possessed two type II heterojunctions at the interface of $TiO_2/g\text{-}C_3N_4$ and TiO_2/MoS_2 [103]. As shown in Figure 3.7c, photogenerated electrons could transfer from the conduction band of g-C_3N_4 (or MoS_2) to the conduction band of TiO_2 and photogenerated holes in the valence band of TiO_2 could migrate to the valence band of g-C_3N_4 (or MoS_2). Eventually,

the photogenerated electrons are mainly collected by TiO_2 which further reduces the O_2 to $\bullet O_2^-$ for dye degradation, while the photogenerated holes are mainly collected by g-C_3N_4 and MoS_2. It is reported that MoS_2 modified TiO_2/g-C_3N_4 nanocomposites have a higher photocatalytic activity relative to TiO_2/g-C_3N_4 binary nanocomposites due to the synergetic effect between TiO_2/g-C_3N_4 and TiO_2/MoS_2 heterojunctions. Specifically, the TiO_2/g-C_3N_4/MoS_2 ternary photocatalyst could not only extend the light absorption range but also enhance the light utilization rate. Other MoS_2-related ternary photocatalysts were also reported to have advanced performances in photocatalysis [104, 105].

In conclusion, a rational design of band alignments to fabricate heterojunctions suggests an efficient approach to enhanced photocatalytic activity.

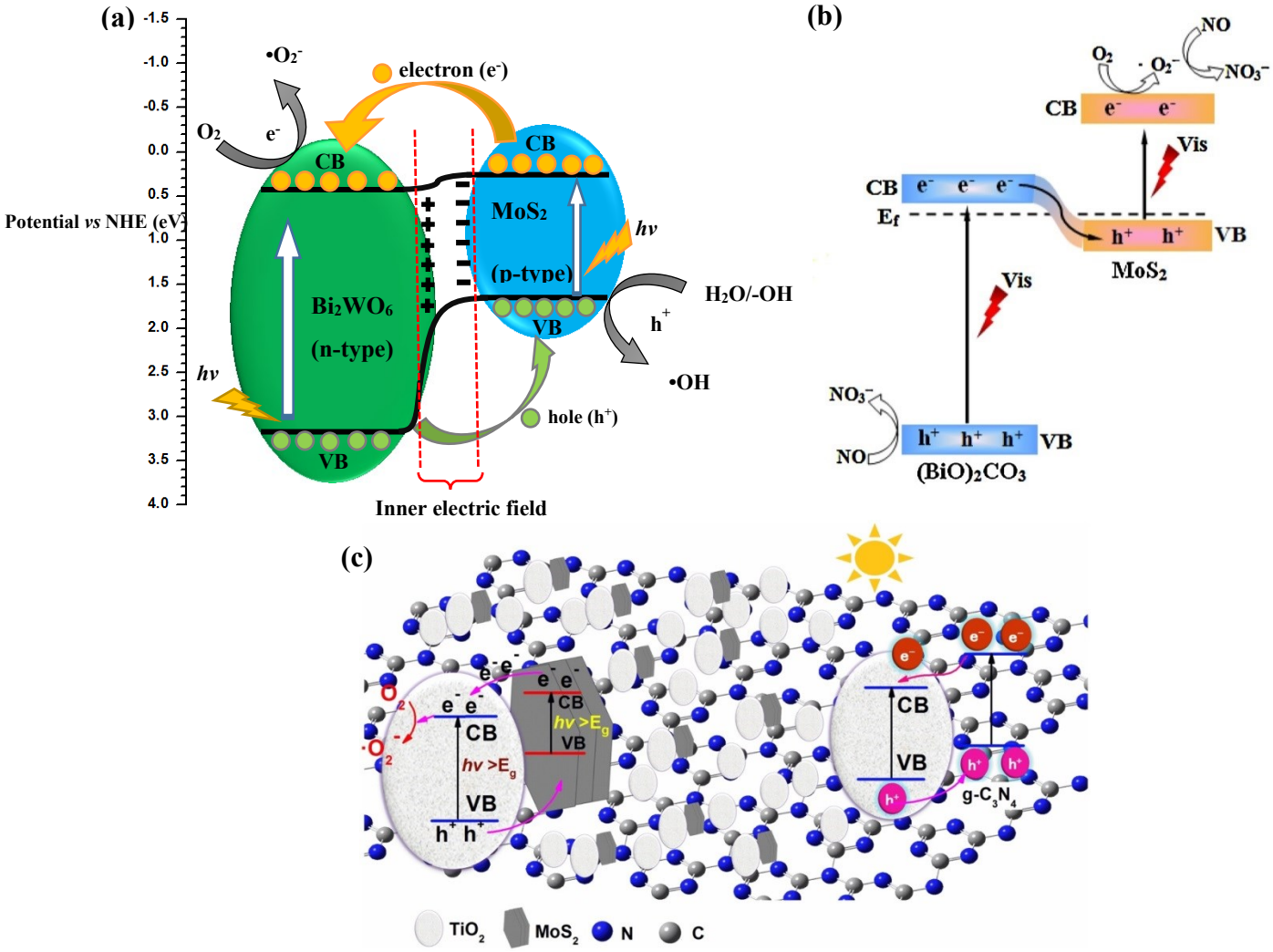

Figure 3.7. Typical samples of heterojunction photocatalysts and their corresponding charge transfer pathways: (a) p-MoS_2 / n-Bi_2WO_6 heterojunction photocatalyst (Adapted from [70]), (b) $(BiO)_2CO_3$/MoS_2 Z-scheme heterojunction system (Adapted from [43]), and (c) TiO_2/g-C_3N_4/MoS_2 ternary heterojunction photocatalyst (Adapted from [103]).

3.4.4 Surface plasmon resonance (SPR)–enhanced photocatalysis

Briefly, SPR is the collective oscillation of electrons induced by the light at the plasmon frequency of plasmonic metallic nanostructures [106-114]. Extensive research has indicated that the nanostructure size, shape, composition, location and proximity to other nanostructures can affect the frequency of this resonance [115-119]. By tuning these factors,

the absorption spectrum of plasmonic-metal assembled semiconductors can be extended from UV to visible light or even NIR. The two major photocatalytic enhancement mechanisms of plasmonic-metal assembled semiconductors include charge transfer enhancement and local electric field enhancement [106]. In the former mechanism, metallic plasmonic nanoparticles act as electron donors injecting plasmon-induced electrons, also known as hot electrons, to the conduction band of adjacent semiconductors to increase the photocatalytic reaction rate. The latter mechanism attributes the enhanced photocatalytic activity to the intense local electric field generated by the plasmonic metallic nanostructures. It is reported that the generation rate of charge carriers in these specific electric fields could be 1000 times higher than that of the incident electromagnetic field [120, 121].

Silver (Ag) and gold (Au) nanostructures have been integrated with MoS_2-based photocatalysts to broaden the absorption spectrum and improve the separation efficiency of photoinduced charge carriers [75, 122]. The assembling of Ag nanoparticles in the ternary photocatalyst, g-C_3N_4/Ag/MoS_2, improved the visible-light absorption of MoS_2 [75]. Due to the surface plasmon resonance effect, hot electrons generated by the Ag nanoparticles could inject to the conduction band of semiconductors, which left behind holes that can combine with other donor ions, further improving the charge carriers' separation. Zhang *et al.* investigated the HER activity of Au nanostructure assembled monolayer MoS_2 [122]. It is shown that the HER activity of a plasmonic photocatalyst relies on the shape of the Au nanostructure. Specifically, Au nanorods (Au NRs) assembled MoS_2 exhibited superior HER activity than that of Au nanospheres (Au NSs) and Au nanotriangles (Au NTs) assembled MoS_2 due to the higher amplitude of the longitudinal

SPR of Au NRs. Moreover, the single particle photoluminescence measurement confirmed the transfer of plasmon-reduced hot electrons at the Au-MoS_2 interface. The hot electrons could further transfer to the active sites of MoS_2 to produce H_2. The resulting holes located in the Au nanostructures could act with lactic acid, thus further facilitating the Au regeneration. The plasmon-induced electric field is also believed to enhance the charge generation rate and increase the recombination lifetime (~800 ps). As a result, promoting the interfacial hot electron transfer in plasmonic photocatalysts is a promising way to improve photocatalytic activity. It is notable that the enhancement of photocatalytic activity could also attribute to the plasmon induced 2H-to-1T phase transition in MoS_2 monolayer [123, 124]. The phase transition of plasmonic MoS_2 photocatalyst and its corresponding photocatalytic efficiency can be tuned by the wavelength and intensity of the incident laser [124]. These pioneering works pave the way for the development of MoS_2-based plasmonic photocatalysis.

3.4.5 Preparation of amorphous MoS_2

The photocatalytic activity of crystalline MoS_2 (c-MoS_2) is inhibited by the sparse active edge sites on the surface of MoS_2 photocatalysts. Unlike crystalline MoS_2, amorphous MoS_x (a-MoS_x) possess many unsaturated atoms or defects acting as the active sites for photocatalysis due to the highly disordered atomic arrangements [22]. Therefore, amorphous MoS_x has recently been considered as an alternative photocatalyst to improve the photocatalytic hydrogen evolution activity [7, 125-127].

Wei *et al.* has firstly shown that amorphous MoS_x has a promoting effect for photocatalytic hydrogen production [125]. This promoting effect can be ascribed to the existence of a large number of unsaturated S atoms which can adsorb hydrogen ions and further lead to

H_2 production. The promoting effect of photocatalysis is also dependent on the loading amount of MoS_2. At the optimum MoS_2 loading amount (0.6 *wt*%), the hydrogen generation rate of $MoS_2/ZnIn_2S_4$ nanocomponent is even higher than that of 1.0 wt% Pt loaded $ZnIn_2S_4$ under similar reaction conditions. In addition, it is reported that amorphous MoS_x existed in the $MoS_2/ZnIn_2S_4$ nanocomponent when the sample was calcinated at a lower temperature (*i.e.* 623K). The increasing calcination temperature could lead to a higher degree of MoS_2 crystallinity and lower HER activity. The similar results have also been reported by Niefind *et al.* [127]. The as-prepared amorphous MoS_x exhibited excellent thermal stability up to 350 °C. The crystallization process can be induced by heat treatment or exposure to an irradiation (*e.g.* electron beam of TEM) leading to a transformation of amorphous MoS_x to 2H-MoS_2. As shown in Figure 3.8, the as prepared amorphous MoS_x exhibited considerably higher HER activity compared to their crystalline counterparts.

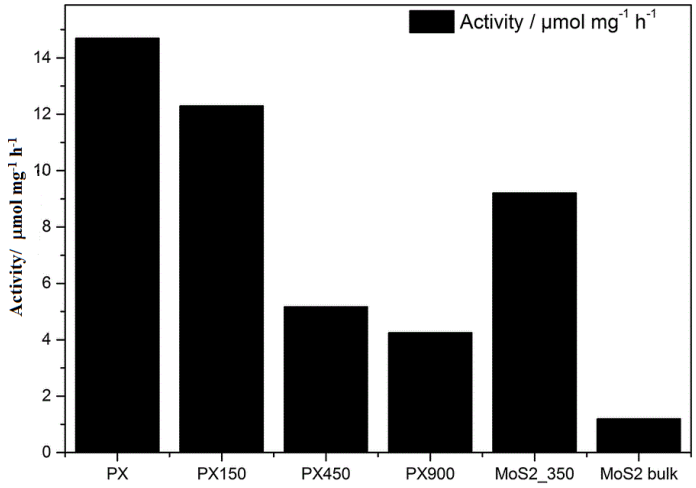

Figure 3.8. HER activity of different photocatalysts. PX represents amorphous MoSx. PX150, PX450 and PX900 represents amorphous MoS_2 heated to 150 °C, 450 °C and 900 °C, respectively. Commercial MoS_2 (MoS_2 bulk) and MoS_2 prepared from $(NH_4)_2MoS_4$ at 350 °C (MoS_2_350) are taking as reference samples [127].

Yu *et al.* integrated amorphous MoS_x on the surface of g-C_3N_4 (a-MoS_x/g-C_3N_4) by an adsorption-in situ transformation method [126]. As shown in Figure 3.9a, the

photocatalytic H_2 production activity of all a-MoS_x/g-C_3N_4 samples are higher than that of crystalline MoS_2 modified sample and pristine g-C_3N_4. The optimal HER activity was achieved when the weight ration of Mo to g-C_3N_4 was 5 wt%. It has been demonstrated that the unsaturated S atoms in molybdenum sulfide material can be classified into terminal S^{2-}, apical S^{2-} and bridging S_2^{2-} (Figure 3.9b) [128-130]. Due to the highly irregular atomic arrangement of amorphous MoS_x, all existing unsaturated S atoms could contribute to the adsorption of H^+ ions and eventually lead to a higher HER activity. Considering the different S-bonding configurations, Yu *et al.* deduced that apical S^{2-} has better H^+-adsorption ability because of its lower coordination state. Moreover, owning to the small size of amorphous MoS_x (2-4 nm), photogenerated charge carriers could transfer to the active sites rapidly to reduce the adsorbed H^+ ions. However, the detailed atomic-scale structure and a deep insight into the mechanisms of amorphous MoS_x-based photocatalysts are limited by lack of precise characterization methods.

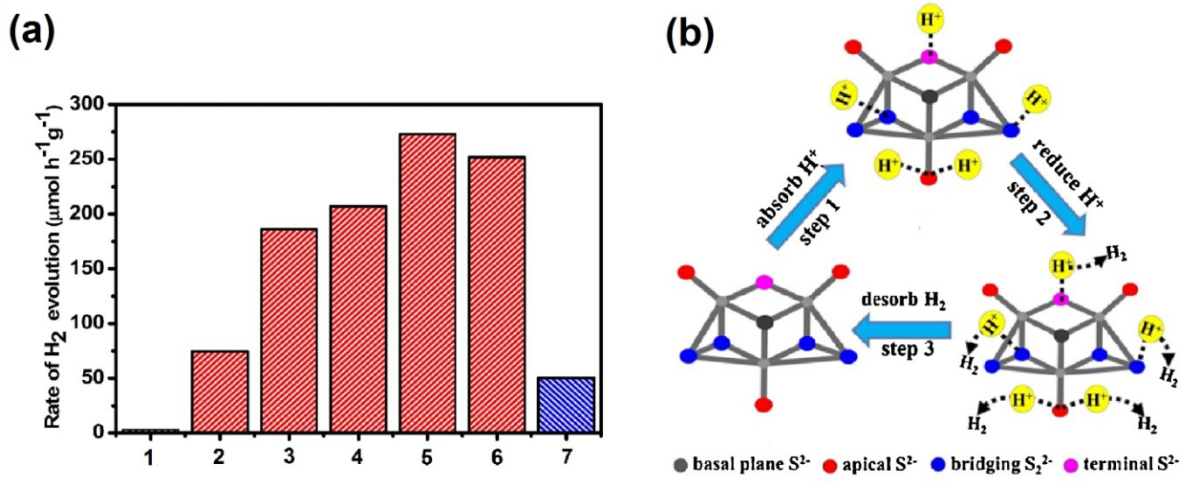

Figure 3.9. (a) HER activity of (1) g-C_3N_4, (2) a-MoS_x/g-C_3N_4 (0.1 wt%), (3) a-MoS_x/g-C_3N_4 (0.5 wt%),(4) a-MoS_x/g-C_3N_4 (1 wt%), (5) a-MoS_x/g-C_3N_4 (3 wt%), (6) a-MoS_x/g-C_3N_4 (5 wt%), and (7) c-MoS_2/g-C_3N_4 (3 wt%). (b)The possible photocatalytic hydrogen production process. (Adapted from [126])

3.4.6 Crystal face engineering

It is reported that the excess sulfur has a positive effect on the photocatalytic activity of the pure flower-like 2H-MoS_2 by affecting the preferential growth orientation of the crystal [131]. The ration of peak intensity, I_{002}/I_{100}, is increasing with the increasing feeding ration of S/Mo in the hydrothermal method, revealing a more complete growth of (002) plane than the (100) plane. Thereby, more active edge sites in the {100} facet are exposed. This corresponds to the photocatalytic studies of the degradation of methylene blue (MB). When the S/Mo ratio reaches 2.75, the MoS_2 exhibits the highest MB degradation rate.

This 'facet effect' also plays a key role in the performance of MoS_2-based heterostructures. Different crystal faces at the interface of the heterostructure leads to the different efficiencies of carriers' transmission. Zhang *et al.* compared the MB photodecomposition rates of MoS_2 composited with {001} and {101} TiO_2 facet [132]. The results indicate that the photocatalytic activity of MoS_2/TiO_2 (001) is 3.4 times higher than that of bare TiO_2 with exposed {001} facets. In contrast, the photocatalytic activity of MoS_2/TiO_2 (101) is only enhanced by 31% compared to that of bare TiO_2 with exposed {101} facets. The higher photocatalytic activity of MoS_2/TiO_2 (001) is due to the effective face-to-face contact between MoS_2 and the {001} facet of TiO_2. This contact can facilitate the transmission of photo-induced carriers and result in a good separation efficiency of charge carriers. It is notable that the simple physical mixture of MoS_2 and TiO_2 [001] cannot improve the activity of pristine TiO_2 [133]. Meanwhile, the {001} facet of TiO_2 possess a more negative valence band edge potential than the {101} facet. Thus, the holes will transfer from the {101} facet to the {001} facet and subsequently move to the valence band

of MoS_2 for organic degradation. Regulating the crystal faces to improve the photocatalytic performance is also reported in other studies [134].

As for photocatalytic hydrogen production, Chen *et al.* [135] synthesized MoS_2-CdS nanohybrids via a facile one-pot wet-chemical method involving the hot-injection procedure. An interesting phenomenon was reported that the single-layer MoS_2 was selectively grown on the Cd-rich (0001) surface of wurtzite CdS nanocrystals. A large number of exposed edge sites and the formation of the p-n junction between MoS_2 and CdS synergistically enhanced the photocatalytic hydrogen evolution. The H_2 evolution rate of MoS_2-CdS nanohybrids (1472 μmol h^{-1} g^{-1}) is 12 times higher than that of CdS (119 μmol h^{-1} g^{-1}).

The influence of the crystal facet and the interface of the heterostructure on the performance of the photocatalyst are often neglected. However, a rational regulation of crystal faces is important for the fabrication of MoS_2-based photocatalysts with high efficiency.

3.4.7 Tuning the phase of MoS_2

It is well known that electrocatalytic HER activity of metallic MoS_2 (*i.e.* 1T-MoS_2) is generally superior to that of semiconducting MoS_2 (*i.e.* 2H-MoS_2) due to the large electron mobility in the 1T phase and the proliferated active sites of 1T phase in both basal plane and edges [22]. In the field of photocatalysis, however, suitable band alignment, interaction between MoS_2 and other photocatalysts, and the light harvesting capacity also play a key role in the photocatalytic activity.

Bai *et al.* evaluated the phase effect on the photocatalytic degradation of RhB [77]. As a co-catalyst, 1T-MoS_2 modified TiO_2 exhibited superior photocatalytic activity than pristine TiO_2 and 2H-MoS_2 modified TiO_2, suggesting a more efficient suppression of charge recombination by 1T phase. Maitra *et al.* explored the photocatalytic H_2 generation activity of 1T-MoS_2, 2H-MoS_2 and nanocomposites of 2H-MoS_2 with nitrogen-doped graphene [136]. It is reported that the H_2 production rate of 2H-MoS_2 is promoted with the coupling of nitrogen-doped graphene. However, the H_2 production rate of nanocomposites based on the 2H-MoS_2 is still lower than that of the single-layer 1T-MoS_2 due to the good conductivity of 1T-MoS_2 [137-139]. It is worth noting that the effect of MoS_2 phases on the photocatalytic HER activity varies with different photo-harvesters when MoS_2 is used as a co-catalyst. For instance, Chang *et al.* revealed that there is no evident enhancement of HER activity for 2H-MoS_2 loaded TiO_2 in comparison with bare TiO_2 [140]. However, the HER activity dramatically improved for 1T-MoS_2 loaded TiO_2 system. The results are opposite when the photo-harvester is changed from TiO_2 to CdS. The rate of H_2 evolution for 1T-MoS_2 loaded CdS (1563.6 μmol h^{-1}) is slightly lower than that of 2H-MoS_2 loaded CdS (1658.5 μmol h^{-1}). The rates of H_2 evolution for different nanocomposites are shown in Figure 3.10a and 3.10b. One of the possible reasons for this difference could be the smaller size of 2H-MoS_2 sheet which can be more easily attached to the surface of CdS. The intimate contact between 2H-MoS_2 and CdS facilitated the transfer of photogenerated charge carriers and improved the charge separation. Therefore, for the MoS_2/CdS nanocomposite the 2H-phase MoS_2 exhibited a better HER activity. One the other hand, a matching band alignment for each photocatalyst in the nanocomposite also plays an important role in the photocatalytic activity. The experimentally determined band energy

level of each component is illustrated in Figure 3.10c. As shown in Figure 3.10c, the conduction band minimum of single-layered 2H-MoS_2 is more negative than that of TiO_2. Thus, the photogenerated electrons would be difficult to transfer from the conduction band of TiO_2 to the active sites of MoS_2 for hydrogen production. In contrast, the electrical energy level of 1T-MoS_2 is more positive than the conduction band of TiO_2 leading to an efficient charge separation ability and better HER activity. However, the conduction band minimum (CBM) of CdS is more negative than both the CBM of 2H-MoS_2 and 1T-MoS_2. As a result, photogenerated electrons could be captured by both 1T-MoS_2 and 2H-MoS_2 for further H_2 reduction. This difference of band alignment could be the reason for the opposite HER performance obtained by the 1T- and 2H-MoS_2 loaded TiO_2 and CdS. This study indicates that 1T-MoS_2, as a co-catalyst, may not always achieve superior performance in the field of photocatalysis. Moreover, 1T phase is a thermodynamically metastable polytype of MoS_2, which could transform to the more stable 2H-MoS_2 with a prolonged reaction time [77]. Therefore, efforts focused on the stability enhancement of 1T-MoS_2 could improve the practical application of 1T-MoS_2 based photocatalysts.

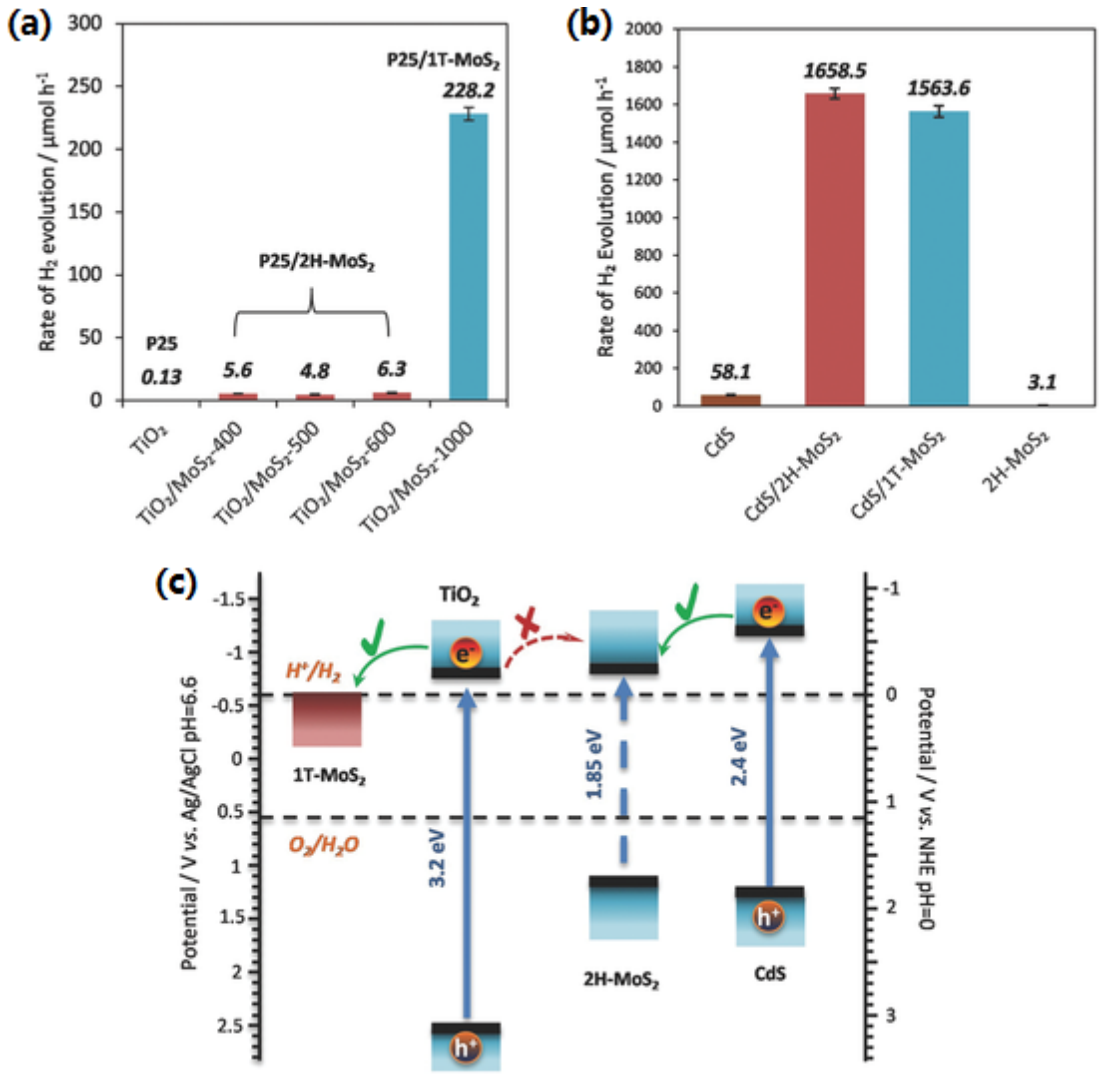

Figure 3.10. Rate of H_2 evolution of 1T- and 2H-MoS_2 over (a) TiO_2 and (b) CdS; (c) Band energy of 1T- MoS_2, 2H-MoS_2, TiO_2 and CdS.

3.4.8 Photosensitivity

To further promote the visible-light activity, Gu *et al.* synthesized a core-shell structure (SSCN@MoS_2) combined with MoS_2 and self-sensitized carbon nitride (SSCN) for photocatalytic hydrogen production [141]. The morphology of prepared SSCN@MoS_2 microsphere is shown in Figure 3.11. Under visible light irradiation, not only the carbon nitride core can be excited, the triazine-based oligomer (TBO) dyes coated on the surface

of SSCN can also be activated and can inject electrons to the conduction band of the carbon nitride core. Subsequently, the electrons generated by the TBO dyes or carbon nitride core can transfer to the active sites of coated MoS_2 on the microsphere surface to reduce protons. The solar-light harvesting property of surface dyes and active sites provided by MoS_2 synergistically improve the activity of H_2 production. It is demonstrated that the SSCN microsphere showed the highest H_2 production rate compared to un-coated SSCN, standard g-C_3N_4@MoS_2 and SSCN-P@MoS_2 (no self-sensitization property). In addition, the synthesized SSCN@MoS_2 sample showed no evident activity loss after three cycles (72 h) due to the dye recovery supplied by the triethanolamine in the solution. Although this study provides a new concept to enhance the activity of visible-light-driven HER, the post-treatment of dye should be considered.

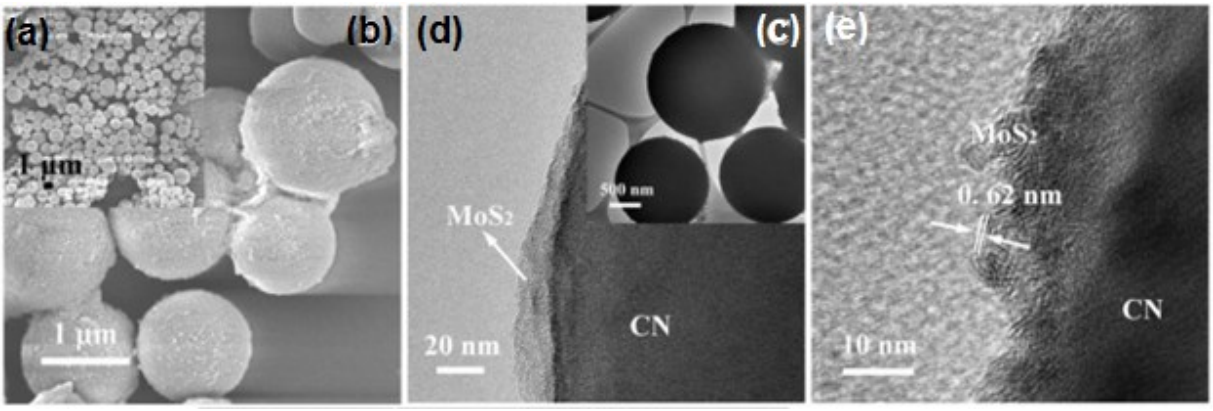

Figure 3.11. The SEM image (a and b), TEM image (c and d), and HRTEM image (e) of SSCN@MoS_2

3.4.9 Photoelectrocatalysis

Photoelectrocatalysis (PEC), via integrating electrochemistry and photocatalytic technology, has been identified as a superior candidate to debottleneck photocatalytic process [142]. The recombination of photogenerated charge carriers may be suppressed by

the external positive bias for the PEC system. Qi *et al.* reported on applying PEC to improve the photocatalytic activity of MoS_2, the scheme was depicted in Figure 3.12 [143]. In this work, improved efficiency of charge transfer was measured via applying external bias. In addition, MoS_2-SiC hybrid structure was also tested and exhibited high PEC performance for hydrogen evolution [144]. Though not too much work about MoS_2-base PEC was reported, PEC can be regard as a promising approach to improve the photocatalytic performance of the MoS_2-based systems.

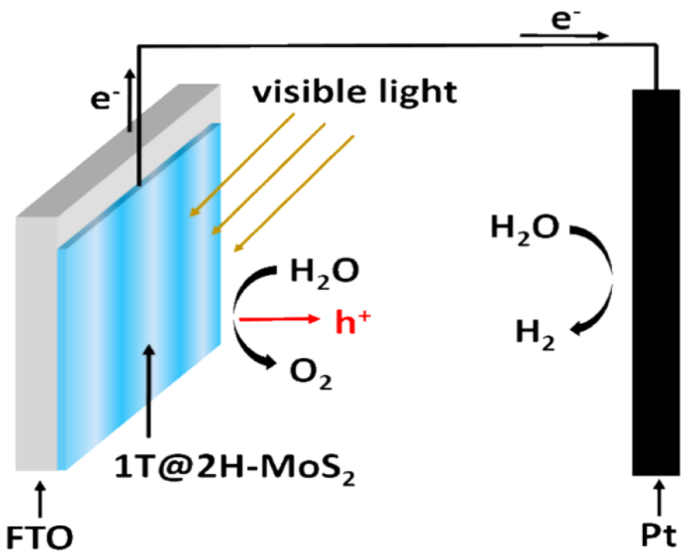

Figure 3.12. Scheme of photoelectrocatalysis with MoS_2 on FTO as photoanode and Pt as photocathode. (Adapted from [143])

3.4.10 Separation strategy

As previously mentioned, MoS_2-based photocatalysts have shown great potential in many fields. However, their practical applications are hindered by the difficult process of photocatalyst recycling from reaction media. Conventional approaches of heterogeneous photocatalyst separation and recovery generally involve filtration or centrifugation steps, which are limited by the small size of photocatalysts. The emergence of magnetically

separable nanoparticles offers a promising way to solve this problem [145-147]. Magnetic separation can achieve photocatalyst recycling by applying an appropriate external magnet on the magnetic component in the nanostructure. This approach could not only meet the requirement of sustainable use of the precious catalysts, but also reduce the aggregation and loss of photocatalysts during the conventional separation process [148]. Some magnetic components can act as magnetic carriers for magnetic separation, and also enhance the generation and separation of photo-induced charge carriers [149, 150]. For example, a possible Z-scheme photocatalyst system, Fe_3O_4@MoS_2/Ag_3PO_4 was prepared by Guo and co-workers [150]. It is reported that Fe_3O_4@MoS_2/Ag_3PO_4 exhibited considerable durability relative to pure Ag_3PO_4 in the recycle test. After 5 repeated cycles, the photocatalytic degradation efficiency of RhB only reduced by 4% in the present of Fe_3O_4@MoS_2/Ag_3PO_4. However, the photocatalytic degradation efficiency of pure Ag_3PO_4 reduced more than 30% after 5 cycles. The enhanced reusability of Fe_3O_4@MoS_2/Ag_3PO_4 could be ascribed to the inhibition of Ag_3PO_4 photocorrosion by the incorporation of MoS_2. A nearly 100% collection of the photocatalysts provided by magnetically recoverable Fe_3O_4 may also contribute to the good photocatalytic performance. Additionally, Fe^{2+} and Fe^{3+} in the Fe_3O_4 could capture the photogenerated electrons to further improve the separation of charge carriers and result in enhanced photocatalytic performance. Liu *et al.* integrated α-Fe_2O_3 with N-doped MoS_2 via hydrothermal method [88]. It is indicated that the incorporation of α-Fe_2O_3 has negligible influence on the photocatalytic performance of N-doped MoS_2. Due to the strong magnetic properties, the as-prepared α-Fe_2O_3@N-doped MoS_2 heterostructures can be separated

from the suspension system in 10s (see Figure 3.13). According to these studies, magnetically separable photocatalysts show great potential in practical applications.

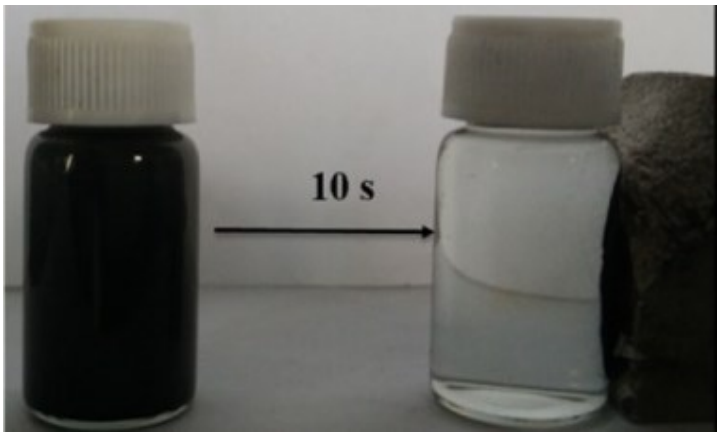

Figure 3.13. Magnetic separation of α-Fe_2O_3@N-doped MoS_2 heterostructures exposed to external magnetic field in 10 seconds. (Adapted from [88])

3.5 Concluding remarks and outlook

As a visible light-responsive photocatalyst, MoS_2 and MoS_2-based photocatalysts have been extensively studied in many fields, such as hydrogen production, environmental remediation, and photosynthesis. However, the rapid recombination of photogenerated carriers, limited active edge sites and difficulties in photocatalyst recycling are the main obstacles that hinder the practical application of MoS_2-based photocatalysts. The corresponding approaches to overcome these obstacles are discussed to fabricate highly efficient and stable MoS_2-based photocatalysts. Although many efforts have been devoted to enhancing the photocatalytic activity, the in-depth understanding of mechanisms is still limited based on the work reported. From a practical point of view, the development of MoS_2-based photocatalysts is still in its infancy. For example, current studies required diverse sacrificial reagents to achieve H_2 evolution, which implied a higher cost in practical applications. For environmental remediation, studies of mechanical strength, antifouling

properties and surface chemistry of prepared samples are still lacking. However, all of these are important for the proper evaluation of their behaviors in real applications. Although a few preliminary reports have studied the effect of morphology on the photocatalytic activity, the insights of this effect on edge sites, adsorption capacity, surface properties (*e.g.* defects and surface charge) and other factors still need to be explored. Additionally, combining the photocatalytic reactor design and utilizing simulated solar light in the current studies may facilitate the commercialization progress of MoS_2-based photocatalysts. In conclusion, the unique properties of MoS_2-based photocatalysts and their good performance in different applications suggest them to be a promising earth-abundant photocatalyst.

References

[1] A. Fujishima, K. Honda, Electrochemical photolysis of water at a semiconductor electrode, Nature, 238 (1972) 37-38.

[2] S.G. Kumar, L.G. Devi, Review on modified TiO_2 photocatalysis under UV/visible light: selected results and related mechanisms on interfacial charge carrier transfer dynamics, The Journal of physical chemistry A, 115 (2011) 13211-13241.

[3] M. Ni, M.K.H. Leung, D.Y.C. Leung, K. Sumathy, A review and recent developments in photocatalytic water-splitting using TiO_2 for hydrogen production, Renewable and Sustainable Energy Reviews, 11 (2007) 401-425.

[4] R. Daghrir, P. Drogui, D. Robert, Modified TiO_2 For Environmental Photocatalytic Applications: A Review, Industrial & Engineering Chemistry Research, 52 (2013) 3581-3599.

[5] X. Chen, S.S. Mao, Titanium Dioxide Nanomaterials: Synthesis, Properties, Modifications, and Applications, Chem Rev, 107 (2007) 2891-2959.

[6] Y. Wang, G. Li, P. Li, J. Hu, Q. Zhao, Research progress of two-dimensional layered material molybdenum disulfide, Bandaoti Guangdian/Semiconductor Optoelectronics, 37 (2016) 461-466.

[7] Y.-J. Yuan, H.-W. Lu, Z.-T. Yu, Z.-G. Zou, Noble-Metal-Free Molybdenum Disulfide Cocatalyst for Photocatalytic Hydrogen Production, Chemsuschem, 8 (2015) 4113-4127.

[8] X. Jin, X. Fan, J. Tian, R. Cheng, M. Li, L. Zhang, MoS_2 quantum dot decorated g-C_3N_4 composite photocatalyst with enhanced hydrogen evolution performance, RSC Advances, 6 (2016) 52611-52619.

[9] Q.H. Wang, K. Kalantar-Zadeh, A. Kis, J.N. Coleman, M.S. Strano, Electronics and optoelectronics of two-dimensional transition metal dichalcogenides, Nat Nano, 7 (2012) 699-712.

[10] J. Low, S. Cao, J. Yu, S. Wageh, Two-dimensional layered composite photocatalysts, Chem Commun, 50 (2014) 10768-10777.

[11] Z. He, W. Que, Molybdenum disulfide nanomaterials: Structures, properties, synthesis and recent progress on hydrogen evolution reaction, Applied Materials Today, 3 (2016) 23-56.

[12] D. Voiry, A. Mohite, M. Chhowalla, Phase engineering of transition metal dichalcogenides, Chem. Soc. Rev., 44 (2015) 2702-2712.

[13] B.L. Abrams, J.P. Wilcoxon, Nanosize Semiconductors for Photooxidation, Crit. Rev. Solid State Mater. Sci., 30 (2005) 153-182.

[14] I. Song, C. Park, H.C. Choi, Synthesis and properties of molybdenum disulphide: from bulk to atomic layers, RSC Advances, 5 (2015) 7495-7514.

[15] K.S. Novoselov, D. Jiang, F. Schedin, T.J. Booth, V.V. Khotkevich, S.V. Morozov, A.K. Geim, Two-dimensional atomic crystals, Proceedings of the National Academy of Sciences of the United States of America, 102 (2005) 10451-10453.

[16] V. Nicolosi, M. Chhowalla, M.G. Kanatzidis, M.S. Strano, J.N. Coleman, Liquid Exfoliation of Layered Materials, Science, 340 (2013).

[17] J.N. Coleman, M. Lotya, A. O'Neill, S.D. Bergin, P.J. King, U. Khan, K. Young, A. Gaucher, S. De, R.J. Smith, I.V. Shvets, S.K. Arora, G. Stanton, H.-Y. Kim, K. Lee, G.T. Kim, G.S. Duesberg, T. Hallam, J.J. Boland, J.J. Wang, J.F. Donegan, J.C. Grunlan, G. Moriarty, A. Shmeliov, R.J. Nicholls, J.M. Perkins, E.M. Grieveson, K. Theuwissen, D.W. McComb, P.D. Nellist, V. Nicolosi, Two-Dimensional Nanosheets Produced by Liquid Exfoliation of Layered Materials, Science, 331 (2011) 568-571.

[18] G. Cunningham, M. Lotya, C.S. Cucinotta, S. Sanvito, S.D. Bergin, R. Menzel, M.S.P. Shaffer, J.N. Coleman, Solvent Exfoliation of Transition Metal Dichalcogenides: Dispersibility of Exfoliated Nanosheets Varies Only Weakly between Compounds, ACS Nano, 6 (2012) 3468-3480.

[19] B. Hinnemann, P.G. Moses, J. Bonde, K.P. Jørgensen, J.H. Nielsen, S. Horch, I. Chorkendorff, J.K. Nørskov, Biomimetic Hydrogen Evolution: MoS2 Nanoparticles as Catalyst for Hydrogen Evolution, J. Am. Chem. Soc., 127 (2005) 5308-5309.

[20] RadisavljevicB, RadenovicA, BrivioJ, GiacomettiV, KisA, Single-layer MoS_2 transistors, Nat Nano, 6 (2011) 147-150.

[21] A. Fujishima, K. Honda, Electrochemical Photolysis of Water at a Semiconductor Electrode, Nature, 238 (1972) 37-38.

[22] Q. Ding, B. Song, P. Xu, S. Jin, Efficient Electrocatalytic and Photoelectrochemical Hydrogen Generation Using MoS2 and Related Compounds, Chem, 1 (2016) 699-726.

[23] H.I. Karunadasa, E. Montalvo, Y. Sun, M. Majda, J.R. Long, C.J. Chang, A Molecular MoS_2 Edge Site Mimic for Catalytic Hydrogen Generation, Science, 335 (2012) 698-702.

[24] K. Chang, M. Li, T. Wang, S. Ouyang, P. Li, L. Liu, J. Ye, Drastic Layer-Number-Dependent Activity Enhancement in Photocatalytic H2 Evolution over nMoS2/CdS (n ⩾ 1) Under Visible Light, Advanced Energy Materials, 5 (2015) n/a-n/a.

[25] K. Chang, Z. Mei, T. Wang, Q. Kang, S. Ouyang, J. Ye, MoS_2/Graphene Cocatalyst for Efficient Photocatalytic H2 Evolution under Visible Light Irradiation, ACS Nano, 8 (2014) 7078-7087.

[26] E. Ha, W. Liu, L. Wang, H.-W. Man, L. Hu, S.C.E. Tsang, C.T.-L. Chan, W.-M. Kwok, L.Y.S. Lee, K.-Y. Wong, Cu2ZnSnS4/MoS2-Reduced Graphene Oxide Heterostructure: Nanoscale Interfacial Contact and Enhanced Photocatalytic Hydrogen Generation, Scientific Reports, 7 (2017) 39411.

[27] S. Ong, E. Toorisaka, M. Hirata, T. Hano, Combination of adsorption and biodegradation processes for textile effluent treatment using a granular activated carbon-bioflm confgured packed column system, Journal of Environmental Sciences, 20 (2008) 952-956.

[28] N. Casas, P. Blánquez, X. Gabarrell, T. Vicent, G. Caminal, M. Sarrà, Degradation of Orange G by Laccase: Fungal Versus Enzymatic Process, Environ. Technol., 28 (2007)

1103-1110.

[29] S.W. Hu, L.W. Yang, Y. Tian, X.L. Wei, J.W. Ding, J.X. Zhong, P.K. Chu, Non-covalent doping of graphitic carbon nitride with ultrathin graphene oxide and molybdenum disulfide nanosheets: An effective binary heterojunction photocatalyst under visible light irradiation, J. Colloid Interface Sci., 431 (2014) 42-49.

[30] N. Singh, G. Jabbour, U. Schwingenschlögl, Optical and photocatalytic properties of two-dimensional MoS_2, The European Physical Journal B, 85 (2012) 392.

[31] M. Marchelek, B. Bajorowicz, P. Mazierski, A. Cybula, T. Klimczuk, M. Winiarski, N. Fijałkowska, A. Zaleska, KTaO3-based nanocomposites for air treatment, Catal. Today, 252 (2015) 47-53.

[32] X. Li, Z. Zhang, C. Yao, X. Lu, X. Zhao, C. Ni, Attapulgite-CeO2/MoS2 ternary nanocomposite for photocatalytic oxidative desulfurization, Appl. Surf. Sci., 364 (2016) 589-596.

[33] Y. Rong, L. Tang, Y. Song, S. Wei, Z. Zhang, J. Wang, A new visible-light driving nanocomposite photocatalyst Er^{3+}:$Y_3Al_5O_{12}$/MoS_2-$NaTaO_3$-PdS for photocatalytic degradation of a refractory pollutant with potentially simultaneous hydrogen evolution, RSC Advances, 6 (2016) 80595-80603.

[34] N. Shao, J. Wang, D. Wang, P. Corvini, Preparation of three-dimensional Ag3PO4/TiO2@MoS2 for enhanced visible-light photocatalytic activity and anti-photocorrosion, Applied Catalysis B: Environmental, 203 (2017) 964-978.

[35] X. Wang, M. Hong, F. Zhang, Z. Zhuang, Y. Yu, Recyclable Nanoscale Zero Valent Iron Doped g-C_3N_4/MoS_2 for Efficient Photocatalysis of RhB and Cr(VI) Driven by Visible

Light, ACS Sustainable Chemistry & Engineering, 4 (2016) 4055-4063.

[36] M. Chatti, V.N.K.B. Adusumalli, S. Ganguli, V. Mahalingam, Near-infrared light triggered superior photocatalytic activity from MoS2-NaYF4:Yb3+/Er3+ nanocomposites, Dalton Transactions, 45 (2016) 12384-12392.

[37] Y. Chen, C. Lu, L. Tang, S. Wei, Y. Song, J. Wang, Efficient photocatalytic hydrogen evolution from methanol/water splitting over Tm^{3+},Yb^{3+}:$NaYF_4$–Er^{3+}:$Y^3Al_5O_{12}$/MoS_2–$NaTaO^3$ nanocomposite particles under infrared–visible light irradiation, Sol. Energy Mater. Sol. Cells, 149 (2016) 128-136.

[38] G. Gong, Y. Liu, B. Mao, B. Wang, L. Tan, D. Li, Y. Liu, W. Shi, Mechanism study on the photocatalytic efficiency enhancement of MoS_2 modified Zn-$AgIn_5S_8$ quantum dots, RSC Advances, 6 (2016) 99023-99033.

[39] S.W. Hu, L.W. Yang, Y. Tian, X.L. Wei, J.W. Ding, J.X. Zhong, P.K. Chu, Simultaneous nanostructure and heterojunction engineering of graphitic carbon nitride via in situ Ag doping for enhanced photoelectrochemical activity, Applied Catalysis B: Environmental, 163 (2015) 611-622.

[40] Y. Gao, C. Chen, X. Tan, H. Xu, K. Zhu, Polyaniline-modified 3D-flower-like molybdenum disulfide composite for efficient adsorption/photocatalytic reduction of Cr(VI), J. Colloid Interface Sci., 476 (2016) 62-70.

[41] W. Zhao, Y. Liu, Z. Wei, S. Yang, H. He, C. Sun, Fabrication of a novel p–n heterojunction photocatalyst n-$BiVO_4$@p-MoS_2 with core–shell structure and its excellent visible-light photocatalytic reduction and oxidation activities, Applied Catalysis B: Environmental, 185 (2016) 242-252.

[42] M.Q. Wen, T. Xiong, Z.G. Zang, W. Wei, X.S. Tang, F. Dong, Synthesis of MoS_2/g-C_3N_4 nanocomposites with enhanced visible-light photocatalytic activity for the removal of nitric oxide (NO), Opt. Express, 24 (2016) 10205-10212.

[43] T. Xiong, M. Wen, F. Dong, J. Yu, L. Han, B. Lei, Y. Zhang, X. Tang, Z. Zang, Three dimensional Z-scheme $(BiO)_2CO_3$/MoS_2 with enhanced visible light photocatalytic NO removal, Applied Catalysis B: Environmental, 199 (2016) 87-95.

[44] Y. Wang, B. Zou, T. Gao, X. Wu, S. Lou, S. Zhou, Synthesis of orange-like Fe_3O_4/PPy composite microspheres and their excellent Cr(VI) ion removal properties, J. Mater. Chem., 22 (2012) 9034-9040.

[45] X. Guo, G.T. Fei, H. Su, L. De Zhang, High-Performance and Reproducible Polyaniline Nanowire/Tubes for Removal of Cr(VI) in Aqueous Solution, The Journal of Physical Chemistry C, 115 (2011) 1608-1613.

[46] H. Wang, F. Wen, X. Li, X. Gan, Y. Yang, P. Chen, Y. Zhang, Cerium-doped MoS_2 nanostructures: Efficient visible photocatalysis for Cr(VI) removal, Sep. Purif. Technol., 170 (2016) 190-198.

[47] M. Bhaumik, A. Maity, V.V. Srinivasu, M.S. Onyango, Removal of hexavalent chromium from aqueous solution using polypyrrole-polyaniline nanofibers, Chem. Eng. J., 181–182 (2012) 323-333.

[48] Y. Hou, A.B. Laursen, J. Zhang, G. Zhang, Y. Zhu, X. Wang, S. Dahl, I. Chorkendorff, Layered Nanojunctions for Hydrogen-Evolution Catalysis, Angew. Chem. Int. Ed., 52 (2013) 3621-3625.

[49] J. Gamage, Z. Zhang, Applications of Photocatalytic Disinfection, International

Journal of Photoenergy, 2010 (2010).

[50] S. Agnihotri, G. Bajaj, S. Mukherji, S. Mukherji, Arginine-assisted immobilization of silver nanoparticles on ZnO nanorods: an enhanced and reusable antibacterial substrate without human cell cytotoxicity, Nanoscale, 7 (2015) 7415-7429.

[51] M.J. Hajipour, K.M. Fromm, A. Akbar Ashkarran, D. Jimenez de Aberasturi, I.R.d. Larramendi, T. Rojo, V. Serpooshan, W.J. Parak, M. Mahmoudi, Antibacterial properties of nanoparticles, Trends Biotechnol., 30 (2012) 499-511.

[52] J.C. Crittenden, R.R. Trussell, D.W. Hand, K.J. Howe, G. Tchobanoglous, MWH's water treatment: principles and design, John Wiley & Sons, 2012.

[53] K. Sunada, T. Watanabe, K. Hashimoto, Studies on photokilling of bacteria on TiO_2 thin film, J. Photochem. Photobiol. A: Chem., 156 (2003) 227-233.

[54] A. Sirelkhatim, S. Mahmud, A. Seeni, N.H.M. Kaus, L.C. Ann, S.K.M. Bakhori, H. Hasan, D. Mohamad, Review on Zinc Oxide Nanoparticles: Antibacterial Activity and Toxicity Mechanism, Nano-Micro Letters, 7 (2015) 219-242.

[55] G.P. Awasthi, S.P. Adhikari, S. Ko, H.J. Kim, C.H. Park, C.S. Kim, Facile synthesis of ZnO flowers modified graphene like MoS_2 sheets for enhanced visible-light-driven photocatalytic activity and antibacterial properties, J. Alloys Compd., 682 (2016) 208-215.

[56] N. Jones, B. Ray, K.T. Ranjit, A.C. Manna, Antibacterial activity of ZnO nanoparticle suspensions on a broad spectrum of microorganisms, FEMS Microbiol. Lett., 279 (2008) 71-76.

[57] W. Liu, Y. Feng, H. Tang, H. Yuan, S. He, S. Miao, Immobilization of silver nanocrystals on carbon nanotubes using ultra-thin molybdenum sulfide sacrificial layers

for antibacterial photocatalysis in visible light, Carbon, 96 (2016) 303-310.

[58] S.N. Habisreutinger, L. Schmidt-Mende, J.K. Stolarczyk, Photocatalytic Reduction of CO_2 on TiO_2 and Other Semiconductors, Angewandte Chemie International Edition, 52 (2013) 7372-7408.

[59] D. Zhu, L. Zhang, R.E. Ruther, R.J. Hamers, Photo-illuminated diamond as a solid-state source of solvated electrons in water for nitrogen reduction, Nat Mater, 12 (2013) 836-841.

[60] G.N. Schrauzer, T.D. Guth, Photocatalytic reactions. 1. Photolysis of water and photoreduction of nitrogen on titanium dioxide, J. Am. Chem. Soc., 99 (1977) 7189-7193.

[61] G. Palmisano, V. Augugliaro, M. Pagliaro, L. Palmisano, Photocatalysis: a promising route for 21st century organic chemistry, Chem. Commun., (2007) 3425-3437.

[62] L. Wang, C. Wang, W. Liu, Q. Chen, M. He, Visible-light-induced aerobic thiocyanation of indoles using reusable TiO_2/MoS_2 nanocomposite photocatalyst, Tetrahedron Lett., 57 (2016) 1771-1774.

[63] J.W. Erisman, M.A. Sutton, J. Galloway, Z. Klimont, W. Winiwarter, How a century of ammonia synthesis changed the world, Nature Geosci, 1 (2008) 636-639.

[64] Y. Tanabe, Y. Nishibayashi, Developing more sustainable processes for ammonia synthesis, Coord. Chem. Rev., 257 (2013) 2551-2564.

[65] O. Rusina, A. Eremenko, G. Frank, H.P. Strunk, H. Kisch, Nitrogen Photofixation at Nanostructured Iron Titanate Films, Angew. Chem. Int. Ed., 40 (2001) 3993-3995.

[66] O.P. Linnik, H. Kisch, Dinitrogen photofixation at ruthenium-modified titania films, Mendeleev Commun., 18 (2008) 10-11.

[67] S. Sun, X. Li, W. Wang, L. Zhang, X. Sun, Photocatalytic robust solar energy reduction of dinitrogen to ammonia on ultrathin MoS_2, Applied Catalysis B: Environmental, 200 (2017) 323-329.

[68] H. Li, Y. Wang, G. Chen, Y. Sang, H. Jiang, J. He, X. Li, H. Liu, Few-layered MoS2 nanosheets wrapped ultrafine TiO_2 nanobelts with enhanced photocatalytic property, Nanoscale, 8 (2016) 6101-6109.

[69] X. Liu, Z. Xing, Y. Zhang, Z. Li, X. Wu, S. Tan, X. Yu, Q. Zhu, W. Zhou, Fabrication of 3D flower-like black N-TiO_2-x@MoS_2 for unprecedented-high visible-light-driven photocatalytic performance, Applied Catalysis B: Environmental, 201 (2017) 119-127.

[70] X. Meng, Z. Li, H. Zeng, J. Chen, Z. Zhang, MoS_2 quantum dots-interspersed Bi_2WO_6 heterostructures for visible light-induced detoxification and disinfection, Applied Catalysis B: Environmental, 210 (2017) 160-172.

[71] M.R. Hoffmann, S.T. Martin, W. Choi, D.W. Bahnemann, Environmental applications of semiconductor photocatalysis, Chem Rev, 95 (1995) 69-96.

[72] J. Yan, Z. Chen, H. Ji, Z. Liu, X. Wang, Y. Xu, X. She, L. Huang, L. Xu, H. Xu, H. Li, Construction of a 2D Graphene-Like MoS_2/C_3N_4 Heterojunction with Enhanced Visible-Light Photocatalytic Activity and Photoelectrochemical Activity, Chemistry – A European Journal, 22 (2016) 4764-4773.

[73] M. Shen, Z. Yan, L. Yang, P. Du, J. Zhang, B. Xiang, MoS_2 nanosheet/TiO_2 nanowire hybrid nanostructures for enhanced visible-light photocatalytic activities, Chem. Commun., 50 (2014) 15447-15449.

[74] X. Liu, Z. Xing, H. Zhang, W. Wang, Y. Zhang, Z. Li, X. Wu, X. Yu, W. Zhou,

Fabrication of 3D Mesoporous Black $TiO_2/MoS_2/TiO_2$ Nanosheets for Visible-Light-Driven Photocatalysis, ChemSusChem, 9 (2016) 1118-1124.

[75] D. Lu, H. Wang, X. Zhao, K.K. Kondamareddy, J. Ding, C. Li, P. Fang, Highly Efficient Visible-Light-Induced Photoactivity of Z-Scheme $g\text{-}C_3N_4/Ag/MoS_2$ Ternary Photocatalysts for Organic Pollutant Degradation and Production of Hydrogen, ACS Sustainable Chemistry & Engineering, 5 (2017) 1436-1445.

[76] W. Zhou, Z. Yin, Y. Du, X. Huang, Z. Zeng, Z. Fan, H. Liu, J. Wang, H. Zhang, Synthesis of Few-Layer MoS_2 Nanosheet-Coated TiO_2 Nanobelt Heterostructures for Enhanced Photocatalytic Activities, Small, 9 (2013) 140-147.

[77] S. Bai, L. Wang, X. Chen, J. Du, Y. Xiong, Chemically exfoliated metallic MoS_2 nanosheets: A promising supporting co-catalyst for enhancing the photocatalytic performance of TiO_2 nanocrystals, Nano Research, 8 (2015) 175-183.

[78] W.Y. Lim, M. Hong, G.W. Ho, In situ photo-assisted deposition and photocatalysis of $ZnIn_2S_4$/transition metal chalcogenides for enhanced degradation and hydrogen evolution under visible light, Dalton Transactions, 45 (2016) 552-560.

[79] K.H. Hu, X.G. Hu, Y.F. Xu, X.Z. Pan, The effect of morphology and size on the photocatalytic properties of MoS_2, Reaction Kinetics, Mechanisms and Catalysis, 100 (2010) 153-163.

[80] Y.-H. Tan, K. Yu, J.-Z. Li, H. Fu, Z.-Q. Zhu, MoS_2@ZnO nano-heterojunctions with enhanced photocatalysis and field emission properties, J Appl Phys, 116 (2014) 064305.

[81] A. Kuc, N. Zibouche, T. Heine, Influence of quantum confinement on the electronic structure of the transition metal sulfide TS_2, Phys Rev B, 83 (2011) 245213.

[82] M.A. Lukowski, A.S. Daniel, F. Meng, A. Forticaux, L. Li, S. Jin, Enhanced Hydrogen Evolution Catalysis from Chemically Exfoliated Metallic MoS_2 Nanosheets, J Am Chem Soc, 135 (2013) 10274-10277.

[83] Y. Yu, S.-Y. Huang, Y. Li, S.N. Steinmann, W. Yang, L. Cao, Layer-Dependent Electrocatalysis of MoS_2 for Hydrogen Evolution, Nano Lett, 14 (2014) 553-558.

[84] X. Li, J. Yu, S. Wageh, A.A. Al-Ghamdi, J. Xie, Graphene in Photocatalysis: A Review, Small, 12 (2016) 6640-6696.

[85] X. Ma, J. Li, C. An, J. Feng, Y. Chi, J. Liu, J. Zhang, Y. Sun, Ultrathin Co(Ni)-doped MoS_2 nanosheets as catalytic promoters enabling efficient solar hydrogen production, Nano Research, 9 (2016) 2284-2293.

[86] C. Liu, J. Chen, H. Che, K. Huang, P.A. Charpentier, W.Z. Xu, W. Shi, H. Dong, Construction and enhanced photocatalytic activities of a hydrogenated TiO_2 nanobelt coated with CDs/MoS_2 nanosheets, RSC Advances, 7 (2017) 8429-8442.

[87] F. Carraro, L. Calvillo, M. Cattelan, M. Favaro, M. Righetto, S. Nappini, I. Píš, V. Celorrio, D.J. Fermín, A. Martucci, S. Agnoli, G. Granozzi, Fast One-Pot Synthesis of MoS_2/Crumpled Graphene p–n Nanonjunctions for Enhanced Photoelectrochemical Hydrogen Production, ACS Applied Materials & Interfaces, 7 (2015) 25685-25692.

[88] L. Peitao, L. Yonggang, Y. Weichun, M. Ji, G. Daqiang, Flower-like N-doped MoS_2 for photocatalytic degradation of RhB by visible light irradiation, Nanotechnology, 27 (2016) 225403.

[89] F. Meng, J. Li, S.K. Cushing, M. Zhi, N. Wu, Solar Hydrogen Generation by Nanoscale p–n Junction of p-type Molybdenum Disulfide/n-type Nitrogen-Doped Reduced

Graphene Oxide, J. Am. Chem. Soc., 135 (2013) 10286-10289.

[90] Y. Liu, S. Xie, H. Li, X. Wang, A Highly Efficient Sunlight Driven ZnO Nanosheet Photocatalyst: Synergetic Effect of P-Doping and MoS_2 Atomic Layer Loading, ChemCatChem, 6 (2014) 2522-2526.

[91] S. Ma, J. Xie, J. Wen, K. He, X. Li, W. Liu, X. Zhang, Constructing 2D layered hybrid CdS nanosheets/MoS_2 heterojunctions for enhanced visible-light photocatalytic H_2 generation, Appl. Surf. Sci., 391 (2017) 580-591.

[92] Y.-J. Yuan, D. Chen, J. Zhong, L.-X. Yang, J. Wang, M.-J. Liu, W.-G. Tu, Z.-T. Yu, Z.-G. Zou, Interface engineering of a noble-metal-free 2D-2D MoS_2/Cu-$ZnIn_2S_4$ photocatalyst for enhanced photocatalytic H_2 production, Journal of Materials Chemistry A, 5 (2017) 15771-15779.

[93] Y.-J. Yuan, Z.-T. Yu, Y.-H. Li, H.-W. Lu, X. Chen, W.-G. Tu, Z.-G. Ji, Z.-G. Zou, A MoS_2/6,13-pentacenequinone composite catalyst for visible-light-induced hydrogen evolution in water, Applied Catalysis B: Environmental, 181 (2016) 16-23.

[94] Y.-J. Yuan, F. Wang, B. Hu, H.-W. Lu, Z.-T. Yu, Z.-G. Zou, Significant enhancement in photocatalytic hydrogen evolution from water using a MoS_2 nanosheet-coated ZnO heterostructure photocatalyst, Dalton T, 44 (2015) 10997-11003.

[95] B. Weng, X. Zhang, N. Zhang, Z.-R. Tang, Y.-J. Xu, Two-Dimensional MoS_2 Nanosheet-Coated Bi_2S_3 Discoids: Synthesis, Formation Mechanism, and Photocatalytic Application, Langmuir, 31 (2015) 4314-4322.

[96] X. Meng, Z. Zhang, Bismuth-based Photocatalytic Semiconductors: Introduction, Challenges and Possible Approaches, Journal of Molecular Catalysis A: Chemical, 423

(2016) 533-549.

[97] X. Lu, Y. Jin, X. Zhang, G. Xu, D. Wang, J. Lv, Z. Zheng, Y. Wu, Controllable synthesis of graphitic C_3N_4/ultrathin MoS_2 nanosheet hybrid nanostructures with enhanced photocatalytic performance, Dalton Transactions, 45 (2016) 15406-15414.

[98] J. Low, J. Yu, M. Jaroniec, S. Wageh, A.A. Al-Ghamdi, Heterojunction Photocatalysts, Adv. Mater., 29 (2017) n/a-n/a.

[99] X. Meng, L. Jiang, W. Wang, Z. Zhang, Enhanced Photocatalytic Activity of BiOBr/ZnO Heterojunction Semiconductors Prepared by Facile Hydrothermal Method, International Journal of Photoenergy, 2015 (2015) 9.

[100] X. Meng, Z. Zhang, Synthesis, Analysis, and Testing of BiOBr-Bi_2WO_6 Photocatalytic Heterojunction Semiconductors, International Journal of Photoenergy, 2015 (2015) 12.

[101] X. Meng, Z. Zhang, Facile synthesis of BiOBr/Bi_2WO_6 heterojunction semiconductors with high visible-light-driven photocatalytic activity, Journal of Photochemistry and Photobiology A: Chemistry, 310 (2015) 33-44.

[102] X. Meng, Z. Zhang, Plasmonic Z-scheme Ag_2O-Bi_2MoO_6 p-n heterojunction photocatalysts with greatly enhanced visible-light responsive activities, Mater Lett, 189 (2017) 267-270.

[103] W. Zhang, X. Xiao, Y. Li, X. Zeng, L. Zheng, C. Wan, Liquid-exfoliation of layered MoS_2 for enhancing photocatalytic activity of TiO_2/g-C_3N_4 photocatalyst and DFT study, Appl. Surf. Sci., 389 (2016) 496-506.

[104] Y.-J. Yuan, J.-R. Tu, Z.-J. Ye, D.-Q. Chen, B. Hu, Y.-W. Huang, T.-T. Chen, D.-P. Cao,

Z.-T. Yu, Z.-G. Zou, MoS_2-graphene/$ZnIn_2S_4$ hierarchical microarchitectures with an electron transport bridge between light-harvesting semiconductor and cocatalyst: A highly efficient photocatalyst for solar hydrogen generation, Applied Catalysis B: Environmental, 188 (2016) 13-22.

[105] Y.-J. Yuan, D. Chen, J. Zhong, L.-X. Yang, J.-J. Wang, Z.-T. Yu, Z.-G. Zou, Construction of a Noble-Metal-Free Photocatalytic H_2 Evolution System Using MoS_2/Reduced Graphene Oxide Catalyst and Zinc Porphyrin Photosensitizer, The Journal of Physical Chemistry C, 121 (2017) 24452-24462.

[106] W. Hou, S.B. Cronin, A Review of Surface Plasmon Resonance-Enhanced Photocatalysis, Adv. Funct. Mater., 23 (2013) 1612-1619.

[107] S. Linic, P. Christopher, D.B. Ingram, Plasmonic-metal nanostructures for efficient conversion of solar to chemical energy, Nat Mater, 10 (2011) 911-921.

[108] X. Meng, Z. Zhang, Ag/AgCl Loaded Bi_2WO_6 Composite: A Plasmonic Z-Scheme Visible Light-Responsive Photocatalyst, International Journal of Photoenergy, 2016 (2016) 11.

[109] X. Meng, Z. Zhang, Pd-doped Bi_2MoO_6 Plasmonic Photocatalysts with Enhanced Visible Light Photocatalytic Performance, Appl Surf Sci, 392 (2016) 169-180.

[110] X. Meng, Z. Zhang, Plasmonic ternary Ag–rGO–Bi_2MoO_6 composites with enhanced visible light-driven photocatalytic activity, Journal of Catalysis, 344 (2016) 616-630.

[111] X. Meng, Z. Li, J. Chen, H. Xie, Z. Zhang, Enhanced visible light-induced photocatalytic activity of surface-modified BiOBr with Pd nanoparticles, Appl Surf Sci, (2017).

[112] X. Meng, Z. Li, Z. Zhang, Pd-nanoparticle-decorated peanut-shaped $BiVO_4$ with improved visible light-driven photocatalytic activity comparable to that of TiO_2 under UV light, Journal of Catalysis, 356 (2017) 53-64.

[113] X. Meng, Z. Zhang, Bi_2MoO_6 co-modified by reduced graphene oxide and palladium (Pd^{2+} and Pd^0) with enhanced photocatalytic decomposition of phenol, Applied Catalysis B: Environmental, 209 (2017) 383-393.

[114] X. Meng, Z. Li, J. Chen, H. Xie, Z. Zhang, Enhanced visible light-induced photocatalytic activity of surface-modified BiOBr with Pd nanoparticles, Appl Surf Sci, 433 (2018) 76-87.

[115] S. Zou, G.C. Schatz, Silver nanoparticle array structures that produce giant enhancements in electromagnetic fields, Chem. Phys. Lett., 403 (2005) 62-67.

[116] J.J. Mock, M. Barbic, D.R. Smith, D.A. Schultz, S. Schultz, Shape effects in plasmon resonance of individual colloidal silver nanoparticles, The Journal of Chemical Physics, 116 (2002) 6755-6759.

[117] K.H. Su, Q.H. Wei, X. Zhang, J.J. Mock, D.R. Smith, S. Schultz, Interparticle Coupling Effects on Plasmon Resonances of Nanogold Particles, Nano Lett., 3 (2003) 1087-1090.

[118] M. Rycenga, C.M. Cobley, J. Zeng, W. Li, C.H. Moran, Q. Zhang, D. Qin, Y. Xia, Controlling the Synthesis and Assembly of Silver Nanostructures for Plasmonic Applications, Chem. Rev., 111 (2011) 3669-3712.

[119] Y. Xia, Y. Xiong, B. Lim, S.E. Skrabalak, Shape-Controlled Synthesis of Metal Nanocrystals: Simple Chemistry Meets Complex Physics?, Angew. Chem. Int. Ed., 48

(2009) 60-103.

[120] F. Le, D.W. Brandl, Y.A. Urzhumov, H. Wang, J. Kundu, N.J. Halas, J. Aizpurua, P. Nordlander, Metallic Nanoparticle Arrays: A Common Substrate for Both Surface-Enhanced Raman Scattering and Surface-Enhanced Infrared Absorption, ACS Nano, 2 (2008) 707-718.

[121] S. Zou, G.C. Schatz, Silver nanoparticle array structures that produce giant enhancements in electromagnetic fields, Chem. Phys. Lett., 403 (2005) 62-67.

[122] P. Zhang, M. Fujitsuka, T. Majima, Hot electron-driven hydrogen evolution using anisotropic gold nanostructure assembled monolayer MoS_2, Nanoscale, 9 (2017) 1520-1526.

[123] Y. Kang, S. Najmaei, Z. Liu, Y. Bao, Y. Wang, X. Zhu, N.J. Halas, P. Nordlander, P.M. Ajayan, J. Lou, Z. Fang, Plasmonic Hot Electron Induced Structural Phase Transition in a MoS_2 Monolayer, Adv. Mater., 26 (2014) 6467-6471.

[124] Y. Kang, Y. Gong, Z. Hu, Z. Li, Z. Qiu, X. Zhu, P.M. Ajayan, Z. Fang, Plasmonic hot electron enhanced MoS_2 photocatalysis in hydrogen evolution, Nanoscale, 7 (2015) 4482-4488.

[125] L. Wei, Y. Chen, Y. Lin, H. Wu, R. Yuan, Z. Li, MoS_2 as non-noble-metal co-catalyst for photocatalytic hydrogen evolution over hexagonal $ZnIn_2S_4$ under visible light irradiations, Applied Catalysis B: Environmental, 144 (2014) 521-527.

[126] H. Yu, P. Xiao, P. Wang, J. Yu, Amorphous molybdenum sulfide as highly efficient electron-cocatalyst for enhanced photocatalytic H_2 evolution, Applied Catalysis B: Environmental, 193 (2016) 217-225.

[127] F. Niefind, J. Djamil, W. Bensch, B.R. Srinivasan, I. Sinev, W. Grunert, M. Deng, L. Kienle, A. Lotnyk, M.B. Mesch, J. Senker, L. Dura, T. Beweries, Room temperature synthesis of an amorphous MoS_2 based composite stabilized by N-donor ligands and its light-driven photocatalytic hydrogen production, RSC Advances, 5 (2015) 67742-67751.

[128] D.J. Li, U.N. Maiti, J. Lim, D.S. Choi, W.J. Lee, Y. Oh, G.Y. Lee, S.O. Kim, Molybdenum Sulfide/N-Doped CNT Forest Hybrid Catalysts for High-Performance Hydrogen Evolution Reaction, Nano Lett., 14 (2014) 1228-1233.

[129] M.L. Tang, D.C. Grauer, B. Lassalle-Kaiser, V.K. Yachandra, L. Amirav, J.R. Long, J. Yano, A.P. Alivisatos, Structural and Electronic Study of an Amorphous MoS_3 Hydrogen-Generation Catalyst on a Quantum-Controlled Photosensitizer, Angew. Chem. Int. Ed., 50 (2011) 10203-10207.

[130] Y.-H. Chang, C.-T. Lin, T.-Y. Chen, C.-L. Hsu, Y.-H. Lee, W. Zhang, K.-H. Wei, L.-J. Li, Highly Efficient Electrocatalytic Hydrogen Production by MoSx Grown on Graphene-Protected 3D Ni Foams, Adv. Mater., 25 (2013) 756-760.

[131] B. Sheng, J. Liu, Z. Li, M. Wang, K. Zhu, J. Qiu, J. Wang, Effects of excess sulfur source on the formation and photocatalytic properties of flower-like MoS2 spheres by hydrothermal synthesis, Mater. Lett., 144 (2015) 153-156.

[132] J. Zhang, L. Huang, Z. Lu, Z. Jin, X. Wang, G. Xu, E. Zhang, H. Wang, Z. Kong, J. Xi, Z. Ji, Crystal face regulating MoS2/TiO2(001) heterostructure for high photocatalytic activity, J. Alloys Compd., 688, Part B (2016) 840-848.

[133] L. Cao, R. Wang, D. Wang, X. Li, H. Jia, MoS_2-hybridized TiO_2 nanosheets with exposed {001} facets to enhance the visible-light photocatalytic activity, Mater. Lett., 160

(2015) 286-290.

[134] J. Zhang, Z. Xu, W. Su, D. Zhu, Development Of A Cathode Designing Method To Avoid Electrodes' Interference During Blisk Electrochemical Machining, KnE Materials Science, 1 (2016) 71-77.

[135] J. Chen, X.-J. Wu, L. Yin, B. Li, X. Hong, Z. Fan, B. Chen, C. Xue, H. Zhang, One-pot Synthesis of CdS Nanocrystals Hybridized with Single-Layer Transition-Metal Dichalcogenide Nanosheets for Efficient Photocatalytic Hydrogen Evolution, Angew. Chem. Int. Ed., 54 (2015) 1210-1214.

[136] U. Maitra, U. Gupta, M. De, R. Datta, A. Govindaraj, C.N.R. Rao, Highly Effective Visible-Light-Induced H_2 Generation by Single-Layer 1T-MoS_2 and a Nanocomposite of Few-Layer 2H-MoS_2 with Heavily Nitrogenated Graphene, Angewandte Chemie International Edition, 52 (2013) 13057-13061.

[137] J. Kibsgaard, J.V. Lauritsen, E. Lægsgaard, B.S. Clausen, H. Topsøe, F. Besenbacher, Cluster−Support Interactions and Morphology of MoS_2 Nanoclusters in a Graphite-Supported Hydrotreating Model Catalyst, J. Am. Chem. Soc., 128 (2006) 13950-13958.

[138] M. Bollinger, J. Lauritsen, K.W. Jacobsen, J.K. Nørskov, S. Helveg, F. Besenbacher, One-dimensional metallic edge states in MoS_2, Phys. Rev. Lett., 87 (2001) 196803.

[139] S. Helveg, J.V. Lauritsen, E. Lægsgaard, I. Stensgaard, J.K. Nørskov, B. Clausen, H. Topsøe, F. Besenbacher, Atomic-scale structure of single-layer MoS_2 nanoclusters, Phys. Rev. Lett., 84 (2000) 951.

[140] K. Chang, X. Hai, H. Pang, H. Zhang, L. Shi, G. Liu, H. Liu, G. Zhao, M. Li, J. Ye, Targeted Synthesis of 2H- and 1T-Phase MoS_2 Monolayers for Catalytic Hydrogen

Evolution, Adv. Mater., 28 (2016) 10033-10041.

[141] Q. Gu, H. Sun, Z. Xie, Z. Gao, C. Xue, MoS2-coated microspheres of self-sensitized carbon nitride for efficient photocatalytic hydrogen generation under visible light irradiation, Appl. Surf. Sci., 396 (2017) 1808-1815.

[142] X. Meng, Z. Zhang, X. Li, Synergetic photoelectrocatalytic reactors for environmental remediation: A review, Journal of Photochemistry and Photobiology C: Photochemistry Reviews, 24 (2015) 83-101.

[143] Y. Qi, Q. Xu, Y. Wang, B. Yan, Y. Ren, Z. Chen, CO_2-Induced Phase Engineering: Protocol for Enhanced Photoelectrocatalytic Performance of 2D MoS_2 Nanosheets, Acs Nano, 10 (2016) 2903-2909.

[144] X. Guo, X. Tong, Y. Wang, C. Chen, G. Jin, X.-Y. Guo, High photoelectrocatalytic performance of a MoS_2-SiC hybrid structure for hydrogen evolution reaction, Journal of Materials Chemistry A, 1 (2013) 4657-4661.

[145] V. Polshettiwar, R. Luque, A. Fihri, H. Zhu, M. Bouhrara, J.-M. Basset, Magnetically Recoverable Nanocatalysts, Chem. Rev., 111 (2011) 3036-3075.

[146] L.M. Rossi, N.J.S. Costa, F.P. Silva, R. Wojcieszak, Magnetic nanomaterials in catalysis: advanced catalysts for magnetic separation and beyond, Green Chemistry, 16 (2014) 2906-2933.

[147] X. Meng, Z. Zhang, Synthesis and characterization of plasmonic and magnetically separable Ag/AgCl-Bi_2WO_6@ Fe_3O_4@SiO_2 core-shell composites for visible light-induced water detoxification, J. Colloid Interface Sci., 485 (2017) 296-307.

[148] M. Shokouhimehr, Magnetically Separable and Sustainable Nanostructured

Catalysts for Heterogeneous Reduction of Nitroaromatics, Catalysts, 5 (2015) 534.

[149] Y. Fu, H. Chen, X. Sun, X. Wang, Combination of cobalt ferrite and graphene: High-performance and recyclable visible-light photocatalysis, Applied Catalysis B: Environmental, 111 (2012) 280-287.

[150] N. Guo, H. Li, X. Xu, H. Yu, Hierarchical Fe_3O_4@MoS_2/Ag_3PO_4 magnetic nanocomposites: Enhanced and stable photocatalytic performance for water purification under visible light irradiation, Appl. Surf. Sci., 389 (2016) 227-239.

Chapter 4 Equilibrium and kinetic modelling of adsorption of *Rhodamine B* on MoS_2

Zizhen Li, Xiangchao Meng and Zisheng Zhang

Materials Research Bulletin, *111*, 238-244 (2019)

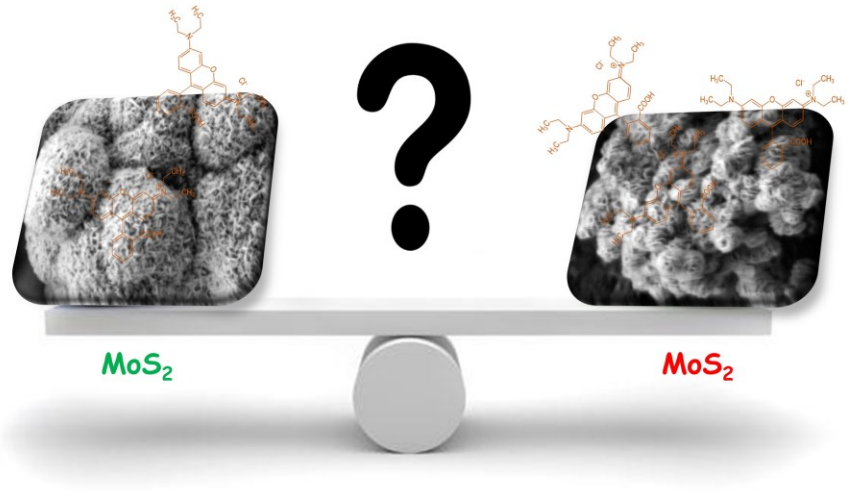

Abstract

The recent emergence of layered MoS_2, which is an earth-abundant material, has gained increasing attention in various fields. In this work, MoS_2 is fabricated via a simple hydrothermal method with different sulfur precursors. The effect of S source on the

morphologies and adsorption capacities of Rhodamine B (RhB) onto MoS_2 were investigated. The results indicated that the MoS_2 prepared by CH_4N_2S exhibited the highest adsorption capacity. The N_2 sorption isotherm indicated that the as-prepared MoS_2-CH_4N_2S is a mesoporous microsphere. In addition, the adsorption process can be well described by the Langmuir isotherm model and the pseudo second-order model. The intra-particle diffusion model was also employed to analyze the adsorption mechanisms, which demonstrated that the intra-particle diffusion within the mesopores played an important role in the overall adsorption process. Based on these results, MoS_2-CH_4N_2S obtained in this work can be served as a promising candidate for dye removal in wastewater.

4.1 Introduction

Synthetic dyes, a type of carcinogenic compound, are major components in industrial wastewater due to their extensive applications in textiles, paper, cosmetics and food. As estimated, approximate 0.7 to 1 million tons of dyes are produced annually [1]. However, over half of the annual dye production is discharged to the environment via effluent or lost during the dying process, which has generated increasing ecological concerns [2]. These dyes not only severely affect the aesthetic qualities of water, but also raise an enormous risk to aquatic organisms and human health. Specifically, the photosynthesis process is hindered by the highly visible property of dyes. As a result, it will cause some problems to aquatic organisms due to low oxygen content and poor sunlight penetration. The toxicity and carcinogenicity of dyes and their degraded products also have a great impact on living organisms [3]. Moreover, it is reported that dyes could hinder the efficiency of some water treatment processes, such as ultraviolet disinfection [4]. The growing dye contaminated water could also accelerate clean water shortages.

Without appropriate treatment, organic dyes may remain in the water for a long time due to their refractory chemical structures (*e.g.* benzene ring) of organic dyes. Therefore, a variety of methods have been developed for the removal/decomposition of organic contaminants, such as adsorption [5], coagulation [6], electrocoagulation [7], biodegradation [8] and advanced oxidation process (AOP) [9-13]. Each method, however, possesses its own advantages and disadvantages. Among them, adsorption has been widely used due to its easy operation, cost-effectiveness and high efficiency [14].

It is well known that design and fabrication of adsorbent with advantageous properties such as large adsorption capacity, high adsorption rate, easy operation for adsorbent collection and separation, good reusability, and cost-effectiveness is of great significance [15]. The emergence of layered-MoS_2 has recently gained increasing attention due to its unique physical and chemical properties [16, 17]. It has been widely used in the fields of hydrogen production [18], photocatalysis [19], solid lubricants [20], electrochemical devices [21], *etc.* Layered MoS_2 also exhibited great potential in the field of adsorption, due to its high specific surface area [22], suitable active edge sites for adsorption [15, 23], and economic feasibility (earth-abundant material) [24]. In addition, the morphologies and number of layers of MoS_2 is tunable via controlling the preparation methods to expose more active edge sites for adsorption [22, 24-26]. Recently, the hierarchical architectures of MoS_2 have exhibited great adsorption properties. For example, Fang *et al.* reported that flower-liked MoS_2-glue sponge obtained by a hydrothermal method had a 127.39 mg/g adsorption capacity towards RhB [15]. Song *et al.* demonstrated that MoS_2 nanosheets prepared by the similar method had around 81.25 mg/g adsorption capacity towards RhB [22]. Although the similar hydrothermal methods were employed in these works, distinct results

were obtained. This may be resulted from different precursors used in the synthesis process [27, 28].

Hence, MoS_2 prepared by a hydrothermal method with different sulfur (S) precursors were reported in this work. The adsorption capacities and morphologies of corresponding MoS_2 samples were compared and discussed. Moreover, different adsorption isotherm models and adsorption kinetic models were applied to analyse adsorption data. The possible adsorption mechanisms were also studied. The results indicated that the S sources used in the synthesis methods significantly influenced the morphologies and adsorption capacities of products. It is hoped that this work could address the importance of choosing synthesis precursors in the fabrication of adsorbents and also shed light on the importance of addressing the adsorption in future photocatalysis or other applications.

4.2 Experimental

4.2.1 Adsorbent preparation

All chemicals were purchased from Fisher Scientific and used as received unless mentioned otherwise. MoS_2 was synthesized via a simple hydrothermal method as reported elsewhere with minor modification [27]. In this method, 0.5 g of $Na_2MoO_4 \cdot 2H_2O$ and 0.7 g of CH_4N_2S (S source) is firstly mixed and dissolved in 70 mL ddH_2O (deionized, distilled water) followed by magnetic stirring for 25 min. Then, 0.47 g of citric acid ($C_6H_8O_7$) was added to adjust the pH value of the solution and magnetically stirred for another 10 min before transferring into a 100-mL Teflon-lined stainless steel autoclave (Parr Instrument Company). The autoclave was heated at 200 °C for 21 h. The resulting black precipitates were washed by ddH_2O and ethanol for several times and dried at 60 °C for 12 h. In order

to test the effect of S source on the adsorption performance, MoS_2 was also synthesized by Na_2S, C_2H_5NS, and $(NH_4)_2S$, respectively using the same methodology as described above.

4.2.2 Characterization of the adsorbent

A field-emission scanning electron microscope (FE-SEM, JEOL JSM-7500F) was used to observe morphologies and structures of the samples. The N_2 sorption isotherms were obtained by automatic adsorption apparatus and measurement systems (ASAP 2020, Micromeritics and Nova 4200E, Quantachrome) to investigate the surface area, pore structure and pore size distribution. The Brunauer, Emmett and Teller (BET) surface area of the samples were obtained using multi-point estimation. Pore volume distributions were calculated using the N_2 desorption branch, and the Barrett-Joyner-Halenda (BJH) method was applied for the desorption branch to calculate the pore size data (d_p) using Equation 1 (where V/A_s is a ratio of volume to surface area of pores) as follows,

$$d_p = 4\left(\frac{V}{A_s}\right)_{BJH} \qquad \textbf{\textit{Equation 1}}$$

4.2.3 Adsorption studies

Batch experiments with respect to S source and initial RhB concentration were performed to test the adsorption process of RhB onto MoS_2 under different conditions. For the equilibrium study of adsorption, 0.01 g MoS_2 was dispersed in 100 mL of RhB solution at a specific concentration. The mixture was continually stirred at 20 °C for 2 hr to reach adsorption/desorption equilibrium. The residual concentration of RhB solution was measured by a UV-vis spectrophotometer (Genesys 10 UV, Thermo Scientific). The

quantity of RhB adsorbed on MoS_2 was calculated by mass balance as shown in Equation 2 [26, 29] and the removal rate of RhB was determined using Equation 3:

$$q_t = \frac{(C_0 - C_t)}{W} \times V = \frac{(C_0 - C_t)}{C_{dosage}} \qquad \textit{Equation 2}$$

$$\text{Removal}(\%) = \frac{(C_0 - C_t)}{C_0} \times 100 \qquad \textit{Equation 3}$$

Where, q_t is the pollutant concentration in solid phase at time t (mg/g); C_0 is the initial pollutant concentration ($mg \cdot L^{-1}$) in the solution (liquid phase); C_t is the pollutant concentration at time t ($mg \cdot L^{-1}$) in the solution (liquid phase); V is the volume of pollutant solution (L); W is the weight of adsorbent (g); and C_{dosage} is the initial adsorbent dosage (g/L).

For adsorption kinetics, the RhB concentration in solution and the quantity adsorbed on MoS_2 is monitored at different time intervals. The pseudo first- and second-order models were employed to study the kinetics. The intra-particle diffusion model was applied to study the mechanisms of adsorption.

4.3 Results and discussion

4.3.1 Effects of precursors

It is reported that the morphologies and corresponding properties of nanomaterials may be varied with precursors used in the synthesis method [27, 28]. Morphologies of MoS_2 prepared by different S sources were investigated using SEM, as shown in Fig. 4.1. It can be found that morphologies as well as particle sizes were moderately different. Hierarchical

microspheres were formed when $(NH_4)_2S$, Na_2S and CH_4N_2S were used as S sources. Instead, large bulks composed of small particles were formed when C_2H_5NS was used as the S source. As for the microspheres, the sizes were extremely different. Specifically, microspheres with sizes of 2 - 3 μm were formed when $(NH_4)_2S$ was used, and the sizes of MoS_2 microspheres prepared by Na_2S and CH_4N_2S were 100 – 300 nm, and 200 – 400 nm, respectively. Even though MoS_2 prepared by Na_2S were with smaller sizes, MoS_2 prepared by CH_4N_2S were composed of more wrinkles. Adsorption of RhB on different MoS_2 was tested and shown in Fig. 4.2. It can be found that the adsorption capacities have the following trend: MoS_2-CH_4N_2S > MoS_2-Na_2S > MoS_2-comercial > MoS_2-C_2H_5NS > MoS_2-$(NH_4)_2S$. Therefore, the following experiments were carried out using MoS_2-CH_4N_2S and referred to as MoS_2 unless mentioned otherwise. The good adsorption capacity of MoS_2-CH_4N_2S may be attributed to the higher degree of wrinkling (Fig. 4.1) as well as the pore structure (Fig. 4.3) [30].

N_2 sorption isotherm was obtained to measure the BET surface area and porous structure of prepared MoS_2-CH_4N_2S. As shown in Fig. 4.3, the N_2 adsorption-desorption isotherm can be assigned as type IV (a), suggesting the existence of a mesoporous structure [31]. The hysteresis loop is an H3 loop, which may be attributed to the plate-like MoS_2 particles with the slit-shaped pores and capillary condensation in the mesopores [26]. This result is consistent with the morphology of MoS_2-CH_4N_2S observed in SEM images. In addition, the calculated BET surface area of hierarchical MoS_2-CH_4N_2S particle was 72.0 m^2/g, indicating abundant sites for RhB adsorption.

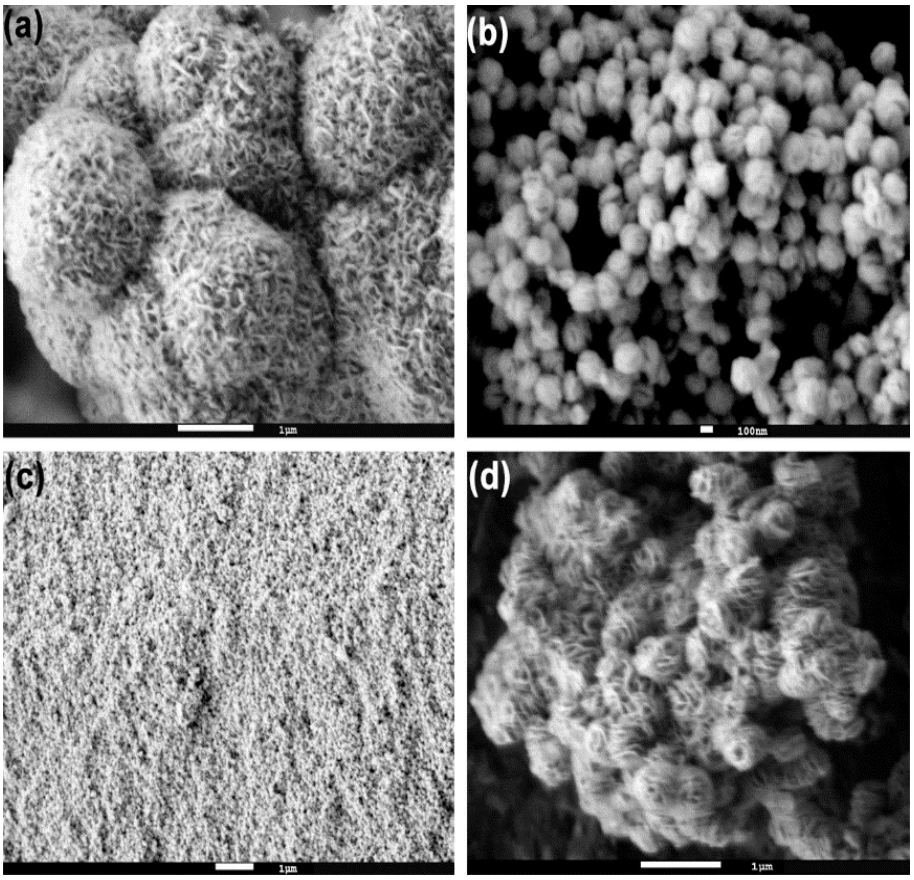

Figure 4.1. SEM images of MoS_2 prepared with different S precursors: (a) $(NH_4)_2S$, (b) Na_2S, (c) C_2H_5NS and (d) CH_4N_2S.

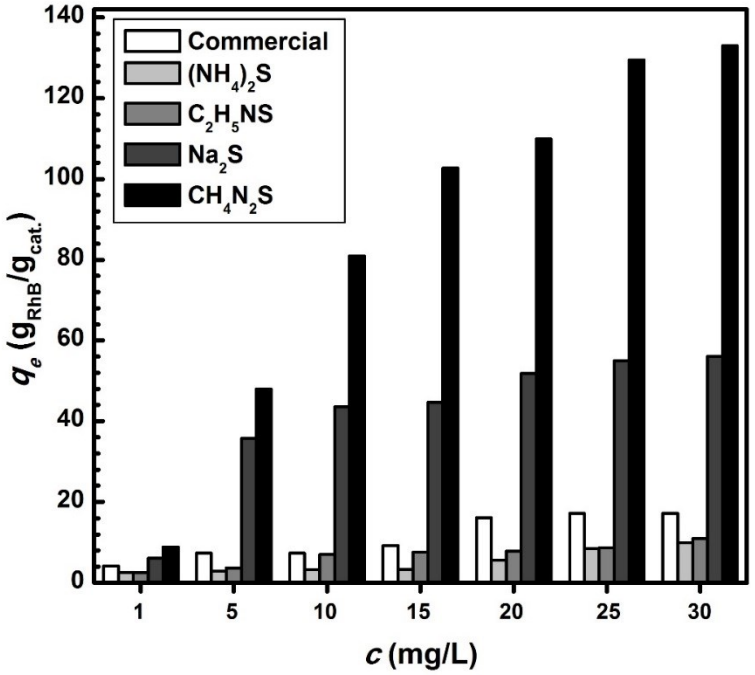

Figure 4.2. The amount of adsorption at equilibrium of RhB with initial concentrations of 1 – 30 mg/L on MoS_2, purchased and prepared with different S sources. (T = 293.15 K, dose: 0.1 g adsorbent/ 100 mL solution)

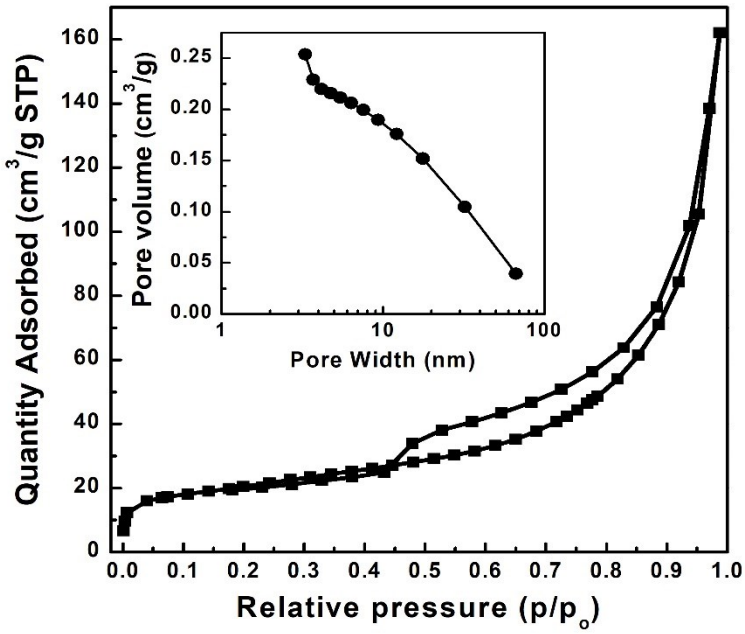

Figure 4.3. N_2 sorption isotherms for MoS_2 (S_{BET} = 72.0 m^2/g). (Inset: Pore size distribution for MoS_2)

4.3.2 Effects of contact time and initial RhB concentration

The effect of contact time on the adsorption capacity is depicted in Fig. 4.4a. For all initial concentrations, the RhB adsorption rate was rapid at the beginning and gradually decreased as contact time increased. This may be attributed to the change in concentration, which is the driving force, and available adsorption sites [32, 33]. The required time to reach equilibrium increased from 5 to 120 min when the initial RhB concentration increased from 1 to 40 mg/L. In addition, the equilibrium adsorption capacity increased with initial RhB concentration and increased from 0.02 to 26.18 mg/g when the initial RhB concentration increased from 1 to 40 mg/L. The possible reason for this could be that the higher RhB concentration generates larger mass transfer as for the larger driving force resulted from the larger difference in concentrations between the bulk solution and the adsorbent, which would facilitate the transportation and adsorption of RhB molecules onto the active sites of MoS_2 [34]. Fig. 4.4b indicated the effect of initial RhB concentration on the RhB removal ratio. The removal ratio remained steady when the initial RhB concentration varied from 1 to 10 mg/L. However, as observed in Fig. 4.4b, the removal ratio decreases when the initial RhB concentration is larger than 10 mg/L. This may be attributed to the saturation of active sites [35, 36]. As a result, RhB with an initial concentration lower than 10 mg/L favors the removal efficiency of RhB by MoS_2.

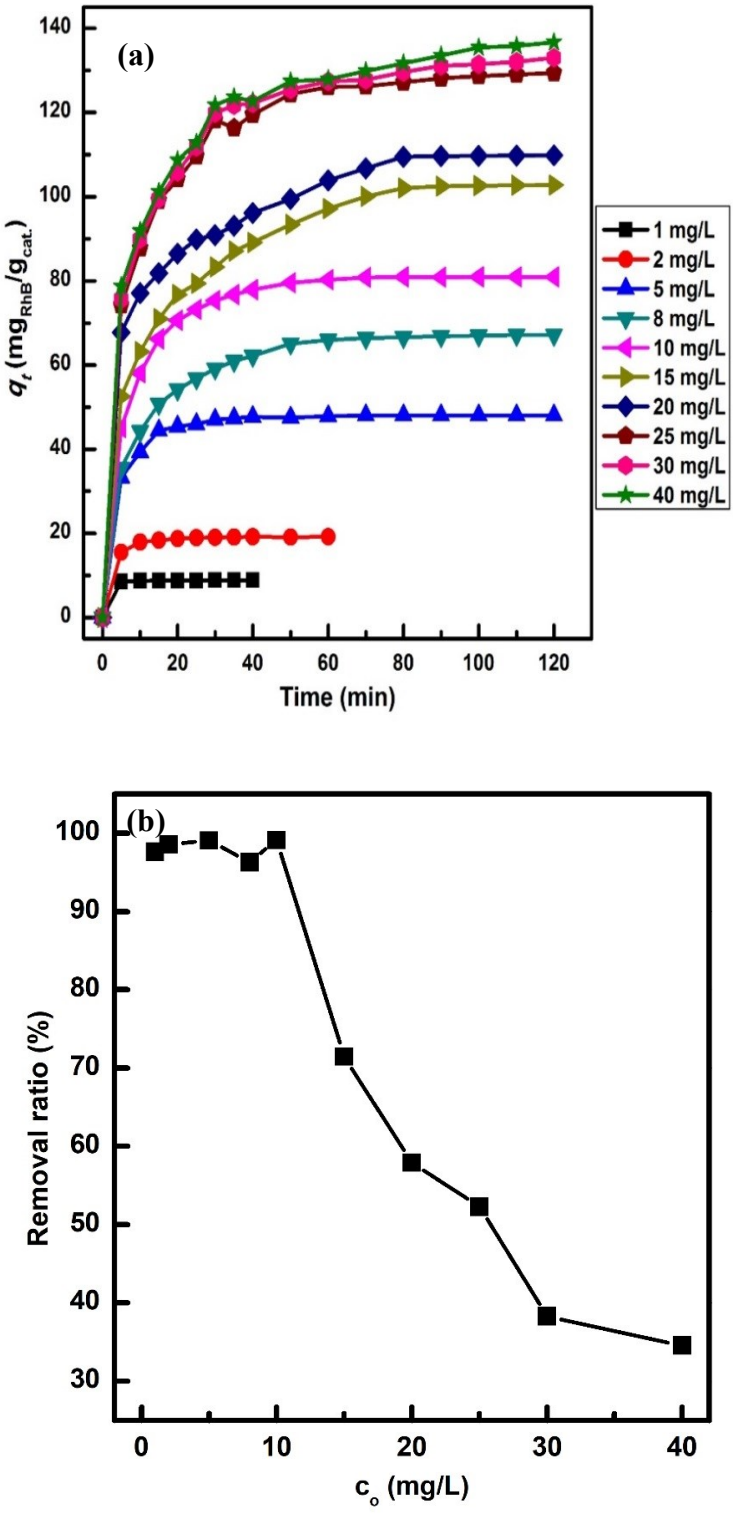

Figure 4.4. (a) Effect of contact time and initial RhB concentration on the adsorption of RhB by MoS_2 (b) Effect of initial RhB concentration on the dye removal efficiency at equilibrium.

4.3.3 Isothermal studies

The Langmuir isotherm, Freundlich isotherm, Temkin isotherm, and Dubinin-Radushkevich isotherm were used to analyze the adsorption process (Fig. 4.5). The validity of the isotherm models can be determined by their linearized plots. The regression coefficient (R^2) is used as a criterion to compare the fitness of each model.

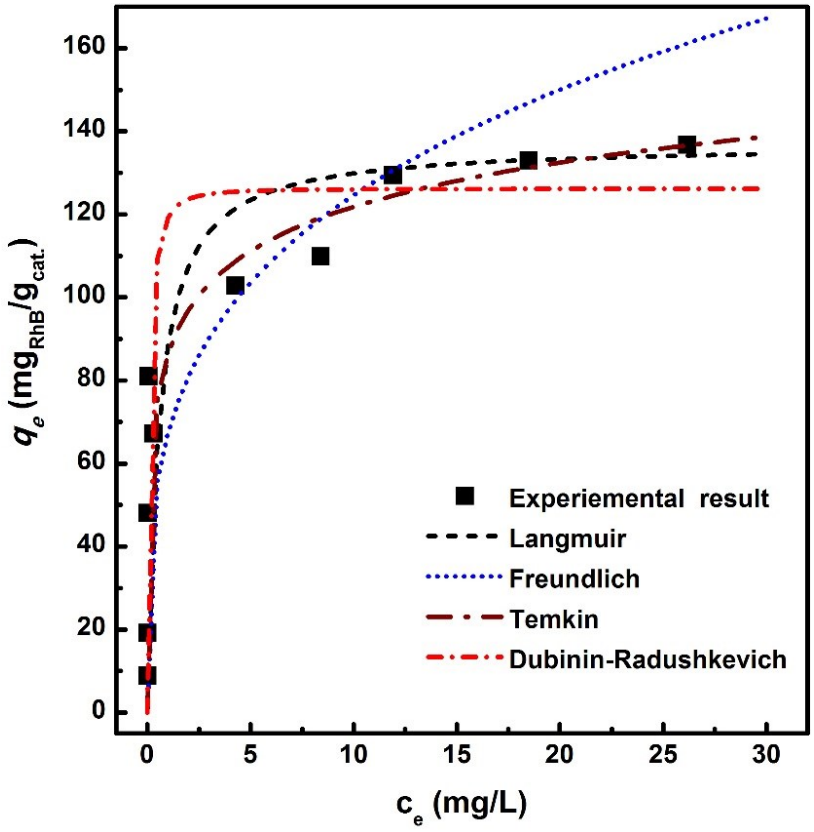

Figure 4.5. Fittings of equilibrium data to various adsorption isotherms

The linear form of Langmuir isotherm is expressed as the following (Equation 4):

$$\frac{C_e}{q_e} = \frac{1}{bQ_0} + \frac{C_e}{Q_0} \qquad \textit{Equation 4}$$

Where, C_e (mg/L) and q_e (mg/g) are the equilibrium concentration of adsorbate in liquid-phase and solid-phase, respectively; Q_0 (mg/g) is the maximum monolayer coverage capacity of adsorbent; and b (L/mg) is the Langmuir adsorption constant. The favourability of the adsorption process can be estimated by a dimensionless constant, R_L, which is expressed as Equation 5 [36, 37]:

$$R_L = \frac{1}{1 + bC_0} \qquad \textbf{Equation 5}$$

For the initial concentration of RhB solution ranging from 40 mg/L to 1 mg/L, the values of R_L varied from 0.014 to 0.354. This range is between 0 ~ 1, which indicated that the adsorption process is 'favorable'.

The Freundlich isotherm is given by the following equation (Equation 6):

$$\log q_e = \log K_F + \frac{1}{n} \log C_e \qquad \textbf{Equation 6}$$

Where K_F (mg/g) is a constant to describe the sorption capacity, and n is a constant representing the favourability of the sorption system [37, 38]. In this work, the value of n is larger than 1 (n = 3.74), which indicated favorable adsorption of RhB onto MoS_2 [39].

The Temkin isotherm is described by the following equations (Equations 7 and 8):

$$q_e = B \ln A_T + B \ln C_e \qquad \textbf{Equation 7}$$

$$B = \frac{RT}{b_T} \qquad \textbf{Equation 8}$$

Where, b_T is the Temkin isotherm constant (J/mol); R is the universal gas constant (8.314 J mol^{-1} K^{-1}); T is temperature (K); A_T is the Temkin isotherm equilibrium binding constant (L/g); and B is the constant related to heat of adsorption

The Dubinin-Radushkevich (D-R) isotherm is expressed as the following (Equations 9, 10 and 11) [36, 39]:

$$\ln q_e = \ln q_s - \beta\varepsilon^2 \qquad \textbf{Equation 9}$$

$$\varepsilon = RT\ln\left(1+\frac{1}{C_e}\right) \qquad \textbf{Equation 10}$$

$$E = \frac{1}{\sqrt{2\beta}} \qquad \textbf{Equation 11}$$

Where q_s is the theoretical isotherm saturation capacity (mg/g); β is the D-R isotherm constant with a dimension of energy, ε is the Polanyi potential; and E is the mean adsorption energy (kJ/mol). From the isotherm plot, the theoretical isotherm saturation capacity was obtained to be 126.17 mg/g. The calculated mean adsorption energy was lower than 8 kJ/mol (E = 5 kJ/mol), suggesting a physisorption process [40].

Table 4.1. Summary of isotherm parameters

Isotherms	**Constants**	**MoS_2**
Langmuir	Q_0 (mg/g)	136.99
	b (L/mg)	1.83
	R^2	0.995
Freundlich	n	3.74
	K_F (L/g)	67.33
	R^2	0.707
Temkin	B	15.38
	A_T (L/g)	247.91
	b_T (J/mol)	158.36
	R^2	0.907
D-R	q_s (mg/g)	126.17
	E (kJ/mol)	5
	R^2	0.875

The various isotherm constants are summarized in Table 4.1. According to the regression coefficients, Langmuir isotherm model best described the adsorption data, which implied that monolayer adsorption with uniform adsorption energies may occur in the RhB-MoS_2 system. However, a uniform distribution of bounding energy rather than a uniform adsorption energy may also take place in the RhB-MoS_2 system, because the regression coefficients for the Temkin isotherm model is relatively high (R^2 = 0.9069). As shown in Fig. 4.5, when the concentration of RhB at equilibrium was within the range of 5 ~ 10 mg/mL, Temkin isotherm model fits much better compared to Langmuir isotherm model. This phenomenon may be due to that the Temkin isotherm is valid for an intermediate range of ion concentration, and RhB is a positively charged dye and can be regarded as positive ions [41]. Similar result was also reported on adsorption of methylene blue which is also a positively charged dye [42]. The mean adsorption energy (E = 5 kJ/mol)

determined by the D-R isotherm model indicated that the type of RhB adsorption onto MoS_2 may be physisorption [40]. The calculated maximum monolayer coverage capacity from Langmuir isotherm was 136.99 mg/g. Comparison of maximum adsorption capacities of RhB for some other reported adsorbents were shown in Table 4.2. It can be seen that MoS_2 prepared in this work exhibited higher adsorption capacity.

Table 4.2. The reported maximum monolayer coverage capacity of RhB onto other adsorbents

Adsorbents	Q_0 **(mg/g)**	**Conditions**	**Ref.**
Kaolinite	46.08	303K, 1 atm	[43]
Fe_3O_4/Al pillared bentonite	62.15	298K, 1 atm	[44]
Iron-pillared bentonite	98.62	298K, 1 atm	[45]
Zn/Co-carbon composite	101.93	300K, 1 atm	[46]
MoS_2	136.99	293K, 1atm	This study

4.3.4 Adsorption kinetics

In order to study the adsorption mechanism and possible rate limiting steps, the pseudo-first order and pseudo-second order models were used to fit the experimental data with different initial RhB concentrations. The fitness of the two kinetic models can be checked by the correlation coefficient (R^2).

The pseudo first-order kinetic model is expressed by the following equation (Equation 12):

$$\ln\left(q_e - q_t\right) = \ln q_e - k_1 t \qquad \textit{Equation 12}$$

Where, k_1 denotes the rate constant of the pseudo first-order adsorption (min^{-1}).

The linear form of the pseudo second-order kinetic model is expressed as follows (Equation 13):

$$\frac{t}{q_t} = \frac{1}{k_2 q_e^2} + \frac{t}{q_e} \qquad \textit{Equation 13}$$

Where, k_2 is the rate constant of the pseudo second-order model (g mg^{-1} min^{-1}).

The plots of pseudo first-order model and second-order model are shown in Fig. 4.6 and the kinetic parameters are listed in Table 4.3. For all concentrations, the linear regression correlation coefficient (R^2) for pseudo second-order was much higher than that of pseudo first-order, indicating better fitness using the pseudo second-order model. This implied that the extremal film diffusion may not be the rate-limiting step for the RhB adsorption onto MoS_2 [47, 48]. Moreover, the calculated values of q_e by the pseudo second-order model were analogous to the corresponding experimental values. Therefore, the pseudo second-order model is more appropriate to describe the RhB adsorption onto MoS_2.

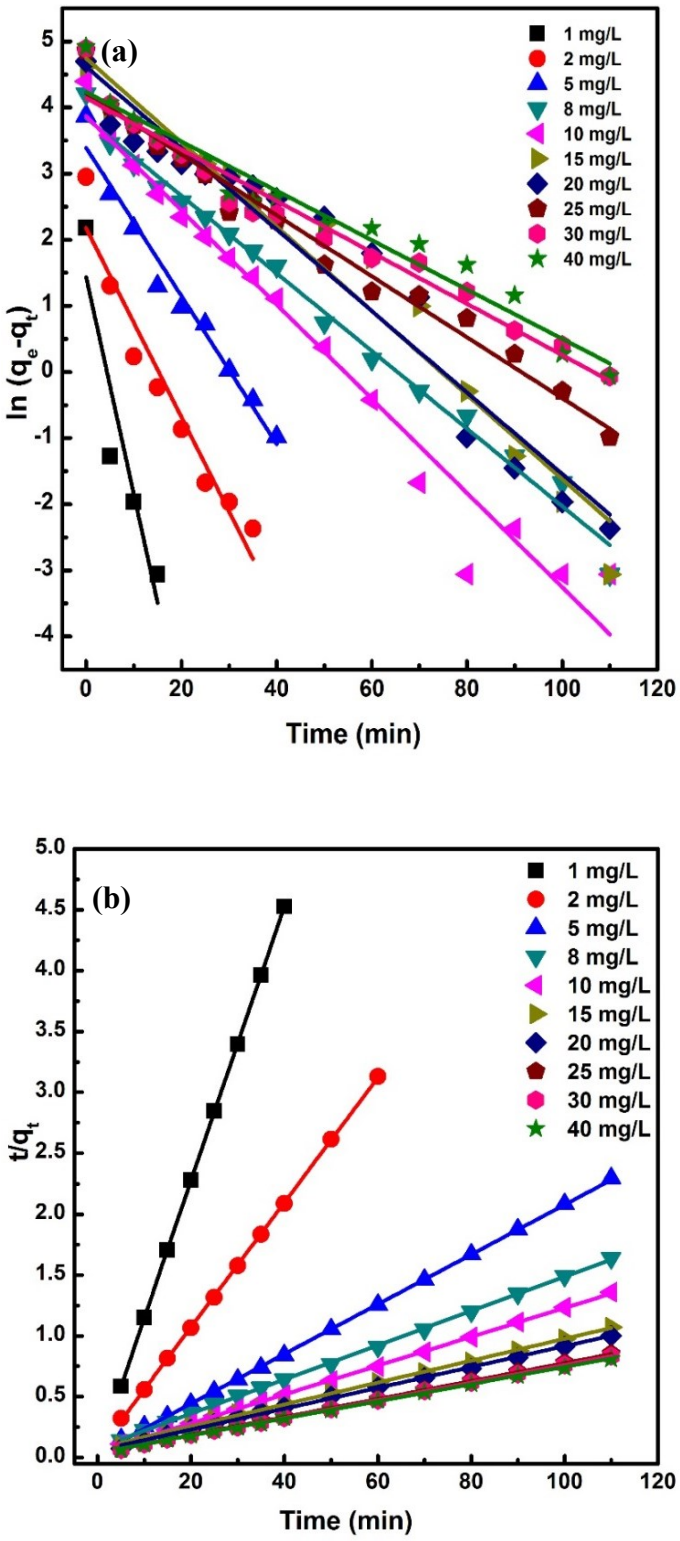

Figure 4.6. (a) Pseudo first-order and pseudo second-order plots for uptake of RhB onto MoS_2 data with different initial RhB concentrations

Table 4.3. Kinetic parameters of pseudo first- and second-order models

		Pseudo first-order model			Pseudo second-order model		
C_o (mg/L)	$q_{e,exp}$ (mg/g)	k_1 (min^{-1})	$q_{e,cal}$ (mg/g)	R^2	k_2 (g mg^{-1} min^{-1})	$q_{e,cal}$ (mg/g)	R^2
1	8.836	0.328	4.191	0.8775	0.569	8.881	1.0000
2	19.168	0.143	8.780	0.9427	0.055	19.531	0.9999
5	48.013	0.080	17.904	0.9417	0.013	48.780	0.9999
8	67.181	0.059	46.530	0.9901	0.003	70.922	0.9997
10	80.972	0.071	47.808	0.9686	0.003	84.034	0.9997
15	102.758	0.064	114.767	0.9577	0.001	111.111	0.9989
20	109.864	0.062	101.099	0.9434	0.001	116.279	0.9985
25	129.406	0.046	67.654	0.9767	0.001	135.135	0.9998
30	132.959	0.039	62.916	0.9626	0.001	138.889	0.9998
40	136.699	0.037	68.820	0.9525	0.001	142.857	0.9996

4.3.5 Adsorption mechanism

As discussed above, the extremal film diffusion may not be the rate-limiting step for the RhB adsorption onto MoS_2. As a result, the intra-particle diffusion model, which is commonly used for a rapidly stirred batch reactor system, was employed to further investigate the adsorption mechanism [32, 49]. The model is defined as Equation 14:

$$q_t = k_{ip} t^{1/2} + C_i \qquad \textit{Equation 14}$$

Where, k_{ip} (mg g^{-1} $min^{-1/2}$) is the intra-particle diffusion rate constant; and the value of the intercept C_i reflects the boundary thickness. A larger C_i indicates a greater boundary layer effect [50].

Generally, the adsorption diffusion model includes three steps - external mass transport, intra-particle diffusion, and adsorption of adsorbate on the interior surface site of adsorbents [51]. The overall rate of adsorption may be controlled by one of the steps or a combination of more steps [52]. If the plot of q_t versus $t^{1/2}$ is a sole straight line and passes through the origin, then the intra-particle diffusion is rate-liming [53]. However, multi-linear plots were observed in Fig. 4.7 and none of them passed through the origin. This indicated that intra-particle diffusion is not the sole rate-limiting step and multiple steps may be involved in the adsorption process of RhB onto MoS_2. For the group with the initial RhB concentration of 2 mg/L, the first portion and second portion could be assigned to the intra-particle diffusion steps and the final equilibrium stages, respectively. For the other concentrations, the adsorption process tends to be divided into three stages. The initial stage is generally associated with the external mass transport [53, 54]. Then, the next two stages are the intra-particle diffusion of the adsorbates within the pores followed by the adsorption-desorption equilibrium. All the relevant parameters are listed in Table 4.4. According to the values of intra-particle diffusion rate constant (k) and C, the intra-particle diffusion played an important role in the overall adsorption process for all groups.

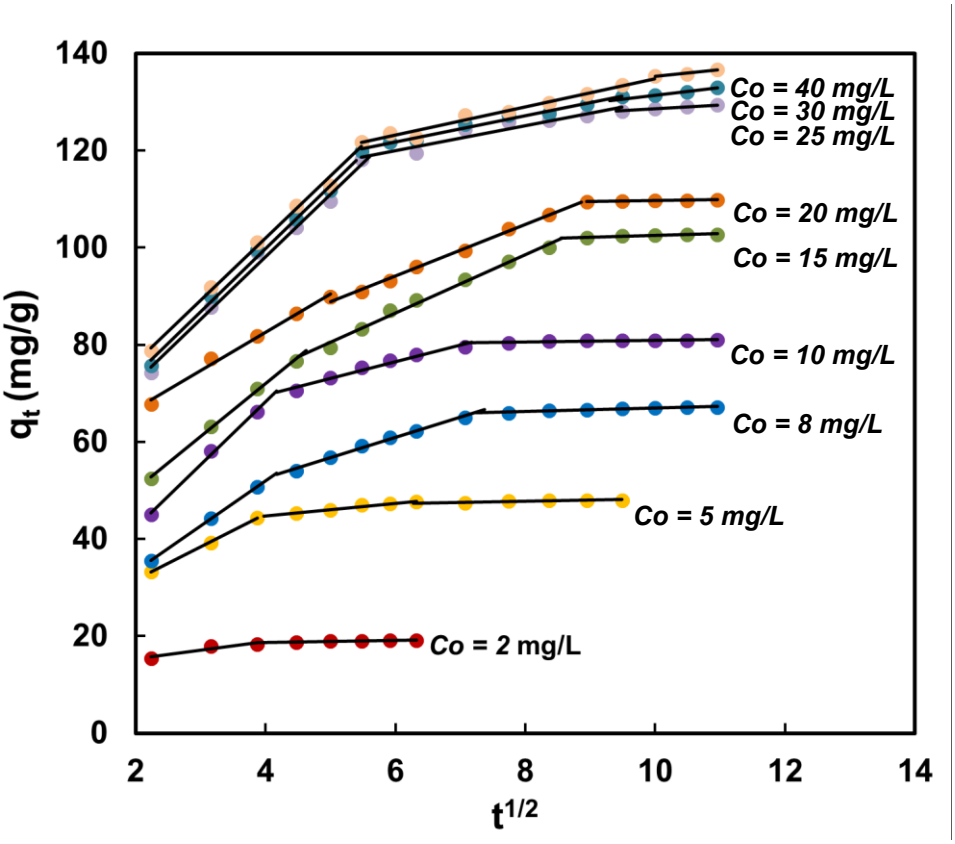

Figure 4.7. Plots of intra-particle diffusion model for RhB uptake onto MoS_2 with different initial RhB concentrations

Table 4.4. Kinetic parameters for intra-particle diffusion model

C_0 (mg/L)	k_{i1} (mg g^{-1} $min^{-1/2}$)	C_1	R^2	k_{i2} (mg g^{-1} $min^{-1/2}$)	C_2	R^2	k_{i3} (mg g^{-1} $min^{-1/2}$)	C_3	R^2
2	1.813	11.648	0.914	0.205	17.887	0.908	-	-	-
5	6.754	18.103	0.999	1.303	39.570	0.965	0.221	45.994	0.826
8	9.287	14.792	1.000	4.186	35.817	0.992	0.365	63.313	0.933
10	12.967	16.358	0.997	3.429	55.984	0.968	0.155	79.355	0.614
15	10.887	28.453	0.998	6.017	50.478	0.990	0.349	99.037	0.842
20	7.896	51.017	0.991	5.272	62.576	0.992	0.178	107.930	0.977
25	12.893	46.629	0.987	2.571	104.600	0.912	0.784	120.820	1.000
30	12.997	47.847	0.994	2.729	105.380	0.981	1.564	115.760	0.976
40	12.820	50.727	0.995	2.905	105.740	0.970	1.367	121.630	0.936

4.4 Conclusion

Different S sources were used to synthesize MoS_2 via a simple hydrothermal method. According to the TEM images, SEM images, and batch experiment for the adsorption study, different morphologies and adsorption capacities were obtained by using different S sources. The hierarchical MoS_2 microspheres prepared by CH_4N_2S exhibited the highest adsorption capacity among all the samples. The N_2 sorption isotherm indicated that the as-prepared MoS_2-CH_4N_2S is mesoporous microsphere with a BET surface area of 72.0 m^2/g. For RhB uptake onto MoS_2, the Langmuir isotherm model best described the adsorption data and the calculated maximum monolayer coverage capacity is 136.99 mg/g. Meanwhile, the mean adsorption energy (E = 5 kJ/mol) determined by D-R isotherm model suggested that the type of RhB adsorption onto MoS_2 may be physisorption. The pseudo first- and second- order models were applied for the adsorption kinetic study. It indicated that the pseudo second-order model is more suitable to describe the RhB adsorption onto MoS_2. Moreover, the intra-particle diffusion model was also employed to analyze the adsorption date, which demonstrated that the intra-particle diffusion within the mesopores played an important role in the overall adsorption process. Therefore, MoS_2-CH_4N_2S obtained in this work can be served as a promising candidate for dye removal in wastewater. In addition, this work may shed light on the importance of addressing the adsorption in photocatalysis for future applications.

References

[1] M. Shaban, M.R. Abukhadra, M.G. Shahien, A.A.P. Khan, Upgraded modified forms of bituminous coal for the removal of safranin-T dye from aqueous solution, Environmental Science and Pollution Research, 24 (2017) 18135-18151.

[2] Z. Carmen, S. Daniela, Textile organic dyes–characteristics, polluting effects and

separation/elimination procedures from industrial effluents–a critical overview, in: Organic Pollutants Ten Years After the Stockholm Convention-Environmental and Analytical Update, InTech: Croatia, 2012, pp. 55-81.

[3] D. Rawat, V. Mishra, R.S. Sharma, Detoxification of azo dyes in the context of environmental processes, Chemosphere, 155 (2016) 591-605.

[4] D. Mazumder, Process evaluation and treatability study of wastewater in a textile dyeing industry, International Journal of Energy and Environment, 2 (2011) 1053-1066.

[5] S. Ong, E. Toorisaka, M. Hirata, T. Hano, Combination of adsorption and biodegradation processes for textile effluent treatment using a granular activated carbon-bioflm confgured packed column system, Journal of Environmental Sciences, 20 (2008) 952-956.

[6] F. Harrelkas, A. Azizi, A. Yaacoubi, A. Benhammou, M.N. Pons, Treatment of textile dye effluents using coagulation–flocculation coupled with membrane processes or adsorption on powdered activated carbon, Desalination, 235 (2009) 330-339.

[7] İ.A. Şengil, M. Özacar, The decolorization of C.I. Reactive Black 5 in aqueous solution by electrocoagulation using sacrificial iron electrodes, J. Hazard. Mater., 161 (2009) 1369-1376.

[8] N. Casas, P. Blánquez, X. Gabarrell, T. Vicent, G. Caminal, M. Sarrà, Degradation of Orange G by Laccase: Fungal Versus Enzymatic Process, Environ. Technol., 28 (2007) 1103-1110.

[9] X. Meng, Z. Zhang, Facile synthesis of $BiOBr/Bi_2WO_6$ heterojunction semiconductors with high visible-light-driven photocatalytic activity, J. Photochem. Photobiol. A: Chem.,

310 (2015) 33-44.

[10] X. Meng, Z. Li, Z. Zhang, Highly efficient degradation of phenol over a Pd-BiOBr Mott–Schottky plasmonic photocatalyst, Mater Res Bull, 99 (2018) 471-478.

[11] X. Meng, Z. Li, Z. Zhang, Pd-nanoparticle-decorated peanut-shaped $BiVO_4$ with improved visible light-driven photocatalytic activity comparable to that of TiO_2 under UV light, Journal of Catalysis, 356 (2017) 53-64.

[12] X. Meng, Z. Zhang, Plasmonic ternary Ag–rGO–Bi_2MoO_6 composites with enhanced visible light-driven photocatalytic activity, Journal of Catalysis, 344 (2016) 616-630.

[13] X. Meng, Z. Zhang, Plasmonic Z-scheme Ag_2O-Bi_2MoO_6 p-n heterojunction photocatalysts with greatly enhanced visible-light responsive activities, Mater Lett, 189 (2017) 267-270.

[14] H. Pei, J. Wang, Q. Yang, W. Yang, N. Hu, Y. Suo, D. Zhang, Z. Li, J. Wang, Interfacial growth of nitrogen-doped carbon with multi-functional groups on the MoS_2 skeleton for efficient Pb(II) removal, Sci. Total Environ., 631-632 (2018) 912-920.

[15] Y. Fang, Q. Huang, P. Liu, J. Shi, G. Xu, Easy-separative MoS_2-glue sponges with high-efficient dye adsorption and excellent reusability for convenient water treatment, Colloids Surf. Physicochem. Eng. Aspects, 540 (2018) 112-122.

[16] Z. Li, X. Meng, Z. Zhang, Recent Development on MoS_2-based Photocatalysis: a Review, Journal of Photochemistry and Photobiology C: Photochemistry Reviews, 35 (2018) 39-55.

[17] M. Wang, W. Wang, M. Ji, X. Cheng, Adsorption of phenol and hydrazine upon pristine and X-decorated (X = Sc, Ti, Cr and Mn) MoS_2 monolayer, Appl. Surf. Sci., 439

(2018) 350-363.

[18] T. Yongwen, L. Pan, C. Luyang, C. Weitao, I. Yoshikazu, H. Jiuhui, G. Xianwei, T. Zheng, F. Takeshi, H. Akihiko, C.M. W., Monolayer MoS_2 Films Supported by 3D Nanoporous Metals for High‐Efficiency Electrocatalytic Hydrogen Production, Adv. Mater., 26 (2014) 8023-8028.

[19] Z. Li, X. Meng, Z. Zhang, Few-layer MoS_2 nanosheets-deposited on Bi_2MoO_6 microspheres: A Z-scheme visible-light photocatalyst with enhanced activity, Catalysis Today, (2018).

[20] S. Watanabe, J. Noshiro, S. Miyake, Tribological characteristics of WS_2/MoS_2 solid lubricating multilayer films, Surf. Coat. Technol., 183 (2004) 347-351.

[21] T. Wang, R. Zhu, J. Zhuo, Z. Zhu, Y. Shao, M. Li, Direct Detection of DNA below ppb Level Based on Thionin-Functionalized Layered MoS_2 Electrochemical Sensors, Anal. Chem., 86 (2014) 12064-12069.

[22] H. Song, S. You, X. Jia, Synthesis of fungus-like MoS_2 nanosheets with ultrafast adsorption capacities toward organic dyes, Appl. Phys. A, 121 (2015) 541-548.

[23] X. Geng, Y. Zhang, Y. Han, J. Li, L. Yang, M. Benamara, L. Chen, H. Zhu, Two-Dimensional Water-Coupled Metallic MoS_2 with Nanochannels for Ultrafast Supercapacitors, Nano Lett., 17 (2017) 1825-1832.

[24] Z. Wang, B. Mi, Environmental Applications of 2D Molybdenum Disulfide (MoS_2) Nanosheets, Environ. Sci. Technol., 51 (2017) 8229-8244.

[25] J.N. Coleman, M. Lotya, A. O'Neill, S.D. Bergin, P.J. King, U. Khan, K. Young, A. Gaucher, S. De, R.J. Smith, I.V. Shvets, S.K. Arora, G. Stanton, H.-Y. Kim, K. Lee, G.T.

Kim, G.S. Duesberg, T. Hallam, J.J. Boland, J.J. Wang, J.F. Donegan, J.C. Grunlan, G. Moriarty, A. Shmeliov, R.J. Nicholls, J.M. Perkins, E.M. Grieveson, K. Theuwissen, D.W. McComb, P.D. Nellist, V. Nicolosi, Two-Dimensional Nanosheets Produced by Liquid Exfoliation of Layered Materials, Science, 331 (2011) 568-571.

[26] X. Meng, Z. Li, H. Zeng, J. Chen, Z. Zhang, MoS_2 quantum dots-interspersed Bi_2WO_6 heterostructures for visible light-induced detoxification and disinfection, Applied Catalysis B: Environmental, 210 (2017) 160-172.

[27] Y.-H. Tan, K. Yu, J.-Z. Li, H. Fu, Z.-Q. Zhu, MoS_2@ZnO nano-heterojunctions with enhanced photocatalysis and field emission properties, J. Appl. Phys., 116 (2014) 064305.

[28] H. Shi, K. Yu, F. Sun, Z. Zhu, Controllable synthesis of novel Cu_2O micro/nano-crystals and their photoluminescence, photocatalytic and field emission properties, CrystEngComm, 14 (2012) 278-285.

[29] A. Taufik, A. Muzakki, R. Saleh, Effect of nanographene platelets on adsorption and sonophotocatalytic performances of TiO_2/CuO composite for removal of organic pollutants, Mater Res Bull, 99 (2018) 109-123.

[30] S. Bai, X. Shen, G. Zhu, A. Yuan, J. Zhang, Z. Ji, D. Qiu, The influence of wrinkling in reduced graphene oxide on their adsorption and catalytic properties, Carbon, 60 (2013) 157-168.

[31] M. Thommes, K. Kaneko, V. Neimark Alexander, P. Olivier James, F. Rodriguez-Reinoso, J. Rouquerol, S.W. Sing Kenneth, Physisorption of gases, with special reference to the evaluation of surface area and pore size distribution (IUPAC Technical Report), in: Pure Appl. Chem., 2015, pp. 1051.

[32] L. Li, S. Liu, T. Zhu, Application of activated carbon derived from scrap tires for adsorption of Rhodamine B, Journal of Environmental Sciences, 22 (2010) 1273-1280.

[33] Y. Pei, M. Wang, Q. Liu, X. Xu, L. Yuan, Y. Zhao, Novel SiO_2@$Mg_xSi_yO_z$ composite with high-efficiency adsorption of Rhodamine B in water, RSC Advances, 4 (2014) 55237-55246.

[34] S. Eftekhari, A. Habibi-Yangjeh, S. Sohrabnezhad, Application of AlMCM-41 for competitive adsorption of methylene blue and rhodamine B: Thermodynamic and kinetic studies, J. Hazard. Mater., 178 (2010) 349-355.

[35] P. Lu, X. Hu, Y. Li, M. Zhang, X. Liu, Y. He, F. Dong, M. Fu, Z. Zhang, One-step preparation of a novel $SrCO_3$/g-C_3N_4 nano-composite and its application in selective adsorption of crystal violet, RSC Advances, 8 (2018) 6315-6325.

[36] A. Günay, E. Arslankaya, İ. Tosun, Lead removal from aqueous solution by natural and pretreated clinoptilolite: Adsorption equilibrium and kinetics, J. Hazard. Mater., 146 (2007) 362-371.

[37] G. McKay, H.S. Blair, J.R. Gardner, Adsorption of dyes on chitin. I. Equilibrium studies, J. Appl. Polym. Sci., 27 (1982) 3043-3057.

[38] A. de Sá, A.S. Abreu, I. Moura, A.V. Machado, 8 - Polymeric materials for metal sorption from hydric resources, in: A.M. Grumezescu (Ed.) Water Purification, Academic Press, 2017, pp. 289-322.

[39] A.A. Inyinbor, F.A. Adekola, G.A. Olatunji, Kinetics, isotherms and thermodynamic modeling of liquid phase adsorption of Rhodamine B dye onto Raphia hookerie fruit epicarp, Water Resources and Industry, 15 (2016) 14-27.

[40] A.A. Inyinbor, F.A. Adekola, G.A. Olatunji, Liquid phase adsorptions of Rhodamine B dye onto raw and chitosan supported mesoporous adsorbents: isotherms and kinetics studies, Applied Water Science, 7 (2017) 2297-2307.

[41] N. Ayawei, A.N. Ebelegi, D. Wankasi, Modelling and Interpretation of Adsorption Isotherms, Journal of Chemistry, 2017 (2017) 11.

[42] T.M. Elmorsi, Equilibrium isotherms and kinetic studies of removal of methylene blue dye by adsorption onto miswak leaves as a natural adsorbent, Journal of Environmental Protection, 2 (2011) 817.

[43] T.A. Khan, S. Dahiya, I. Ali, Use of kaolinite as adsorbent: Equilibrium, dynamics and thermodynamic studies on the adsorption of Rhodamine B from aqueous solution, Applied Clay Science, 69 (2012) 58-66.

[44] D. Wan, W. Li, G. Wang, K. Chen, L. Lu, Q. Hu, Adsorption and heterogeneous degradation of rhodamine B on the surface of magnetic bentonite material, Appl. Surf. Sci., 349 (2015) 988-996.

[45] M.-F. Hou, C.-X. Ma, W.-D. Zhang, X.-Y. Tang, Y.-N. Fan, H.-F. Wan, Removal of rhodamine B using iron-pillared bentonite, J. Hazard. Mater., 186 (2011) 1118-1123.

[46] H. Zhao, Y. Wang, L. Zhao, Magnetic Nanocomposites Derived from Hollow ZIF‐67 and Core‐Shell ZIF‐67@ZIF‐8: Synthesis, Properties, and Adsorption of Rhodamine B, Eur. J. Inorg. Chem., 2017 (2017) 4110-4116.

[47] J. Zhang, F. Li, Q. Sun, Rapid and selective adsorption of cationic dyes by a unique metal-organic framework with decorated pore surface, Appl. Surf. Sci., 440 (2018) 1219-1226.

[48] T. Wang, K. Kailasam, P. Xiao, G. Chen, L. Chen, L. Wang, J. Li, J. Zhu, Adsorption removal of organic dyes on covalent triazine framework (CTF), Microporous Mesoporous Mater., 187 (2014) 63-70.

[49] G. McKay, The adsorption of dyestuffs from aqueous solution using activated carbon: Analytical solution for batch adsorption based on external mass transfer and, The Chemical Engineering Journal, 27 (1983) 187-196.

[50] V. Vimonses, S. Lei, B. Jin, C.W.K. Chow, C. Saint, Kinetic study and equilibrium isotherm analysis of Congo Red adsorption by clay materials, Chem. Eng. J., 148 (2009) 354-364.

[51] R.M.C. Viegas, M. Campinas, H. Costa, M.J. Rosa, How do the HSDM and Boyd's model compare for estimating intraparticle diffusion coefficients in adsorption processes, Adsorption, 20 (2014) 737-746.

[52] L. Ding, B. Zou, W. Gao, Q. Liu, Z. Wang, Y. Guo, X. Wang, Y. Liu, Adsorption of Rhodamine-B from aqueous solution using treated rice husk-based activated carbon, Colloids Surf. Physicochem. Eng. Aspects, 446 (2014) 1-7.

[53] P. Sun, L. Xu, J. Li, P. Zhai, H. Zhang, Z. Zhang, W. Zhu, Hydrothermal synthesis of mesoporous $Mg_3Si_2O_5(OH)_4$ microspheres as high-performance adsorbents for dye removal, Chem. Eng. J., 334 (2018) 377-388.

[54] B.I. Olu-Owolabi, P.N. Diagboya, K.O. Adebowale, Evaluation of pyrene sorption–desorption on tropical soils, J. Environ. Manage., 137 (2014) 1-9.

Chapter 5 Few-layer MoS_2 nanosheets-deposited on Bi_2MoO_6 microspheres: a Z-scheme visible-light photocatalyst with enhanced activity

Zizhen Li, Xiangchao Meng and Zisheng Zhang

Catalysis Today, *315*, 67-78, (2018)

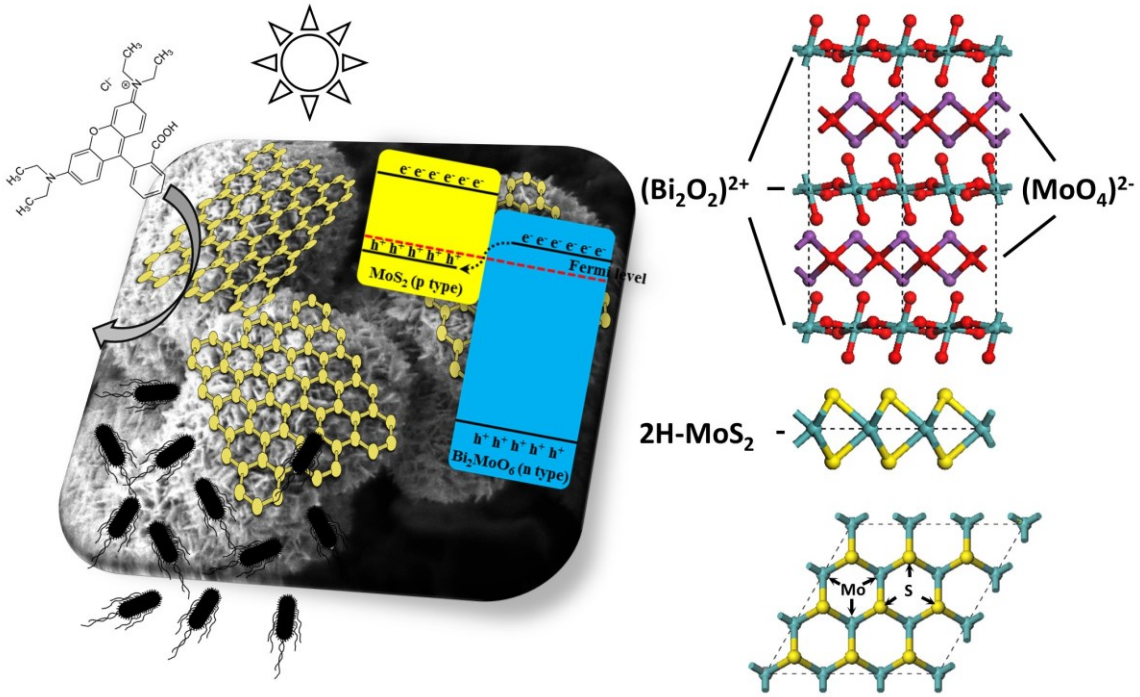

Abstract

A Z-scheme heterostructure, few-layer MoS_2/Bi_2MoO_6, was synthesized and exhibited excellent photocatalytic activity in oxidation of organics and inactivation of bacteria in water under visible light. Layered MoS_2 with a thickness of ~1nm were successfully deposited on the surface of Bi_2MoO_6 hierarchical microspheres. Compared with the MoS_2 bulk, the band gap of layered MoS_2 is widened, which is in favor of the separation of photogenerated charge carriers. After the introduction of MoS_2, the photocurrent density was greatly improved on Bi_2MoO_6 electrode under visible light. This indicates that the recombination of photogenerated h^+/e^- was effectively suppressed with the modification of MoS_2 nanosheets. Correspondingly, the photocatalytic oxidation activity in both the decomposition of organics in water and the inactivation of bacteria was enhanced. Possible mechanisms were proposed and discussed. This work sheds a light on the importance of applying layered MoS_2 to improve the oxidation activity of a photocatalyst under visible light.

5.1 Introduction

With the global economic growth in recent times, the treatment of tremendous pollutants has become a global priority. Compared with other technologies, photocatalysis has become a superior technology in environmental remediation due to its facile reaction conditions, eco-friendly performance and lack of toxic by-products [1, 2]. Among recently developed photocatalytic materials, noble-metal-free MoS_2 has attracted increasing attentions in the field of organic pollutant decomposition [3-10], inorganic pollutant treatment [11, 12], and photocatalytic disinfection [13, 14]. The major merits of these two-

dimensional (2D) nanosheets include (1) a suitable band gap for harvesting visible light, (2) high conductivity for photogenerated charge carriers, and (3) low cost as an earth–abundant material. However, the rapid recombination of photogenerated electron-hole pairs, limited quantity of active edge sites, and difficult photocatalyst separation and recycling hinder the practical application of this material. As a result, a rational design of a heterostructure by using MoS_2 as a co-catalyst in the nanocomposite may improve the light adsorption capacity and charge separation efficiency of the prepared photocatalysts [13, 15-18].

As a transition metal dichalcogenide (TMD), MoS_2 has attracted extensive attention [19-24]. For layered MoS_2, it not only exhibited graphene-like properties, such as good electronic conductivity [25-27]. In addition, it exhibits semiconducting properties and has a relatively narrow band gap [28-30]. Kuc *et al.* reported on the electronic band structures of MS_2 (M = Mo and W) using the first-principle theory [31]. It was found that the band gap for Bulk MoS_2 is 1.2 eV, and it increased to 1.9 eV for a monolayer MoS_2. Moreover, the band gap transition was changed from indirect to direct transition. All these changes are beneficial to improving the photocatalytic activity. As the band gap is still too narrow for photocatalysis, since photogenerated charge carriers are easily recombined, MoS_2 are mostly applied as a co-catalyst (electrons transporter) in photocatalysis.

Bi_2MoO_6 has been widely studied and is considered a promising visible-light-responsive photocatalyst due to its relatively narrow band gap (~2.63 eV) [32-35]. However, the fast charge recombination is the major obstacle of this material to be used in practice. In order to solve this problem, modifications of Bi_2MoO_6 with a co-catalyst, such as MoS_2, may generate a positive synergetic effect and lead to an enhanced photocatalytic activity.

Hierarchical MoS_2/Bi_2MoO_6 composites have been prepared via a solvothermal method and showed an enhanced photocatalytic activity [36]. However, the limited active sites on the surface of MoS_2 may be partially blocked by the Bi_2MoO_6 nanoflakes. In addition, the relatively large MoS_2 loading quantity could potentially reduce the light absorption of Bi_2MoO_6 due to the black body of MoS_2 [13].

In this work, a simple bath evaporation method was applied to fabricate a heterostructure of layered MoS_2 deposited on Bi_2MoO_6. Compared with pristine MoS_2 and Bi_2MoO_6, a small MoS_2 loading amount in the MoS_2/Bi_2MoO_6 composites showed enhanced photocatalytic activity in both organics degradation and bacteria inactivation under visible light irradiation. Comprehensive characterizations of as-prepared samples were conducted, and results indicated that the enhanced photocatalytic activity may be attributed to the formation of a unique Z-scheme heterostructure between MoS_2 and Bi_2MoO_6, leading to an efficient photogenerated charge separation. The mechanism was also explored and proposed.

5.2 Experimental

5.2.1 Preparation of Bi_2MoO_6

All chemicals were purchased from Fisher Scientific unless otherwise mentioned, and used as received. Hierarchical Bi_2MoO_6 was synthesized via a facile solvothermal method. Specifically, 1.69 g of $Bi(NO_3)_3 \cdot 5H_2O$ were mixed with 5 mL ethylene glycol under magnetically stirring (solution A). Subsequently, 0.42 g of $Na_2MoO_4 \cdot 2H_2O$ were mixed with 5 mL ethylene glycol under magnetically stirring (solution B). Solution A and solution B were sequentially dropwise added to 20 mL ethanol, and magnetically stirred for 30 min.

The mixture was then transferred to a 45-mL Teflon-lined stainless-steel autoclave (Parr Instrument Company), heated up at 160°C for 20 h. and then naturally cooled down to room temperature. The resulting precipitates were filtered out and washed with ethanol and ddH_2O (deionized, distilled water) for several times. Eventually, the samples were dried at 60°C overnight.

5.2.2 Preparation of few-layer MoS_2-deposited Bi_2MoO_6 Composites

MoS_2/Bi_2MoO_6 composites were synthesised by a simple bath evaporation method with minor modifications [13]. A designed volume of MoS_2 suspension (~0.25 mg/mL dispersed in H_2O, Sigma-Aldrich) was ultrasonicated for 30 min prior to the synthesis of MoS_2/Bi_2MoO_6 composites. Then, the above solution and 0.5 g of Bi_2MoO_6 were mixed with separate volumes of 7.5 mL hydrous ethanol (50% v/v of ethanol in ddH_20). The MoS_2 solution was then dropwise added into the Bi_2MoO_6 solution, and the resulting suspension was heated at 60 °C and continually stirred until the solvent was completely evaporated. The samples were collected and dried at 60 °C overnight. Different MoS_2 to Bi_2MoO_6 weight ratios (0.02, 0.05 and 0.10 wt%) were synthesized and labeled as 0.02 Mo-Bi, 0.05 Mo-Bi and 0.10 Mo-Bi, respectively.

5.2.3 Characterization

The morphology and structure of samples were observed using a field-emission scanning electron microscope (FE-SEM, JEOL JSM-7500F) and a transmission electron microscope (JEM-2100F FE-TEM (JEOL)). The TEM was also equipped with an Energy-dispersive X-ray spectroscopy (EDS). For AFM characterizations, diluted MoS_2 suspension was carefully dropped onto a mica surface pre-treated by 5 mM $NiCl_2$ and incubated at room

temperature for 20 min. Subsequently, the coated mica surface was carefully rinsed by filtered Milli-Q water and dried by pure nitrogen. The resulting samples were imaged using a Veeco Multimode AFM with NanoScope V controller (Bruker, Santa Barbara, CA) in Bruker's ScanAsyst or PeakForce QNM modes. X-ray powder diffraction (Bruker-AXS, Karlsruhe, Germany) patterns of samples were collected with filtered Cu-Kα radiation (λ = 1.5418 Å) from 5°-90° (2θ). The Raman spectrum was collected at room temperature using HORIBA XploRA^{TM} Plus Raman Microscope with an excitation laser wavelength of 532 nm. An XSAM-800 X-ray Photoelectron Spectroscope (XPS) was employed to analyze the surface chemical composition and the chemical sates of selected samples. The optical properties of the samples were investigated by the UV-vis diffuse reflectance spectrometer (DRS). The Brunauer, Emmett and Teller (BET) surface area of the samples were calculated using multi-point estimation. The pore volumes were calculated using the volumes of adsorbed N_2 at p/p_o = 0.9941. Pore volume distributions are calculated using the N_2 desorption branch, and the Barrett-Joyner-Halenda (BJH) method was used for the desorption branch to calculate the pore size data (d_p) using Equation 1 (where V/A_s is a ratio of volume to surface area of pores) as follows,

$$d_p = 4\left(\frac{V}{A_s}\right)_{BJH} \qquad \textbf{\textit{Equation 1}}$$

The photoluminescence (PL) spectra were measured using a fluorescence Spectrophotometer (F-4500, Hitachi) under excitation with a wavelength of 450 nm. Electrochemical properties of prepared samples were analyzed on a CHI 604E electrochemical analyzer (CH Instruments Inc., USA) with a platinum wire as a counter electrode, a calomel reference electrode and a working electrode. The working electrode

composed of indium tin oxide (ITO, 75 × 25 × 1.1 mm, 15 - 25 Ω, Sigma-Aldrich Canada Co.), glass coated with the prepared samples. Electrochemical impedance spectroscopy (EIS) was performed with frequencies in the range of 0 – 1,000,000 Hz and a sinusoidal wave of 5 mV. The photocurrent was also measured with an on-off lamp. The electrolyte used was Na_2SO_4 with a concentration of 0.05 mol/L.

5.2.4 Electronic structure calculation

The DFT simulations were performed using the Vienna *ab initio* simulation package (VASP) [37, 38]. The ion-electron interaction is described with the projector augmented wave (PAW) method [39]. Electron exchange-correlation is represented by the function of Perdew, Burke, and Ernzerhof (PBE) of generalized gradient approximation (GGA) [40]. A cut-off energy of 400 eV was used for the plane-wave basis set. The calculations were done on periodical supercells of 2H MoS_2 monolayer and Bi_2MoO_6 with 6×6×1 and 6×6×2 Monkhorst Pack k-point sampling, respectively. Models for Bi_2MoO_6 and 2H MoS_2 monolayer are depicted in Figure 5.1. An open-source software, p4vasp written by Orest Dubay has been used for the analysis of the Density of States (DOS).

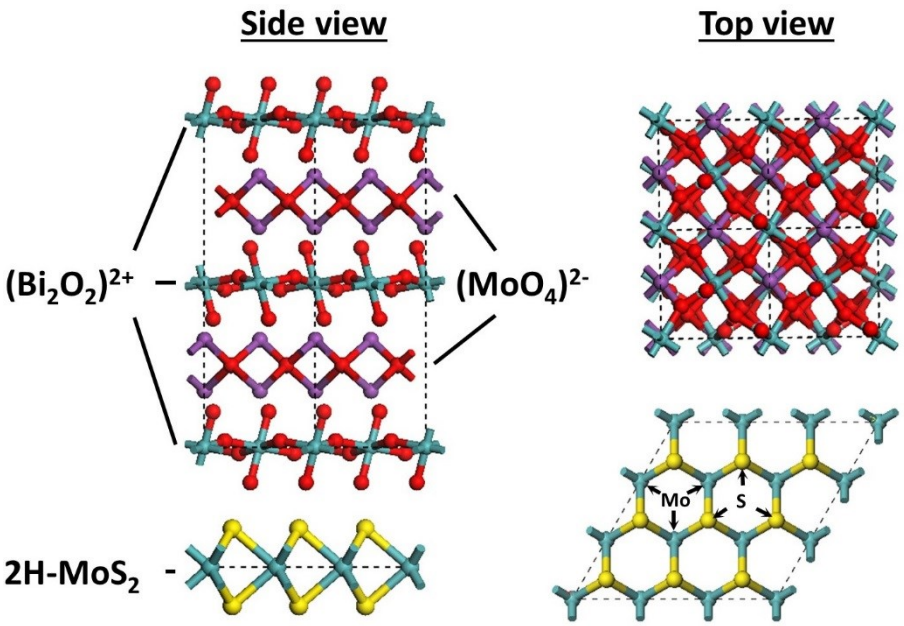

Figure 5.1. Side view and top view of Bi_2MoO_6 and 2H-MoS_2 monolayer models for DFT computations [41].

5.2.4 Photocatalytic activity testing

The photocatalytic activity of pure MoS_2, Bi_2MoO_6 and MoS_2/Bi_2MoO_6 composites were investigated by photocatalytic degradation of RhB under visible light. The light source was provided by a 300-W halogen tungsten projector lamp (Ushio) equipped with a UV cut-off filter. For each experiment, 0.10 g photocatalyst was mixed with 100 mL RhB solution with an initial concentration of 10 mg/L. The mixture was magnetically stirred in the dark for 30 min to reach an adsorption/desorption equilibrium prior to the photocatalysis experiment. Afterwards, 1 mL aliquots were collected and centrifuged every 10 mins. The resulting supernatant was tested at 554 nm (characteristic absorption peak of RhB) by a UV-vis spectrophotometer (Genesys 10 UV, Thermo Scientific) to determine the concentration of RhB. The UV-vis adsorption spectra of resulting supernatant ranging from 300-700 nm was also obtained by UV-vis spectrophotometer (Biochrom Ultrospec 60) to

analyze the photocatalytic degradation process of RhB. For stability test, 1 mL aliquots were collected and centrifuged every 30 min. After four cycling tests, the photocatalysts were collected, dried and characterized by XRD. In order to explore the role of major active oxidative species, a variety of scavengers were added into the photocatalysis system. Specifically, 0.1 M iso-propanol, 0.1 M EDTA and N_2 bubbling were used to trap hydroxyl radicals (•OH), holes and superoxide radicals ($\bullet O_2^-$), respectively.

5.2.5 Temporal course of inactivation

Wild-type *Escherichia coli* K-12 (*E. coli*, TG1 strain) was used to evaluate the photocatalytic disinfection performance of prepared samples. Bacteria were cultured aerobically in Luria-Bertani medium (Difco LB broth, Miller; containing 10 g/L tryptone, 5 g/L yeast extract, and 10 g/L NaCl) on a rotary shaker at 37 °C for 18 h until the stationary phase was reached. For the bacterial inactivation study, 0.1 g photocatalyst was mixed with bacteria in 100 mL saline solution and reached a final concentration of 10^6 CFU (colony forming units)/ mL. Before illumination, the suspension was magnetically stirred for 30 min in the dark. After that, aliquots were collected every 10 mins and serially diluted in saline. The diluted samples were then spread onto solid LB agar plates using 25 μL aliquot and incubated at 37 °C for 18 h. Bacterial enumeration was performed by standard plate counts to quantify viable and cultivable bacteria in unit of CFU/mL [42]. All experiments were performed in triplicate, and all materials were sterilized before use.

5.3 Results and discussion

5.3.1 Morphologies

The morphologies of MoS_2, Bi_2MoO_6 and MoS_2/Bi_2MoO_6 composites were observed by SEM, TEM, HRTEM and AFM. As shown in Figure 5.2a and 5.2b, the as-prepared Bi_2MoO_6 exhibited a flowerlike hierarchical structure with a size of ~4 μm. With the modification of MoS_2, small particles were covered on the surface of Bi_2MoO_6 (Figure 5.2c and 5.2d). As shown in the TEM images (Figure 5.3), it can be observed that Bi_2MoO_6 hierarchical microspheres consist of nanoplates (Figure 5.3a). The observed lattice fringes of Bi_2MoO_6 nanoplates in Figure 5.3a suggested the well-defined crystal structure of as-prepared samples. A graphene shaped morphology was observed in the TEM image of MoS_2 layers (Figure 5.3b). Moreover, the observed fringes with a lattice spacing of ca. 0.62 nm in the HRTEM image of MoS_2 (Figure 5.4b) corresponded to the (002) planes of hexagonal MoS_2. The TEM images of MoS_2/Bi_2MoO_6 composites (Figure 5.3c) illustrated that MoS_2/Bi_2MoO_6 composites also exhibited flowerlike morphology with some MoS_2 nanoslices deposited on the surface. However some randomly stacked nanoplates were also observed (Figure 5.3c and 5.3d), which may be resulted from sonication treatment before TEM test [13]. The HRTEM image of MoS_2/Bi_2MoO_6 composites (Figure 5.4c) exhibited fringes with a lattice spacing of ca. 0.62 and 0.31 nm, which can be assigned to the (002) planes of hexagonal MoS_2 and (131) planes of orthorhombic Bi_2MoO_6, respectively. In addition, the intimate contact between MoS_2 and Bi_2MoO_6 may further confirm the formation of heterostructure and favors charge separation and electron transfer [36, 43]. The composition of as-prepared Bi_2MoO_6 and MoS_2/Bi_2MoO_6 composites were investigated by EDS, and the results are illustrated in Figure 5.4d. For pure Bi_2MoO_6,

elements of Bi, Mo and O were observed, and no impure elements were emerged. In comparison, a peak for sulfur was observed in the curve of MoS_2/Bi_2MoO_6 composites, indicating the possible presence of MoS_2 in the composites. To confirm the thickness of the MoS_2 layers, AFM was employed and the results were depicted in Figure 5.5. The thickness of these nanosheets were measured to be around 0.96 - 1.25 nm which corresponds to the thickness of few-layered MoS_2 [44, 45].

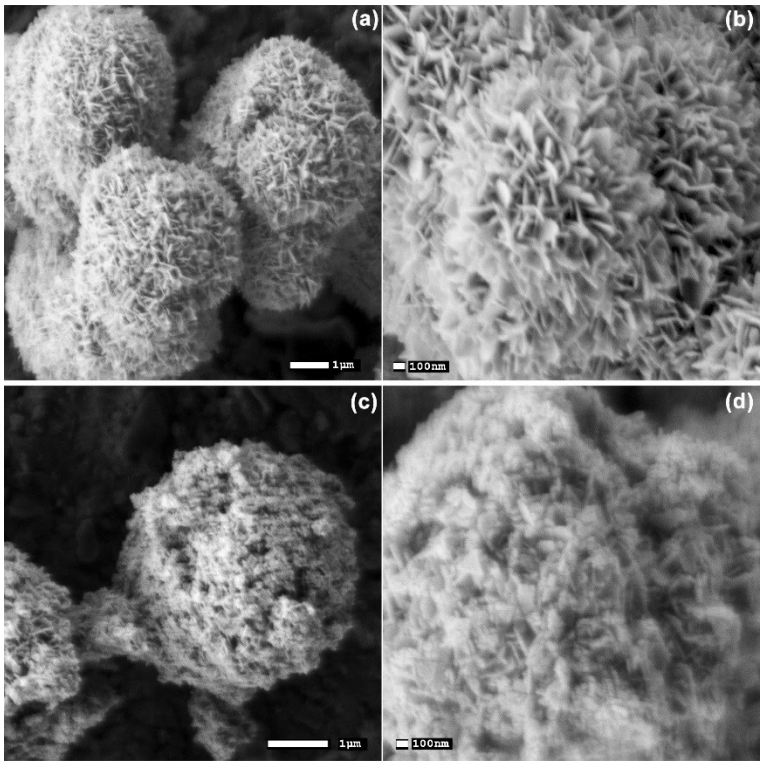

Figure 5.2. SEM images of Bi_2MoO_6 in low (a) and high (b) magnification, and 0.05 Mo-Bi in low (c) and high (d) magnification.

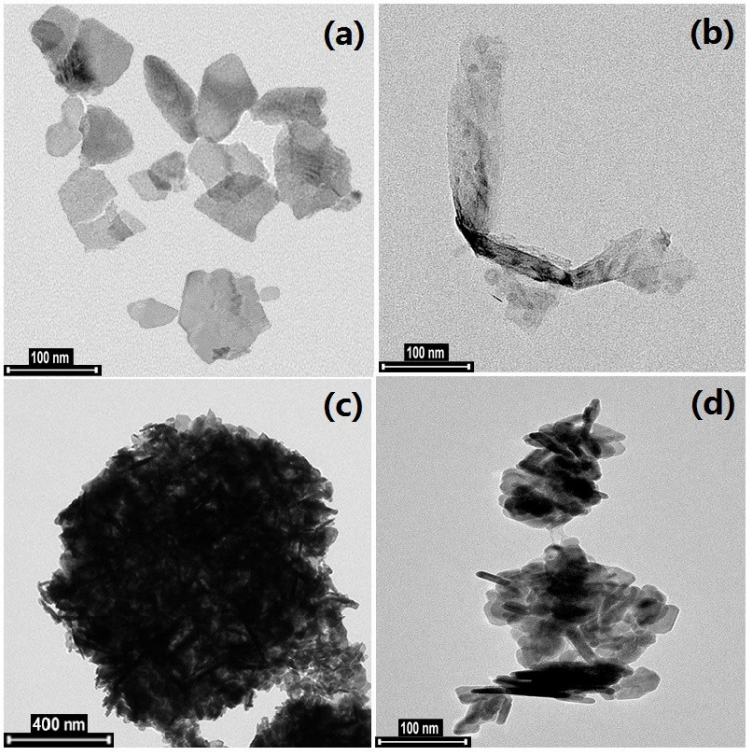

Figure 5.3. TEM image of (a) Bi_2MoO_6, (b) MoS_2, (c) and (d) 0.05 Mo-Bi at low and high magnification.

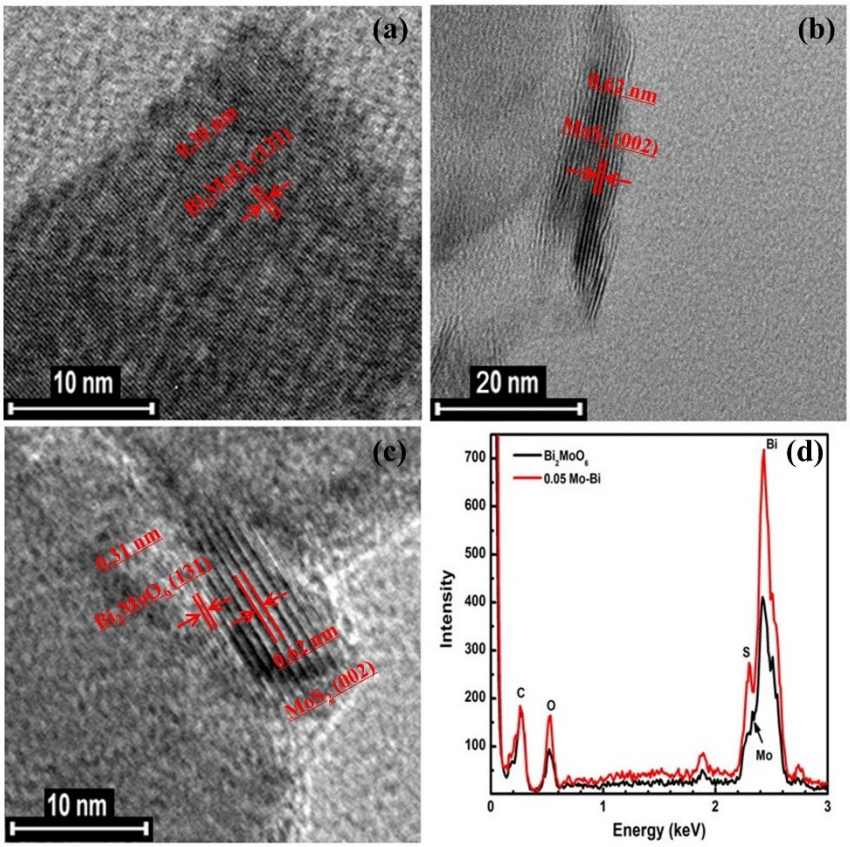

Figure 5.4. HRTEM image of (a) Bi_2MoO_6, (b) MoS_2 and (c) 0.05 Mo-Bi; (d) EDS spectra for Bi_2MoO_6 and 0.05 Mo-Bi;

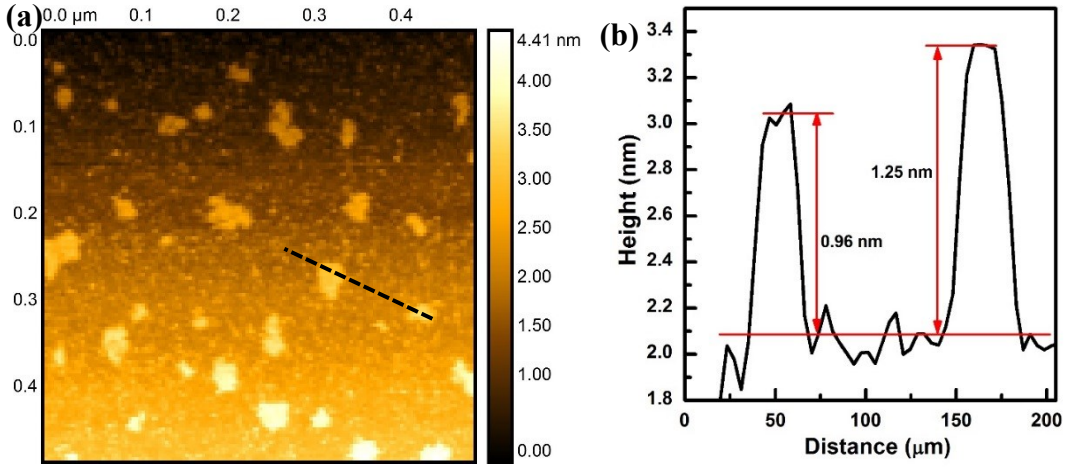

Figure 5.5. (a) AFM image of MoS_2 film, and (b) the thickness of the MoS_2 layer from the AFM cross-sectional profile among the line indicated in (a).

5.3.2 Crystal structure and chemical states analysis

The XRD patterns of as-prepared Bi_2MoO_6 and MoS_2/Bi_2MoO_6 composites were obtained and shown in Figure 5.6. For pure Bi_2MoO_6, all diffraction peaks are well indexed to the orthorhombic phase of Bi_2MoO_6 (PDF card #: 72-1524) indicating a good crystallinity of prepared Bi_2MoO_6 sample. The hexagonal polytype layered crystals (2H) of MoS_2 was verified by Raman spectroscopy (Figure 5.7). The peaks at 384, 405 and 457 cm^{-1} can be assigned to the in-plane E^1_{2g} and out-of-plane A_{1g} modes, as well as longitudinal acoustic phonon modes of 2H- MoS_2. For XRD patterns of MoS_2/Bi_2MoO_6 composites, no obvious differences can be found compared with the XRD pattern of pure Bi_2MoO_6. This is probably due to the low loading quantity of MoS_2 ($\leq$ 0.1 wt%) and the disordered stacking of MoS_2 nanosheets on the surface [46]. The lattice parameters of Bi_2MoO_6 and MoS_2/Bi_2MoO_6 composites were calculated and shown in Figure 5.6. The lattice parameters of MoS_2/Bi_2MoO_6 composites with varying MoS_2 contents were similar to that of pure Bi_2MoO_6, further indicating that the incorporation of MoS_2 has negligible effect on the crystal structure of Bi_2MoO_6. This result indicated that MoS_2 only dispersed on the surface of Bi_2MoO_6 instead of covalently anchoring into the lattice of Bi_2MoO_6 [13, 47].

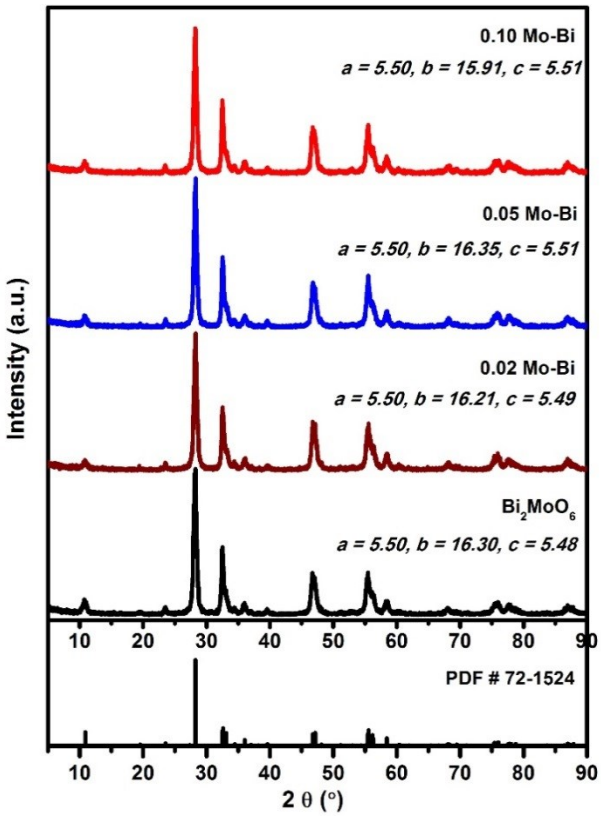

Figure 5.6. XRD patterns of pure Bi_2MoO_6 and MoS_2/Bi_2MoO_6 composites with various MoS_2 loading quantities.

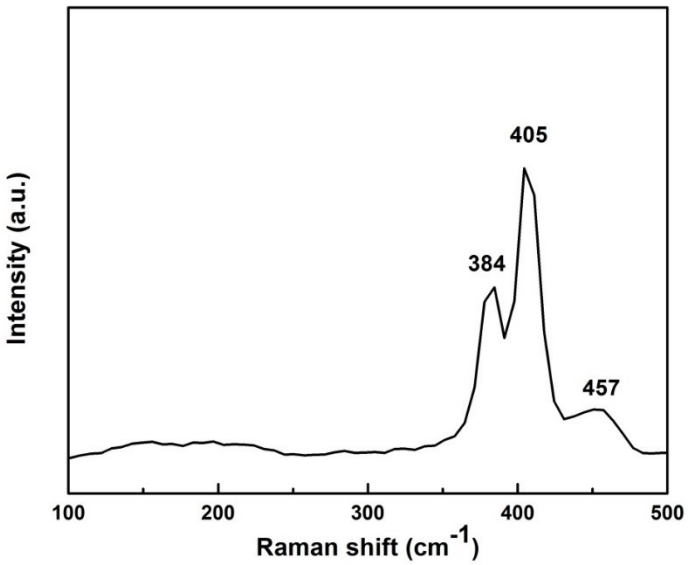

Figure 5.7. Raman spectrum of MoS_2

The XPS spectra were employed to confirm the introduction of MoS_2 and analyze the chemical status of surface elements. All data were calibrated with the banding energy of C1s, which is fixed at 284.6 eV. For survey spectra (Figure 5.8a), no impurity peaks were found and no evident difference was shown after loading MoS_2 on the surface of Bi_2MoO_6. However, the introduction of MoS_2 can be proven by the high-resolution orbit scans. In the Mo 3d spectrum for Bi_2MoO_6 (Figure 5.8b), a set of spin-orbit doublet was located at binding energy values of 234.9 eV and 231.7 eV, which can be assigned to a Mo^{6+} oxidation state [48]. With the introduction of MoS_2, the Mo 3d spectrum consists of two sets of spin-orbit doublets and one peak located at 234.5 eV, which may be assigned to S 2s in MoS_2 [49]. The two sets of doublets with binding energy of (237.0, 233.45 eV) and (235.8, 232.0 eV) indicated the Mo^{6+} in Bi_2MoO_6 and Mo^{4+} in MoS_2, respectively [36]. In S 2p spectrum for Bi_2MoO_6 (Figure 5.8c), a peak at the binding energy of 163.33 eV was observed, corresponding to a trivalent oxidation state of Bi. As for S 2p spectrum of MoS_2/Bi_2MoO_6 composites, S 2p doublet was found adjacent to Bi $4f_{5/2}$, which can be assigned to S $2p_{1/2}$ and S $2p_{3/2}$ of MoS_2 [13]. Therefore, the XPS spectra confirmed the introduction of MoS_2 on the surface of Bi_2MoO_6.

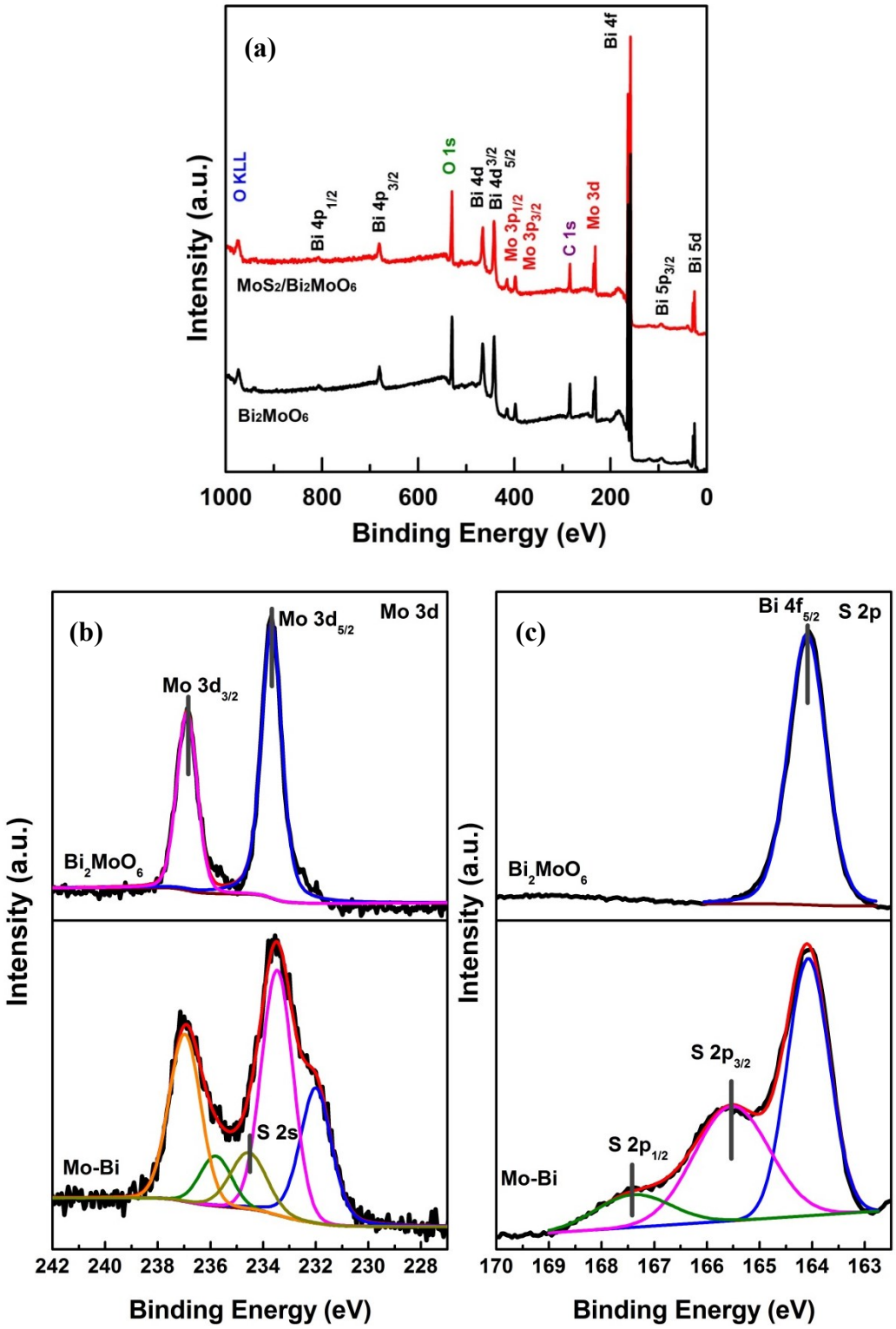

Figure 5.8. XPS spectra of (a) MoS_2/Bi_2MoO_6 composites, (b) Mo 3d, and (c) S 2p

5.3.4 N_2 sorption isotherms

The N_2 sorption isotherms and pore size distribution of prepared samples are depicted in Figure 5.9. An inflexion point close to the saturation vapor pressure can be observed in both isotherm, which can be assigned to a typical feature of type IV physisorption isotherm. This adsorption behavior is generally given by a mesoporous material associated with the capillary condensation process. The hysteresis loop may be identified as an H3 loop, which implies that the samples are plate-like particles with slit-like pores [50, 51]. This morphology has been confirmed by SEM and TEM images. In addition, the BET (Brunauer-Emmett-Teller) surface area, pore volume, and average pore size were calculated and shown in Table 5.1. The introduction of MoS_2 lead to a reduction of BET surface area and pore volume. A possible reason for this could be that the small MoS_2 nanosheets blocked the slit-like pores [13]. A reduced surface area and pore volume may suggest less adsorption sites and lower photocatalytic activity. However, as indicated by the photocatalytic degradation and disinfection experiments, this effect is negligible compared to the improvement in charge separation given by the MoS_2 coupling.

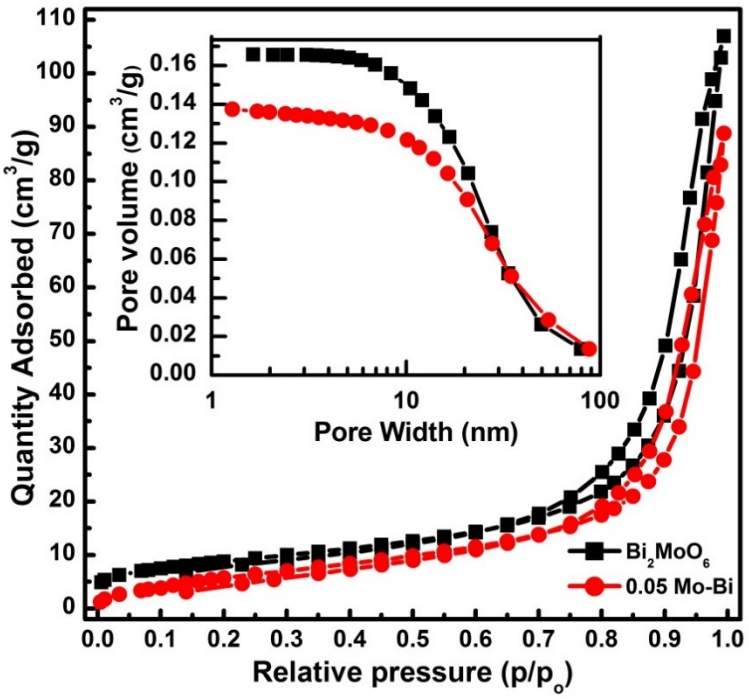

Figure 5.9. N_2 sorption isotherms and pore size distributions for Bi_2MoO_6 and Mo-Bi composite.

Table 5.1. Specific surface area, pore volume (with pore width: 1-300 nm), and average pore size of Bi_2MoO_6 and Mo-Bi composites.

Sample	S_{BET} (m^2/g)	Pore volume (cm^3/g)	Average pore size (nm)
Bi_2MoO_6	31.72	0.17	21.6
Mo-Bi	24.92	0.14	22.4

5.3.3 Optical properties and energy band composition

The optical properties of the prepared Bi_2MoO_6 and MoS_2/Bi_2MoO_6 composites are depicted in Figure 5.10. The band gap absorption edge of pure Bi_2MoO_6 was around 480 nm. Compared with pure Bi_2MoO_6, MoS_2/Bi_2MoO_6 composites showed enhanced visible-light adsorption and the visible-light adsorption spectrum increased with the increasing

content of MoS_2. This enhanced visible-light adsorption may be ascribed to the formation of surface defects [46] and the black body of MoS_2 [52]. The bandgap energy of Bi_2MoO_6, 0.02 Mo-Bi, 0.05 Mo-Bi, and 0.10 Mo-Bi, were calculated using the Kubelka-Munk function to be about 2.60, 2.45, 2.42 and 2.38 eV, respectively. As a result, the increasing content of MoS_2 lead to a slight decrease in the bandgap energy, which may also lead to the enhanced visible light adsorption.

To further study the valence band and conduction band for Bi_2MoO_6 and MoS_2, density of states were computed using a DFT method, and the results are depicted in Figure 5.11. The valence band of Bi_2MoO_6 was mainly composed of O 2p with a little Bi 5s orbits, and its conduction band mainly consisted of O 2p and Mo 4d orbits. The valence band of MoS_2 was mainly composed of Mo 3p and S 3p, and its conduction band consisted of Mo 4d and S 3p. The calculated band-gap values for Bi_2MoO_6 and MoS_2 were 1.75 and 1.50 eV, respectively. The lower values of band gaps, compared to the experimental results, may have resulted from the well-known limitations of generalized gradient approximation (GGA) [53]. It should be noted that the band gap for MoS_2 bulk was estimated to be about 1.2 eV, which is very narrow. As such, the photogenerated charge carriers can easily recombine. When the MoS_2 is in the form of a monolayer, the band gap becomes wider, which favors the separation of the photogenerated charge carriers.

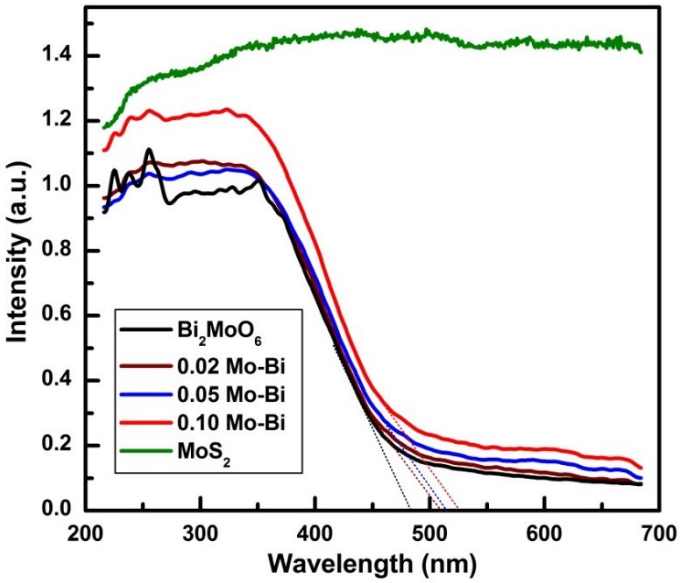

Figure 5.10. UV-vis diffuse reflectance spectra of pure Bi_2MoO_6, MoS_2 and MoS_2/Bi_2MoO_6 composites

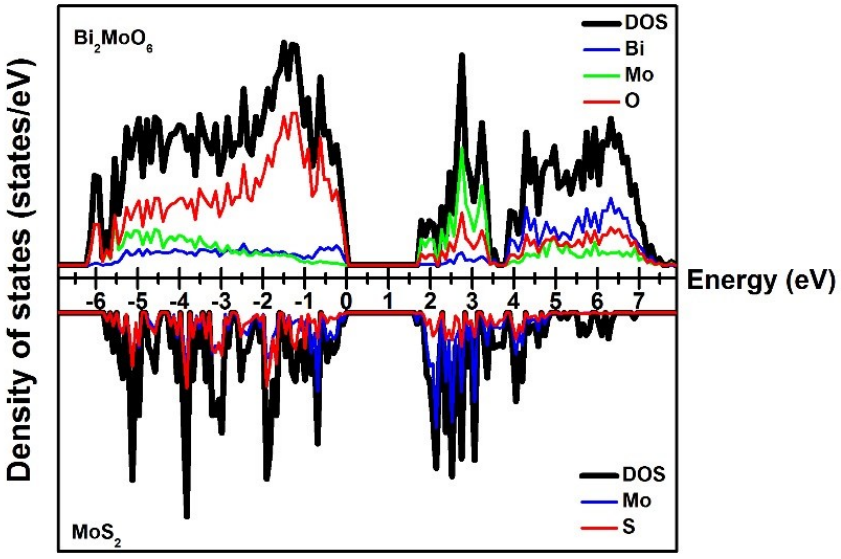

Figure 5.11. Density of states for Bi_2MoO_6 and 2H MoS_2 monolayer.

5.3.4 Photocatalytic activity testing

5.3.4.1 Degradation of RhB

The photocatalytic activities of prepared samples were evaluated by the photocatalytic degradation of RhB under visible light (Figure 5.12). The adsorption-desorption

equilibrium was reached in darkness prior to the photocatalytic degradation of RhB. Under illumination, MoS_2/Bi_2MoO_6 composites exhibited enhanced photocatalytic activity relative to pure MoS_2 and Bi_2MoO_6, indicating a positive synergetic effect between MoS_2 and Bi_2MoO_6. Specifically, the photocatalytic activity of MoS_2/Bi_2MoO_6 increased with the increasing content of MoS_2 and reached the highest activity when the loading amount of MoS_2 is 0.05 wt%. Almost 100% of RhB were removed at 90 min for the system with 0.05 Mo-Bi, while only about 57% of RhB were removed at 90 min for the system with pure Bi_2MoO_6. However, further increasing content of MoS_2 (0.10 wt%) lead to a reduction of photocatalytic activity. This may be attributed to the "blocking effect" of excess MoS_2 that hindered the light adsorption of Bi_2MoO_6 [13] and restricted light penetration into the reaction mixture due to the black body property of MoS_2 [36].

The stability of as-prepared MoS_2/Bi_2MoO_6 composites was investigated via cycling tests. As shown in Figure 5.13, about 98% RhB was degraded within 120 min after 4 successive cycles. Moreover, no distinct difference is observed in the XRD pattern of MoS_2/Bi_2MoO_6 composites before and after 4 cycling runs, which further indicated the high stability of as-prepared photocatalysts.

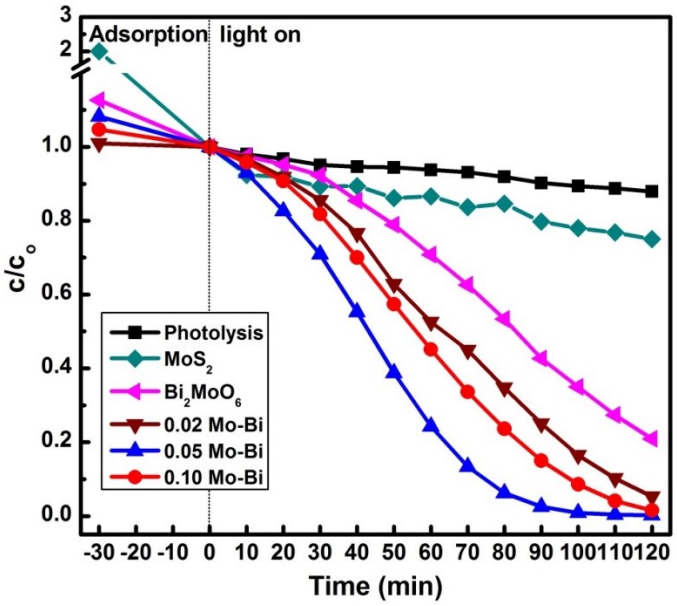

Figure 5.12. Photocatalytic degradation of RhB in the presence of different samples under visible light irradiation.

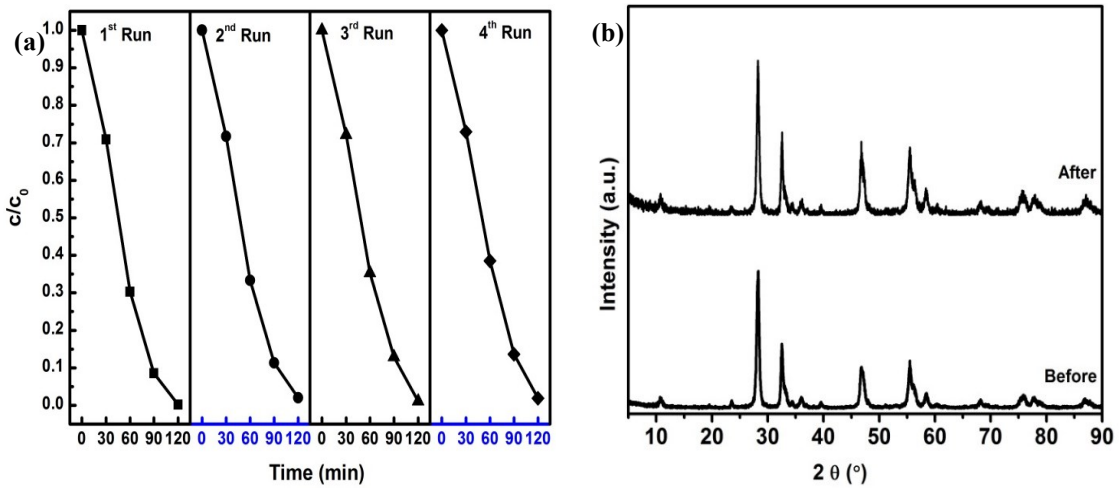

Figure 5.13. (a) Cycling tests of photocatalytic activity of 0.05 Mo-Bi for RhB degradation; (b) XRD pattern of 0.005Mo-Bi before and after 4 cycling runs.

The temporal evolution of the spectral changes that occurred during the photocatalytic degradation of RhB in the presence of 0.05 Mo-Bi is depicted in Figure 5.14. The blue shift of the major peak wavelength suggested that a step-by-step N-demethylation

process predominates during the initial photocatalytic degradation process [54]. The characteristic adsorption peak wavelengths at 539, 522, 510 and 498 nm represent intermediates of each *N*-demethylation step, which are *N,N,N'*-triethyl-rhodamine, *N,N'*-diethyl-rhodamine, *N*-ethyl-rhodamine and rhodamine, respectively [55]. After 70 min, the peak intensity of complete N-demethylated product (rhodamine) decreased due to the cleavage of the aromatic chromophore structure [56]. This indicates that RhB may be decomposed into small molecules (*e.g.* CO_2 and H_2O) with a prolonged reaction time. The total organic carbon concentration was also tested and illustrated in Figure 5.15. As shown in Figure 5.15, the mineralization rate reached up to 64% in the presence of 0.05 Mo-Bi at 120 min. This result revealed that although RhB was completely degraded within 120 min, some other organic compounds may still remained in the reaction mixture. Therefore, a prolonged reaction time is required to achieve a completely mineralization of the dye.

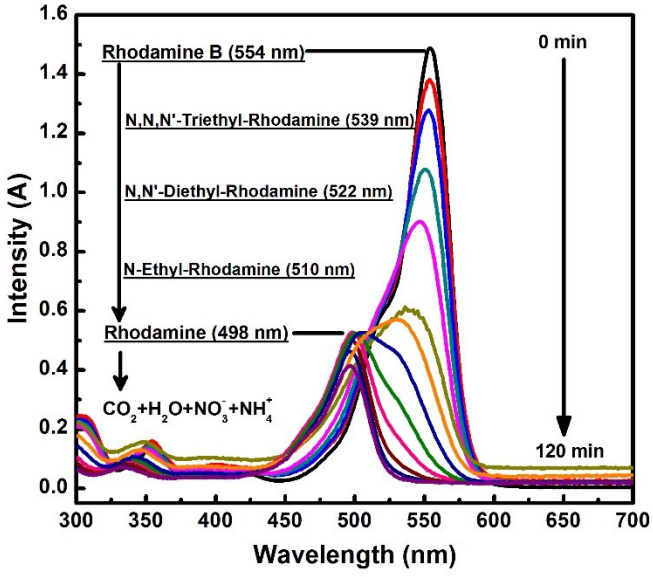

Figure 5.14. UV-vis pectral changes of RhB during photocatalytic degradation process.

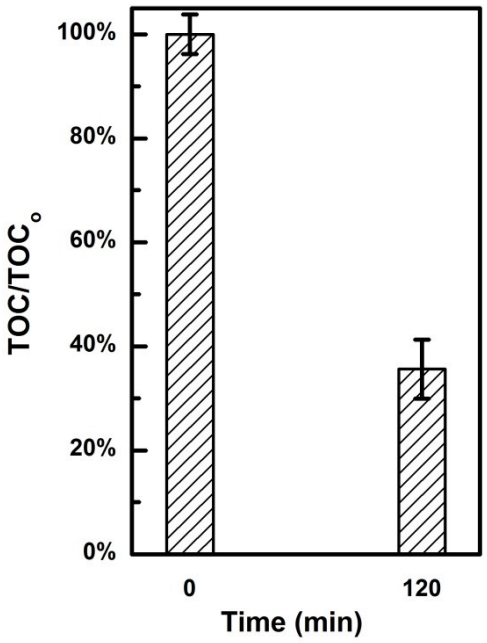

Figure 5.15. TOC concentration at 120 min in the presence of 0.05 Mo-Bi under visible light irradiation.

5.3.4.2 Inactivation of *E.Coli*

Photocatalytic disinfection performance of MoS_2, Bi_2MoO_6, and 0.05 Mo-Bi are shown in Figure 5.16. In the dark control group, photocatalysts exhibited no evident cytotoxicity to bacteria. The survival ratio of bacteria decreased slightly (6.4%) at 60 min, which may be contributed to the adsorption of photocatalysts. The slight reduction in the survival ratio for the photolysis group represents the disinfection effect without any photocatalysis, absorption or cytotoxicity of photocatalysts. Compared with the dark control group, MoS_2 showed a negligible disinfection effect to bacteria which may be attributed to its narrow band gap and fast recombination rate of photogenerated charge carriers. The survival ratio was (77.1 ± 4.6)% at 60 min in the presence of pure Bi_2MoO_6, suggesting a higher photocatalytic activity than MoS_2. For 0.05 Mo-Bi, the survival ratio reduced to (60.3 ± 3.7)% at 60 min due to a positive synergetic effect between MoS_2 and Bi_2MoO_6. It was

reported that the major mechanism of photocatalytic disinfection is attributed to the reactive oxidative species (ROS), such as h^+, •OH, and $•O_2^-$ [57]. An integral component of bacterial cell membrane, polyunsaturated phospholipids, can be degraded by photocatalytic ROS, leading to the breakdown of the membrane structure. Thereafter, the function loss due to the damaged cell membranes could eventually lead to cell death. As a result, improving the separation efficiency of photogenerated electrons and holes is in favor of photocatalytic disinfection. The inactivation results also agree well with the photocatalytic degradation experiment.

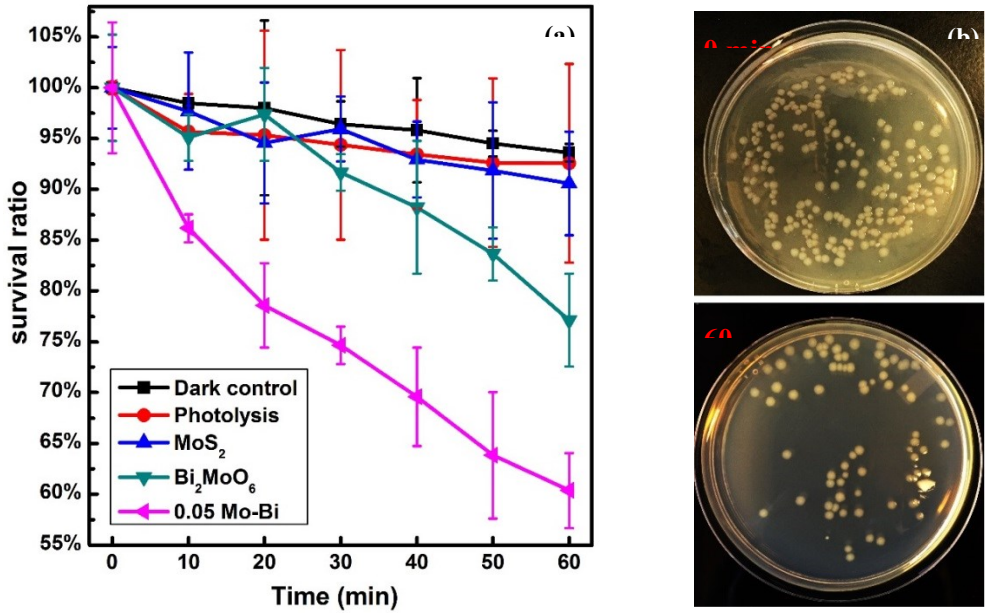

Figure 5.16. (a) Photocatalytic disinfection performance of various samples; (b) photos of E. coli colonies which are cultured by the samples collected at different time during photocatalytic disinfection process.

5.3.5 Mechanism exploration

5.3.5.1 Electrochemical analysis

Electrochemical impedance spectra (EIS) were employed to assess the charge transfer and separation efficiency of photogenerated electron-hole pairs. The EIS Nyquist plots of pure Bi_2MoO_6 and MoS_2/Bi_2MoO_6 composites are shown in Figure 5.17. The charge transfer and recombination process can be depicted by equivalent circuits (inset of Figure 5.17). R_s and *CPE* respectively represent the resistance of solution and constant phase element which may be considered as a double-layered capacitor [48]. R_{ct} represents the resistance to electron transfer that can be determined by the arc radius in the EIS Nyquist plot. Specifically, a smaller radius indicates a smaller value of R_{ct} and results in efficient separation of photogenerated charge carriers. Values of these electrical parameters are summarized in Table 5.2. Compared with pure Bi_2MoO_6, the value of R_{ct} reduced form 16.79 Ω to 10.03 Ω via coupling with MoS_2. It suggested that the introduction of MoS_2 could improve the charge transfer rate and charge separation efficiency, which further promotes the photocatalytic activity. The enhanced charge separation efficiency may be attributed to the high conductivity of MoS_2 [58] and the heterojunction formation on the surface of Bi_2MoO_6 and MoS_2.

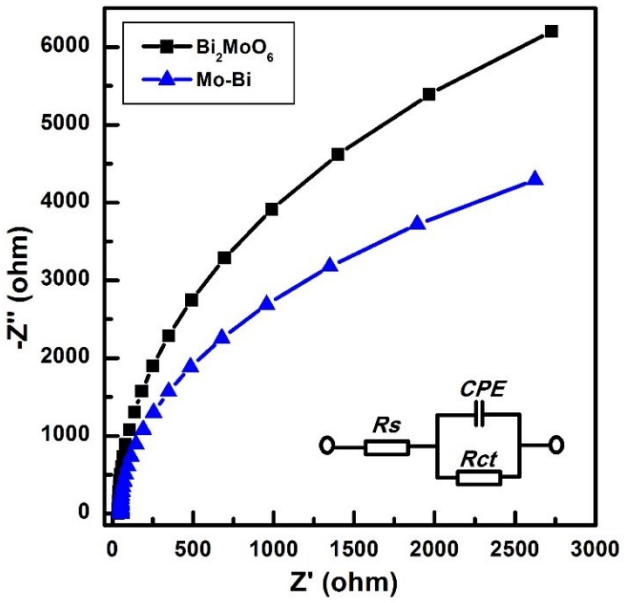

Figure 5.17. EIS Nyquist plots of pure Bi_2MoO_6 and 0.05 Mo-Bi composites.

Table 5.2. Fitting results for equivalent circuits of different prepared samples.

Samples	R_s (Ω)	R_{ct} (kΩ)	*CPE* (μf)
Bi_2MoO_6	34.02	16.79	21.59
0.05 Mo-Bi	39.45	10.03	22.06

The transient photocurrent responses of pure Bi_2MoO_6 and MoS_2/Bi_2MoO_6 composites under pulsed visible-light were recorded to further analyze the photogenerated charge transfer and separation efficiency. As observed in Figure 5.18, the traces of both pure Bi_2MoO_6 and MoS_2/Bi_2MoO_6 composites are reproducible, suggesting that the electrodes are stable. Moreover, the photocurrent intensity of MoS_2/Bi_2MoO_6 composites was around 1.6-fold higher than that of pure Bi_2MoO_6 which corresponds to the photocatalytic

activities of RhB degradation. This result may also deduce the heterostructure formation between MoS_2 and Bi_2MoO_6 with matched energy band positions.

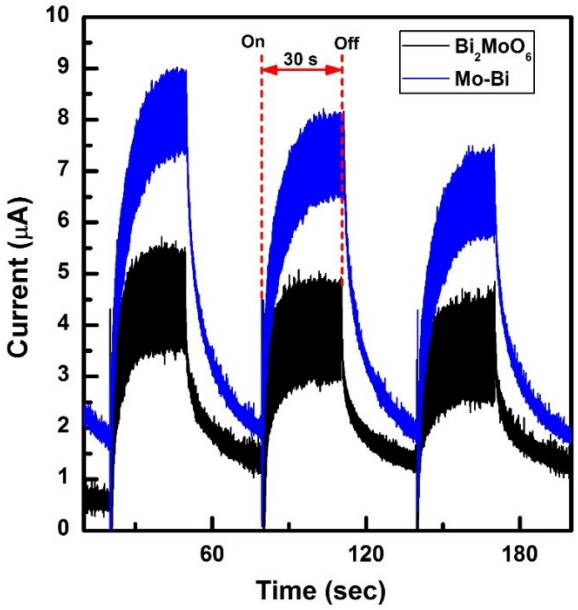

Figure 5.18. Transient photocurrent responses of pure Bi_2MoO_6 and 0.05 Mo-Bi composites under pulsed visible-light.

5.3.5.2 Photoluminescence

Given that the florescence intensity arises from charge recombination, the transfer and separation efficiency of photogenerated charge carriers can be estimated by the photoluminescence (PL) spectrum [59]. A lower PL intensity represents lower charge recombination rate and better photocatalytic performance. The photoluminescence spectra of MoS_2 (Figure 5.19) demonstrated its semiconducting phase and the peaks located at around 553 and 625 nm may be attributed to the band gap photoluminescence form the K point. This result agrees well with other reports [60-62]. As shown in Figure 5.20, the pure Bi_2MoO_6 and 0.05 Mo-Bi have similar PL profile and the major fluorescence peak is located at around 700 nm, which is in accordance with previous studies [63, 64]. Compared to pure Bi_2MoO_6, 0.05 Mo-Bi displayed a decrease in fluorescence intensity, suggesting a

lower recombination rate of photogenerated charge carriers. This result implies that the prepared MoS_2/ Bi_2MoO_6 composites have matched energy band positions, leading to a fast charge transfer and separation rate. These results agreed well with the results of photocatalytic degradation of RhB and photocatalytic inactivation of *E.Coli*, which demonstrated that MoS_2/Bi_2MoO_6 composites have an enhanced photocatalytic activity compared to pure Bi_2MoO_6.

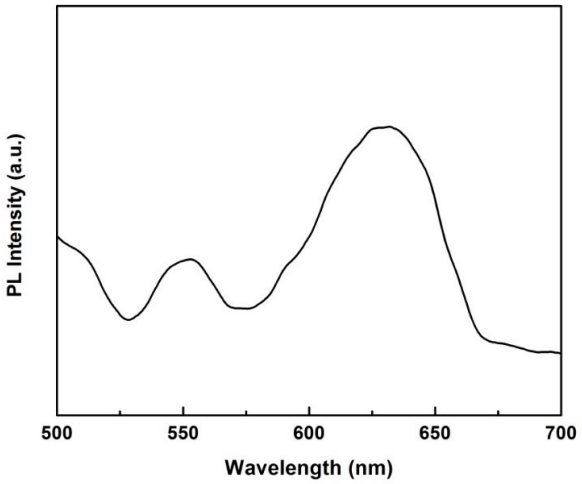

Figure 5 19. Fluorescence emission* of MoS_2 obtained *with an excitation wavelength of 450 nm.

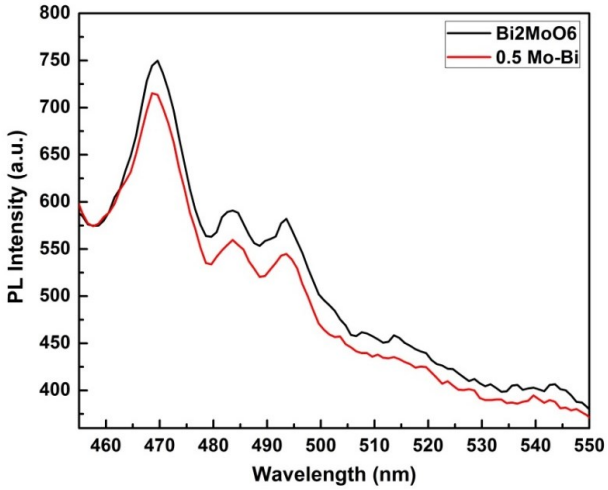

Figure 5.20. Fluorescence emission of Bi_2MoO_6 and MoS_2/Bi_2MoO_6 composites obtained with an excitation wavelength of 450 nm.

5.3.5.3 Roles of reactive species

It is well known that three major reactive oxidants are contributed to the photocatalytic degradation of organic pollutants in waste water [48, 65], including •OH, holes and $•O_2^-$. In order to evaluate the effect of each reactive species in the system, quenching experiments and kinetic analysis were performed and the results are shown in Figure 5.21 and Table 5.3, respectively. For kinetic analysis of RhB degradation, the pseudo-first-order reaction model was applied and expressed as follows (Equation 2) [66]:

$$\ln\left(\frac{c_0}{c}\right) = k_r \times K \times t = k't \qquad \textit{Equation 2}$$

where t is the reaction time; c_0 and c are the initial concentration and concentration at each reaction time; k_r is the reaction rate constant; K is the adsorption coefficient of the RhB on the photocatalyst; and k' is the pseudo-first-order reaction kinetics constant. Therefore, the slope of a plot of $\ln(c_0/c)$ vs t is the value of k'.

As shown in Figure 5.21, more than 99% of RhB was degraded at 100 min without scavengers. The corresponding pseudo-first-order reaction kinetics constant is 1.88×10^{-2} min^{-1}. In contrast, the RhB degradation activities were reduced to some extent with various scavengers. For example, only 10.7% and 42.5% of RhB was degraded at 100 min in the presence of EDTA and N_2, respectively. As a result, holes and $•O_2^-$ played important roles in the photocatalytic degradation of RhB. Moreover, the strongest inhibiting effect of EDTA ($k' = 0.12\times10^{-2}$ min^{-1}) suggests that the photocatalytic degradation of RhB may be dominated by holes due to their strong oxidative capacity in the system. In comparison with other scavengers, iso-propanol showed a relatively low inhibition effect ($k' = 1.19\times10^{-2}$ min^{-1}) to the photocatalytic degradation process, which indicates that •OH is not the major

active oxidative species in the system. The possible reactions are proposed as follows [54, 65]:

$$\text{Photocatalysts} + h\nu \rightarrow h^+ + e^-$$

$$H_2O + h^+ \rightarrow \cdot OH + H^+$$

$$h^+ + \text{Pollutant} \rightarrow \text{Pollutant}^*$$

$$\cdot OH + \text{Pollutant} \rightarrow CO_2 + H_2O$$

$$O_2 + e^- \rightarrow \cdot O_2^-$$

$$O_2 + e^- + H^+ \rightarrow \cdot HO_2$$

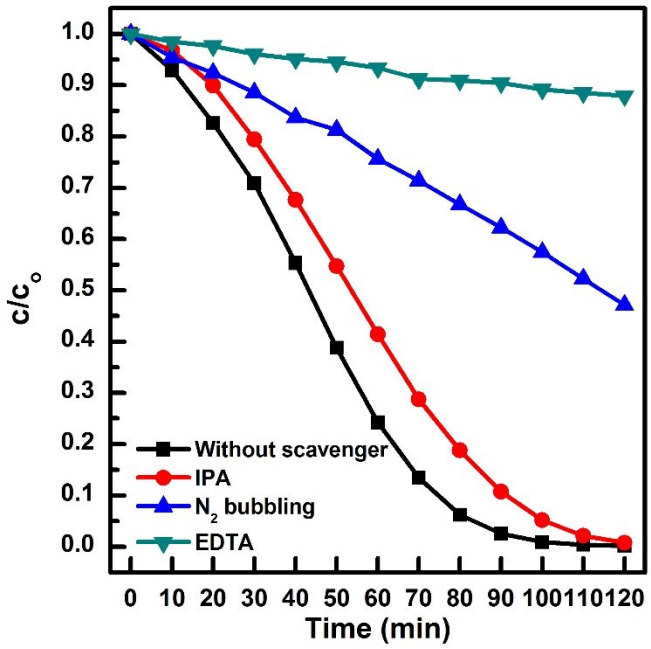

Figure 5.21. Photocatalytic degradation of RhB over 0.05 Mo-Bi in the presence of different scavengers.

Table 5.3. Quecching effect of differenct scarvengers added in the photocatalytic system.

	Without scavengers	IPA	N_2 bubbling	EDTA
Species suppressed	--	•OH	$•O_2^-$	holes
k' (10^{-2} min^{-1})	1.88	1.19	0.44	0.12
k'/k'(no quenching)	1	0.63	0.23	0.06

5.3.5.4 Mechanism of photocatalytic reactions.

In general, the energy band configuration is directly related to the mechanism of photocatalyst in terms of redox capacity and the recombination rate of photogenerated charge carriers. The band position can be estimated by the Mulliken electronegativity and expressed as [13, 34]:

$$E_{CB} = \chi_P - E^e - 0.5E_g$$

$$E_{VB} = E_{CB} + E_g$$

Where, E_{CB} and E_{VB} are the edge potentials of conduction band and valence band, respectively; χ_p is the electronegativity of the semiconductor which is given by the geometric mean of the electronegativities of the constituent atoms; E^e is the energy of free electrons on the hydrogen scale (~4.5 eV); and E_g is the band gap energy of semiconductor. The Mulliken electronegativity for atom can be determined by the arithmetic average of the electron affinity and first ionization potential [67]. The calculated edge potentials for MoS_2 and Bi_2MoO_6 are summarized in Table 5.4.

Table 5.4. Energy band engineering analysis of Bi_2MoO_6 and MoS_2

Composites	E_g/eV	χ_p/eV	E^e/eV	E_{CB} for NHE[a]/eV	E_{VB} for NHE[a]/eV
Bi_2MoO_6	2.60	6.20	4.50	0.40	3.0
MoS_2	1.75	5.33	4.50	-0.045	1.705

a. NHE: Normal Hydrogen Electrode

Based on the above results, the possible band gap configuration and photocatalytic mechanism is illustrated in Figure 5.22. Both Bi_2MoO_6 and MoS_2 can be excited to generate electron-hole pairs under visible light irradiation. Although the as-prepared MoS_2/Bi_2MoO_6 composites consist of n-type Bi_2MoO_6 and p-type MoS_2, the p-n heterojunction mechanism is not proposed. This is because the photogenerated electrons from the conduction band (CB) of Bi_2MoO_6 (E_{CB} = 0.4 eV vs NHE) is not strong enough to reduce O_2 to $\bullet O_2^-$ or other hydro oxygen radicals [68, 69], however, the quenching experiment revealed that $\bullet O_2^-$ played an important role in the photocatalytic degradation of RhB. Therefore, a possible Z-scheme photocatalyst was fabricated in this work. Under visible light irradiation, the photogenerated electrons on the CB of Bi_2MoO_6 could migrate and recombine with the holes on the valence band (VB) of MoS_2. As a result, the holes on the VB of Bi_2MoO_6 and electrons on the CB of MoS_2 are spatially separated without compromising their redox capacities. When coupling MoS_2 with Bi_2MoO_6, the band positions of MoS_2 could shift slightly upwards in order to reach a Fermi level equilibrium with Bi_2MoO_6 [70]. Moreover, the CB potential of MoS_2 could shift to a higher level due to the quantum confinement effect [71]. Therefore, the potential of electrons on the CB of MoS_2 is negative enough to produce $\bullet O_2^-$, $\bullet HO_2$, and H_2O_2[69], which could further oxidize RhB or inactivate cells. The holes accumulated on the VB of Bi_2MoO_6 could directly

degrade RhB or damage cells. In addition, a fraction of holes may react to the H_2O adsorbed on the surface of the photocatalyst to produce •OH, which could also participate in the photocatalytic process.

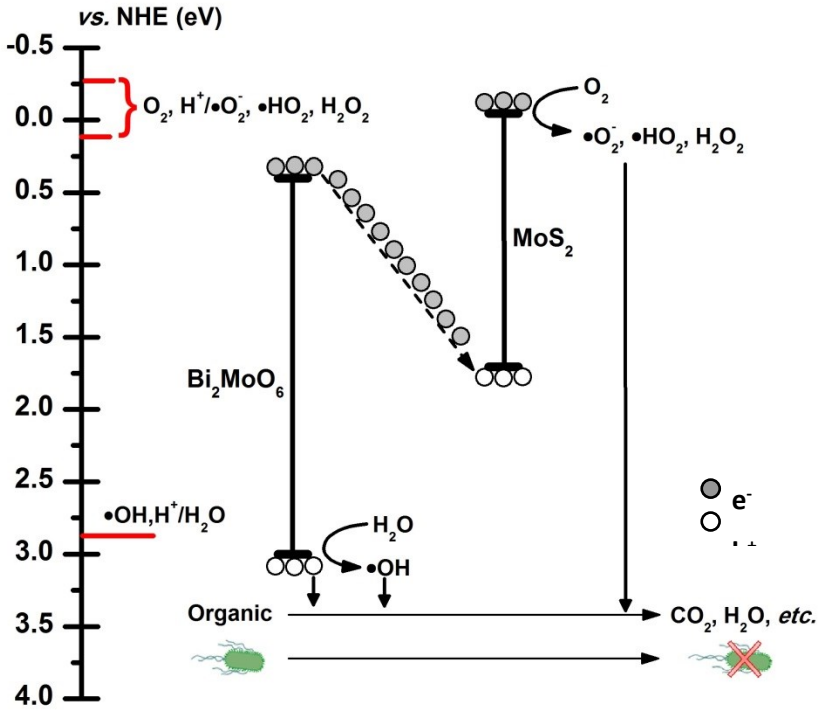

Figure 5.22. Proposed photocatalytic mechanisms of MoS_2/Bi_2MoO_6 composites and feasible photogenerated electron-hole pair transfer and separation process.

5.4 Conclusions

Layered MoS_2-deposited Bi_2MoO_6 were successfully prepared using a simple bath evaporation method. Photocatalytic degradation experiments and photocatalytic inactivation experiments indicated that MoS_2/Bi_2MoO_6 composites exhibited enhanced photocatalytic activities relative to pristine Bi_2MoO_6. Meanwhile, the MoS_2/Bi_2MoO_6 composites displayed the highest photocatalytic activity when the MoS_2 loading amount reached 0.05 wt%. The enhanced photocatalytic activity may be attributed to the formation of Z-scheme heterostructure and the high conductivity of MoS_2. In addition, the quenching

experiment revealed that photogenerated holes may be the dominating oxidative species in the system. This work provides a promising candidate for photocatalytic degradation of organic dyes and photocatalytic disinfection in the area of wastewater treatment, and may broaden the range of MoS_2 modified visible-light-induced photocatalyst.

References

[1] M.N. Chong, B. Jin, C.W.K. Chow, C. Saint, Recent developments in photocatalytic water treatment technology: A review, Water Res., 44 (2010) 2997-3027.

[2] X. Meng, Z. Zhang, Bismuth-based Photocatalytic Semiconductors: Introduction, Challenges and Possible Approaches, Journal of Molecular Catalysis A: Chemical, 423 (2016) 533-549.

[3] X. Hu, X. Meng, Z. Zhang, Synthesis and Characterization of Graphene Oxide-Modified Bi_2WO_6 and Its Use as Photocatalyst, International Journal of Photoenergy, 2016 (2016) 8.

[4] M. Marchelek, B. Bajorowicz, P. Mazierski, A. Cybula, T. Klimczuk, M. Winiarski, N. Fijałkowska, A. Zaleska, $KTaO_3$-based nanocomposites for air treatment, Catal. Today, 252 (2015) 47-53.

[5] X. Meng, L. Jiang, W. Wang, Z. Zhang, Enhanced Photocatalytic Activity of BiOBr/ZnO Heterojunction Semiconductors Prepared by Facile Hydrothermal Method, International Journal of Photoenergy, 2015 (2015) 9.

[6] X. Meng, Z. Li, J. Chen, H. Xie, Z. Zhang, Enhanced visible light-induced photocatalytic activity of surface-modified BiOBr with Pd nanoparticles, Appl. Surf. Sci., 433 (2018) 76-87.

[7] X. Meng, Z. Li, Z. Zhang, Pd-nanoparticle-decorated peanut-shaped $BiVO_4$ with improved visible light-driven photocatalytic activity comparable to that of TiO_2 under UV light, Journal of Catalysis, 356 (2017) 53-64.

[8] X. Meng, Z. Zhang, Synthesis, Analysis, and Testing of BiOBr-Bi_2WO_6 Photocatalytic Heterojunction Semiconductors, International Journal of Photoenergy, 2015 (2015) 12.

[9] X. Meng, Z. Zhang, Synthesis and characterization of plasmonic and magnetically separable Ag/AgCl-Bi_2WO_6@ Fe_3O_4@SiO_2 core-shell composites for visible light-induced water detoxification, J. Colloid Interface Sci., 485 (2017) 296-307.

[10] N. Shao, J. Wang, D. Wang, P. Corvini, Preparation of three-dimensional Ag_3PO_4/TiO_2@MoS_2 for enhanced visible-light photocatalytic activity and anti-photocorrosion, Applied Catalysis B: Environmental, 203 (2017) 964-978.

[11] Y. Gao, C. Chen, X. Tan, H. Xu, K. Zhu, Polyaniline-modified 3D-flower-like molybdenum disulfide composite for efficient adsorption/photocatalytic reduction of Cr(VI), J. Colloid Interface Sci., 476 (2016) 62-70.

[12] M.Q. Wen, T. Xiong, Z.G. Zang, W. Wei, X.S. Tang, F. Dong, Synthesis of MoS_2/g-C_3N_4 nanocomposites with enhanced visible-light photocatalytic activity for the removal of nitric oxide (NO), Opt. Express, 24 (2016) 10205-10212.

[13] X. Meng, Z. Li, H. Zeng, J. Chen, Z. Zhang, MoS_2 quantum dots-interspersed Bi_2WO_6 heterostructures for visible light-induced detoxification and disinfection, Applied Catalysis B: Environmental, 210 (2017) 160-172.

[14] A. Ahmad, X. Meng, N. Yun, Z. Zhang, Preparation of Hierarchical BiOBr Microspheres for Visible Light-Induced Photocatalytic Detoxification and Disinfection, J

Nanomater, 2016 (2016) 10.

[15] J. Zhang, L. Huang, H. Jin, Y. Sun, X. Ma, E. Zhang, H. Wang, Z. Kong, J. Xi, Z. Ji, Constructing two-dimension MoS_2/Bi_2WO_6 core-shell heterostructure as carriers transfer channel for enhancing photocatalytic activity, Mater. Res. Bull., 85 (2017) 140-146.

[16] J. Ke, J. Liu, H. Sun, H. Zhang, X. Duan, P. Liang, X. Li, M.O. Tade, S. Liu, S. Wang, Facile assembly of $Bi_2O_3/Bi_2S_3/MoS_2$ n-p heterojunction with layered n-Bi_2O_3 and p-MoS_2 for enhanced photocatalytic water oxidation and pollutant degradation, Applied Catalysis B: Environmental, 200 (2017) 47-55.

[17] N. Shao, J. Wang, D. Wang, P. Corvini, Preparation of three-dimensional $Ag_3PO_4/TiO_2@MoS_2$ for enhanced visible-light photocatalytic activity and anti-photocorrosion, Applied Catalysis B: Environmental, 203 (2017) 964-978.

[18] M.-Q. Yang, C. Han, Y.-J. Xu, Insight into the Effect of Highly Dispersed MoS_2 versus Layer-Structured MoS_2 on the Photocorrosion and Photoactivity of CdS in Graphene–CdS–MoS_2 Composites, The Journal of Physical Chemistry C, 119 (2015) 27234-27246.

[19] M. Xu, T. Liang, M. Shi, H. Chen, Graphene-Like Two-Dimensional Materials, Chem Rev, 113 (2013) 3766-3798.

[20] G. Fiori, F. Bonaccorso, G. Iannaccone, T. Palacios, D. Neumaier, A. Seabaugh, S.K. Banerjee, L. Colombo, Electronics based on two-dimensional materials, Nat Nanotechnol, 9 (2014) 768.

[21] O. Lopez-Sanchez, D. Lembke, M. Kayci, A. Radenovic, A. Kis, Ultrasensitive photodetectors based on monolayer MoS_2, Nat Nanotechnol, 8 (2013) 497.

[22] T. Ohta, A. Bostwick, T. Seyller, K. Horn, E. Rotenberg, Controlling the Electronic

Structure of Bilayer Graphene, Science, 313 (2006) 951-954.

[23] B. Han, S. Liu, N. Zhang, Y.-J. Xu, Z.-R. Tang, One-dimensional CdS@MoS_2 core-shell nanowires for boosted photocatalytic hydrogen evolution under visible light, Applied Catalysis B: Environmental, 202 (2017) 298-304.

[24] Z. Li, X. Meng, Z. Zhang, Recent Development on MoS_2-based Photocatalysis: a Review, Journal of Photochemistry and Photobiology C: Photochemistry Reviews, 35 (2018) 39-55.

[25] Y. Wang, G. Li, P. Li, J. Hu, Q. Zhao, Research progress of two-dimensional layered material molybdenum disulfide, Bandaoti Guangdian/Semiconductor Optoelectronics, 37 (2016) 461-466.

[26] Y.-J. Yuan, H.-W. Lu, Z.-T. Yu, Z.-G. Zou, Noble-Metal-Free Molybdenum Disulfide Cocatalyst for Photocatalytic Hydrogen Production, Chemsuschem, 8 (2015) 4113-4127.

[27] X. Jin, X. Fan, J. Tian, R. Cheng, M. Li, L. Zhang, MoS_2 quantum dot decorated g-C_3N_4 composite photocatalyst with enhanced hydrogen evolution performance, RSC Advances, 6 (2016) 52611-52619.

[28] Y. Zhu, S. Murali, W. Cai, X. Li, J.W. Suk, J.R. Potts, R.S. Ruoff, Graphene and Graphene Oxide: Synthesis, Properties, and Applications, Adv Mater, 22 (2010) 3906-3924.

[29] X. Li, J. Yu, S. Wageh, A.A. Al-Ghamdi, J. Xie, Graphene in Photocatalysis: A Review, Small, 12 (2016) 6640-6696.

[30] B. Weng, X. Zhang, N. Zhang, Z.-R. Tang, Y.-J. Xu, Two-Dimensional MoS_2 Nanosheet-Coated Bi_2S_3 Discoids: Synthesis, Formation Mechanism, and Photocatalytic Application, Langmuir, 31 (2015) 4314-4322.

[31] A. Kuc, N. Zibouche, T. Heine, Influence of quantum confinement on the electronic structure of the transition metal sulfide TS_2, Phys Rev B, 83 (2011) 245213.

[32] G. Tian, Y. Chen, W. Zhou, K. Pan, Y. Dong, C. Tian, H. Fu, Facile solvothermal synthesis of hierarchical flower-like Bi_2MoO_6 hollow spheres as high performance visible-light driven photocatalysts, J. Mater. Chem., 21 (2011) 887-892.

[33] L. Zhang, T. Xu, X. Zhao, Y. Zhu, Controllable synthesis of Bi_2MoO_6 and effect of morphology and variation in local structure on photocatalytic activities, Applied Catalysis B: Environmental, 98 (2010) 138-146.

[34] X. Meng, Z. Zhang, Bismuth-based photocatalytic semiconductors: Introduction, challenges and possible approaches, J. Mol. Catal. A: Chem., 423 (2016) 533-549.

[35] X. Meng, Z. Zhang, Pd-doped Bi_2MoO_6 Plasmonic Photocatalysts with Enhanced Visible Light Photocatalytic Performance, Appl Surf Sci, 392 (2016) 169-180.

[36] Y. Chen, G. Tian, Y. Shi, Y. Xiao, H. Fu, Hierarchical MoS_2/Bi_2MoO_6 composites with synergistic effect for enhanced visible photocatalytic activity, Applied Catalysis B: Environmental, 164 (2015) 40-47.

[37] G. Kresse, J. Furthmüller, Efficient iterative schemes for ab initio total-energy calculations using a plane-wave basis set, Phys Rev B, 54 (1996) 11169-11186.

[38] G. Kresse, J. Hafner, Ab initio, Phys Rev B, 47 (1993) 558-561.

[39] P.E. Blöchl, Projector augmented-wave method, Phys Rev B, 50 (1994) 17953-17979.

[40] J.P. Perdew, K. Burke, M. Ernzerhof, Generalized Gradient Approximation Made Simple, Phys Rev Lett, 77 (1996) 3865-3868.

[41] K. Momma, F. Izumi, VESTA 3 for three-dimensional visualization of crystal, volumetric and morphology data, J Appl Crystallogr, 44 (2011) 1272-1276.

[42] J. Gamage McEvoy, D.A. Bilodeau, W. Cui, Z. Zhang, Visible-light-driven inactivation of Escherichia coli K-12 using an Ag/AgCl–activated carbon composite photocatalyst, J. Photochem. Photobiol. A: Chem., 267 (2013) 25-34.

[43] X. Zong, H. Yan, G. Wu, G. Ma, F. Wen, L. Wang, C. Li, Enhancement of Photocatalytic H_2 Evolution on CdS by Loading MoS_2 as Cocatalyst under Visible Light Irradiation, J. Am. Chem. Soc., 130 (2008) 7176-7177.

[44] RadisavljevicB, RadenovicA, BrivioJ, GiacomettiV, KisA, Single-layer MoS_2 transistors, Nat Nano, 6 (2011) 147-150.

[45] H.S.S. Ramakrishna Matte, A. Gomathi, A.K. Manna, D.J. Late, R. Datta, S.K. Pati, C.N.R. Rao, MoS_2 and WS_2 Analogues of Graphene, Angew. Chem. Int. Ed., 49 (2010) 4059-4062.

[46] M. Liu, X. Xue, S. Yu, X. Wang, X. Hu, H. Tian, H. Chen, W. Zheng, Improving Photocatalytic Performance from Bi_2WO_6@MoS_2/graphene Hybrids via Gradual Charge Transferred Pathway, Scientific Reports, 7 (2017) 3637.

[47] Y. Xu, H. Xu, H. Li, J. Xia, C. Liu, L. Liu, Enhanced photocatalytic activity of new photocatalyst Ag/AgCl/ZnO, J. Alloys Compd., 509 (2011) 3286-3292.

[48] X. Meng, Z. Zhang, Plasmonic ternary Ag–rGO–Bi_2MoO_6 composites with enhanced visible light-driven photocatalytic activity, J. Catal., 344 (2016) 616-630.

[49] H.W. Wang, P. Skeldon, G.E. Thompson, XPS studies of MoS_2 formation from ammonium tetrathiomolybdate solutions, Surface and Coatings Technology, 91 (1997)

200-207.

[50] M. Kruk, M. Jaroniec, Gas Adsorption Characterization of Ordered Organic−Inorganic Nanocomposite Materials, Chem Mater, 13 (2001) 3169-3183.

[51] J. Bi, W. Fang, L. Li, X. Li, M. Liu, S. Liang, Z. Zhang, Y. He, H. Lin, L. Wu, S. Liu, P.K. Wong, Ternary reduced-graphene-oxide/Bi_2MoO_6/Au nanocomposites with enhanced photocatalytic activity under visible light, J. Alloys Compd., 649 (2015) 28-34.

[52] X. Meng, Z. Zhang, Bi_2MoO_6 co-modified by reduced graphene oxide and palladium (Pd^{2+} and Pd^0) with enhanced photocatalytic decomposition of phenol, Applied Catalysis B: Environmental, 209 (2017) 383-393.

[53] K. Lai, W. Wei, Y. Dai, R. Zhang, B. Huang, DFT calculations on structural and electronic properties of Bi_2MO_6 (M = Cr, Mo, W), Rare Metals, 30 (2011) 166-172.

[54] X. Meng, Z. Zhang, Facile synthesis of BiOBr/Bi_2WO_6 heterojunction semiconductors with high visible-light-driven photocatalytic activity, J. Photochem. Photobiol. A: Chem., 310 (2015) 33-44.

[55] T. Watanabe, T. Takizawa, K. Honda, Photocatalysis through excitation of adsorbates. 1. Highly efficient N-deethylation of rhodamine B adsorbed to cadmium sulfide, The Journal of Physical Chemistry, 81 (1977) 1845-1851.

[56] T. Wu, G. Liu, J. Zhao, H. Hidaka, N. Serpone, Photoassisted Degradation of Dye Pollutants. V. Self-Photosensitized Oxidative Transformation of Rhodamine B under Visible Light Irradiation in Aqueous TiO_2 Dispersions, The Journal of Physical Chemistry B, 102 (1998) 5845-5851.

[57] P.-C. Maness, S. Smolinski, D.M. Blake, Z. Huang, E.J. Wolfrum, W.A. Jacoby,

Bactericidal Activity of Photocatalytic TiO_2 Reaction: toward an Understanding of Its Killing Mechanism, Appl Environ Microb, 65 (1999) 4094-4098.

[58] Y. Zhu, Q. Ling, Y. Liu, H. Wang, Y. Zhu, Photocatalytic H_2 evolution on MoS_2-TiO_2 catalysts synthesized via mechanochemistry, PCCP, 17 (2015) 933-940.

[59] G. Tian, Y. Chen, J. Zhou, C. Tian, R. Li, C. Wang, H. Fu, In situ growth of Bi_2MoO_6 on reduced graphene oxide nanosheets for improved visible-light photocatalytic activity, Crystengcomm, 16 (2014) 842-849.

[60] G. Eda, H. Yamaguchi, D. Voiry, T. Fujita, M. Chen, M. Chhowalla, Photoluminescence from Chemically Exfoliated MoS_2, Nano Lett., 11 (2011) 5111-5116.

[61] C. Liu, L. Wang, Y. Tang, S. Luo, Y. Liu, S. Zhang, Y. Zeng, Y. Xu, Vertical single or few-layer MoS_2 nanosheets rooting into TiO_2 nanofibers for highly efficient photocatalytic hydrogen evolution, Applied Catalysis B: Environmental, 164 (2015) 1-9.

[62] J. Zhang, Z. Zhu, X. Feng, Construction of Two-Dimensional MoS_2/CdS p–n Nanohybrids for Highly Efficient Photocatalytic Hydrogen Evolution, Chemistry – A European Journal, 20 (2014) 10632-10635.

[63] D. Wang, H. Shen, L. Guo, F. Fu, Y. Liang, Design and construction of the sandwich-like Z-scheme multicomponent CdS/Ag/Bi_2MoO_6 heterostructure with enhanced photocatalytic performance in RhB photodegradation, New J. Chem., 40 (2016) 8614-8624.

[64] W. Zhao, C. Li, A. Wang, C. Lv, W. Zhu, S. Dou, Q. Wang, Q. Zhong, Polyaniline decorated Bi_2MoO_6 nanosheets with effective interfacial charge transfer as photocatalysts and optical limiters, PCCP, 19 (2017) 28696-28709.

[65] Y. Zheng, C. Li, X. Meng, Z. Zhang, A conjugated composite of α-Fe_2O_3 and BiOBr

with enhanced visible-light-induced photocatalytic activity, J. Mol. Catal. A: Chem., 421 (2016) 16-28.

[66] X. Meng, Z. Zhang, Ag/AgCl Loaded Bi_2WO_6 Composite: A Plasmonic Z-Scheme Visible Light-Responsive Photocatalyst, International Journal of Photoenergy, 2016 (2016) 11.

[67] H.L. Zhuang, R.G. Hennig, Theoretical perspective of photocatalytic properties of single-layer SnS_2, Physical Review B, 88 (2013) 115314.

[68] S. Fang, Y. Zhou, H. Cui, Z. Li, S. Xu, L. Wang, Fabrication of BiOCl@CdS/Ag_2CO_3 heterojunctions with enhanced photocatalytic activity under visible-light irradiation, Journal of Materials Science: Materials in Electronics, 28 (2017) 14575-14583.

[69] Y.A. Ilan, G. Czapski, D. Meisel, The one-electron transfer redox potentials of free radicals. I. The oxygen/superoxide system, Biochimica et Biophysica Acta (BBA) - Bioenergetics, 430 (1976) 209-224.

[70] T. Xiong, M. Wen, F. Dong, J. Yu, L. Han, B. Lei, Y. Zhang, X. Tang, Z. Zang, Three dimensional Z-scheme $(BiO)_2CO_3$/MoS_2 with enhanced visible light photocatalytic NO removal, Applied Catalysis B: Environmental, 199 (2016) 87-95.

[71] L. Cao, Novel MoS_2-modified $AgVO_3$ composites with remarkably enhanced photocatalytic activity under visible-light irradiation, Mater. Lett., 188 (2017) 252-256.

SECTION III: SnS ENHANCED PHOTOCATALYSIS

Chapter 6 Hexagonal SnS nanoplates assembled onto hierarchical Bi_2WO_6 with enhanced photocatalytic activity in detoxification and disinfection

Zizhen Li, Xiangchao Meng and Zisheng Zhang

Journal of Colloid and Interface Science, *537*, 345-357 (2019)

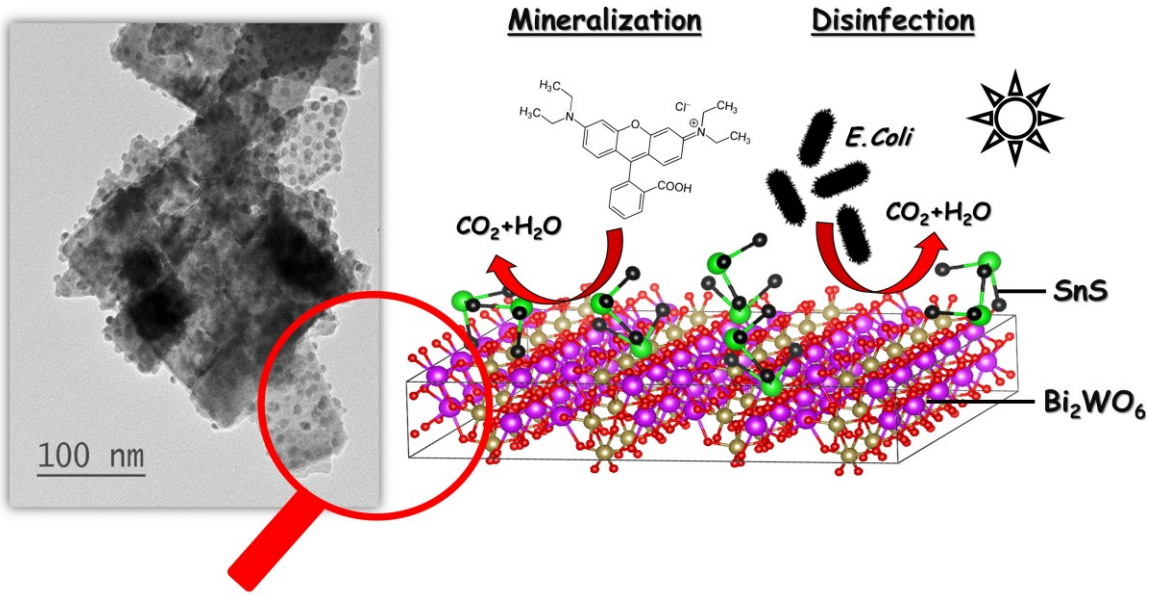

Abstract

A novel Z-scheme heterostructure, SnS nanoplates deposited Bi_2WO_6, was successfully fabricated via a simple bath sonication method. The positive synergetic effect between SnS and Bi_2WO_6 greatly improved the photocatalytic activity of SnS-Bi_2WO_6 composites in

dye degradation and bacterial inactivation. Under visible light irradiation, the photocatalytic degradation activity of SnS-Bi_2WO_6 composites (0.50 wt% SnS) was about 5.8 times higher than that of pure Bi_2WO_6. As for the disinfection experiment, the survival ratio for 60 min in the presence of Bi_2WO_6 and SnS-Bi_2WO_6 composites was 50% and 32%, respectively. This result was consistent with the photocatalytic degradation reaction. The mechanism of photocatalytic reactions was also explored by the quenching experiment and electrochemical analysis. It indicated that the main oxidative species in the photocatalytic degradation process were holes and hydro oxygen radicals (*e.g.* $\bullet HO_2$ and H_2O_2). In addition, the formation of the heterostructure could greatly suppress the recombination of photogenerated charge carriers. All these results suggested that the as-prepared SnS-Bi_2WO_6 composites could be served as efficient photocatalysts for wastewater treatment.

6.1 Introduction

The semiconductor, tin sulfide (SnS), has recently attracted increasing attention in the fields of photodetectors [1], solar cells [2], Li ion batteries [3], and photocatalysis [4]. As an earth abundant material, SnS is an inexpensive, chemically inert and heavy-metal-free material that possesses a suitable bandgap (~1.3 eV) for light absorption in the visible-light region and near-infrared region [5]. Therefore, SnS is expected to be a promising visible-light-responsive photocatalyst. However, its fast charge recombination and low photocatalytic activity hindered its potential application. It is well known that fabrication of a heterostructure is an efficient method to facilitate photogenerated charge separation and improve photocatalytic performance [6]. For example, Hu *et al.* synthesized SnS/SnS_2 heterostructure nanocrystals by the pyrolysis method and their performance on

photocatalytic dye degradation were greatly improved compared with pure SnS [6]. Similar results were also reported by Yao's group [7]. In their work, urchinlike SnS/SnS_2 p-n heterogeneous composites were prepared by a one-step solvothermal method. The pseudo-first-order reaction rate for methyl orange (MO) degradation was determined to be 3.351×10^{-2} min^{-1}, which is higher than that of pristine SnS (2.985×10^{-2} min^{-1}) and SnS_2 (0.957×10^{-2} min^{-1}). Wang and co-workers fabricated a novel p-n heterojunction by combining SnS with ZnO and the material also displayed improved photocatalytic activity [8]. The heterostructure combined the large surface area and high redox ability of ZnO with visible-light absorption capacity of SnS, which could facilitate the generation of photo-induced charge carriers and promote charge separation. Under visible light irradiation, the RhB degradation rate constant of the ZnO-SnS p-n heterojunction was 10-fold and 2-fold higher than that of ZnO and SnS, respectively.

In this work, a unique heterostructure is established by coupling SnS with Bi_2WO_6. As one of bismuth-based photocatalysts, Bi_2WO_6 exhibited well-dispersed orbits, which favors the transfer of photogenerated carriers [9-16]. Numerous works have been reported on Bi_2WO_6-based photocatalysts for environmental remediation [14, 17-19]. However, the bandgap energy of Bi_2WO_6 (~2.70 eV) indicated that this material can only be activated by light with wavelengths below 460 nm. Thus, prepared $SnS\text{-}Bi_2WO_6$ hybrid composites may simultaneously enlarge the light absorption capacity and improve the charge separation efficiency. Tang *et al.* reported on one-step preparation of $SnS\text{-}Bi_2WO_6$, and found that the photocatalytic activity of Bi_2WO_6 was slightly improved [20]. This result confirmed the effectiveness of loading SnS to improve the photocatalytic activity of Bi_2WO_6. As motivated by the work our group reported on $MoS_2\text{-}Bi_2WO_6$ using a two-step

method [21], the objective of this work is to prepare SnS-Bi_2WO_6 through a two-step method with SnS loaded onto the surface.

Herein, we prepared a novel Z-scheme heterostructure consisting of SnS and Bi_2WO_6 via a simple bath sonication method. Compared with pure SnS and Bi_2WO_6, the positive synergetic effect between SnS and Bi_2WO_6 lead to improved photocatalytic activity in dye degradation and disinfection. The good photocatalytic performance of this material may further indicate the potential application of SnS-Bi_2WO_6 composites in wastewater treatment.

6.2 Experimental

6.2.1 Preparation of Bi_2WO_6, SnS and SnS-Bi_2WO_6 composites

Hierarchical Bi_2WO_6 were prepared using an acetic acid-assisted hydrothermal method as we reported previously [22]. Typically, 2 mmol of $Bi(NO_3)_3$•$5H_2O$ (ACS grade, 98%, Alfa Aesar^{TM}) were dissolved into 30 mL acetic acid (glacial, certified ACS, Fisher Scientific, Canada) under magnetically stirring for 10 min, termed solution A. And 1 mmol of Na_2WO_4•$2H_2O$ (ACS grade, 99^{+}%, ACROS Organics^{TM}) were dissolved into 50 mL deionized distilled water (DDW), termed solution B. After that, solution B was dropwise added into solution A under magnetically stirring for another 20 min. Then, the mixture was transferred into a 100-mL Teflon-line stainless steel autoclave (Parr Instrument Company, USA). The autoclave was heated up to 180°C, and maintained for 20h. After the autoclave was naturally cooled down to room temperature, the white precipitates were filtered out and washed three times with DDW, and dried at 60 °C for 12h before collected for further use.

Hexagonal SnS nanoplates were prepared using a facile hydrothermal method with minor modifications [23]. In a typical process, 1 mmol of $SnCl_2 \cdot 2H_2O$ (98%, Alfa Aesar^{TM}) and 2 mmol of $_L$-cysteine ($C_3H_7NO_2S$, Cell Culture Reagent Grade, Alfa Aesar^{TM}) were separately dissolved into 40 mL DDW. These two solutions were then mixed together under magnetically stirring for 30 min. After that, the mixed solution was transferred into a 100-mL Teflon-lined stainless-steel autoclave, and heated at 180 °C for 12h. After naturally cooling down to room temperature, black precipitates were filtered out, washed with DDW for three times, and dried at 60 °C for 12h before collected for further use.

SnS-Bi_2WO_6 hybrid composites were prepared using a simple bath sonication method, as schematically depicted in Figure 6.1. Specifically, a designated amount of hexagonal SnS nanoplates were mixed with 0.30 g of as-prepared Bi_2WO_6 in 40 mL ethanol. This suspension was then ultrasonicated for 30min, and then magnetically stirred until the solvent was naturally evaporated. Then, the product was dried at 60 °C for 12h before collated. Composites of 0.25, 0.50 and 1.00 wt% SnS loaded onto Bi_2WO_6 were prepared and labelled as 0.25 SB, 0.50 SB and 1.0 SB.

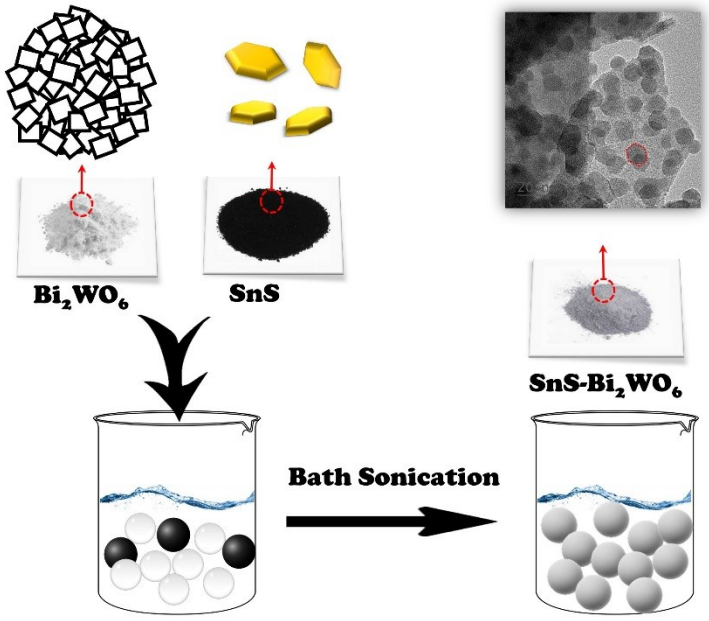

Figure 6.1. Schematic preparation of SnS dispersed on Bi_2WO_6 via a bath sonication method.

6.2.2 Characterizations

The morphology of as-prepared samples was investigated using a field-emission scanning electron microscopy (FE-SEM, JEOL JSM-7500F) and a transmission electron microscopy (TEM, JEM-2100F). An Energy-dispersive X-ray spectroscopy (EDS) was also equipped in the TEM for the elemental analysis of prepared samples. The crystal structure was measured using a Rigaku Ultima IV diffractometer with Cu Kα radiation ($\lambda = 0.15418$ nm) at 40 kV and 44 mA. Surface composition and chemical states were performed on an XSAM-800 X-ray Photoelectron Spectroscope (XPS). The Brunauer, Emmett and Teller (BET) surface area of the samples were calculated using multi-point estimation. The pore volumes were calculated using the volumes of adsorbed N_2 at $p/p_o = 0.9941$. Pore volume distributions are calculated using the N_2 desorption branch, A thermos Evolution 300 spectrophotometer was applied to detect the ultraviolet-visible diffuse reflectance spectra (DRS). Electrochemical properties of prepared samples were performed on a CHI 604E

electrochemical analyzer (CH Instruments Inc., USA) with a platinum wire as a counter electrode, a calomel reference electrode and a working electrode. The working electrode was composed of indium tin oxide (ITO, 75 × 25 × 1.1 mm, 15 - 25 Ω, Sigma-Aldrich Canada Co.) and glass coated with the prepared samples. The electrochemical impedance spectroscopies (EIS) were recorded with frequencies in the range of 0.01 – 1000000 Hz and a sinusoidal wave of 5 mV. The electrolyte was Na_2SO_4 with a concentration of 0.50 mol/L.

6.2.3 Photocatalytic activity tests

6.2.3.1 Degradation of organics

The photocatalytic activities of prepared samples were evaluated by RhB degradation under visible light and the temperature of the photocatalytic process was maintained at 20 °C via a cooling jacket. A 300 W halogen tungsten projector lamp (Ushio) equipped with a UV cut-off ($\lambda > 410$ nm) was applied to provide light source. Typically, 0.10 g photocatalyst was mixed with 100 mL RhB solution with an initial concentration of 10 ppm. Before illumination, the mixture was magnetically stirred for 30 min to obtain adsorption/desorption equilibrium. Afterwards, 1 mL aliquots were collected at given irradiation time intervals and the concentrations of aliquots were determined by a UV-vis spectrophotometer (Genesys 10 UV, Thermo Scientific) at 554 nm. The time-dependent UV-vis adsorption spectra of reaction mixture were also measured by UV-vis spectrophotometer (Biochrom Ultrospec 60) to monitor the photocatalytic degradation process.

Quenching experiments were performed to analyze the roles of each reactive oxidative species (ROS). Specifically, 0.1 M iso-propanol (IPA), 10 vol% triethanolamine (TEOA) and N_2 bubbling were used to trap hydroxyl radicals (•OH), holes and superoxide radicals ($•O_2^-$), respectively.

6.2.3.2 Temporal course of inactivation

E.coli K-12 was chosen as a target microorganism to evaluate the photocatalytic disinfection performance of the prepared samples, because it is a representative non-pathogenic biological indicator of disinfection efficiency in water systems [24]. Before experiments, all materials were sterilized at 121 °C for 20 min. Bacteria were aerobically incubated in Luria-Bertani medium at 37 °C with constant agitation. At the stationary phase, bacteria were collected and re-suspended in sterilized saline. The concentration of bacterial suspension was measured by a spectrophotometer at OD_{600} with appropriate dilutions. For each disinfection trail, 0.10 g photocatalysts were mixed with 100 mL bacterial suspension with the initial concentration of 10^6 colony forming units per milliliter (CFU/mL), followed by magnetic stirring for 30 min in the dark. Under illumination, small aliquots were collected every 10 mins and serially diluted. Afterwards, the diluted samples were plated on LB agar plates using a standard spread plate method and incubated at 37 °C for 18 h. Bacterial enumeration was performed by viable cell counts and all experiments were performed in triplicate [25].

6.2.4 Electronic structure calculation

The DFT simulations were performed using the Vienna *ab initio* simulation package (VASP) [26, 27]. The ion-electron interaction is described with the projector augmented

wave (PAW) method [28]. Electron exchange-correlation is represented by the function of Perdew, Burke, and Ernzerhof (PBE) of generalized gradient approximation (GGA) [29]. A cut-off energy of 380 eV was used for the plane-wave basis set. The calculations were done on periodical supercells of SnS and Bi_2WO_6 with 4×6×6 and 6×6×2 Monkhorst Pack k-point sampling, respectively. Models for Bi_2WO_6 and SnS are depicted in Figure 6.2. An open-source software for VASP visualization, P4VASP written by Orest Dubay (http://www.p4vasp.at) has been used for the analysis of the Density of States (DOS) and bands.

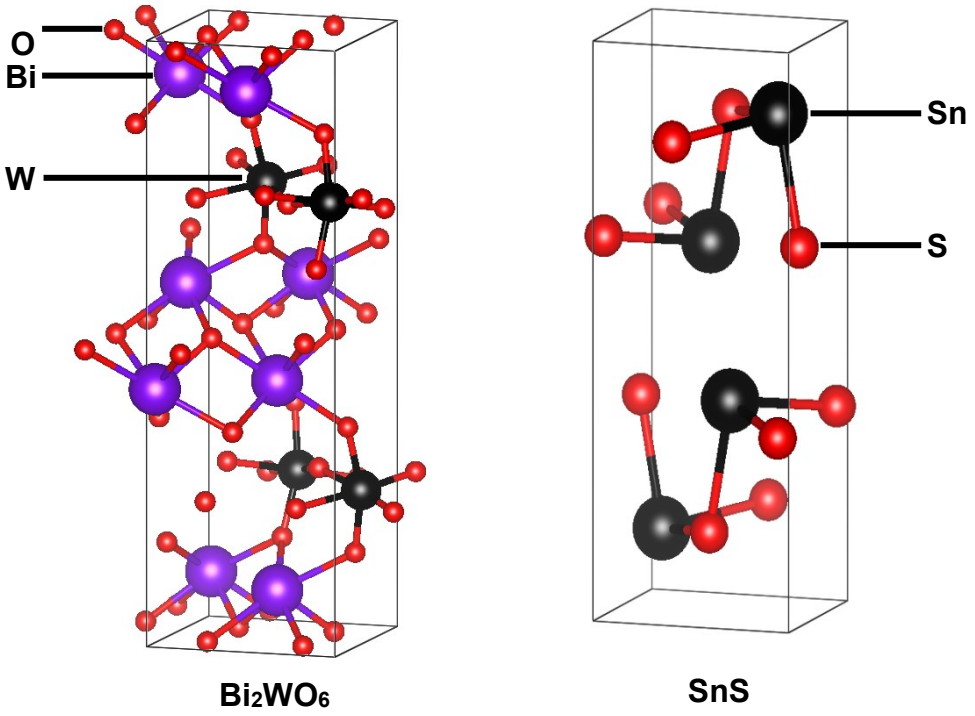

Figure 6.2. Bi_2WO_6 and SnS models for DFT computations (depicted using VESTA [30]).

6.3 Results and discussions

6.3.1 Morphology

The SEM images of Bi_2WO_6 and SnS-Bi_2WO_6 hybrid composites are shown in Fig. 6.3a and 6.3b. It can be observed that pure Bi_2WO_6 exhibited hierarchical flower-like structures with a diameter around 2 μm. After integrating with SnS, some plate-like SnS were deposited on the surface of Bi_2WO_6. The morphology and microstructure of as-prepared Bi_2WO_6, SnS and SnS-Bi_2WO_6 composites were further investigated by TEM images and the lattice spacings were determined from the corresponding FFT patterns. As shown in Fig. 6.3c, SnS nanoplates displayed relatively uniform size dispersion with the diameter ranging from 4 to 13 nm (Fig. 6.3g). In addition, the fringe spacing shown in FFT patterns (inset of Fig. 6.3c) can be indexed to the (011) and (210) planes of SnS, respectively. The FFT pattern for Bi_2WO_6 (inset of Fig. 6.3d) indicated the distances characteristic of (111) and (022) planes, respectively. As for SnS-Bi_2WO_6 composites, Fig. 6.3e clearly revealed that the SnS nanoplates were successfully deposited on the surface of Bi_2WO_6 nanoplates. When viewed at higher magnification (Fig. 6.3f), SnS nanoplates displayed hexagonal/ faceted structure, which showed similar morphology to the SnS prepared by other groups [31]. The FFT pattern for the selected area (red square) of SnS-Bi_2WO_6 composites showed lattice spacing of 3.54, 3.02, and 2.52 Å, which may be assigned to the (201) plane and (011) plane of orthorhombic SnS, and (151) plane of orthorhombic Bi_2WO_6, respectively. The composition of as-prepared SnS-Bi_2WO_6 composites was investigated by EDS analysis (Fig. 6.3h) and the results confirmed the existence of Sn and S elements, further suggesting the successful integrating of Bi_2WO_6 and SnS.

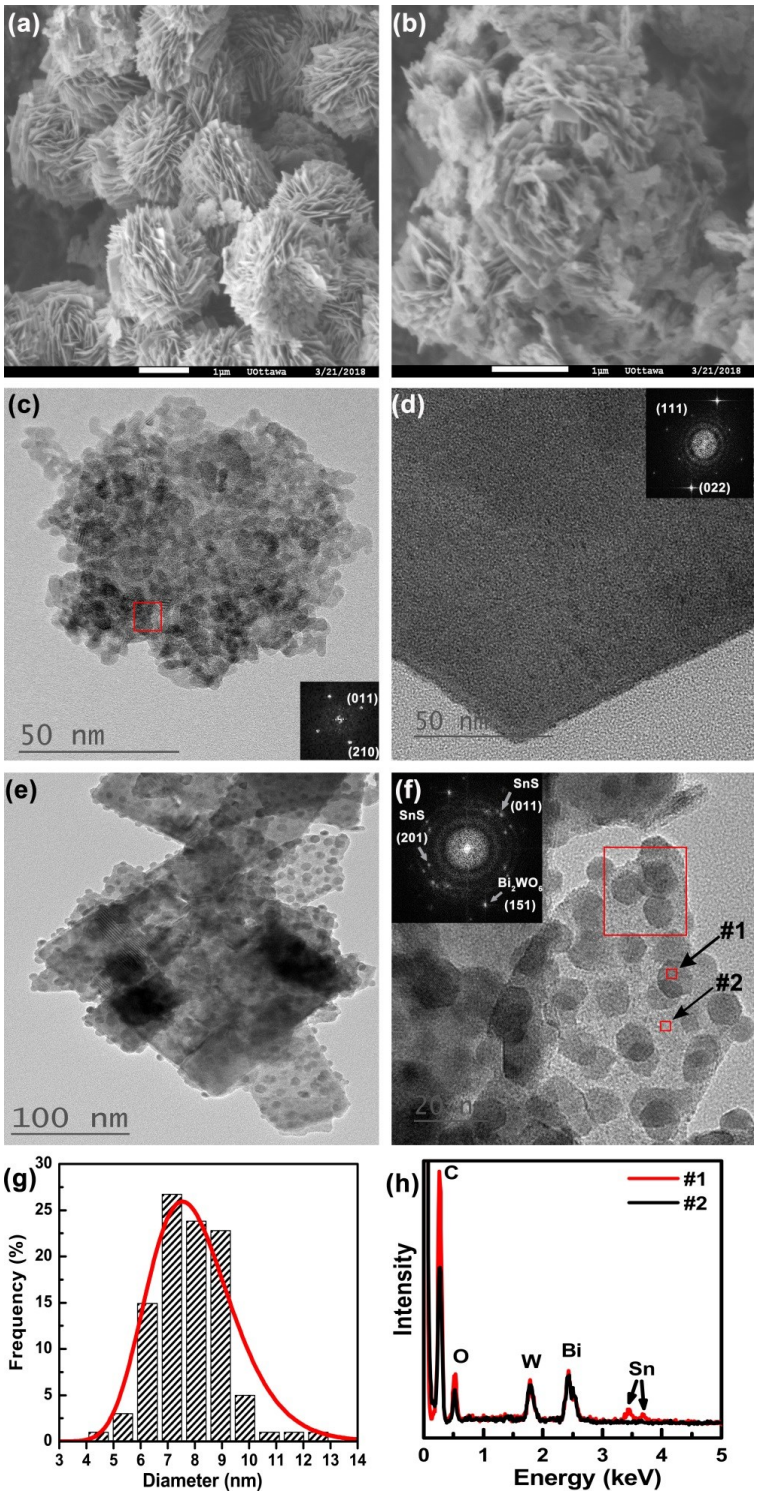

Figure 6.3. SEM images of (a) Bi_2WO_6 and (b) 0.50 SB; TEM images of (c) SnS, (d) Bi_2WO_6, and 0.50 SB in (e) low and (f) high magnification (the insets showing the FFT patterns obtained from the corresponding images); (g) size distribution of SnS nanoplates measured from Fig. 6.3f; and (h) EDS spectra of two sites shown in Fig. 6.3f.

6.3.2 Crystal structure and surface composition

The XRD patterns of Bi_2WO_6, SnS and SnS-Bi_2WO_6 composites were illustrated in Fig. 6.4. For pure Bi_2WO_6, all diffraction peaks agreed well with the orthorhombic Bi_2WO_6 (space group: *Aba2* (41), PDF card number: 01-073-1126) [32] and no impurity peak was found in the XRD pattern. The XRD diffraction peaks for SnS can be indexed to the orthorhombic SnS (space group: *Pnma* (62), PDF card number: 01-073-1859) [33], which is in good agreement with the previous TEM and FFT results. For various SnS-Bi_2WO_6 composites, no characteristic peaks of SnS were observed in the corresponding XRD patterns, which may be attributed to the low loading amount of SnS nanoplates ($\leq$ 1 wt%) [21]. The lattice parameters of Bi_2WO_6 and SnS-Bi_2WO_6 composites were calculated and summarized in Table 6.1. It can be seen that the introduction of SnS showed negligible influence to the crystal structure of Bi_2WO_6. In addition, no obvious peak shift can be observed in the XRD pattern of various SnS-Bi_2WO_6 composites (Fig. 6.4b), further indicating that the SnS nanoplates may be merely loaded on the surface of Bi_2WO_6 particles instead of covalently anchoring into its lattice [11, 34].

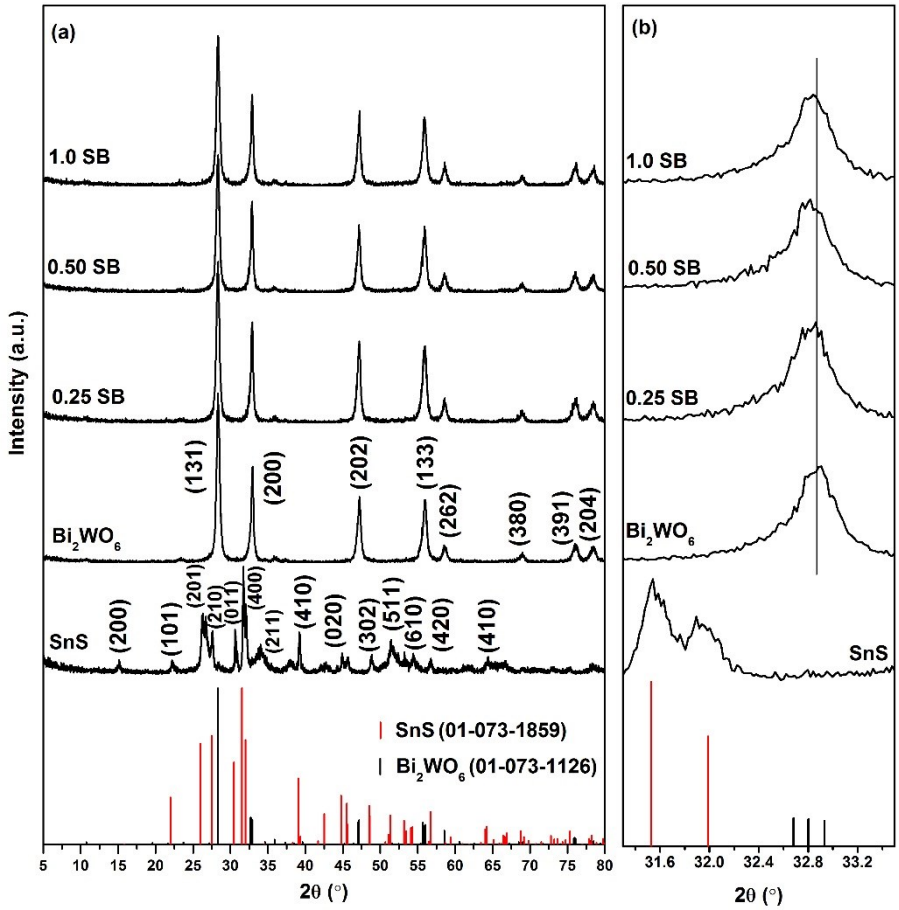

Figure 6.4. XRD patterns of SnS, Bi_2WO_6 and SnS-Bi_2WO_6 composites with various SnS loading quantities in the range of (a) 5-80° and (b) 31.3-33.5°.

Table 6.1. Summary of lattice parameters and volume of a lattice cell for Bi_2WO_6 and SnS-Bi_2WO_6 composites.

Composite	a (Å)	b (Å)	c (Å)	α = β = γ (°)	V (Å^3)
Bi_2WO_6	5.42	5.42	16.30	90.0	479
0.25 SB	5.43	5.45	16.12	90.0	477
0.50 SB	5.45	5.42	16.30	90.0	481
1.0 SB	5.45	5.47	16.37	90.0	487

The XPS technique was used to analyze the surface elemental compositions and chemical status of as-prepared samples. All data were calibrated with the banding energy of C 1s, which is fixed at 284.6 eV. In the survey spectra (Fig. 6.5) of SnS-Bi_2WO_6 composites, the characteristic peaks of Bi, W, O, and Sn can be detected, and no impurity peaks were found. The high-resolution Sn 3d and S 2p orbit scans of pure SnS and SnS-Bi_2WO_6 composites were obtained and compared to further confirm the introduction of SnS (Fig. 6.6). As shown in Fig. 6.6a and 6.6c, a set of spin-orbit doublet located at binding energy values of 494.9 eV and 486.3 eV can be ascribed to Sn $3d_{3/2}$ and Sn $3d_{5/2}$, respectively. This result indicated a bivalent oxidation state of Sn [20, 35]. As for S 2p orbit scans (Fig. 6.6b and 6.6d), peaks at 162.4 eV and 161.1eV is in accordance with the instance of S^{2-} [6]. The peak (164.2 eV) adjacent to S 2p doublet (Fig. 6.6b) may be attributed to the Bi $4f_{5/2}$ of Bi_2WO_6 [21]. Therefore, it can be confirmed that SnS nanoplates is fabricated and loaded on the surface of SnS-Bi_2WO_6 composites.

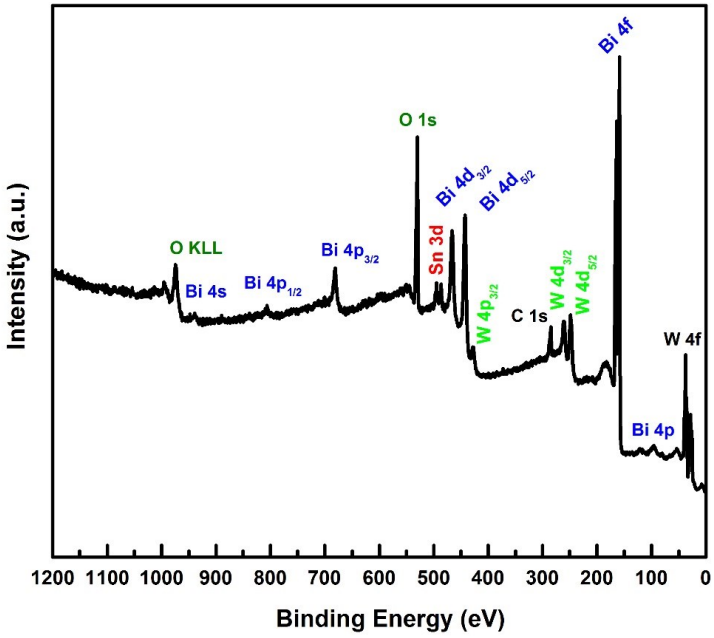

Figure 6.5. XPS survey spectrum of SnS-Bi_2WO_6 composites

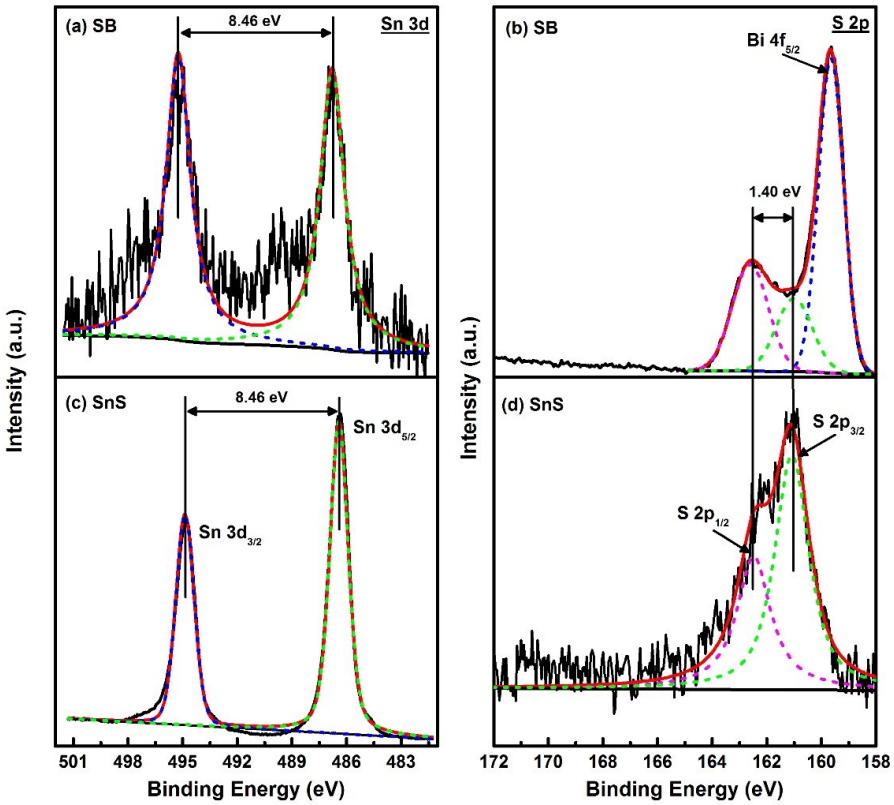

Figure 6.6. High-resolution orbital scans of Sn 3d for (a) SnS-Bi_2WO_6 composites and (c) pure SnS; and S 2p for (b) SnS-Bi_2WO_6 composites and (d) pure SnS.

6.3.3 N_2 sorption analysis

Nitrogen isotherms were tested to evaluate the adsorption-desorption property of prepared samples, the results were depicted in Figure 6.7. All isotherms are attributed to the type-IV physisorption isotherm. For type-IV isotherm, it is primarily resulted from the mesoporous materials, and a monolayer was firstly formed at low relative pressure and multilayer adsorption occurred at high relative pressure. For both isotherms at high relative pressure, no plateau was observed, which indicates that the capillary condensation did not occur on the surface of macropores. H3-type hysteresis loop was observed for each isotherm, which may due to the slit-shaped pores formed by aggregation of plate-like particles. This agrees well with the morphologies as observed in SEM images. Quantitively, the BET surface area as well as pore volumes were estimated and summarized in Table 6.2. The BET surface area was reduced from 28.4 to 21.3 m^2/g after loading SnS plates onto Bi_2WO_6, which may be resulted from the SnS plates blocked the slit-shaped pores. However, the volume of pores was slightly increased, which may due to the slit-shaped pores were formed between SnS and Bi2WO6. The decrease in specific surface area may reduce the photocatalytic activity, but compared to the improvement of the charge carriers' separation with the SnS modification, the influence of the decrease in specific surface area is negligible for the overall photocatalytic activity.

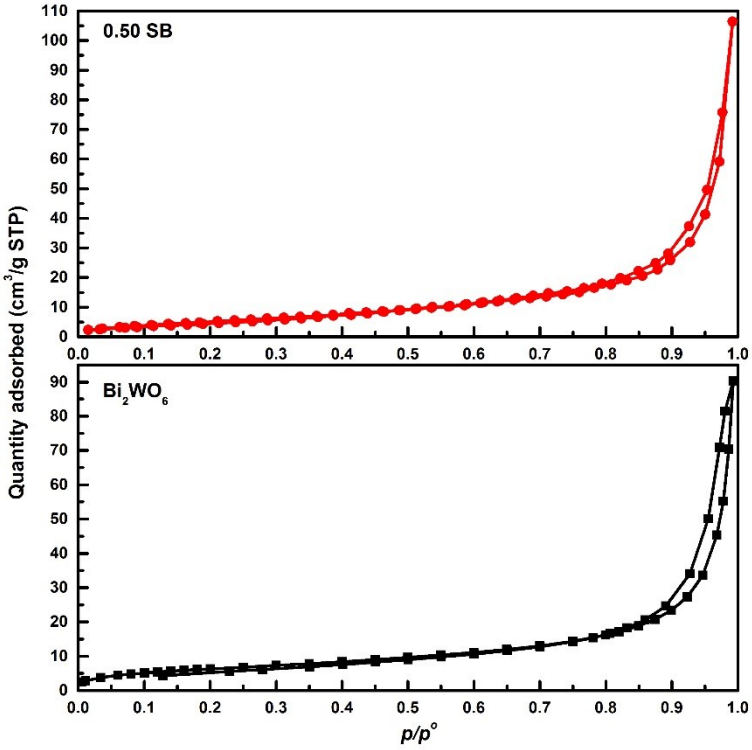

Figure 6.7. N_2 sorption isotherms for Bi_2WO_6 and 0.50 SB composite.

Table 6.2. Specific surface area and pore volume of prepared sample.

Sample	S_{BET} (m^2/g)	Pore volume (cm^3/g)
Bi_2WO_6	28.4	0.14
0.50 SB	21.3	0.17

6.3.3 Optical Properties

Optical properties of Bi_2WO_6, SnS and SnS-Bi_2WO_6 composites were measured by DRS and depicted in Fig. 6.8a and 6.8b. All samples showed light adsorption within the scope of ultraviolet-vis spectrum. The adsorption edge of Bi_2WO_6 is around 422 nm, while pure SnS displayed stronger and wider light adsorption than pure Bi_2WO_6 over the range of 200-900 nm. As a result, the light adsorption capacity of SnS-Bi_2WO_6 composites was slightly

increased compared with pure Bi_2WO_6 across the entire spectrum. Moreover, the adsorption intensity was gradually boosted in the region over 450 nm when the loading amount of SnS was increased. These results indicated that the as-prepared SnS-Bi_2WO_6 composites can be used as visible light-responsive photocatalysts with enhanced photocatalytic activity. The bandgap energy (E_g) of as-prepared samples can be calculated by the following equation (Equation 1) [22]:

$$\alpha h\upsilon = K\left(h\upsilon - E_g\right)^{\frac{n}{2}} \quad \textbf{\textit{Equation 1}}$$

Where α, h, v, K, E_g, and n represent the adsorption coefficient, Plank's constant, light frequency, a constant for semiconductor (usually equal to 1), bandgap energy, and a constant related to the electronic transition type of the semiconductor (direct transition: $n = 1$; indirect transition: $n = 4$), respectively. According to the previous reports, the values of n for SnS and Bi_2WO_6 are 4 and 1, respectively [11, 36]. The corresponding Tauc plots are shown in Fig. 6.8b. Therefore, the bandgap energy of pure SnS and Bi_2WO_6 were determined to be around 1.42 and 2.82 eV, respectively.

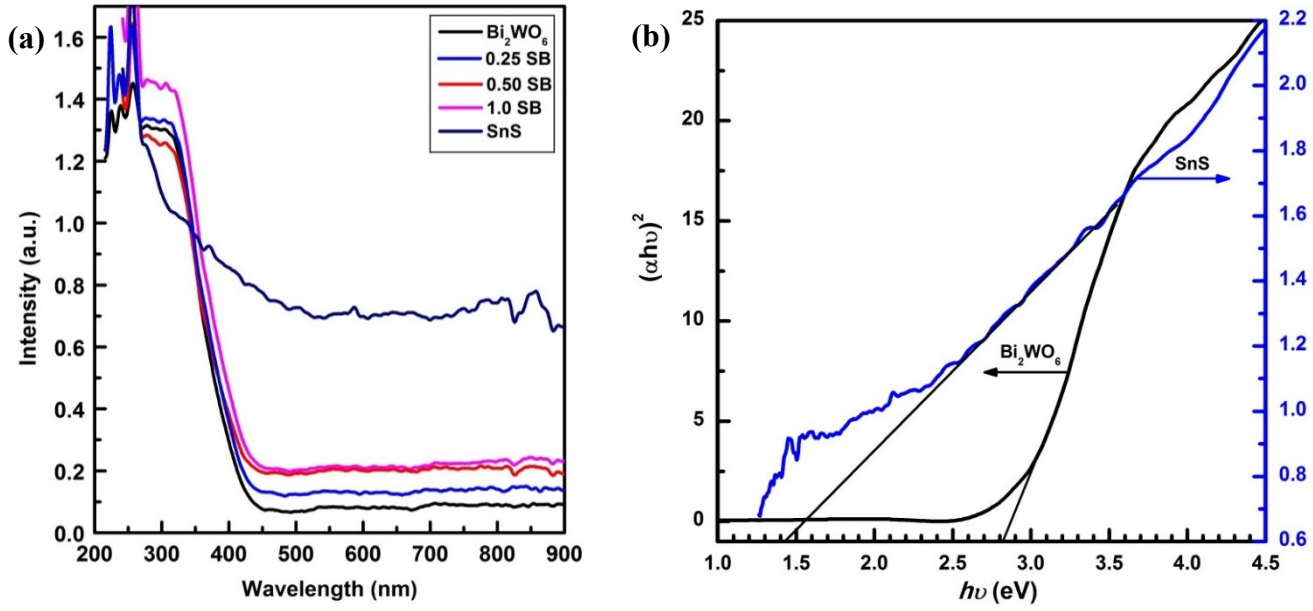

Figure 6.8. (a) UV-Vis diffused reflectance spectra of prepared samples; and (b) the $(\alpha hv)^2$ and $(\alpha hv)^{1/2}$ plots as a function of the photo energy (hv).

6.3.4 Energy band structure analysis

The band structure as well as total/ partial density of states of Bi_2WO_6 and SnS were simulated based on density functional theory (DFT), and were depicted in Fig. 6.9 and 6.10, respectively. The top of valence band for both simulations was fixed at 0.00 eV. Band gap values for Bi_2WO_6 and SnS can be measured as 1.915 and 1.815 eV, respectively (Fig. 6.9). Both band gaps were narrower than those measured using DRS, which may be due to the limitations of simulation [37]. However, the calculated band gaps indicate that both Bi_2WO_6 and SnS are visible-light-responsive. As shown in Fig. 6.10, the top of the valence bands for Bi_2WO_6 and SnS were separately composed of Bi 6s and O 2p, and S 3p, Sn 5s and Sn 5p hybrid orbitals, while the bottom of their conduction bands were composed of W 5d and Sn 5p orbitals, respectively. It should also be noted that the correlation between

the effective mass of electrons or holes and the curvature of the bands can be simply described by Equation 2 [38, 39]:

$$m^* = \frac{\hbar}{\frac{d^2 E_\kappa}{d\kappa^2}} \qquad \textit{Equation 2}$$

$$\frac{m_e^*}{m_h^*} = \left| \frac{\left. \frac{d^2 E_\kappa}{d\kappa^2} \right|_h}{\left. \frac{d^2 E_\kappa}{d\kappa^2} \right|_e} \right| \qquad \textit{Equation 3}$$

where m^* is the effective mass of the electrons or holes, κ is the wave vector, and $E\kappa$ is the energy corresponding to the wave vector κ. A higher effective mass of the charge carrier implies a lower mobility of the charge carrier. The relative ratio of effective mass between electrons on conduction band minimum (CBM) and holes on valence band maximum (VBM) can be obtained via Equation 3. The values of the second-order term of $E\kappa$ for electrons on CBM and holes on VBM and the absolute ratio are calculated using the top of the valence band and the bottom of the conduction band (shown in Fig. 6.11) and shown in Table 6.3. It reveals that, for Bi_2WO_6, mobility of the electron is similar to that of the hole. This characteristic is not beneficial in the photogenerated charge carriers' separation on Bi_2WO_6, and possibly results in low photocatalytic efficiency. As for SnS, the mobility of electrons is far lower compared to holes, which suggests that SnS may be promising as a modifier. Furthermore, as shown in Fig. 6.11, direct and indirect band transitions for Bi_2WO_6 and SnS were separately observed. The processes of photogenerated carriers' recombination were also proposed in Fig. 6.11. Specifically, activated electrons on the conduction band may return to the valence band to recombine with the holes. The

difference in energy between electron on the conduction band and valence band will be released as photons. This process takes place only when it follows the transition selection rule of momentum conservation, as illustrated in Equation 4,

$$\hbar \quad \hbar \quad \hbar \qquad \textbf{\textit{Equation 4}}$$

where $\hbar$ is the reduced Planck constant, k_e' and k_e are electron wave vectors at the top of the valence band and bottom of the conduction band, respectively, and q_{photon} is the wave vector of the assisted photon [40]. For direct band-gap transition, $k_e' = k_e$, whereas $k_e' \neq k_e$ for indirect band-gap transition. For Bi_2WO_6 (Fig. 6.11a), activated electrons on the conduction band are easily returned to the valence band with releasing photons. However, for SnS, the activated electrons on the conduction band cannot directly come back to the valence band as shown in Fig. 6.11b. Instead, assistance by additional photons is needed for the transfer within an indirect band gap. As a result, the lifetime of photogenerated electrons and holes for SnS within an indirect band gap is longer than that for Bi_2WO_6 within a direct band gap, thus increasing the diffusion length and reaction time of the photogenerated charge carriers. Correspondingly, photocatalytic activity of materials with indirect band-gap transitions exhibited higher activity in photocatalysis compared to those with direct band-gap transitions, further suggesting SnS may be an excellent modifier [41].

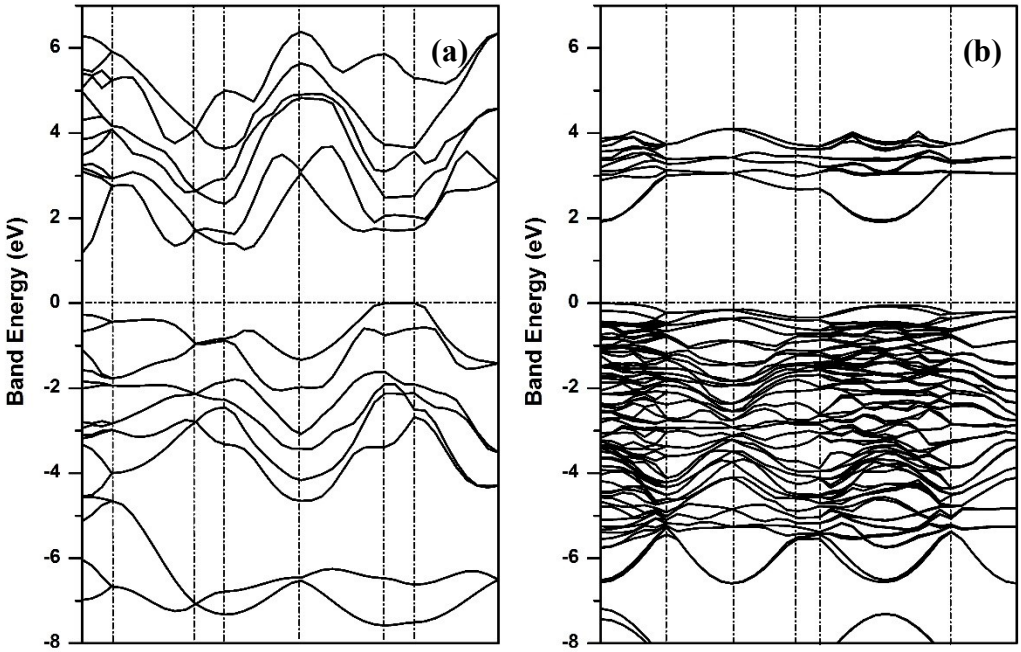

Figure 6.9. Band structure of (a) SnS and (b) Bi_2WO_6.

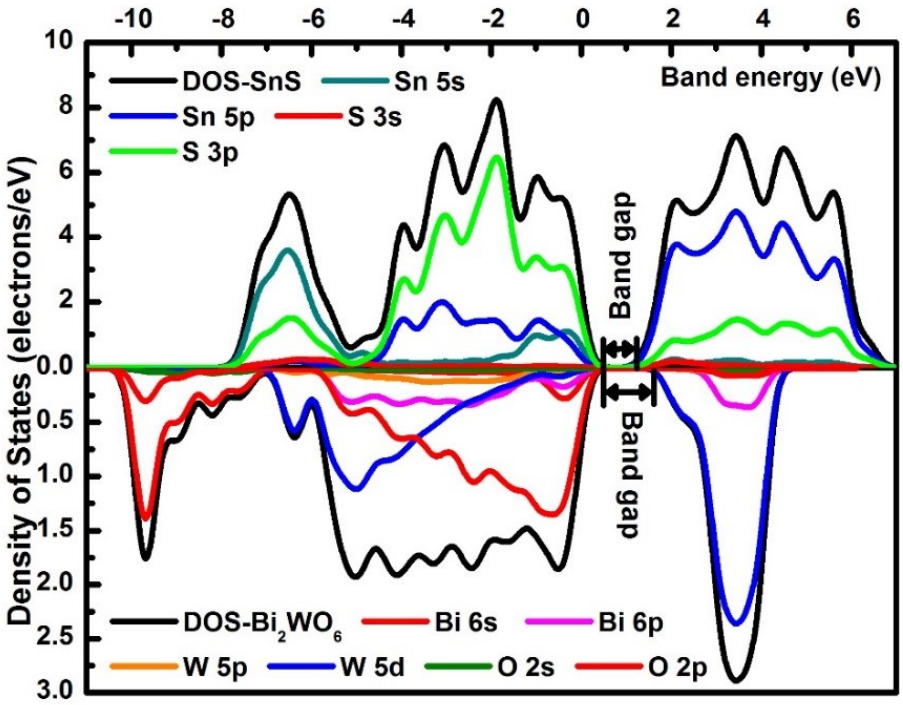

Figure 6.10. Density of states for SnS and Bi_2WO_6.

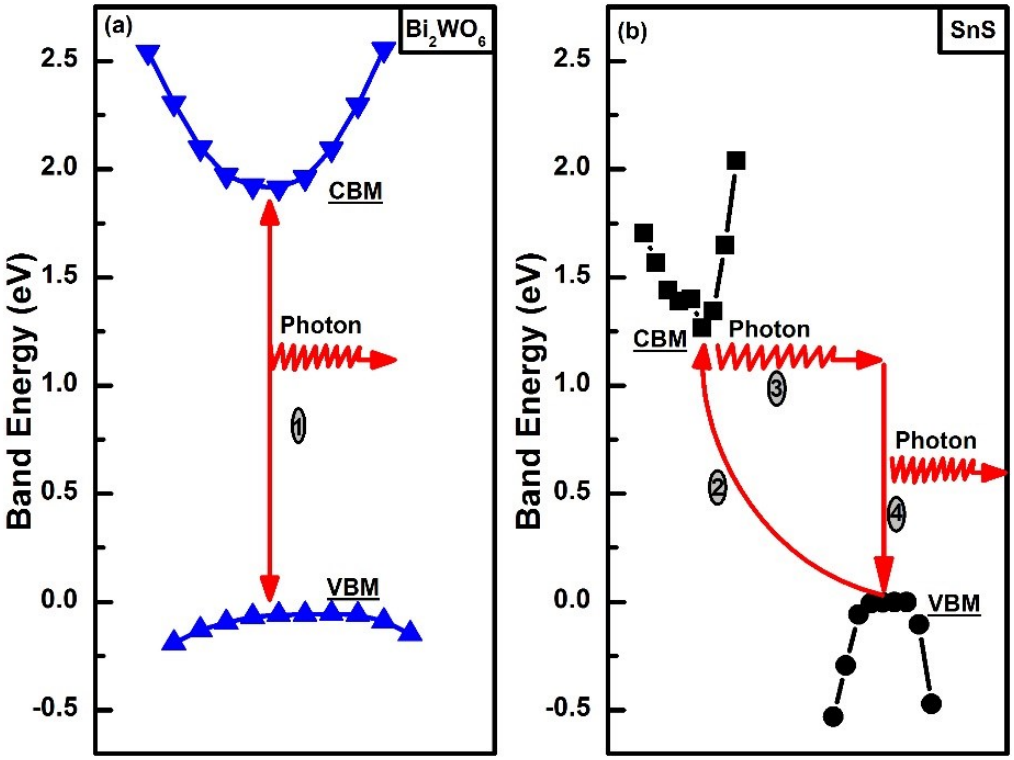

Figure 6.11. Proposed transition of photogenerated charge carriers on Bi_2WO_6 and SnS.

Table 6.3. Parameter values for Equation 2 and 3.

Parameter	$\left.\frac{d^2E_\kappa}{d\kappa^2}\right\|_h$	$\left.\frac{d^2E_\kappa}{d\kappa^2}\right\|_e$	$\lvert\frac{m_e^*}{m_h^*}\rvert$
Bi_2WO_6	-0.191	0.192	1.005
SnS	-0.108	0.010	0.093

6.3.4 Photocatalytic activity tests

The photocatalytic activities of prepared samples were evaluated by the photocatalytic degradation of RhB under visible light irradiation. As shown in Fig. 6.12, all samples reached the adsorption-desorption equilibrium in darkness within 30 min. According to Table 6.4, the adsorption capacity of pure SnS is more than 3-fold higher than that of

Bi_2WO_6. When coupling with SnS, the adsorption capacity of Bi_2WO_6 is greatly improved due to the good adsorption performance of SnS. Under illumination, RhB was further decomposed in the presence of Bi_2WO_6 and SnS-Bi_2WO_6 composites. In contrast, the photocatalytic activity of pure SnS is negligible. This may be resulted from the narrow bandgap of SnS, which could lead to fast charge recombination and low activity. Compared with pure SnS and Bi_2WO_6, a positive synergetic effect is observed when coupling SnS with Bi_2WO_6. The enhanced photocatalytic activity may be ascribed to the formation of the heterostructure between the surface of SnS and Bi_2WO_6, which could facilitate the migration and separation of photogenerated charge carriers.

The kinetic study of RhB degradation in the presence of various photocatalysts was also performed. The pseudo-first-order reaction model was used to fit the experimental data and expressed as Equation 5 [42]:

$$\ln\left(\frac{c_0}{c_t}\right) = k't \qquad \textit{Equation 5}$$

Where c_0, c_t, k' and t represent the initial concentration of RhB, concentration of RhB at reaction time t, pseudo-first-order reaction rate constant and time, respectively. The kinetic parameters were calculated and listed in Table 6.4. The value of rate constant (k') can be used to quantitatively analyze the reaction rate for each process. It can be observed that the rate constant of SnS-Bi_2WO_6 composites were significantly improved compared with that of pure SnS (k' = 0.001 min^{-1}) and Bi_2WO_6 (k' = 0.018 min^{-1}). In addition, the value of k' was enhanced as the loading amount of SnS was increased and reached a highest value of 0.105 min^{-1} when the SnS loading amount was 0.50 wt%. However, further increasing the

amount of SnS hindered the improvement of photocatalytic activity. This may be resulted from the light blocking effect of materials with dark colors, which could prevent light penetration into the reaction mixture [43, 44]. In addition, excessive SnS may block the mesopores of Bi_2WO_6, leading to the decrease in surface area, pore volume and reactive sites [21, 44].

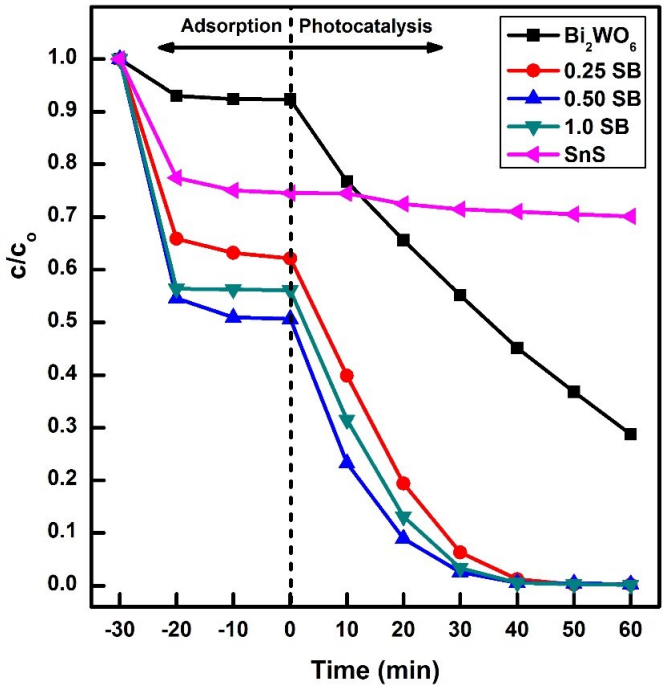

Figure 6.12. Photocatalytic degradation performance of prepared samples under visible light irradiation.

Table 6.4. Equilibrium adsorption capacities and kinetic parameters of pseudo first-order model for different samples

Composite	q_e ($mg_{RhB}/g_{cat.}$)	k' (min^{-1})	R^2
Bi_2WO_6	0.692	0.018	0.998
SnS	2.338	0.001	0.932
0.25 SB	3.460	0.098	0.917
0.50 SB	4.441	0.105	0.975
1.0 SB	4.119	0.101	0.960

The time-dependent spectral changes of RhB during the photocatalytic degradation process were depicted in Fig. 6.13. The intensity decrease of major peaks with a concomitant wavelength blue shift revealed that the step-by step N-deethylation process and the destruction of the RhB chromophore ring structure were occurred during the degradation process [45]. In the first 50 min, the characteristic peaks at 539, 522, 510 and 498 nm represent intermediates of the *N*-demethylation process, which are *N,N,N'*-triethyl-rhodamine, *N,N'*-diethyl-rhodamine, *N*-ethyl-rhodamine and rhodamine, respectively [46]. Subsequently, no characteristic peak of rhodamine can be found in the spectra due to the further cleavage of the aromatic ring structure. This phenomenon indicated that RhB may be degraded into small molecules such as CO_2 and H_2O in the presence of SnS-Bi_2WO_6 composites (0.50 SB) under visible light [47, 48].

Reusability of as-prepared sample was evaluated by recycling use of the 0.50 SB composite for five runs in the decomposition of RhB under visible light. The concentration profiles of RhB in the solution were shown in Fig. 6.14. Complete removal of RhB can be obtained in 60 for these five runs. A negligible difference among these five profiles can be observed, indicating the high stability of SnS-Bi_2WO_6 composites in the photocatalytic organic degradation process. The slight decrease in the RhB conversion may be resulted from some refractory intermediates adsorbed on the surface of the catalysts, reducing the number of reactive sites in the following run. The high reusability of SnS-Bi_2WO_6 composites make them an attractive candidate for use as visible light-induced photocatalysts.

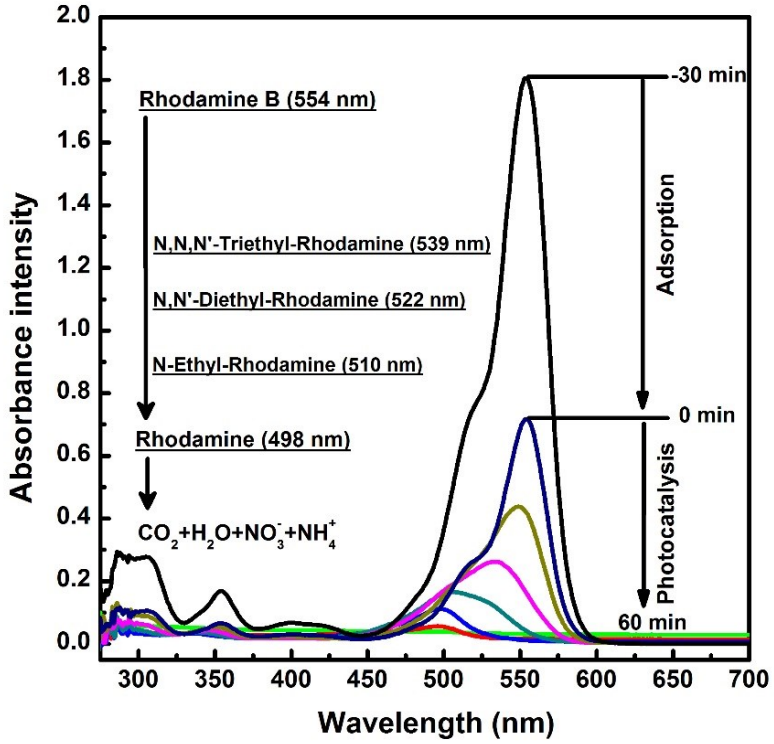

Figure 6.13. Time-dependent UV-Vis spectral of RhB during photocatalytic degradation process

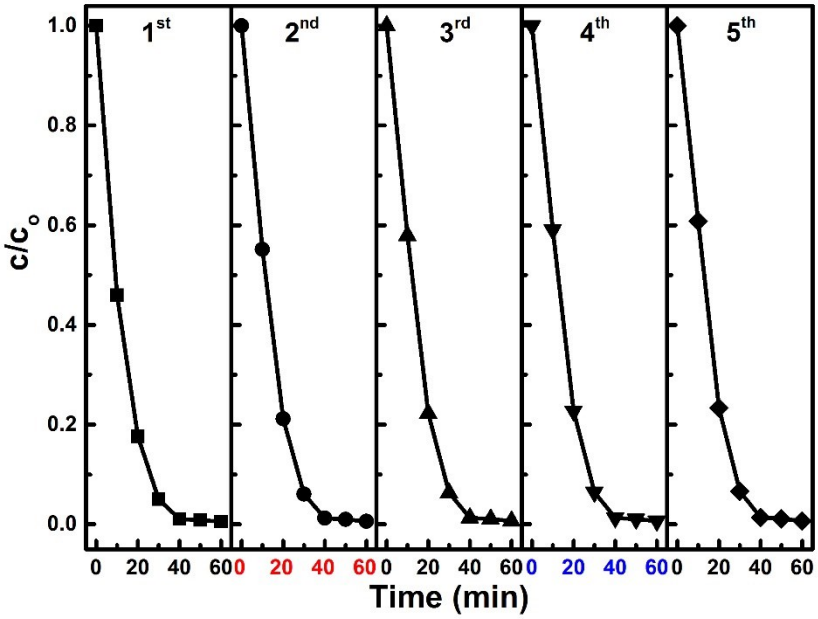

Figure 6.14. Recycling tests of 0.50 SB sample in the degradation of RhB under visible light.

The disinfection effects of all samples toward E. coli, a common waterborne pathogenic microorganism, were also evaluated. As shown in Fig. 6.15, no evident loss of cell survival ratio was observed in the dark, indicating negligible cytotoxicity of the photocatalyst (0.50 SB). For the light control group (photolysis), the reduction of survival ratio represented the disinfection effect without any photocatalysis, absorption or cytotoxicity of the photocatalysts. In comparison with other photocatalysts, the photocatalytic disinfection effect of pure SnS was relatively low due to its narrow bandgap and low charge separation efficiency. However, the disinfection effect of Bi_2WO_6 and SnS-Bi_2WO_6 composites were largely improved with visible light irradiation compared with the dark control group. After illumination for 60 min, the survival ratios in the presence of Bi_2WO_6 and SnS-Bi_2WO_6 composites were 50% and 32%, respectively. These results are consistent with the photocatalytic performance of RhB degradation. The enhanced photocatalytic disinfection ability of SnS-Bi_2WO_6 composites may be attributed to the formation of the heterostructure, which favors charge separation and the generation of reactive oxidative species (ROS) [49]. It is reported that the ROS such as h^+, •OH, and $•O_2^-$ could act on the surface of cells to degrade some component of bacterial cell membrane (*i.e.* polyunsaturated phospholipids) [50]. The cell rupture could cause function loss of the bacteria and eventually lead to cell death. Therefore, the synergetic effect between SnS and Bi_2WO_6 facilitates the separation of photogenerated charge carriers and thus improves the disinfection performance.

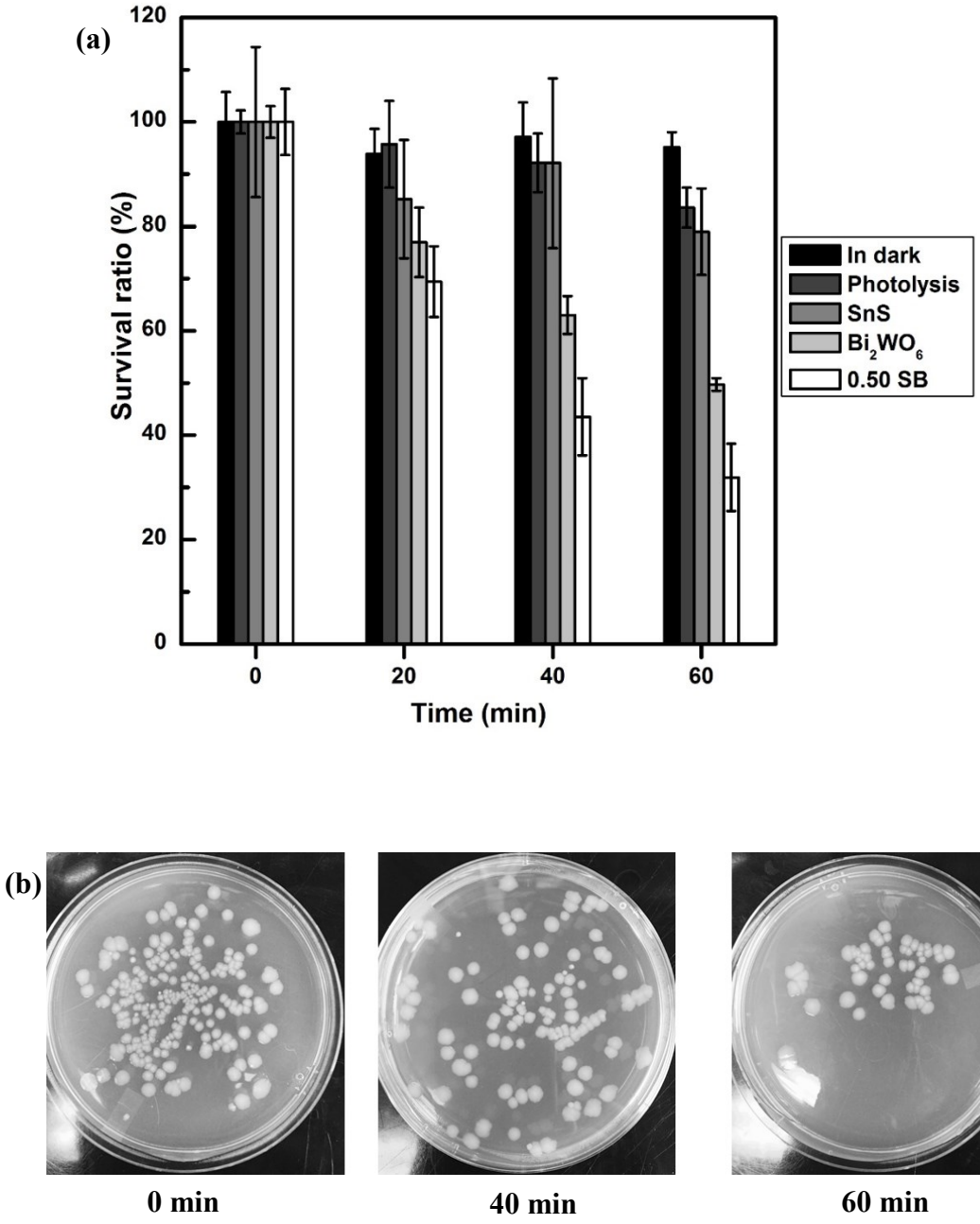

Figure 6.15. (a) Photocatalytic disinfection effect of different samples; and (b) photos of E. coli colonies which are cultured by the samples collected at different time during photocatalytic disinfection process.

6.3.5 Mechanism exploration

6.3.5.1 Roles of reactive species

Investigating the roles of each reactive species is important to the understanding of photocatalytic mechanisms. As a result, IPA, TEOA and N_2 bubbling were added to the reaction system to explore the roles of •OH, holes and $•O^{2-}$, respectively. As demonstrated in Fig. 6.16, almost all RhB can be removed within 40 min in the absence of scavengers. Different quenching effects can be founded after adding various scavengers. IPA only exhibited little influence on the photocatalytic activity; in contrast, a dramatic inhibiting effect can be observed after the addition of TEOA. This phenomenon indicated that the photogenerated holes played a dominant role in the photocatalytic degradation process and may directly oxidize pollutants instead of forming •OH. When N_2 bubbling was applied, only 31% RhB was removed within 40 min. all these results revealed that holes and $•O^{2-}$ are the main oxidative species in the photocatalytic degradation process.

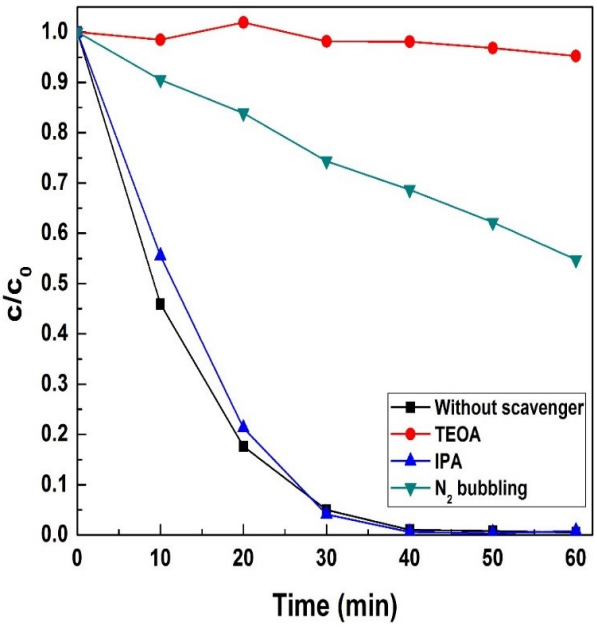

Figure 6.16. Photocatalytic degradation performance of 0.50 SB in the presence of different scavengers.

6.3.5.2 Electrochemical analysis

Photoelectrochemical properties for Bi_2WO_6 and 0.50 SB electrodes were measured in a 0.5 mol/L Na_2SO_4 solution, and results were shown in Fig. 6.17. Electrochemical impedance spectroscopy (EIS) was employed for the explorations of both the charge transfer properties in the electrolyte and electrode interface and charge separation efficiency. EIS Nyquist plots were depicted in Fig. 6.17a, and only one arc was observed for each plot, indicating that both photocatalytic processes were just simple electrode reactions. In addition, a smaller arc radius correlated to higher charge carriers' separation. To quantitively evaluate the charge carriers' separation efficiency, an equivalent circuit was shown in the inset of Fig. 6.17a. Specifically, R_s, R_{ct} and *CPE* represent resistance of the solution, resistance to electron transfer on the electrode, and constant phase element, respectively. The fitted values for these EIS parameters were calculated and shown in Table 6.5. It can be found the values for both R_s and *CPE* were negligibly different between these two processes, as a same testing system was applied. R_{ct} for 0.50 SB electrode was about half of that for Bi_2WO_6 electrode. This result indicates with SnS loading, the charge carriers' separation efficiency was greatly improved. Furthermore, Bode-phase spectra were shown in Fig. 6.17b. The characteristic frequency peak (f_{min}) of Bi_2WO_6 shifted from 0.464 to 0.215 Hz after being decorated with SnS. Using Equation 6, the lifetime of injected electrons (τ) can be estimated, and the calculated results were shown in Table 6.5. The enhancement in the lifetime of injected electrons may be due to the suppressed recombination of photogenerated charge carriers. To further study the photoelectric response of Bi_2WO_6 and 0.50 SB under light on and off conditions, the transient photocurrent was tested in 0.5 mol/L Na_2SO_4 solution at 0.0 V *vs* SCE, and results were

shown in Fig. 17c. Uniform and fast photocurrent responses were observed for both electrodes, and the responses were reversible. Upon illumination, the photocurrent density on 0.50 SB electrode is approximately 4-fold higher than that on pure Bi_2WO_6 electrode. The apparent increase in photocurrent density may be resulted from suppressed recombination of photogenerated charge carriers, which further confirmed that the loading of SnS was in favor of improving the photocatalytic activity by suppressing the recombination of charge carriers.

Mott-Schottky (M-S) plots of Bi_2WO_6 and 0.50 SB electrodes in dark were shown in Fig. 6.17d. It can be found that both as-prepared Bi_2WO_6 and SnS are n-type semiconductors. Flat-band potential (E_{FB}) can be calculated using Equation 7, where C is the semiconductor space charge layer capacitance (cm^4/F^2), N_D is donor density (cm^{-3}), e is element charge (= 1.602×10^{-19}C), ε_0 is the vacuum permittivity (= 8.85×10^{-14} F/cm), ε_r is the dielectric constant of the semiconductor (for Bi_2WO_6, $\varepsilon_r \approx 50$ [51]), E is the applied potential (V *vs* SCE), κ is Boltzmann constant (= 8.617×10^{-5} eV/K), and T represents temperature (= 293.15 K). The flat-band potential can be calculated from the intercept by extrapolating the linear part of the M-S plot as shown in Fig. 6.17d. Flat-band potentials for Bi_2WO_6 and 0.50 SB were shown in Table 6.5 and are equivalent to 0.219 and -0.161 V *vs* NHE (-0.025 V and -0.405 V *vs* SCE), respectively. The negative shift of the flat-band potential for Bi_2WO_6 after decoration with SnS may be due to the more negative flat-band potential for SnS (~ -0.381 V *vs* NHE). The donor density, N_D, is derived by the slope of the M-S plot and can be calculated via Equation 8 [52, 53]. The donor densities for Bi_2WO_6 and 0.50 SB were about 2.823×10^{20} cm^{-3} and 7.424×10^{20} cm^{-3}, respectively. It indicated that there

was a higher carrier density after loading SnS on Bi_2WO_6, which may be due to more defects being produced on SB composites, leading to a higher photocatalytic activity.

$$\tau = \frac{1}{2\pi f_{\min}} \qquad \textit{Equation 6}$$

$$\frac{1}{C^2} = \frac{2}{N_D e \varepsilon_r \varepsilon_0}\left(E - E_{FB} - \frac{\kappa T}{e}\right) \qquad \textit{Equation 7}$$

$$N_D = \frac{-2}{e\varepsilon_r\varepsilon_0}\left(\frac{dE}{d\frac{1}{C^2}}\right) \qquad \textit{Equation 8}$$

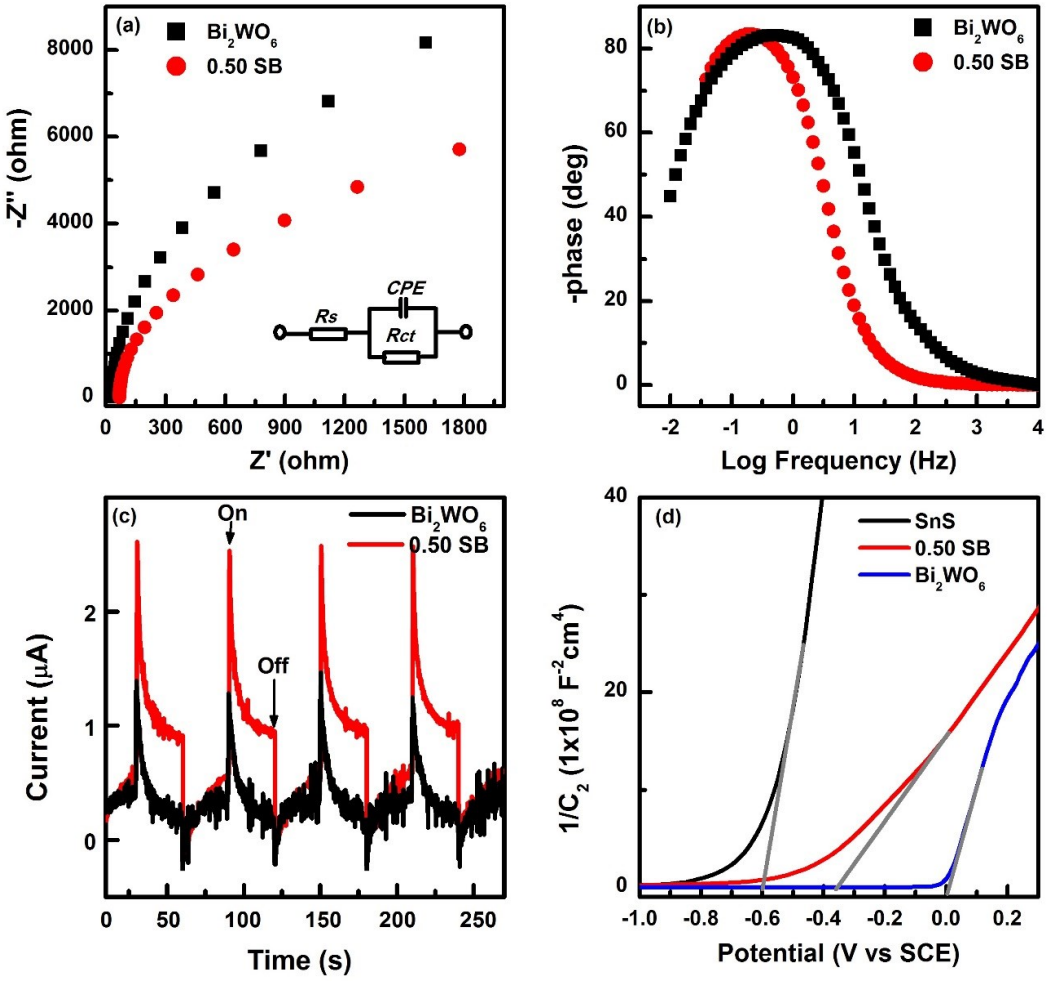

Figure 6.17. (a) EIS Nyquist plots, (b) Bode plot curves, (c) transient photocurrent response and (d) Mott-Schottky plots of Bi_2WO_6 and 0.50 SB electrodes.

Table 6.5. EIS fitting results, lifetime of photogenerated charge carriers, and band structure parameters for different electrodes.

Electrode	R_s (Ω)	R_{ct} (kΩ)	*CPE* (μF)	f_{min} (Hz)	τ (ms)	E_{FB} (V *vs* NHE)	N_D (cm^{-3})
Bi_2WO_6	47.74	44.10	235.8	0.464	343.2	0.219	2.823×10^{20}
0.50 SB	44.46	20.81	667.8	0.215	740.6	-0.161	7.424×10^{20}

6.3.5.3 Mechanism of photocatalytic reactions.

The band configuration could greatly impact the photocatalytic activity and mechanism in terms of redox capacity and recombination rate of photoinduced charge carriers [54]. To explore the band positions of prepared samples, the Mulliken electronegativity concept were used and expressed as (Equations 9 and 10) [7, 55]:

$$E_{CB} = \chi_P - E^e - 0.5E_g \qquad \textit{Equation 9}$$

$$E_{VB} = E_{CB} + E_g \qquad \textit{Equation 10}$$

Where E^e is the energy of free electrons on the hydrogen scale (~4.5 eV); E_g is the band gap energy of semiconductor; and χ_p is the absolute electronegativity of the semiconductor which can be determined by the geometric mean of the electronegativities of the constituent atoms. The calculated conduction band potential (E_{CB}) and valence band potential (E_{VB}) were summarized in Table 6.6. The corresponding band positions and possible photocatalytic mechanism were depicted in Fig. 6.18. Although the band alignments of SnS-Bi_2WO_6 composites are consistent with type-II heterojunction, the type II electron-hole pairs separation and migration is not proposed to occur because the electrons on the conduction band of Bi_2WO_6 is not negative enough to produce $\bullet O^{2-}$ or other hydro oxygen

radicals (*e.g.* $\bullet HO_2$ and H_2O_2) [56, 57]. However, in the aforementioned quenching experiments, oxidizing agents may be produced from oxygen. Hence, a more efficient Z-scheme heterojunction may be fabricated in this work. Upon illumination, both SnS and Bi_2WO_6 can be activated and generate electron-hole pairs. The electrons on the CB of Bi_2WO_6 and holes on the VB can be recombined, and thus holes and electrons could eventually accumulate on the VB of Bi_2WO_6 and CB of SnS, respectively. This phenomenon agreed well with the previous reports [44, 58]. By this means, electrons and holes can be spatially separated without compromising their redox potentials. As a result, holes on the VB of Bi_2WO_6 could directly oxidize organic pollutants or inactive cells. A small fraction of holes may also oxidize H_2O to form $\bullet OH$, which could also participate in the photocatalytic process. Electrons on the conduction band of SnS were not capable of reducing O_2 to produce $\bullet O_2^-$, as the position of conduction band bottom is more positive compared to the redox potential of $O_2/\bullet O_2^-$. While electrons left on the CB of SnS could reduce the adsorbed O_2 to $\bullet HO_2$, and H_2O_2, which could further degrade organic pollutants or damage cells.

Table 6.6. Bandgap energy and band positions of Bi_2WO_6 and SnS

Composite	E_g (eV)	χ (eV)	E_{CB} (eV)	E_{VB} (eV)
Bi_2WO_6	2.82	6.20	0.29	3.11
SnS	1.42	5.13	-0.08	1.34

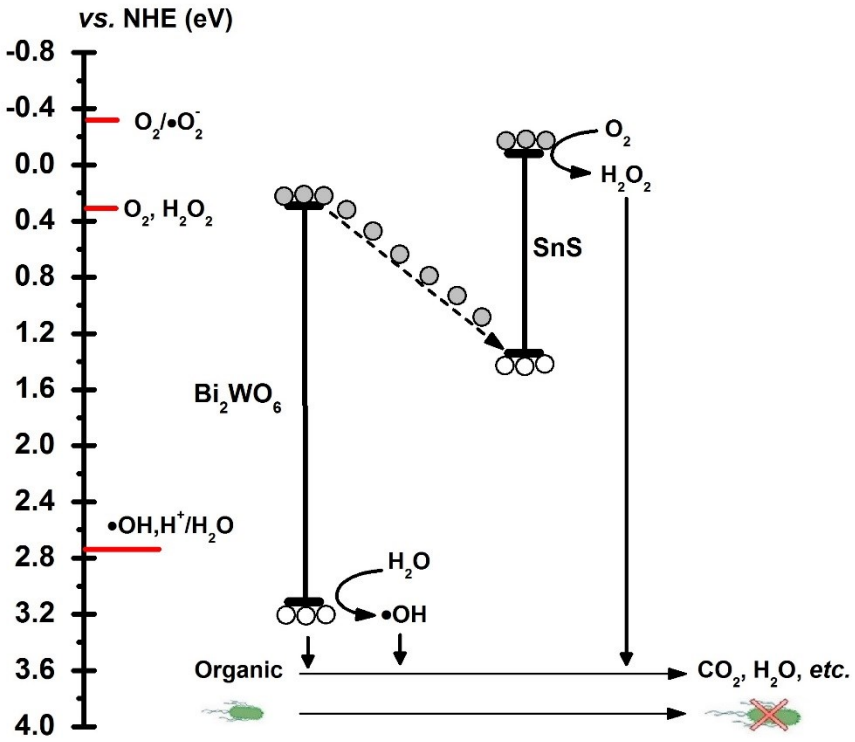

Figure 6.18. Proposed photocatalytic mechanisms of SnS-Bi_2WO_6 composites and possible photogenerated electron-hole pair transfer and separation process.

6.4 Conclusions

SnS nanoplates were successfully deposited on the surface of Bi_2WO_6 via a simple bath sonication method. According to the quenching experiment, a possible Z-scheme heterostructure may be fabricated and the main oxidative species in the photocatalytic degradation process were holes and hydro oxygen radicals (*e.g.* $•HO_2$ and H_2O_2). Compared with pure SnS and Bi_2WO_6, SnS-Bi_2WO_6 hybrid composites exhibited enhanced photocatalytic activity in both dye degradation and disinfection experiments. The enhanced photocatalytic activity may be attributed to the efficient Z-scheme system, which could facilitate charge separation without compromising redox capacity. In addition, the narrow band gap of SnS may also improve light harvesting and thus further promote

photocatalytic performance of SnS-Bi_2WO_6 composites. The good photocatalytic performance indicated that the as-prepared heterostructure could be a promising candidate for wastewater treatment.

References

[1] J. Chao, Z. Wang, X. Xu, Q. Xiang, W. Song, G. Chen, J. Hu, D. Chen, Tin sulfide nanoribbons as high performance photoelectrochemical cells, flexible photodetectors and visible-light-driven photocatalysts, RSC Advances, 3 (2013) 2746-2753.

[2] R.W. Miles, O.E. Ogah, G. Zoppi, I. Forbes, Thermally evaporated thin films of SnS for application in solar cell devices, Thin Solid Films, 517 (2009) 4702-4705.

[3] D.D. Vaughn, O.D. Hentz, S. Chen, D. Wang, R.E. Schaak, Formation of SnS nanoflowers for lithium ion batteries, Chem. Commun., 48 (2012) 5608-5610.

[4] J. Chao, Z. Xie, X. Duan, Y. Dong, Z. Wang, J. Xu, B. Liang, B. Shan, J. Ye, D. Chen, G. Shen, Visible-light-driven photocatalytic and photoelectrochemical properties of porous SnSx(x = 1,2) architectures, CrystEngComm, 14 (2012) 3163-3168.

[5] A.J. Biacchi, D.D. Vaughn, R.E. Schaak, Synthesis and Crystallographic Analysis of Shape-Controlled SnS Nanocrystal Photocatalysts: Evidence for a Pseudotetragonal Structural Modification, J. Am. Chem. Soc., 135 (2013) 11634-11644.

[6] X. Hu, G. Song, W. Li, Y. Peng, L. Jiang, Y. Xue, Q. Liu, Z. Chen, J. Hu, Phase-controlled synthesis and photocatalytic properties of SnS, SnS_2 and SnS/SnS_2 heterostructure nanocrystals, Mater. Res. Bull., 48 (2013) 2325-2332.

[7] K. Yao, J. Li, S. Shan, Q. Jia, One-step synthesis of urchinlike SnS/SnS_2

heterostructures with superior visible-light photocatalytic performance, Catal. Commun., 101 (2017) 51-56.

[8] L. Wang, H. Zhai, G. Jin, X. Li, C. Dong, H. Zhang, B. Yang, H. Xie, H. Sun, 3D porous ZnO-SnS p-n heterojunction for visible light driven photocatalysis, PCCP, 19 (2017) 16576-16585.

[9] H. An, Y. Du, T. Wang, C. Wang, W. Hao, J. Zhang, Photocatalytic properties of BiOX (X = Cl, Br, and I), Rare Metals, 27 (2008) 243-250.

[10] S. Li, S. Hu, W. Jiang, Y. Liu, J. Liu, Z. Wang, Facile synthesis of flower-like Ag_3VO_4/Bi_2WO_6 heterojunction with enhanced visible-light photocatalytic activity, J Colloid Interf Sci, 501 (2017) 156-163.

[11] X. Meng, Z. Zhang, Ag/AgCl Loaded Bi_2WO_6 Composite: A Plasmonic Z-Scheme Visible Light-Responsive Photocatalyst, International Journal of Photoenergy, 2016 (2016) 11.

[12] X. Meng, Z. Zhang, Facile synthesis of $BiOBr/Bi_2WO_6$ heterojunction semiconductors with high visible-light-driven photocatalytic activity, Journal of Photochemistry and Photobiology A: Chemistry, 310 (2015) 33-44.

[13] X. Meng, H. Qin, Z. Zhang, New insight into the enhanced visible light-driven photocatalytic activity of $Pd/PdCl_2$-doped Bi_2WO_6 photocatalysts, J Colloid Interf Sci, 513 (2018) 877-890.

[14] X. Hu, X. Meng, Z. Zhang, Synthesis and Characterization of Graphene Oxide-Modified Bi_2WO_6 and Its Use as Photocatalyst, International Journal of Photoenergy, 2016 (2016) 8.

[15] X. Meng, Z. Zhang, Synthesis and characterization of plasmonic and magnetically separable Ag/AgCl-Bi_2WO_6@ Fe_3O_4@SiO_2 core-shell composites for visible light-induced water detoxification, J Colloid Interf Sci, 485 (2017) 296-307.

[16] X. Meng, Z. Zhang, Synthesis, Analysis, and Testing of BiOBr-Bi_2WO_6 Photocatalytic Heterojunction Semiconductors, International Journal of Photoenergy, 2015 (2015) 12.

[17] C. Zhang, Y. Zhu, Synthesis of Square Bi_2WO_6 Nanoplates as High-Activity Visible-Light-Driven Photocatalysts, Chem. Mater., 17 (2005) 3537-3545.

[18] Z. Lisha, W. Wenzhong, Z. Lin, X. Haolan, Bi_2WO_6 Nano- and Microstructures: Shape Control and Associated Visible-Light-Driven Photocatalytic Activities, Small, 3 (2007) 1618-1625.

[19] Y. Huang, Z. Ai, W. Ho, M. Chen, S. Lee, Ultrasonic Spray Pyrolysis Synthesis of Porous Bi_2WO_6 Microspheres and Their Visible-Light-Induced Photocatalytic Removal of NO, The Journal of Physical Chemistry C, 114 (2010) 6342-6349.

[20] R. Tang, H. Su, Y. Sun, X. Zhang, L. Li, C. Liu, S. Zeng, D. Sun, Enhanced photocatalytic performance in Bi_2WO_6/SnS heterostructures: Facile synthesis, influencing factors and mechanism of the photocatalytic process, J Colloid Interf Sci, 466 (2016) 388-399.

[21] X. Meng, Z. Li, H. Zeng, J. Chen, Z. Zhang, MoS_2 quantum dots-interspersed Bi_2WO_6 heterostructures for visible light-induced detoxification and disinfection, Applied Catalysis B: Environmental, 210 (2017) 160-172.

[22] X. Meng, Z. Zhang, Facile synthesis of BiOBr/Bi_2WO_6 heterojunction semiconductors with high visible-light-driven photocatalytic activity, J. Photochem. Photobiol. A: Chem.,

310 (2015) 33-44.

[23] K. Chang, Z. Wang, G. Huang, H. Li, W. Chen, J.Y. Lee, Few-layer SnS_2/graphene hybrid with exceptional electrochemical performance as lithium-ion battery anode, J Power Sources, 201 (2012) 259-266.

[24] A.-G. Rincón, C. Pulgarin, Effect of pH, inorganic ions, organic matter and H_2O_2 on E. coli K12 photocatalytic inactivation by TiO_2: Implications in solar water disinfection, Applied Catalysis B: Environmental, 51 (2004) 283-302.

[25] J. Gamage McEvoy, D.A. Bilodeau, W. Cui, Z. Zhang, Visible-light-driven inactivation of Escherichia coli K-12 using an Ag/AgCl–activated carbon composite photocatalyst, J. Photochem. Photobiol. A: Chem., 267 (2013) 25-34.

[26] G. Kresse, J. Furthmüller, Efficient iterative schemes for ab initio total-energy calculations using a plane-wave basis set, Phys Rev B, 54 (1996) 11169-11186.

[27] G. Kresse, J. Hafner, Ab initio, Phys Rev B, 47 (1993) 558-561.

[28] P.E. Blöchl, Projector augmented-wave method, Phys Rev B, 50 (1994) 17953-17979.

[29] J.P. Perdew, K. Burke, M. Ernzerhof, Generalized Gradient Approximation Made Simple, Phys Rev Lett, 77 (1996) 3865-3868.

[30] K. Momma, F. Izumi, VESTA 3 for three-dimensional visualization of crystal, volumetric and morphology data, J Appl Crystallogr, 44 (2011) 1272-1276.

[31] A. de Kergommeaux, M. Lopez-Haro, S. Pouget, J.-M. Zuo, C. Lebrun, F. Chandezon, D. Aldakov, P. Reiss, Synthesis, Internal Structure, and Formation Mechanism of Monodisperse Tin Sulfide Nanoplatelets, J. Am. Chem. Soc., 137 (2015) 9943-9952.

[32] R.W. Wolfe, R.E. Newnahm, M.I. Kay, Crystal structure of Bi_2WO_6, Solid State Commun., 7 (1969) 1797-1801.

[33] S. Del Bucchia, J.-C. Jumas, M. Maurin, Contribution a l'etude de composes sulfures d'etain(II): affinement de la structure de SnS, Acta Crystallographica Section B, 37 (1981) 1903-1905.

[34] Y. Xu, H. Xu, H. Li, J. Xia, C. Liu, L. Liu, Enhanced photocatalytic activity of new photocatalyst Ag/AgCl/ZnO, J. Alloys Compd., 509 (2011) 3286-3292.

[35] P.D. Antunez, D.A. Torelli, F. Yang, F.A. Rabuffetti, N.S. Lewis, R.L. Brutchey, Low Temperature Solution-Phase Deposition of SnS Thin Films, Chem. Mater., 26 (2014) 5444-5446.

[36] S. Juntrapirom, D. Tantraviwat, S. Suntalelat, O. Thongsook, S. Phanichphant, B. Inceesungvorn, Visible light photocatalytic performance and mechanism of highly efficient SnS/BiOI heterojunction, J. Colloid Interface Sci., 504 (2017) 711-720.

[37] K. Lai, W. Wei, Y. Dai, R. Zhang, B. Huang, DFT calculations on structural and electronic properties of Bi_2MO_6 (M = Cr, Mo, W), Rare Metals, 30 (2011) 166-172.

[38] H. Zhang, L. Liu, Z. Zhou, Towards better photocatalysts: first-principles studies of the alloying effects on the photocatalytic activities of bismuth oxyhalides under visible light, Phys Chem Chem Phys, 14 (2012) 1286-1292.

[39] X. Ma, Y. Dai, M. Guo, B. Huang, The Role of Effective Mass of Carrier in the Photocatalytic Behavior of Silver Halide-Based Ag@AgX (X=Cl, Br, I): A Theoretical Study, Chemphyschem, 13 (2012) 2304-2309.

[40] J. Zhang, P. Zhou, J. Liu, J. Yu, New understanding of the difference of photocatalytic

activity among anatase, rutile and brookite TiO_2, Phys Chem Chem Phys, 16 (2014) 20382-20386.

[41] R. López, R. Gómez, Band-gap energy estimation from diffuse reflectance measurements on sol–gel and commercial TiO2: a comparative study, J Sol-Gel Sci Techn, 61 (2012) 1-7.

[42] X. Meng, Z. Zhang, Bi_2MoO_6 co-modified by reduced graphene oxide and palladium (Pd^{2+} and Pd^0) with enhanced photocatalytic decomposition of phenol, Applied Catalysis B: Environmental, 209 (2017) 383-393.

[43] Y. Chen, G. Tian, Y. Shi, Y. Xiao, H. Fu, Hierarchical MoS_2/Bi_2MoO_6 composites with synergistic effect for enhanced visible photocatalytic activity, Applied Catalysis B: Environmental, 164 (2015) 40-47.

[44] Z. Li, X. Meng, Z. Zhang, Few-layer MoS_2 nanosheets-deposited on Bi_2MoO_6 microspheres: A Z-scheme visible-light photocatalyst with enhanced activity, Catalysis Today, (2018).

[45] T. Wu, G. Liu, J. Zhao, H. Hidaka, N. Serpone, Photoassisted Degradation of Dye Pollutants. V. Self-Photosensitized Oxidative Transformation of Rhodamine B under Visible Light Irradiation in Aqueous TiO_2 Dispersions, The Journal of Physical Chemistry B, 102 (1998) 5845-5851.

[46] T. Watanabe, T. Takizawa, K. Honda, Photocatalysis through excitation of adsorbates. 1. Highly efficient N-deethylation of rhodamine B adsorbed to cadmium sulfide, The Journal of Physical Chemistry, 81 (1977) 1845-1851.

[47] H. Fu, S. Zhang, T. Xu, Y. Zhu, J. Chen, Photocatalytic Degradation of RhB by

Fluorinated Bi_2WO_6 and Distributions of the Intermediate Products, Environ. Sci. Technol., 42 (2008) 2085-2091.

[48] X. Meng, Z. Zhang, Plasmonic Z-scheme Ag_2O-Bi_2MoO_6 p-n heterojunction photocatalysts with greatly enhanced visible-light responsive activities, Mater Lett, 189 (2017) 267-270.

[49] Y. Jia, S. Zhan, S. Ma, Q. Zhou, Fabrication of TiO_2–Bi_2WO_6 Binanosheet for Enhanced Solar Photocatalytic Disinfection of E. coli: Insights on the Mechanism, ACS Applied Materials & Interfaces, 8 (2016) 6841-6851.

[50] P.-C. Maness, S. Smolinski, D.M. Blake, Z. Huang, E.J. Wolfrum, W.A. Jacoby, Bactericidal Activity of Photocatalytic TiO_2 Reaction: toward an Understanding of Its Killing Mechanism, Appl Environ Microb, 65 (1999) 4094-4098.

[51] H.W. Newkirk, P. Quadflieg, J. Liebertz, A. Kockel, Growth, crystallography and dielectric properties of Bi_2WO_6, Ferroelectrics, 4 (1972) 51-55.

[52] W. Abraham, S.W. A., K.T. R., Z. Yiping, Z.J. Z., Photoelectrochemical Water Splitting Using Dense and Aligned TiO_2 Nanorod Arrays, Small, 5 (2009) 104-111.

[53] Z. Zhang, Y. Yu, P. Wang, Hierarchical Top-Porous/Bottom-Tubular TiO_2 Nanostructures Decorated with Pd Nanoparticles for Efficient Photoelectrocatalytic Decomposition of Synergistic Pollutants, ACS Applied Materials & Interfaces, 4 (2012) 990-996.

[54] C. Zeng, H. Huang, T. Zhang, F. Dong, Y. Zhang, Y. Hu, Fabrication of Heterogeneous-Phase Solid-Solution Promoting Band Structure and Charge Separation for Enhancing Photocatalytic CO_2 Reduction: A Case of $Zn_XCa_{1-X}In_2S_4$, ACS Applied Materials &

Interfaces, 9 (2017) 27773-27783.

[55] X. Meng, Z. Zhang, Bismuth-based photocatalytic semiconductors: Introduction, challenges and possible approaches, J. Mol. Catal. A: Chem., 423 (2016) 533-549.

[56] S. Fang, Y. Zhou, H. Cui, Z. Li, S. Xu, L. Wang, Fabrication of BiOCl@CdS/Ag_2CO_3 heterojunctions with enhanced photocatalytic activity under visible-light irradiation, Journal of Materials Science: Materials in Electronics, 28 (2017) 14575-14583.

[57] Y.A. Ilan, G. Czapski, D. Meisel, The one-electron transfer redox potentials of free radicals. I. The oxygen/superoxide system, Biochimica et Biophysica Acta (BBA) - Bioenergetics, 430 (1976) 209-224.

[58] T. Xiong, M. Wen, F. Dong, J. Yu, L. Han, B. Lei, Y. Zhang, X. Tang, Z. Zang, Three dimensional Z-scheme $(BiO)_2CO_3/MoS_2$ with enhanced visible light photocatalytic NO removal, Applied Catalysis B: Environmental, 199 (2016) 87-95.

SECTION IV: BN ENHANCED PHOTOCATALYSIS

Chapter 7 Fewer-layer BN nanosheets-deposited on Bi_2MoO_6 microspheres with enhanced visible light-driven photocatalytic activity

Zizhen Li, Xiangchao Meng and Zisheng Zhang

Applied Surface Science, *483*, 572-580 (2019)

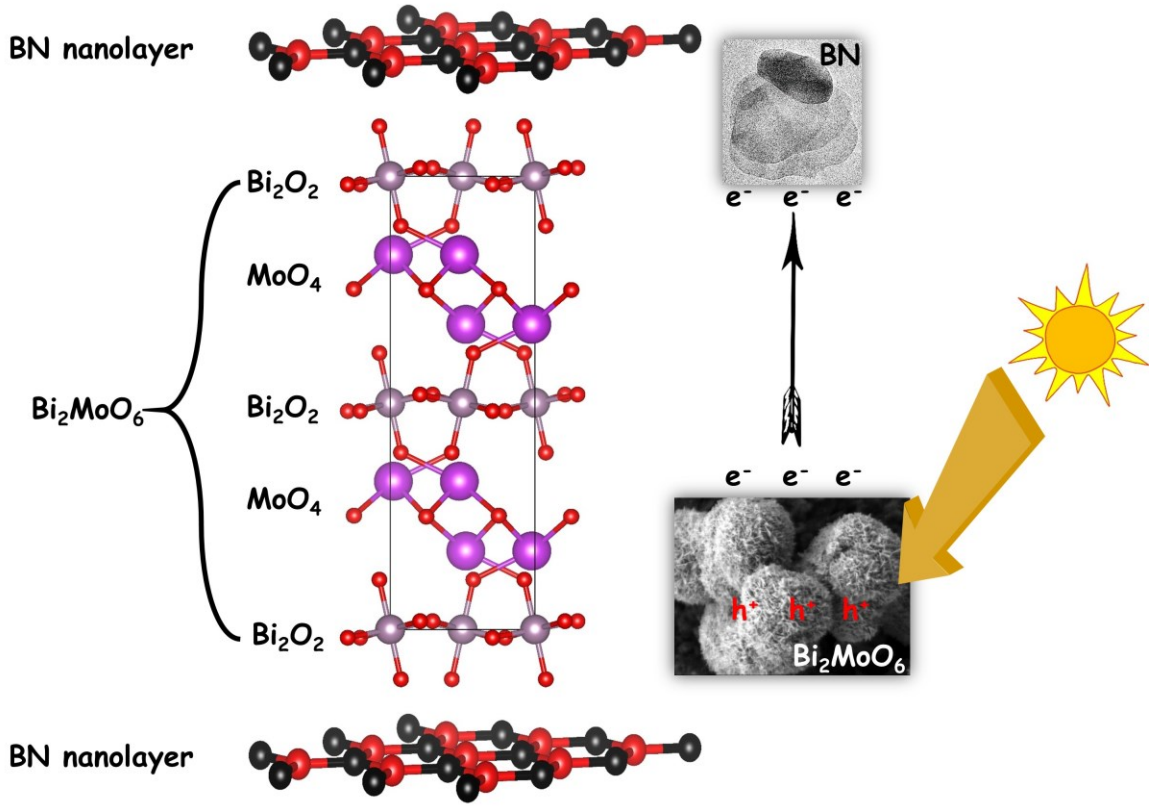

Abstract

Photocatalysis is a process to convert light energy into chemical energy. And photocatalysis has been widely implemented into various areas, such as energy storage and

environmental remediation. In this work, we focused on photocatalytic oxidation of organic pollutants in water on a new composite, *i.e.* BN-Bi_2MoO_6. The result suggests BN nanosheets may be an excellent co-catalyst in boosting the photocatalytic activity of the substrate (Bi_2MoO_6) in the decomposition of organics in water under visible light. This work sheds a light on addressing the importance of two-dimensional materials to supress the recombination of photogenerated charge carriers, therefore to improve the visible light-induced photocatalytic activity.

7.1 Introduction

Photocatalysis has been extensively explored in energy storage and environmental remediation in recent years [1]. As one of the advanced oxidation processes (AOPs), photocatalysis exhibits great potentials in water/ wastewater treatment. As for the intrinsic property of TiO_2, the band gap is too wide to be responsive to visible light. In aiming to expand the utilization of solar spectrum, various visible light-responsive (VLR) semiconductors have been developed and investigated. Bismuth-based semiconductors (BBS), as a group of promising VLR photocatalysts, have been widely studied by our group and other groups [2-6]. Bi_2MoO_6, as one of BBS has been found with a suitable band gap (~2.6 eV) for VLR photocatalysis. However, as for the high recombination of photogenerated charge carriers, the quantum yield of Bi_2MoO_6-based photocatalytic system is still pretty low. Approaches to supress the recombination of charge carriers are required to improve the photocatalytic activity of Bi_2MoO_6. We recently reported on few-layered MoS_2 nanosheets deposited onto Bi_2MoO_6 with enhanced VLR photocatalytic activity [7, 8]. Other two-dimensional materials were also reported as an excellent cocatalyst to supress the chargers' recombination, such as graphene, carbon nitride (C_3N_4)

and boron nitride (BN) [9-14]. BN nanosheet was reported as an efficient carrier transfer promoter and stabilizer to enhance the photocatalytic performance of the substrate [15-17]. In this work, BN nanosheets were prepared based on the reported method [18], and loaded onto Bi_2MoO_6 so as to improve its photocatalytic activity. This is the first time a report on BN- Bi_2MoO_6 composites is applied in photocatalysis.

7.2 Experimental

7.2.1 Synthesis of Bi_2MoO_6

All chemicals were purchased from Fisher Scientific (Canada) unless otherwise mentioned, and used as received. Bi_2MoO_6 microspheres were prepared using a solvothermal method as we reported previously [8]. Typically, 1.69 g of $Bi(NO_3)_3 \cdot 5H_2O$ and 0.42 g of $Na_2MoO_4 \cdot 2H_2O$ were separately mixed with 5 mL ethylene glycol (EG) under magnetically stirring. Subsequently, the above solutions were sequentially dropwise added to 20-mL ethanol. After magnetically stirring for 30 min, the suspension was transferred to a 45-mL Teflon-lined stainless-steel autoclave and heated up to 160°C for 20 h. Once the autoclave was naturally cooled down to room temperature, the obtained samples were filtered out and washed with ethanol and ddH_2O (deionized, distilled water) for several times to remove possible organic and ionic species. After that, as-prepared samples were dried at 60°C overnight.

7.2.2 Synthesis of few-layer BN

Few-layer BN were prepared using a liquid exfoliation of BN powders [18]. In a typical process, 50 mL of BN powders were dispersed in isopropanol (IPA) with an initial concentration of 3 mg/mL in a 100-mL round bottomed flask. The suspension was then

sonicated using a sonic bath for 24h, and the temperature of the sonic bath was kept at ~4°C. After sonication, the suspension was centrifuged at 1500 rpm for 45 min, and the supernatant was decanted for further use. The concentration of the obtained BN was estimated using a UV-Vis spectrometer at 300 nm (absorption coefficient: α = 2367 mL mg^{-1} m^{-1}).

7.2.3 Synthesis of BN- Bi_2MoO_6 composites

BN-Bi_2MoO_6 composites were synthesized by a simple bath evaporation method, as we previously reported [19, 20]. Specifically, 0.50 g of Bi_2MoO_6 were dispersed in 30 mL hydrous ethanol (50% v/v of ethanol in deionized distilled water), and a designated amount of layered BN was added dropwise into the Bi_2MoO_6 suspension, and the suspension was then heated at 60°C and continually stirred until the solvent was completely evaporated. The samples were collected and dried at 60 °C overnight. BN-Bi_2MoO_6 composites with different BN to Bi_2MoO_6 weight ratios (0.5, 1.0 and 2.0 wt.%) were synthesized.

7.2.4 Characterization

Morphology of prepared samples were investigated using a field-emission scanning electron microscope (FE-SEM, JEOL JSM-7500F) and a transmission electron microscope (JEM-2100F FE-TEM (JEOL)). The Park AFM NX10 unit was used to carry out atomic force microscopy (AFM) measurements. The liquid sample solution was prepared by using an ultrasonicator at 80 kHz for 5 minutes. A single droplet was then placed on a piece of Silicon prime polished wafer and set to evaporate. The remaining particulates were measured with AFM. X-ray powder diffraction (Bruker-AXS, Karlsruhe, Germany) patterns of samples were collected with filtered Cu-Kα radiation (λ = 1.5418 Å) from 5°–

90° (2θ). An XSAM-800 X-ray Photoelectron Spectroscope (XPS) was employed to analyze the surface chemical composition and the chemical sates of selected samples. The Brunauer, Emmett and Teller (BET) surface area of the samples were calculated using multi-point estimation. The pore volumes were calculated using the volumes of adsorbed N_2 at p/p_o = 0.9941. Barrett-Joyner-Halenda (BJH) method was used for the desorption branch to calculate the pore size data (d_p) using Equation 1 (where V/A_s is a ratio of volume to surface area of pores) as follows,

$$d_p = 4\left(\frac{V}{A_s}\right)_{BJH} \qquad \textbf{\textit{Equation 1}}$$

A thermos Evolution 300 spectrophotometer was applied to detect the ultraviolet-visible diffuse reflectance spectra (DRS). Electrochemical properties of prepared samples were analyzed on a CHI 604E electrochemical analyzer (CH Instruments Inc., USA) with a platinum wire as a counter electrode, a calomel reference electrode and a working electrode. The working electrode composed of indium tin oxide (ITO, 75 × 25 × 1.1 mm, 15–25 Ω, Sigma-Aldrich Canada Co.), glass coated with the prepared samples. Electrochemical impedance spectroscopy (EIS) was performed with frequencies in the range of 0–1,000,000 Hz and a sinusoidal wave of 5 mV. The electrolyte used was Na_2SO_4 with a concentration of 5 mmol/L. Photoluminescence spectra of the samples were recorded with a Hitachi F-7000 fluorescence spectrophotometer.

7.2.5 Electronic structure calculation

The DFT simulations for the influence of the number of BN layers on the band structure were performed using the Vienna *ab initio* simulation package (VASP) [21, 22]. The ion-

electron interaction is described with the projector augmented wave (PAW) method [23]. Electron exchange-correlation is represented by the function of Perdew, Burke, and Ernzerhof (PBE) of generalized gradient approximation (GGA) [24]. A cut-off energy of 400 eV was used for the set plane-wave basis. An open-source software for VASP visualization, P4VASP written by Orest Dubay (http://www.p4vasp.at) has been used for the analysis of electronic band structures.

7.2.6 Photocatalytic activity test

Photocatalytic activity of as-prepared samples were evaluated with regard to the degradation of rhodamine B (RhB) under visible light irradiation. The light source was provided by a 300-W halogen tungsten projector lamp (Ushio) equipped with a UV cut-off filter. The irradiation intensity on the surface of the solution was measured by a quantum meter (Biospherical QSL-2100, $400 < \lambda < 700$ nm) to be 1.1×10^{-2} Einsteins m^{-2} s^{-1}. Typically, in each test, 1.0 g/L photocatalyst were added into a 100 mL RhB solution with an initial concentration of 10 mg/L. The mixture was magnetically stirred in the dark for 30 min to reach an adsorption/desorption equilibrium prior to the photocatalysis experiment. Afterwards, 1 mL of aliquots was collected and centrifuged every 10 min. The resulting supernatant was tested at 554 nm (characteristic absorption peak of RhB) by a UV–vis spectrophotometer (Genesys 10 UV, Thermo Scientific) to determine the concentration of RhB. Meanwhile, the total organic carbon (TOC) of samples collected at 0min, 60min and 120min were investigated by an Apollo 9000 TOC analyzer equipped with a Non-Dispersive Infra-Red (NDIR) detector at a combustion temperature of 750 °C. The UV–vis adsorption spectra of resulting supernatant ranging from 300-650 nm was also obtained using a UV–vis spectrophotometer (Biochrom Ultrospec 60) to analyze the

photocatalytic degradation process of RhB. Photocatalytic degradation of phenol was also carried out. Typically, for each batch, 0.10 g of photocatalyst was mixed with 100 mL of phenol solution (10 ppm) in a 500 mL beaker. Before illumination, the reaction mixture was magnetically stirred for 60 min to reach the adsorption/desorption equilibrium. After that, aliquots were collected every 1 h and the concentration of the supernatant was analyzed by a high-performance liquid chromatograph (HPLC, Agilent 1100 series) equipped with a UV–vis detector. A ZORBAX Eclipse Plus C18 column (4.6 × 250 mm) was used at a temperature of 60°C. The detecting wavelength was fixed at 270 nm for the detection of phenol and possible intermediates. The flow phase was composed of methanol (55%, V/V) and water (45%, V/V) at a flow rate of 0.6 mL/min. The injection volume was set to 25 μL.

The reusability of the prepared sample (1.0 wt% BN-Bi_2MoO_6) was also studied by separating the photocatalysts from the suspension following a single run. Catalysts were then mixed with fresh wastewater to start another run. Three runs were performed in total for these tests. Quenching experiments were performed to analyze the roles of each reactive oxidative species (ROS). Specifically, 0.1 M iso-propanol (IPA), 10 vol% triethanolamine (TEOA) and N_2 bubbling were used to trap hydroxyl radicals (•OH), holes and superoxide radicals ($•O_2^-$), respectively. Each scavenger was mixed with the RhB solution before the test, and then tested with same procedures as described in the photocatalytic degradation of RhB.

7.3 Results and Discussions

7.3.1 Morphologies

Morphologies of as-prepared samples were investigated using SEM (Fig. 7.1a and 7.1b) and TEM (Fig. 7.1c and 7.1d). It can be found that as-prepared Bi_2MoO_6 exhibited a flower-shaped hierarchical microsphere structure with an average diameter of 2-4 μm. With surface modification of BN, the primary structure of Bi_2MoO_6 was negligibly influenced (Fig. 7.1b), and small flakes were covered on the surface of Bi_2MoO_6 (Fig. 7.1d). It suggests that the layered BN were successfully prepared and loaded onto the Bi_2MoO_6 microspheres. The TEM image of BN (Fig. 7.1c) further confirmed the as-prepared BN sheets have a layered structure. According to the AFM image and corresponding height profile of selected area (Fig. 7.1e), the thickness of the BN layers ranged from 20 to 27 nm. It should be noted that the BN layers were stacked together, instead of single BN layer present on the surface, which is favorable of improving the light photons capture. The effect of the number of BN layers on the optical properties was explored by band structure simulation using DFT, and the computed results were shown in Table 7.1. For a bulk BN, the band gap energy was 4.47 eV. In comparison, the band gap value for a single-layer BN was increased to 5.58 eV. And the increase of the layer numbers will narrow the band gap values. This result suggests the more the BN layer numbers, the lower activation energy required to initiate a photocatalytic process.

Table 7.1. Band structures and band gap energies for BN (bulk) and layered BN sheets.

Compounds	BN (bulk)	BN (one-layer)	BN (two-layer)	BN (five-layer)
Band structure	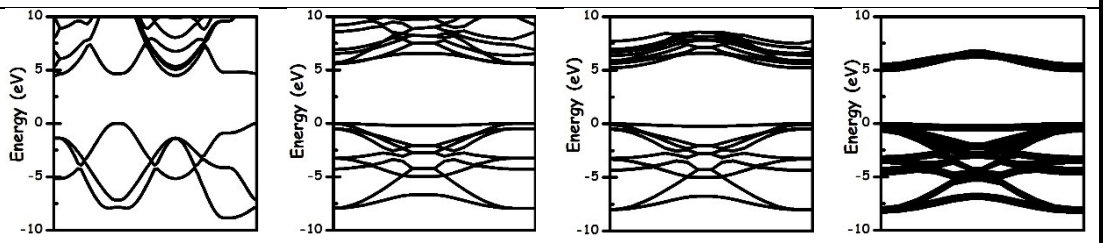			
Band gap	4.47 eV	5.58 eV	5.23 eV	4.92 eV

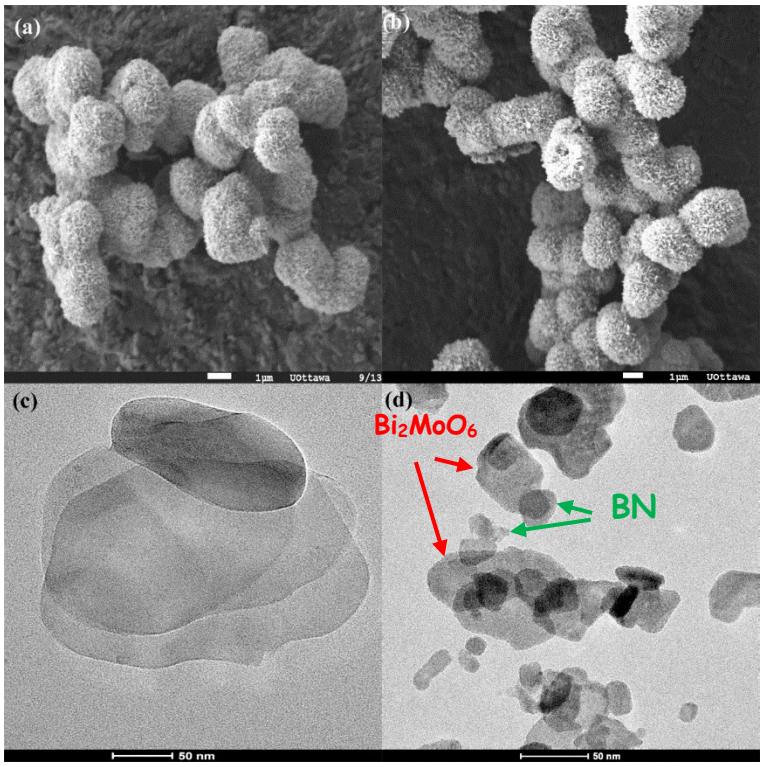

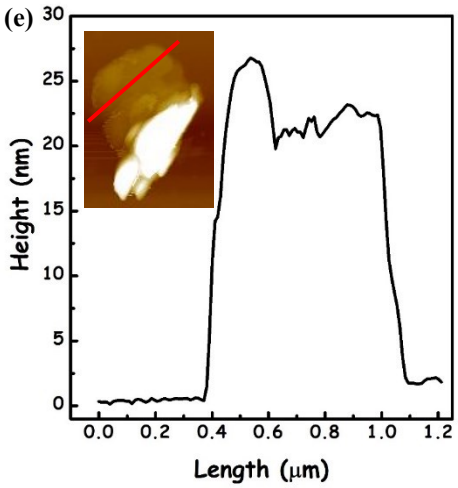

Figure 7.1. SEM images of (a) Bi_2MoO_6 and (b) BN-Bi_2MoO_6; TEM images of (c) BN sheets and (d) BN-Bi_2MoO_6 composites; and (e) AFM image of layered BN sheets and the height profile among the red line indicated.

7.3.2 Crystal structure and surface chemical composition analysis

Crystal structure and surface compositions of as-prepared samples were measured using XRD and XPS, respectively, and the results were illustrated in Fig. 7.2. For the XRD patterns for pure Bi_2MoO_6 (Fig. 7.2a), all diffraction peaks were well indexed to the orthorhombic phase of Bi_2MoO_6 (PDF card #:72-1524) indicating a good crystallinity of prepared Bi_2MoO_6 sample. Loading of BN sheets, influences on the Bi_2MoO_6 lattice structure insignificantly. It indicated that BN may only loaded on the surface of Bi_2MoO_6 instead of covalently anchoring into the Bi_2MoO_6 lattice [8, 25]. To further confirm the successfully loading of BN on the surface of Bi_2MoO_6, XPS was employed to analyze the surface chemical compositions. In the survey spectra as shown in Fig. 7.2b, no impurity peaks were found for both samples. Compared with the survey spectrum of pure Bi_2MoO_6, the peak for N was observed in the survey spectrum of BN-Bi_2MoO_6, indicating the successful loading of BN onto Bi_2MoO_6. In the high-resolution XPS spectra for N and B, as shown in Fig. 7.2c and 7.2d, respectively, a shoulder peak for N1s and a peak for B 1s

were separately observed. Specifically, the peak of N 1s at 400.59 eV and the peak of B 1s at 188.49 eV can be assigned to the N^{3-} and B-N bond, respectively [26], which confirmed that the BN were successfully loaded onto the Bi_2MoO_6.

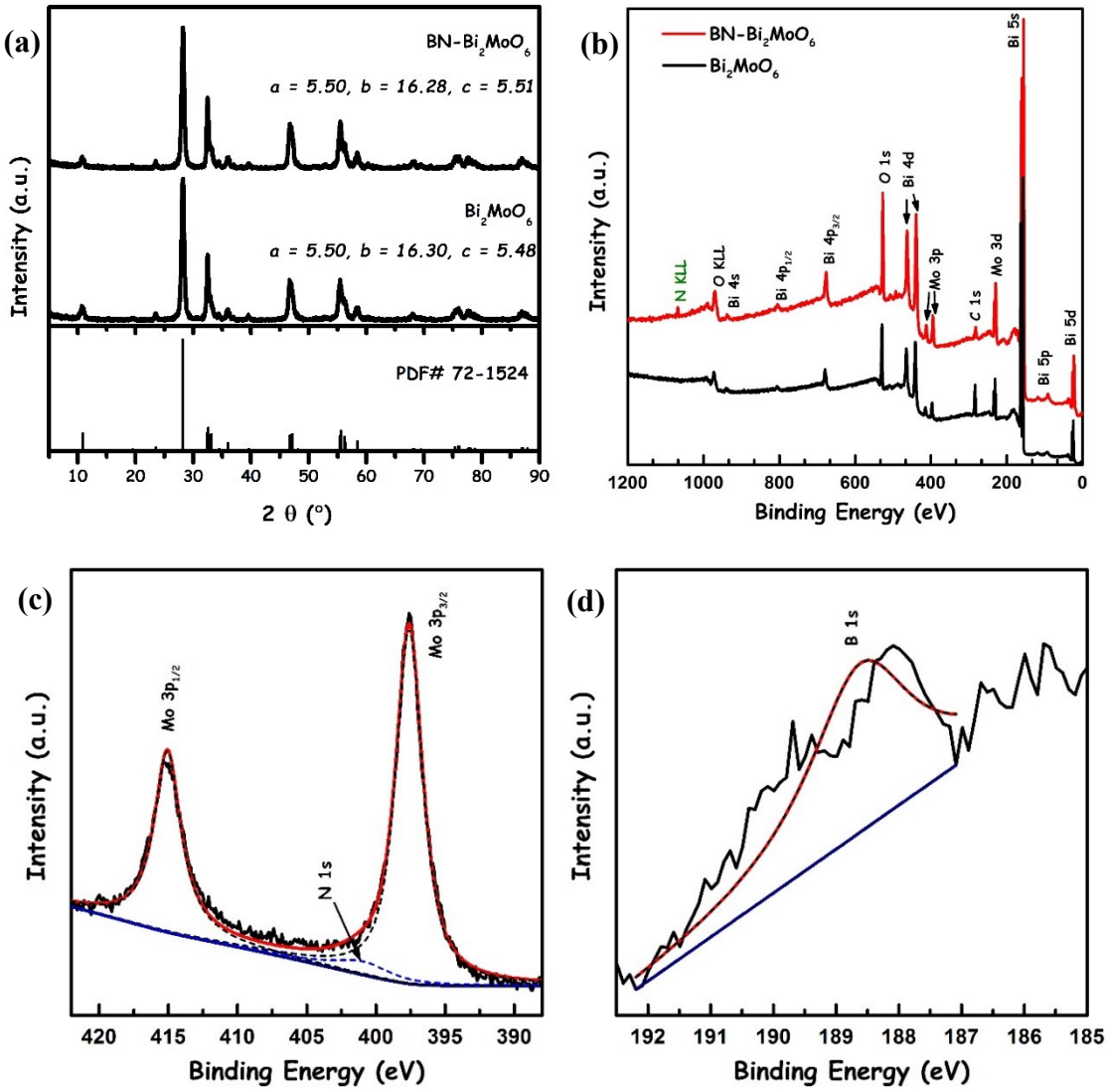

Figure 7.2. (a) XRD patterns and (b) XPS survey spectra for Bi_2MoO_6 and BN-Bi_2MoO_6; high-resolution XPS orbital scans of (c) Mo3p and (d) B1s for BN-Bi_2MoO_6.

7.3.3 N_2 sorption isotherms

To explore the surface properties, including surface area as well as pore size and volume, N_2 sorption isotherms for prepared samples were investigated and depicted in Fig. 7.3. For

both isotherms, an inflexion point close to the saturation vapor pressure was observed, suggesting both isotherms were attributed to type-IV physisorption isotherm. This adsorption behavior is generally given by a mesoporous material associated with the capillary condensation process. Hysteresis loop was observed for both isotherms, and may be identified as an H3 loop, indicating that the samples are plate-shaped particles with slit-like pores [27, 28]. This morphology was confirmed by the SEM and TEM images. Quantitively, BET (Brunauer-Emmett-Teller) surface area, pore volume, and average pore size were calculated from the isotherms and summarized in Table 7.2. A reduction of BET surface area from 31.7 m^2/g to 30.0 m^2/g after BN loaded on Bi_2MoO_6 may be resulted from the BN sheets blocked the slit-shape pores [20]. However, both pore volume and average pore size were slightly increased, which may be due to more slit-shape pores formed between BN sheets and Bi_2MoO_6. A reduced surface area may lead to less adsorption sites and lower photocatalytic activity. However, as indicated by the photocatalytic degradation experiments, this effect was negligible compared to the improvement in charge separation given by the BN coupling.

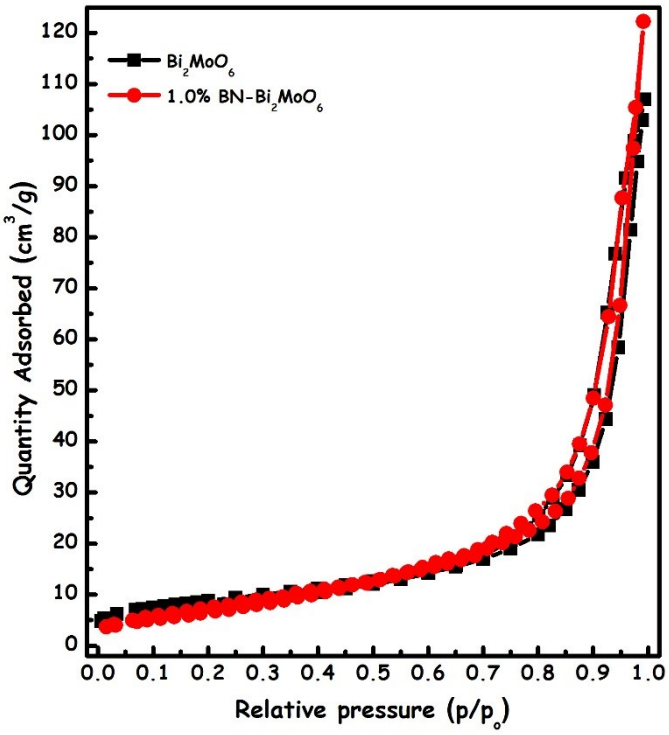

Figure 7.3. N_2 sorption isotherms for Bi_2MoO_6 and 1.0% BN-Bi_2MoO_6.

Table 7.2. Specific surface area, pore volume, and average pore size of Bi_2MoO_6 and 1.0% BN-Bi_2MoO_6.

Sample	S_{BET} (m^2/g)	Pore volume (cm^3/g)	Average pore size (nm)
Bi_2MoO_6	31.7	0.17	21.6
1.0% BN- Bi_2MoO_6	30.0	0.19	23.3

7.3.4 Optical properties

To evaluate the optical properties of as prepared samples, DRS was employed to determine the absorption properties and band gap energy, and results of which were illustrated in Fig. 7.4. All samples showed light adsorption within the scope of ultraviolet-vis spectrum. The

adsorption edge of Bi_2MoO_6 is around 489 nm, while pure BN displayed weaker light adsorption than pure Bi_2MoO_6. As a result, the light adsorption capacity of BN-Bi_2MoO_6 composites was slightly decreased compared with pure Bi_2MoO_6 across the entire spectrum. These results indicated that the as-prepared BN-Bi_2MoO_6 composites can be used as visible light-responsive photocatalysts. The bandgap energy of pure BN, pure Bi_2MoO_6, 0.5% BN, 1.0% BN, and 2.0% BN were estimated to be around 5.54, 2.53, 2.55, 2.58, and 2.60 eV respectively, based on the Kubelka-Munk method [29]. It revealed that the increasing content of BN can lead to the larger bandgap energy of BN-Bi_2MoO_6 composites due to the intrinsic wide band gap of BN. This results agreed well with other reports [15]. Compared to the great improvement in the charge carriers' separation, the slightly increase in the band gap value negligibly influence on the photocatalytic activity.

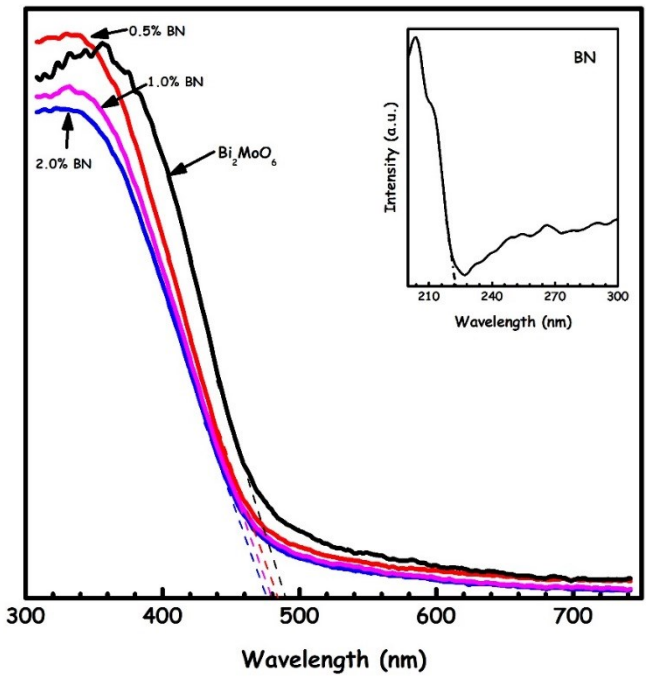

Figure 7.4. UV–vis diffuse reflectance spectra of pure Bi_2MoO_6, BN-Bi_2MoO_6 composites and BN (inset).

7.3.5 Photocatalytic activity test

The photocatalytic activities of prepared samples were evaluated with regard to the degradation of RhB under visible light, and testing results were shown in Fig. 7.5a. Under illumination, BN-Bi_2MoO_6 composites exhibited enhanced photocatalytic activity compare to pure Bi_2MoO_6, indicating a positive synergetic effect between BN and Bi_2MoO_6. Specifically, the RhB removal efficiency increased as the BN to Bi_2MoO_6 weight ratio increased from 0.5% to 1.0%. However, the further increasing BN to Bi_2MoO_6 weight ratio led to the slightly decreased rate of removal. This phenomenon may be due to the large quantity of BN, which is irresponsible to visible light, blocking the visible-light absorption by Bi_2MoO_6, so as to reduce the generation of photoinduced charge carriers [30]. The highest removal efficiency was reached when the BN to Bi_2MoO_6 weight ratio is 1.0%. After illumination for 120 min, almost 100% RhB was removed in the presence of 1.0% BN-Bi_2MoO_6, whereas about 80% RhB was removed in the presence of pure Bi_2MoO_6. Therefore, the suitable loading amount of BN could facilitate the charge generation and separation rate of the BN-Bi_2MoO_6 composites.

The temporal evolution of the spectral changes that occurred during the photocatalytic degradation of RhB in the presence of BN-Bi_2MoO_6 was depicted in Fig. 7.5b. The blue shift of the major peak wavelength suggested that a step-by-step N-deethylation process predominates during the initial photocatalytic degradation process [8, 20]. The characteristic adsorption peak wavelengths at 539, 522, 510 and 498 nm represent intermediates of each *N*-deethylation step, which are *N,N,N'*-triethyl-rhodamine, *N,N'*-diethyl-rhodamine, *N*-ethyl-rhodamine and rhodamine, respectively [31-35]. After 120 min, the peak intensity of complete *N*-deethylated product (rhodamine) decreased due to the

cleavage of the aromatic chromophore structure. Deethylation was the first step in the decomposition of RhB, and converted RhB into rhodamine (Fig. 7.7). The second step, ring cleavage, was explored by measuring the relative TOC removal ratios, results were illustrated in Fig. 7.6. There were around 18% and 30% of TOC removed from the photocatalytic processes over 120 min in presence of pure Bi_2MoO_6 and BN-Bi_2MoO_6, respectively. This indicates that RhB may be decomposed into small molecules (*e.g.* CO_2 and H_2O) with a prolonged reaction time. And BN loaded on the surface promoted the photocatalytic mineralization of organics in water under visible light.

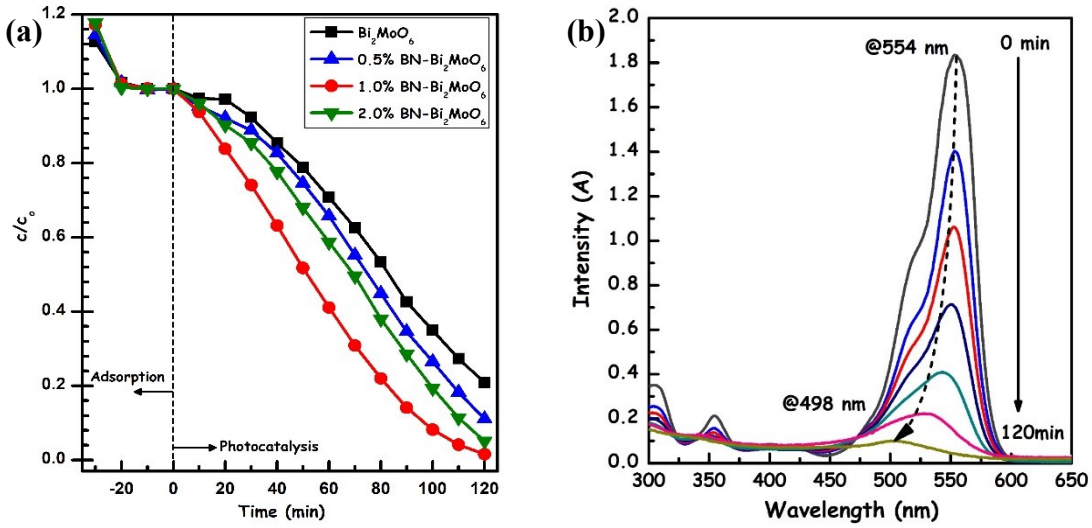

Figure 7.5. (a) Photocatalytic degradation of RhB in the presence of different samples under visible light, and (b) UV-Vis spectral changes of RhB during photocatalytic degradation process.

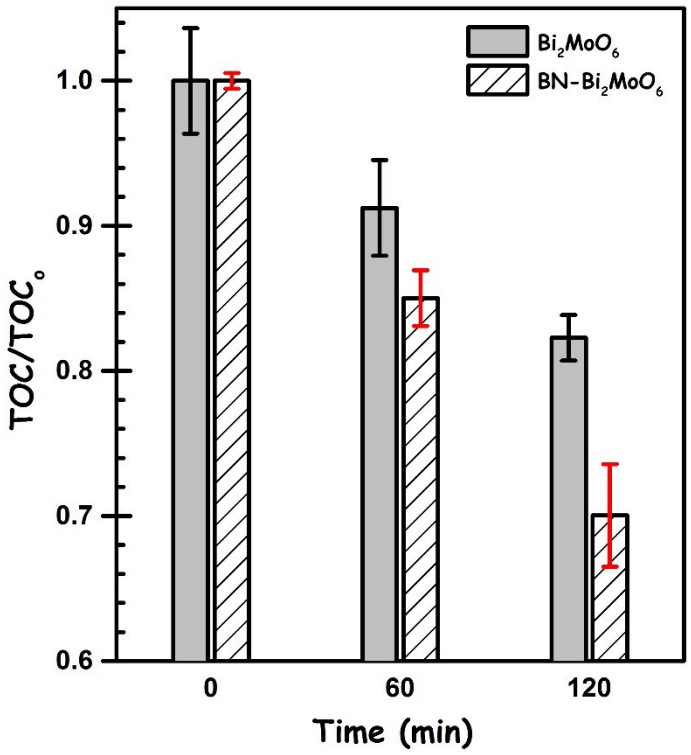

Figure 7.6. TOC removal ratios in photocatalytic processes with Bi_2MoO_6 and BN-Bi_2MoO_6 under visible light irradiation.

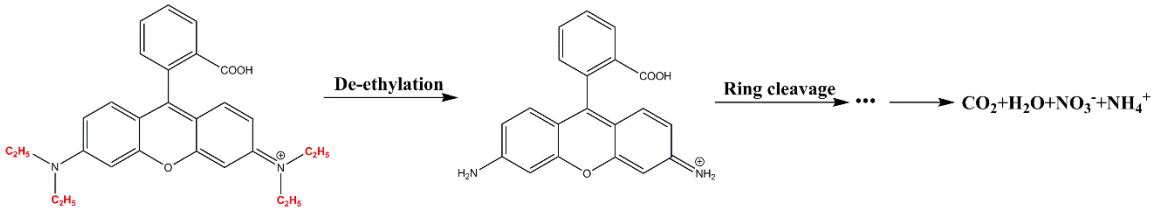

Figure 7.7. Pathways of RhB in photocatalytic decomposition process.

Reusability of as-prepared sample was evaluated by recycling use of the BN-$Bi_2MoO_6$for three runs in the decomposition of RhB under visible light. Concentration profiles of RhB were plotted in Fig. 7.8. Complete removal of RhB can be obtained for all these three runs. A negligible difference among these three profiles suggests the high stability of BN-Bi_2MoO_6 composites in the photocatalytic degradation of organics. A slight reduction in the adsorption may be resulted from some refractory intermediates adsorbed on the surface

of the catalysts, which will further reduce the number of reactive sites in the following run. The high reusability of BN-Bi_2MoO_6 composites make them an attractive candidate for use as visible light-responsive photocatalysts.

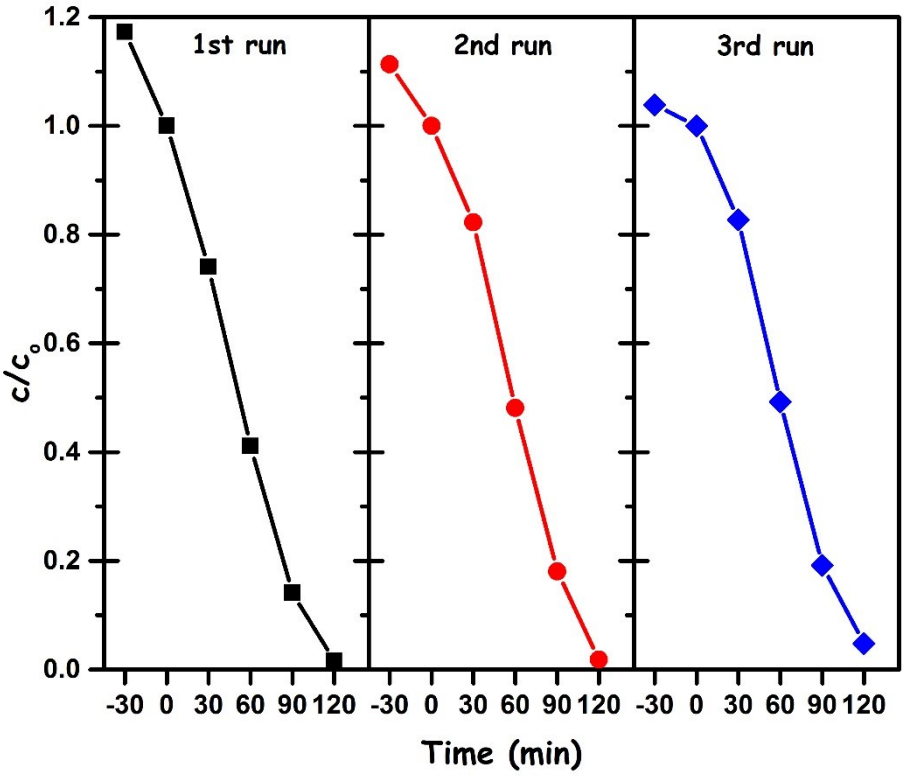

Figure 7.8. Recycling tests of BN-Bi_2MoO_6 sample in the degradation of RhB under visible light.

As the dye self-sensitization contributed to the decomposition of RhB in photocatalysis, a colorless organic, phenol was used as a probe molecule to evaluate the performance of BN loaded on Bi_2MoO_6 [36, 37]. The concentration of phenol during the photocatalytic processes in presence of pure $Bi_2MoO_6$and BN-$Bi_2MoO_6$was illustrated in Fig. 7.9. There were approximately 4% and 16% of phenol removed from the systems over 300 min with Bi_2MoO_6 and BN-Bi_2MoO_6, respectively. This result further confirms the effectiveness of

loading BN on the surface of Bi_2MoO_6 to improve its photocatalytic activity in the decomposition of organics in water under visible light.

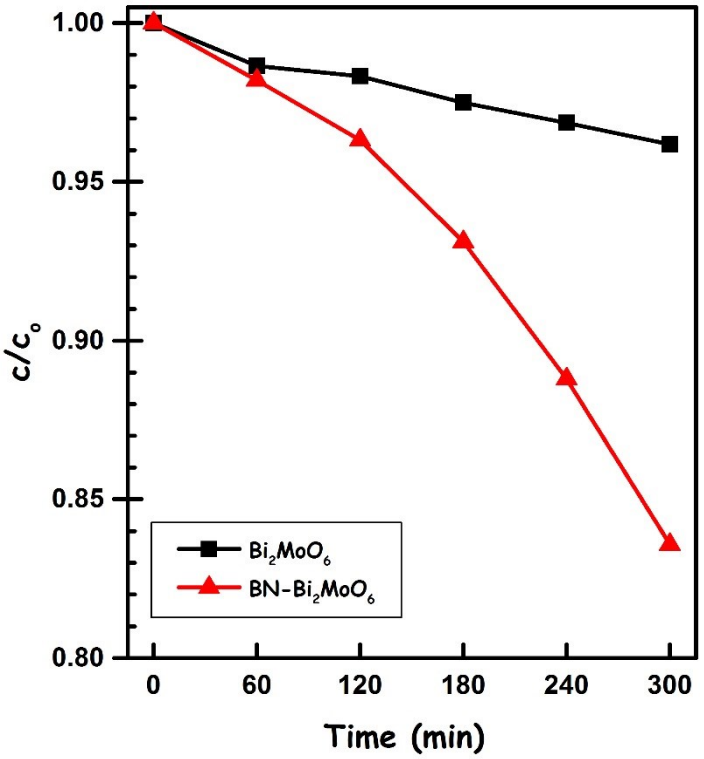

Figure 7.9. Photocatalytic degradation of phenol in presence of Bi_2MoO_6 and BN-Bi_2MoO_6 under visible light.

7.3.6 Electrochemistry analysis

To explore the interface charge separation efficiency, electrochemical impedance spectroscopy (EIS) was measured, and the EIS Nyquist plots of Bi_2MoO_6 as well as BN-Bi_2MoO_6 composites under visible light were shown in Fig. 7.10a. Only one semicircle is observed for each EIS Nyquist plot, indicates these photocatalytic process in the presence of prepared samples may be a simple electrode reaction that only involved in the surface charge transfer [38, 39]. And the photogenerated electrical carriers transfer rate is able to be determined by their recombination rate. The diameter of the arc in the EIS Nyquist plot

determines the resistance of the photocatalyst electrode [40, 41]. And the larger diameters resulting in higher values of resistance. It can be observed that with loading of BN on the surface of Bi_2MoO_6, the resistance on the photocatalyst electrode (R_s) was reduced from 15047Ω (pure Bi_2MoO_6) to 9685Ω (BN-Bi_2MoO_6), which suggest the charge carriers' separation was greatly improved, and so as to improve the photocatalytic activity.

The transient photocurrent response of pure Bi_2MoO_6 and BN-Bi_2MoO_6 composites were also recorded under visible light (Fig. 7.10b). The reproducible photocurrent of both samples indicated that the prepared electrodes are stable. Moreover, the photocurrent intensity of BN-Bi_2MoO_6 composites was more than 2 times higher than that of pure Bi_2MoO_6, which is consistent with the results of RhB degradation. Due to the proportional relationship between the photocurrent and the separation efficiency of photogenerated charge carriers, it can be deduced that the incorporation of BN could successfully suppress the charge recombination and improve the photocatalytic activity [42, 43].

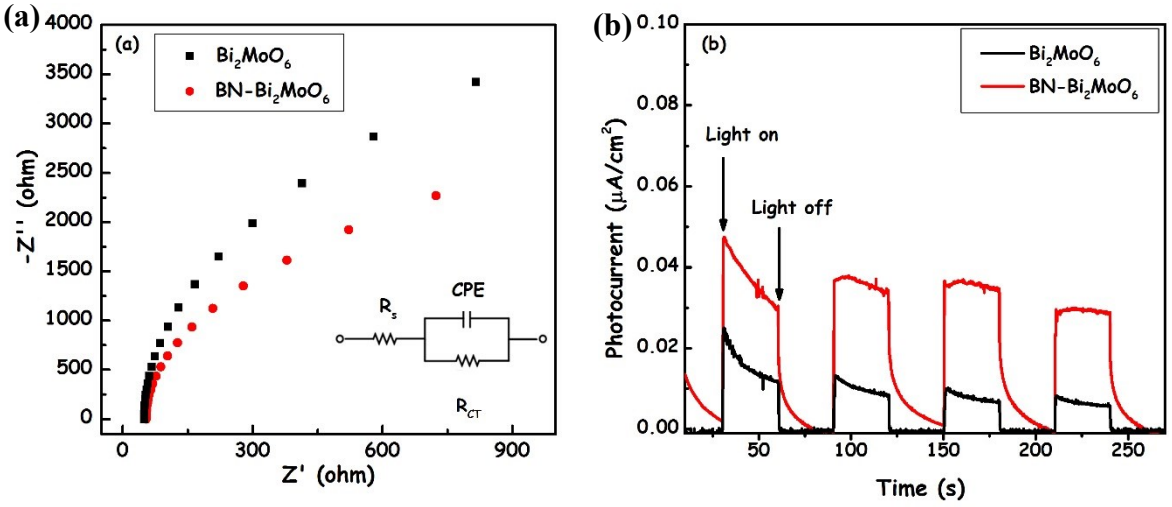

Figure 7.10. (a) EIS Nyquist plots for prepared samples, and (b) proposed photocatalytic process with presence of BN-Bi_2MoO_6.

7.3.7 Band energy level analysis

Energy band configuration plays an important role in the photocatalytic mechanisms in respect of the charge transfer and separation as well as redox capacity of photogenerated charge carriers. As a result, the band position were calculated by the following equations (Equation 2 and 3) [44, 45]:

$$E_{CB} = \chi_P - E^e - 0.5E_g \qquad \textit{Equation 2}$$

$$E_{VB} = E_{CB} + E_g \qquad \textit{Equation 3}$$

Where, E_{CB} and E_{VB} are the bottom of the conduction band (CB) and the top of the valence band (VB), respectively; χ_p is the electronegativity of the semiconductor which can be estimated by the geometric mean of the electronegativities of the constituent atoms; E^e represents the energy of free electrons on the hydrogen scale (~4.5 eV); and E_g is the band gap energy of the semiconductor. The corresponding results were summarized in Table 7.3.

Table 7.3. Bandgap energy and band positions of Bi_2MoO_6 and BN

Composites	E_g/eV	χ_p/eV	E^e/eV	E_{CB} (*vs* NHE)/eV	E_{VB} (*vs* NHE[a])/eV
Bi_2MoO_6	2.53	6.13	4.50	0.37	2.90
BN	5.54	5.58	4.50	-1.69	3.85

7.3.8 Mechanism exploration

To confirm the effective oxidative species in the decomposition of organic pollutants when BN-Bi_2MoO_6 applied, three different scavengers, namely IPA, TEOA and N_2 were selected

to supress the formation of hydroxyl radicals (•OH), holes (h^+) and superoxide radicals ($•O_2^-$), respectively, and the results were illustrated in Fig. 7.11. When IPA added in the solution, the degradation rate was negligibly influenced, indicating •OH played negligible role in this process. While the addition of TEOA, almost no RhB were decomposed over 120 min, which suggests the significance of holes in this process. And with adding TEOA, photocatalytic degradation of RhB was also significantly suppressed. This result suggests $•O_2^-$ may also an effective species. As reported, in the testing system with pH 7, the redox potentials of electrons on the conduction band and holes on the valence band are -0.32 V and +2.34 V (vs. NHE) [46]. It suggests that holes on the valence band is very oxidative, but less positive to oxidize water to produce •OH ($E_{•OH/H2O}$ = 2.68 V), and electrons are negative enough to reduce oxygen to produce $•O_2^-$. Even though holes on the valence band of BN are capable to oxidize water to produce •OH, but the wide band gap of BN resulted in the none visible light responsivity and with no production of separated holes. BN in this system may only serve as an electrons accepter, to confirm this, the photoluminescence (PL) spectra were recorded as shown in Fig. 7.12. PL emission arises from the recombination of photogenerated charge carriers, and the higher the PL intensity is, the lower separation rate of charge carriers is. It can be found that with combination of BN with Bi_2MoO_6, charge separation on Bi_2MoO_6 was greatly improved with lower PL intensity after excitation. This is a solid evidence to prove the effectiveness of BN in the improvement of photocatalytic activity via increasing the charge separation.

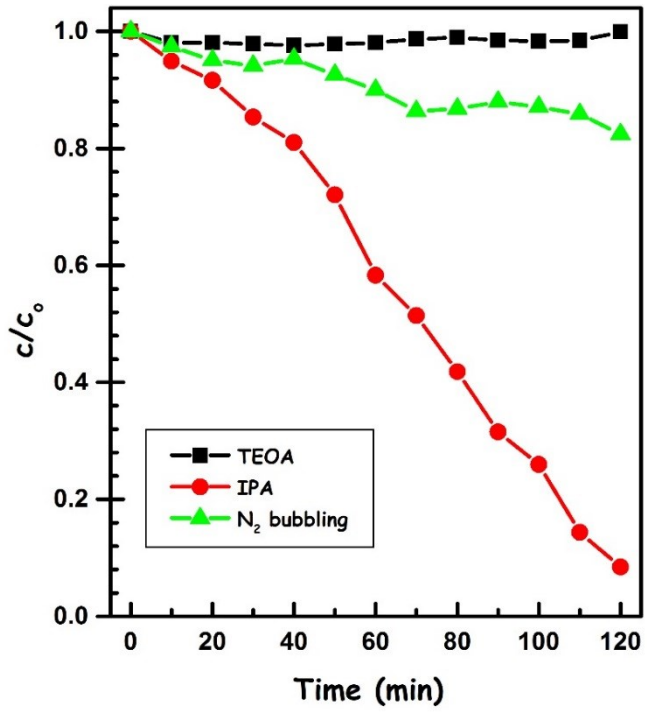

Figure 7.11. Photocatalytic degradation of RhB in the presence of BN-Bi_2MoO_6 and different scavengers.

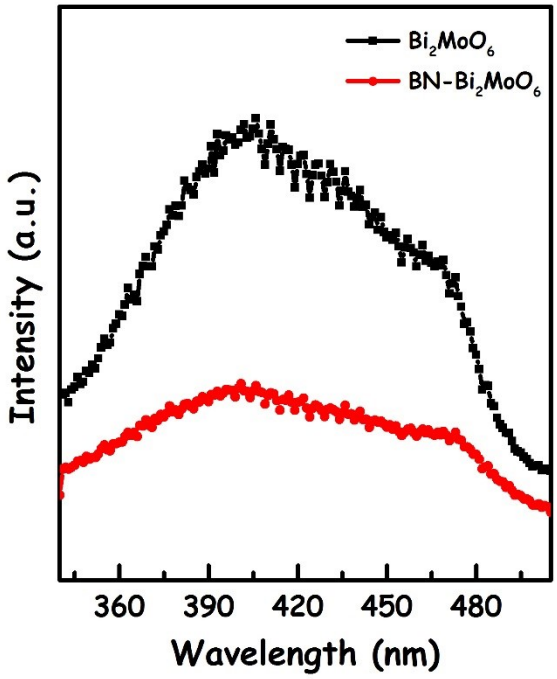

Figure 7.12. Photoluminescence spectra of Bi_2MoO_6 and BN-Bi_2MoO_6 excited by monochromatic light at wavelength of 290 nm at room temperature.

With all above-mentioned discussions, the proposed mechanism of the enhancement with loading BN on Bi_2MoO_6 was shown in Fig. 7.13. Specifically, under visible light, valence electrons of Bi_2MoO_6 may be activated by visible light photons, and jumped to its conduction band with positive holes left behind. The positive holes on the valence band were capable of reacting with adsorbed species, such as H_2O, to produce highly oxidative species, such as HOO• and HOO^-. These free radicals as well as separated positive holes on the valence band were oxidative enough to decompose most of the organic pollutants in water. Meanwhile, electrons on the Conduction band of Bi_2MoO_6 may be transferred to the BN sheets, which will increase the charge carriers' separation, and as a result, the photocatalytic activity of Bi_2MoO_6 was promoted with loading of BN sheets.

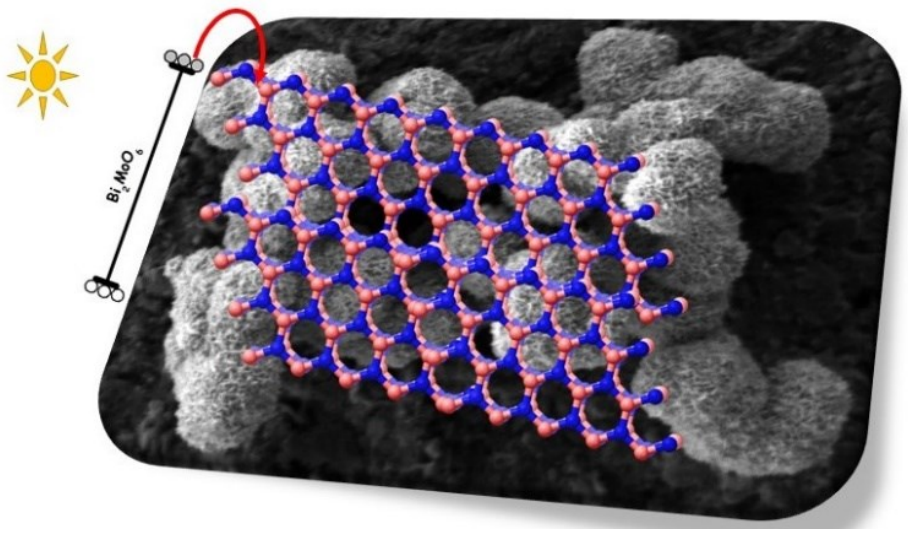

Figure 7.13. Proposed photocatalytic mechanisms of BN-Bi_2MoO_6 composites and possible photogenerated electron-hole pair transfer and separation process.

7.4 Conclusions

Layered BN were successfully prepared and loaded onto the surface of Bi_2MoO_6. The photocatalytic oxidizing activity of Bi_2MoO_6 was improved in the decomposition of organic pollutants in water. The mechanism of the enhancement may be resulted from the increase of the charge carriers' separation, which was confirmed by the electrochemical test. This work provides a solid evidence that BN sheets may be an excellent cocatalyst in promote the visible light-induced photocatalytic activity of a photocatalyst.

References

[1] A. Fujishima, K. Honda, Electrochemical photolysis of water at a semiconductor electrode, Nature, 238 (1972) 37-38.

[2] X. Meng, Z. Zhang, Bismuth-based Photocatalytic Semiconductors: Introduction, Challenges and Possible Approaches, Journal of Molecular Catalysis A: Chemical, 423 (2016) 533-549.

[3] X. Meng, Z. Li, Z. Zhang, Pd-nanoparticle-decorated peanut-shaped $BiVO_4$ with improved visible light-driven photocatalytic activity comparable to that of TiO_2 under UV light, Journal of Catalysis, 356 (2017) 53-64.

[4] X. Meng, Z. Zhang, Bi_2MoO_6 co-modified by reduced graphene oxide and palladium (Pd^{2+} and Pd^0) with enhanced photocatalytic decomposition of phenol, Applied Catalysis B: Environmental, 209 (2017) 383-393.

[5] X. Meng, Z. Li, Z. Zhang, Highly efficient degradation of phenol over a Pd-BiOBr Mott–Schottky plasmonic photocatalyst, Mater Res Bull, 99 (2018) 471-478.

[6] R.a. He, S. Cao, P. Zhou, J. Yu, Recent advances in visible light Bi-based photocatalysts, Chinese J Catal, 35 (2014) 989-1007.

[7] Z. Li, X. Meng, Z. Zhang, Recent Development on MoS_2-based Photocatalysis: a Review, Journal of Photochemistry and Photobiology C: Photochemistry Reviews, 35 (2018) 39-55.

[8] Z. Li, X. Meng, Z. Zhang, Few-layer MoS_2 nanosheets-deposited on Bi_2MoO_6 microspheres: A Z-scheme visible-light photocatalyst with enhanced activity, Catal. Today, 315 (2018) 67-78.

[9] D. Amaranatha Reddy, R. Ma, M.Y. Choi, T.K. Kim, Reduced graphene oxide wrapped ZnS–Ag_2S ternary composites synthesized via hydrothermal method: Applications in photocatalyst degradation of organic pollutants, Appl Surf Sci, 324 (2015) 725-735.

[10] D.A. Reddy, S. Lee, J. Choi, S. Park, R. Ma, H. Yang, T.K. Kim, Green synthesis of AgI-reduced graphene oxide nanocomposites: Toward enhanced visible-light photocatalytic activity for organic dye removal, Appl Surf Sci, 341 (2015) 175-184.

[11] J. Choi, D.A. Reddy, M.J. Islam, R. Ma, T.K. Kim, Self-assembly of CeO_2 nanostructures/reduced graphene oxide composite aerogels for efficient photocatalytic degradation of organic pollutants in water, Journal of Alloys and Compounds, 688 (2016) 527-536.

[12] S. Lee, D. Amaranatha Reddy, T.K. Kim, Well-wrapped reduced graphene oxide nanosheets on $Nb_3O_7(OH)$ nanostructures as good electron collectors and transporters for efficient photocatalytic degradation of rhodamine B and phenol, RSC Advances, 6 (2016) 37180-37188.

[13] Z. Li, X. Meng, Z. Zhang, Hexagonal SnS nanoplates assembled onto hierarchical Bi_2WO_6 with enhanced photocatalytic activity in detoxification and disinfection, J Colloid Interf Sci, 537 (2019) 345-357.

[14] Z. Li, X. Meng, Z. Zhang, An Effective Approach to Improve the Photocatalytic Activity of Graphitic Carbon Nitride via Hydroxyl Surface Modification, Catalysts, 9 (2018) 17.

[15] J. Wang, J. Shen, D. Fan, Z. Cui, X. Lü, J. Xie, M. Chen, BN nanosheet: An efficient carriers transfer promoter and stabilizer to enhance the photocatalytic performance of Ag_2CO_3, Mater. Lett., 147 (2015) 8-11.

[16] X. Meng, Z. Zisheng, Two Dimensional Graphitic Materials for Photoelectrocatalysis: A Short Review, Catalysis Today, (2018).

[17] J. Choi, D.A. Reddy, T.K. Kim, Enhanced photocatalytic activity and anti-photocorrosion of AgI nanostructures by coupling with graphene-analogue boron nitride nanosheets, Ceram Int, 41 (2015) 13793-13803.

[18] J.N. Coleman, M. Lotya, A. O'Neill, S.D. Bergin, P.J. King, U. Khan, K. Young, A. Gaucher, S. De, R.J. Smith, I.V. Shvets, S.K. Arora, G. Stanton, H.-Y. Kim, K. Lee, G.T. Kim, G.S. Duesberg, T. Hallam, J.J. Boland, J.J. Wang, J.F. Donegan, J.C. Grunlan, G. Moriarty, A. Shmeliov, R.J. Nicholls, J.M. Perkins, E.M. Grieveson, K. Theuwissen, D.W. McComb, P.D. Nellist, V. Nicolosi, Two-Dimensional Nanosheets Produced by Liquid Exfoliation of Layered Materials, Science, 331 (2011) 568-571.

[19] Z. Li, X. Meng, Z. Zhang, Few-layer MoS_2 nanosheets-deposited on Bi_2MoO_6 microspheres: A Z-scheme visible-light photocatalyst with enhanced activity, Catalysis

Today, (2018).

[20] X. Meng, Z. Li, H. Zeng, J. Chen, Z. Zhang, MoS_2 quantum dots-interspersed Bi_2WO_6 heterostructures for visible light-induced detoxification and disinfection, Applied Catalysis B: Environmental, 210 (2017) 160-172.

[21] G. Kresse, J. Furthmüller, Efficient iterative schemes for ab initio total-energy calculations using a plane-wave basis set, Phys Rev B, 54 (1996) 11169-11186.

[22] G. Kresse, J. Hafner, Ab initio, Phys Rev B, 47 (1993) 558-561.

[23] P.E. Blöchl, Projector augmented-wave method, Phys Rev B, 50 (1994) 17953-17979.

[24] J.P. Perdew, K. Burke, M. Ernzerhof, Generalized Gradient Approximation Made Simple, Phys Rev Lett, 77 (1996) 3865-3868.

[25] Y. Xu, H. Xu, H. Li, J. Xia, C. Liu, L. Liu, Enhanced photocatalytic activity of new photocatalyst Ag/AgCl/ZnO, J. Alloys Compd., 509 (2011) 3286-3292.

[26] H. Xu, L. Liu, Y. Song, L. Huang, Y. Li, Z. Chen, Q. Zhang, H. Li, BN nanosheets modified WO_3 photocatalysts for enhancing photocatalytic properties under visible light irradiation, J. Alloys Compd., 660 (2016) 48-54.

[27] M. Kruk, M. Jaroniec, Gas Adsorption Characterization of Ordered Organic−Inorganic Nanocomposite Materials, Chem Mater, 13 (2001) 3169-3183.

[28] J. Bi, W. Fang, L. Li, X. Li, M. Liu, S. Liang, Z. Zhang, Y. He, H. Lin, L. Wu, S. Liu, P.K. Wong, Ternary reduced-graphene-oxide/Bi_2MoO_6/Au nanocomposites with enhanced photocatalytic activity under visible light, J. Alloys Compd., 649 (2015) 28-34.

[29] J. Ma, L.-Z. Zhang, Y.-H. Wang, S.-L. Lei, X.-B. Luo, S.-H. Chen, G.-S. Zeng, J.-P.

Zou, S.-L. Luo, C.-T. Au, Mechanism of 2,4-dinitrophenol photocatalytic degradation by ζ-Bi_2O_3/Bi_2MoO_6 composites under solar and visible light irradiation, Chem. Eng. J., 251 (2014) 371-380.

[30] J. Di, J. Xia, M. Ji, B. Wang, S. Yin, Q. Zhang, Z. Chen, H. Li, Advanced photocatalytic performance of graphene-like BN modified BiOBr flower-like materials for the removal of pollutants and mechanism insight, Applied Catalysis B: Environmental, 183 (2016) 254-262.

[31] X. Meng, L. Jiang, W. Wang, Z. Zhang, Enhanced Photocatalytic Activity of BiOBr/ZnO Heterojunction Semiconductors Prepared by Facile Hydrothermal Method, International Journal of Photoenergy, 2015 (2015) 9.

[32] X. Meng, Z. Zhang, Synthesis, Analysis, and Testing of BiOBr-Bi_2WO_6 Photocatalytic Heterojunction Semiconductors, International Journal of Photoenergy, 2015 (2015) 12.

[33] X. Meng, Z. Zhang, Facile synthesis of BiOBr/Bi_2WO_6 heterojunction semiconductors with high visible-light-driven photocatalytic activity, Journal of Photochemistry and Photobiology A: Chemistry, 310 (2015) 33-44.

[34] X. Hu, X. Meng, Z. Zhang, Synthesis and Characterization of Graphene Oxide-Modified Bi_2WO_6 and Its Use as Photocatalyst, International Journal of Photoenergy, 2016 (2016) 8.

[35] X. Meng, Z. Zhang, Ag/AgCl Loaded Bi_2WO_6 Composite: A Plasmonic Z-Scheme Visible Light-Responsive Photocatalyst, International Journal of Photoenergy, 2016 (2016) 11.

[36] L. Pan, J.-J. Zou, S. Wang, Z.-F. Huang, X. Zhang, L. Wang, Enhancement of visible-

light-induced photodegradation over hierarchical porous TiO_2 by nonmetal doping and water-mediated dye sensitization, Appl Surf Sci, 268 (2013) 252-258.

[37] P. Chen, Y. Cai, J. Wang, K. Wang, Y. Tao, J. Xue, H. Wang, Preparation of protonized titanate nanotubes/Fe_3O_4/TiO_2 ternary composites and dye self-sensitization for visible-light-driven photodegradation of Rhodamine B, Powder Technol, 326 (2018) 272-280.

[38] S. Meng, X. Ye, X. Ning, M. Xie, X. Fu, S. Chen, Selective oxidation of aromatic alcohols to aromatic aldehydes by BN/metal sulfide with enhanced photocatalytic activity, Applied Catalysis B: Environmental, 182 (2016) 356-368.

[39] F.-X. Xiao, S.-F. Hung, H.B. Tao, J. Miao, H.B. Yang, B. Liu, Spatially branched hierarchical ZnO nanorod-TiO_2 nanotube array heterostructures for versatile photocatalytic and photoelectrocatalytic applications: towards intimate integration of 1D–1D hybrid nanostructures, Nanoscale, 6 (2014) 14950-14961.

[40] X. Meng, Z. Zhang, Plasmonic ternary Ag–rGO–Bi_2MoO_6 composites with enhanced visible light-driven photocatalytic activity, J. Catal., 344 (2016) 616-630.

[41] B. Xin, Z. Ren, P. Wang, J. Liu, L. Jing, H. Fu, Study on the mechanisms of photoinduced carriers separation and recombination for Fe^{3+}–TiO_2 photocatalysts, Appl Surf Sci, 253 (2007) 4390-4395.

[42] J. Chen, J. Zhu, Z. Da, H. Xu, J. Yan, H. Ji, H. Shu, H. Li, Improving the photocatalytic activity and stability of graphene-like BN/AgBr composites, Appl. Surf. Sci., 313 (2014) 1-9.

[43] Q. Xiang, J. Yu, M. Jaroniec, Preparation and Enhanced Visible-Light Photocatalytic H_2-Production Activity of Graphene/C_3N_4 Composites, The Journal of Physical Chemistry

C, 115 (2011) 7355-7363.

[44] Y.-S. Xu, W.-D. Zhang, Anion exchange strategy for construction of sesame-biscuit-like $Bi_2O_2CO_3/Bi_2MoO_6$ nanocomposites with enhanced photocatalytic activity, Applied Catalysis B: Environmental, 140-141 (2013) 306-316.

[45] Y. Xu, M.A.A. Schoonen, The absolute energy positions of conduction and valence bands of selected semiconducting minerals, Am. Mineral., 85 (2000) 543-556.

[46] Y. Chen, G. Tian, Y. Shi, Y. Xiao, H. Fu, Hierarchical MoS_2/Bi_2MoO_6 composites with synergistic effect for enhanced visible photocatalytic activity, Applied Catalysis B: Environmental, 164 (2015) 40-47.

SECTION V: SURFACE MODIFIED C_3N_4 WITH ENHANCED PHOTOCATALYTIC ACTIVITY

Chapter 8 An Effective Approach to Improve the Photocatalytic Activity of Graphitic Carbon Nitride via Hydroxyl Surface Modification

Zizhen Li, Xiangchao Meng and Zisheng Zhang

Catalysts, *9 (1)*, 17 (2019)

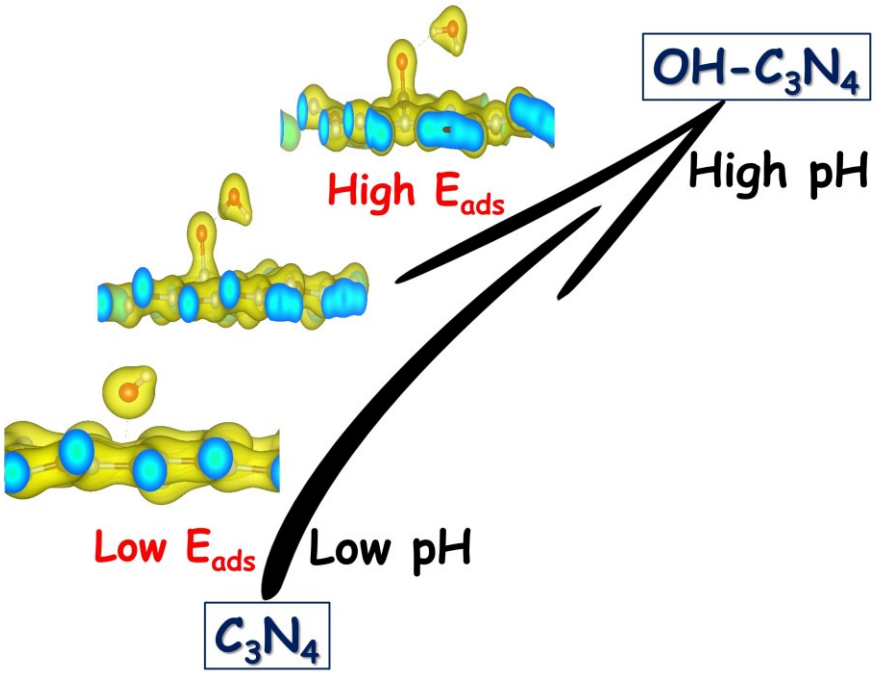

Abstract

In this work, we have developed a hydrothermal method to modify g-C_3N_4 with hydroxyl surface modification. Modified g-C_3N_4 has exhibited higher photocatalytic activity in the removal of phenolic compounds under visible light. The improvement may be due to the following merits: 1) Tuning of the hydrophobic surface of g-C_3N_4 to be hydrophilic; 2) improved adsorption energy, and 3) narrowed band gap for g-C_3N_4 after hydroxyl surface modification. This method is easy-to-operate, very effective in adding hydroxyl groups on

the surface of C_3N_4, and may be extended to other systems to promote their photocatalytic activities in water treatment.

8.1 Introduction

Graphitic carbon nitride (g-C_3N_4), as a fascinating conjugated polymer, has become a hot research topic [1]. As a metal-free photocatalytic semiconductor, g-C_3N_4 is very promising in energy storage and environmental remediation [2]. When g-C_3N_4 is implemented in photocatalytic water treatment, one of the hindrances is the hydrophobic properties of the surface. Photocatalysis is a process that occurs at the interface between the liquid and the solid phase, therefore, the adsorption of water as well as of the target pollutants is the first step and very significant. Surface modification may be an effective approach to improve the adsorption of water onto the surface of g-C_3N_4. Hydroxyl functional groups may be potential candidates in improving the hydrophilicity of C_3N_4 [3]. Our group had reported on the surface modification of C_3N_4 with hydroxyls using hydrogen peroxide (H_2O_2), and found that the photocatalytic activity of C_3N_4 was promoted [4]. Additionally, as reported by Li *et al.*, that the photocatalytic activity of C_3N_4 treated in an ammonia solution was improved due to the hydroxyl surface modification [5]. Motivated by this work, we herein developed a hydrothermal method to modify C_3N_4 by the addition of hydroxyls onto the surface. The pH of the hydrothermal treatment solution was explored, and the insight into the photocatalytic activity improvement was performed and discussed in this work.

8.2 Experimental

All chemicals were purchased from Fisher Scientific (Canada) unless otherwise mentioned, and used as received. C_3N_4 was prepared by directly heating melamine in a semi-closed

system to prevent the sublimation of melamine [6]. Typically, 10 g of melamine powder, in a crucible with a cover, was heated up to 550 °C in a muffle furnace with a heating rate of 2.5 °C/min, and the further deamination treatment was performed for 4h. After the crucible was naturally cooled down to room temperature, the yellowish powder was mounted and collected for further use. The surface modification of C_3N_4 with hydroxyls was conducted by hydrothermal treatment. Typically, 0.3 g of C_3N_4 was first dispersed into a 35 mL solution under ultrasonication for 30 min. Then, the suspension was transferred to a 50 mL Teflon-lined autoclave, which was heated up to 160 °C for 4h. The autoclave was then allowed to naturally cool down to room temperature, and the precipitates in the suspension were separated out through centrifugation, and washed with deionized distilled water, several times. To explore the effect of the pH of the solution in the hydrothermal treatment, it was adjusted using NaOH (1 mol/L) and HNO_3 (1 mol/L).

Morphology of the as-prepared C_3N_4 was investigated by a transmission electron microscope (TEM, JEM-2100F). Crystal structures of the as-prepared samples were explored using an X-ray powder diffraction instrument (Bruker-AXS, Karlsruhe, Germany). An ultraviolet-visible light diffuse reflectance spectrophotometer (DRS) was employed to determine the optical properties of the as-prepared samples. Fourier transform infrared spectroscopy (FTIR) was also done at room temperature with a Cary 630 (Agilent Technologies). Zeta potentials of hydroxyl-modified C_3N_4 were tested using a Zetasizer (Malvern Panalytical). DFT simulations were performed using the Vienna ab initio simulation package (VASP) [7, 8]. The ion-electron interaction is described with the projector augmented wave (PAW) method [9]. The electron exchange-correlation is represented by the Perdew, Burke, and Ernzerhof (PBE) function of the generalized

gradient approximation (GGA) [10]. A cut-off energy of 450 eV was used for the plane-wave basis set. The calculations were done on periodical supercells of the C_3N_4 monolayer with a 3 × 3 × 1 Monkhorst Pack k-point sampling. The charge density distribution and the distance between bonds were analyzed using VESTA [11].

The photocatalytic activity of as-prepared samples was evaluated with regard to the degradation of phenol under visible light irradiation. The light source was provided by a 300-W halogen tungsten projector lamp (Ushio) equipped with a UV cut-off (Kenko Zeta, transmittance >90%) to filter out wavelength below 400 nm. Typically, in each test, 0.10 g of photocatalyst was added into a 100 mL of phenol solution with an initial concentration of 10 mg (phenol)/L (pH 4.5). The mixture was magnetically stirred in the dark for 1h to reach an adsorption/desorption equilibrium prior to the photocatalysis experiment. After 3h, 1 mL aliquots were drawn and centrifuged. The supernatant was analyzed using a high-performance liquid chromatograph (HPLC, Agilent 1100 series) equipped with a UV-Vis detector. The total organic carbon (TOC) was evaluated on an Appollo 9000 TOC analyzer equipped with a non-dispersive Infra-Red (NDIR) detector. The combustion temperature was fixed at 750 °C. To explore the repeatability of the activity test, the photocatalytic activity for each sample was repeated for three times.

8.3 Results and discussions

The morphology of the as-prepared samples was investigated through TEM. As shown in the TEM image of C_3N_4 (Figure 8.1a), a layered structure was observed. Due to the ultrathin structure, the edge of the prepared C_3N_4 is partially curly, which is intended to decrease the surface tension. This is typical construction of exfoliated carbon scrolls by

peeling graphite [12]. After hydrothermal treatment, the morphology as shown in Figure 8.1b was negligibly influenced. The crystal structure of pure C_3N_4 as shown in Figure 8.1c, two obvious peaks can be observed at the 2θ of 13.0° and 27.5°, which agree well with the hexagonal phase of graphitic C_3N_4 (JCPDS 87-1526) [2]. With hydroxyl group modifications, as shown in Figure 8.1c, the crystal structure of C_3N_4 was negligibly influenced, indicating that the hydrothermal treatment may not influence the crystal structure of C_3N_4. The O 1s high-resolution spectra in Figure 8.1d can be fitted with a single peak located at 529.44 eV for g-C_3N_4, corresponding to the O-H bond. After hydrothermal treatment, the peak was negatively shifted by 0.66 eV, which may have resulted from the hydroxyl group being bonded with g-C_3N_4. The optical properties of the as-prepared samples were investigated using DRS, as plotted in Figure 8.1e, and a rapid increase of the intensity was found with a decrease in the wavelength of the incident to 490 nm. This may be due to the band transition. To evaluate the band gap energy for each sample, the classical Tauc equation was used as plotted in Figure 8.1f. It was found that the band gap for C_3N_4, as well as for hydroxyl-modified C_3N_4, was approximately equivalent to 2.54 eV. This confirms that there are no doped impurity energy levels within the band gap after the hydroxyl surface modification.

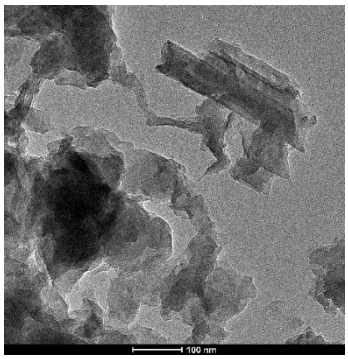

(**a**)

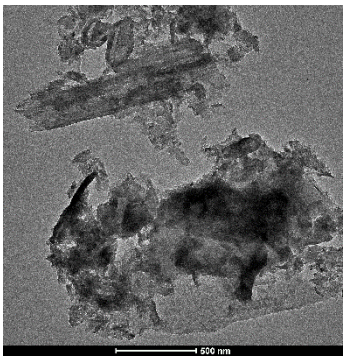

(**b**)

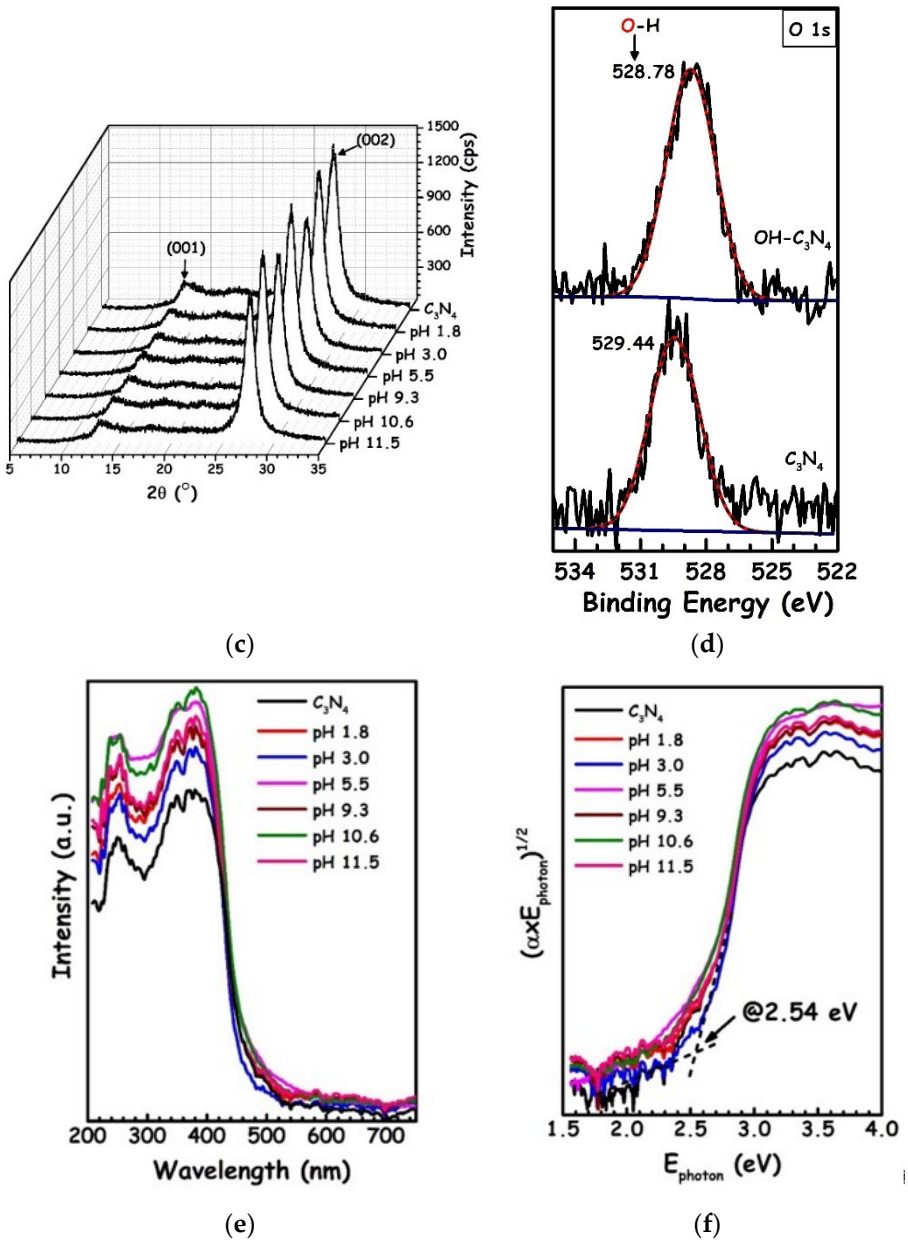

Figure 8.1. (a) TEM image of C_3N_4, (b) TEM image of C_3N_4 treated with a precursor solution with pH 5.5, (c) XRD patterns, (d) XPS scan for O 1s orbit, (e) DRS, and (f) $(\alpha \times E_{photon})^{1/2}$-$E_{photon}$ curves for the as-prepared samples.

To further explore the composition of the hydroxyl-modified C_3N_4, FT-IR spectra were used, and plotted in Figure 8.2a. The peak located at 810 cm^{-1} was assigned to the typical breathing mode of an *s*-triazine ring, and the peak located at 890 cm^{-1} may be due to the out-of-plane bending mode of N-H. A bunch of peaks located at the range of 1200–1700

cm^{-1} were ascribed to the stretching vibration modes of C-N and C=N heterocycles. The broad peak at 3000–3250 cm^{-1} may have resulted from the N-H stretching vibration of uncondensed amine and hydroxyl groups [13]. It can be found that the intensity of this peak increased when the pH of the solution increased. This phenomenon may be due to more hydroxyl groups being adsorbed on the surface of C_3N_4 in a solution with a higher pH; and the amine groups being possibly dissolved in a solution with a lower pH during the hydrothermal treatment, resulting in the reduction of the intensity of this peak. This is also confirmed by the fact that hydrothermal treatment in a solution with a high pH favors the addition of more hydroxyls onto C_3N_4. Zeta potentials for the as-prepared samples (Figure 8.2b) were negatively shifted with an increase in the pH of the solution in the hydrothermal treatment. This suggests that the zeta potentials became more negative as the amount of hydroxyl groups increased. The more negatively charged surface of the catalyst favors the adsorption of organic pollutants in water, which improves the photocatalytic activity.

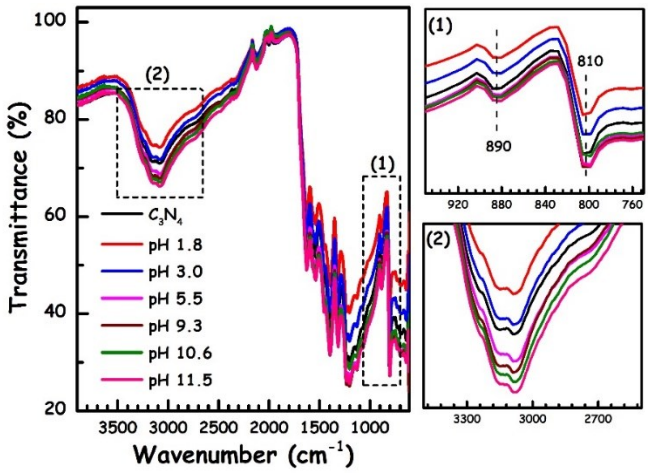

(a)

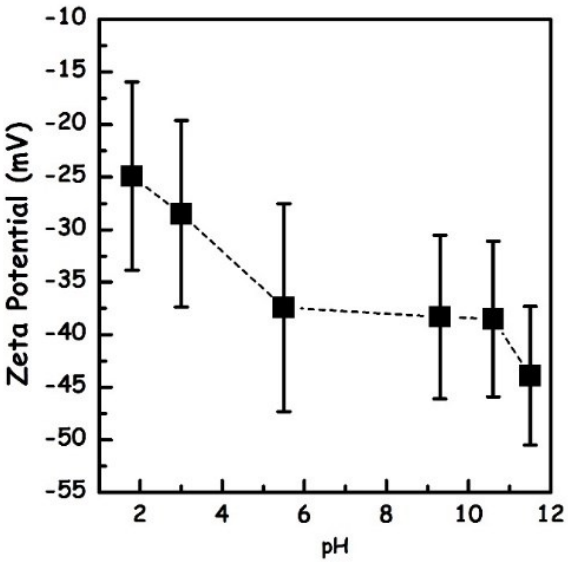

(**b**)

Figure 8.2. FT-IR spectra (full spectra and enlarged spectra), and zeta potentials for the as-prepared samples.

To further determine the mechanism of the hydroxyl modifications, DFT simulation was conducted, and the results were shown in Table 8.1. To determine the site on hydroxyl-bonded C_3N_4, the free energies of the crystals were calculated. It was found that the free energy of the crystal with OH that was bonded to the carbon of C_3N_4 (OH-C) was lower than that of the crystal with OH that was bonded to the nitrogen of C_3N_4 (OH-N). This suggests that the crystal may be more stable when the OH was bonded with the carbon of C_3N_4. The distance between H_2O and the site on C_3N_4 was also measured, and it was found that the distance was shortened when the C_3N_4 was modified with –OH. The adsorption energy of H_2O also increased with the modification of –OH onto C_3N_4. This suggests that the hydroxyl modification may be very promising in the improvement of the photocatalytic activity of C_3N_4 by enhancing the adsorption between the H_2O/organic and the photocatalyst surface. To further confirm this verdict, the photocatalytic activity of the as-prepared samples was evaluated in the decomposition of phenol under visible light, the

results of which were shown in Figure 8.3. It was found that with hydroxyl modification, both the conversion of phenol and the TOC (total organic carbon) in the solution was enhanced. In addition, the improvement also increased with an increase in the number of hydroxyls on the surface. This provides solid evidence that hydroxyl modification was very effective in enhancing the photocatalytic activity of C_3N_4 through the improvement of the adsorption capacity.

Table 8.1. Properties of hydroxyl-modified C_3N_4 and water adsorbed on the surface of C_3N_4 with/without hydroxyl modification. (d is the distance between the atom in H_2O and the adsorption site on C_3N_4).

Composition	**Charge Density Distribution**	**Free Energy (eV)**	***d* (Å)**	***E_{ads}* (eV)**
C_3N_4	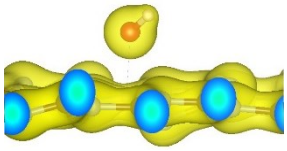	-235.01	2.025	-0.67
OH-C	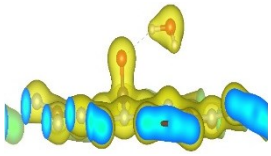	-243.98	1.936	-0.89
OH-N	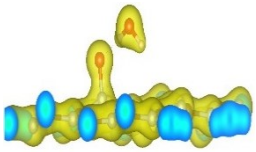	-240.08	1.762	-1.07

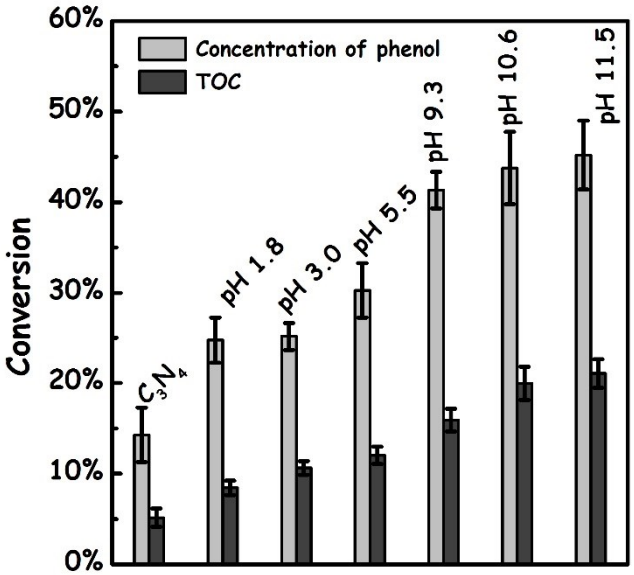

Figure 8.3. Photocatalytic conversion of phenol in the presence of g-C_3N_4 and modified g-C_3N_4 under visible light for 3h. (pH in this figure represents the pH of the solution in the hydrothermal surface modification, each data point and error bar represents the mean and the standard errors, respectively, of independent triplicates).

8.4 Conclusions

Hydrothermal treatment may be an effective approach in the modification of the surface of g-C_3N_4 via the addition of hydroxyl functional groups. The primary function of hydroxyls on the surface is to increase the adsorption rate of water, as well as that of organics in water. This improvement may directly improve the photocatalytic activity. This work provides an effective method to modify the surface with hydroxyls, which can be extended to other applications, such as for other semiconductors with a hydrophobic surface and in membrane science.

References

[1] W.-J. Ong, L.-L. Tan, Y.H. Ng, S.-T. Yong, S.-P. Chai, Graphitic Carbon Nitride (g-C_3N_4)-Based Photocatalysts for Artificial Photosynthesis and Environmental Remediation:

Are We a Step Closer To Achieving Sustainability?, Chem Rev, 116 (2016) 7159-7329.

[2] X. Wang, K. Maeda, A. Thomas, K. Takanabe, G. Xin, J.M. Carlsson, K. Domen, M. Antonietti, A metal-free polymeric photocatalyst for hydrogen production from water under visible light, Nat Mater, 8 (2008) 76.

[3] W.-J. Kim, S. Kim, B.S. Lee, A. Kim, C.S. Ah, C. Huh, G.Y. Sung, W.S. Yun, Enhanced Protein Immobilization Efficiency on a TiO2 Surface Modified with a Hydroxyl Functional Group, Langmuir, 25 (2009) 11692-11697.

[4] Y. Zheng, Z. Zhang, C. Li, S. Proulx, Surface hydroxylation of graphitic carbon nitride: Enhanced visible light photocatalytic activity, Mater Res Bull, 84 (2016) 46-56.

[5] F.-t. Li, Y. Zhao, Q. Wang, X.-j. Wang, Y.-j. Hao, R.-h. Liu, D. Zhao, Enhanced visible-light photocatalytic activity of active Al2O3/g-C3N4 heterojunctions synthesized via surface hydroxyl modification, J Hazard Mater, 283 (2015) 371-381.

[6] S.C. Yan, Z.S. Li, Z.G. Zou, Photodegradation Performance of g-C3N4 Fabricated by Directly Heating Melamine, Langmuir, 25 (2009) 10397-10401.

[7] G. Kresse, J. Hafner, Ab initio, Phys Rev B, 47 (1993) 558-561.

[8] G. Kresse, J. Furthmüller, Efficient iterative schemes for ab initio total-energy calculations using a plane-wave basis set, Phys Rev B, 54 (1996) 11169-11186.

[9] P.E. Blöchl, Projector augmented-wave method, Phys Rev B, 50 (1994) 17953-17979.

[10] J.P. Perdew, K. Burke, M. Ernzerhof, Generalized Gradient Approximation Made Simple, Phys Rev Lett, 77 (1996) 3865-3868.

[11] K. Momma, F. Izumi, VESTA 3 for three-dimensional visualization of crystal,

volumetric and morphology data, J Appl Crystallogr, 44 (2011) 1272-1276.

[12] Z. Lin, X. Wang, Nanostructure Engineering and Doping of Conjugated Carbon Nitride Semiconductors for Hydrogen Photosynthesis, Angew Chem-Ger Edit, 125 (2013) 1779-1782.

[13] Y. Huang, Y. Wang, Y. Bi, J. Jin, M.F. Ehsan, M. Fu, T. He, Preparation of 2D hydroxyl-rich carbon nitride nanosheets for photocatalytic reduction of CO2, RSC Advances, 5 (2015) 33254-33261.

Chapter 9 Fabrication of Surface hydroxyl modified g-C_3N_4 with enhanced photocatalytic oxidation activity

Zizhen Li, Xiangchao Meng and Zisheng Zhang

Catalysis Science and Technology, *9*, 3979-3993, 2019

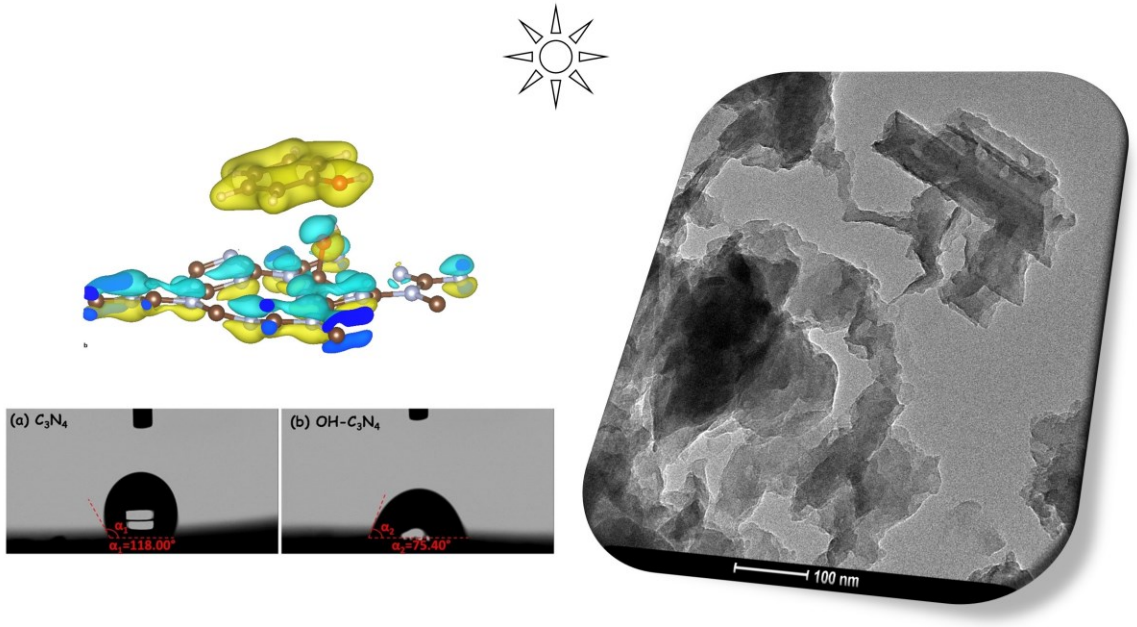

Abstract

Graphitic carbon nitride (g-C_3N_4), a fascinating conjugated polymer, has drawn extensive attention as a metal-free, visible light-responsive photocatalyst in the areas of solar energy conversion and environmental remediation. In this work, the visible light-driven photocatalytic properties of g-C_3N_4 were enhanced by a simple surface hydroxyl modification without damage to its composite structure. A facile hydrothermal approach

was developed and systematically studied. The photocatalytic activity of hydroxyl-modified g-C_3N_4 was evaluated with regard to the degradation of a group of refractory organic pollutants, phenol, and phenolic compounds in water under visible light. The enhancement of the photocatalytic activity of g-C_3N_4 after surface hydroxyl modification was assessed by experimental testing results and by theoretical studies using DFT. The following merits synergistically contribute to the improvement: 1) improved adsorption energy between organic pollutants and the surface of the photocatalyst; 2) reinforced hydrophilicity of the surface of g-C_3N_4; 3) positively-shifted valence-band potential; and 4) improved charge separation in the formation of a heterostructure between g-C_3N_4 and OH-C_3N_4. This work provides an effective method to modify a surface with hydroxyl functional groups, so as to improve its photocatalytic activity of the support.

9.1 Introduction

Photocatalysis is a process where light energy is converted into chemical energy in the presence of a catalyst. The process has gained attention in recent years due to its applications in environmental remediation and energy storage. For energy storage photocatalysis, photogenerated electrons with a strong reductive capacity are used to reduce chemicals such as water, CO_2 and N_2 into highly valued products, such as H_2, hydrocarbons and ammonia [1-3]. The flat-band potential of the conduction band plays a significant role in the photolysis implemented in energy storage, and a more negative conduction band potential favors the improvement of photocatalytic reduction processes. By contrast, for environmental remediation photocatalysis, a photocatalytic oxidization process occurs between the adsorbed species, such as organics and bacteria, and the photogenerated oxidative species. Notably, the photocatalytic reduction process is an ‘up-

hill' process, while the photocatalytic oxidation process is a 'down-hill' process [4]. As a result, photocatalysis implemented in energy storage is usually more challenging compared to that in environmental remediation.

The properties of a photocatalyst are crucial in determining its viability for application in a given photocatalytic process. Since the discovery of the Honda-Fujishima effect in 1967 [5], TiO_2 has become the most studied and commercialized photocatalyst due to its superior properties, including its non-toxicity, low cost and straightforward synthesis [6-8]. However, the drawbacks of this material in practical applications are still apparent. The most well-known drawback of TiO_2 is the intrinsically wide band gap that prevents TiO_2 from responding to anything but ultraviolet (UV) light. To fully utilize solar light, either modifications to TiO_2 or the development of new materials with narrow band gaps is required. Among these newly-reported photocatalytic materials, graphitic carbon nitride (g-C_3N_4) is a fascinating conjugated polymer that has become the focus of new research and has drawn broad interdisciplinary attention as a metal-free, visible light-responsive photocatalyst in the area of solar energy conversion and environmental remediation [9]. Polymeric g-C_3N_4 consists of earth-abundant carbon and nitrogen elements and it is versatile in providing reactions to alter its surface activity without fundamentally changing its theoretical structure or composition. The discovery and implementation of g-C_3N_4 into photocatalysis was first reported in 2009 by Wang et al. [10] Since then, g-C_3N_4 has been extensively studied, and the superiorities of g-C_3N_4 in photocatalysis applications have been shown, including its facile synthesis, advantageous electronic band structure, high physicochemical stability and 'earth-abundant' nature [11-14]. Notably, g-C_3N_4 can be fabricated by a thermal polymerization of abundant nitrogen-rich precursors such as urea,

melamine, dicyandiamide, thiourea and ammonium thiocyanate [15]. For applications of g-C_3N_4 in photocatalytic oxidation processes, there still remain several challenges, namely, the high recombination of photogenerated charge carriers and the weak adsorption energy of organic pollutants. Aiming to overcome these problems, various approaches were adopted, such as surface modification [16], doping [17], formation of heterostructures [18] and fabrication of plasmonic photocatalysts [19].

We have reported on the surface modification of g-C_3N_4 by loading hydroxyl functional groups using hydrogen peroxide [20]. It was found that the photocatalytic activity of g-C_3N_4 was greatly improved with the surface hydroxyl modification. In order to find an alternative method so as to simplify this process, and motivated by the work reported by Zhao et al. [21], we systematically studied hydroxyl surface modification when using a hydrothermal method. The photocatalytic activity of OH-modified g-C_3N_4 was evaluated by the degradation of a refractory organic pollutant, phenol, and phenolic compounds in water under visible light.

9.2 Experimental

9.2.1 Preparation of g-C_3N_4

All chemicals were purchased from Fisher Scientific (Canada) and used as received unless otherwise mentioned. Bulk g-C_3N_4 was prepared via a simple thermal polycondensation method [10]. In a typical run, 10 g of melamine was put into a covered crucible and heated to 550°C at a rate of 2.5°C/min in a muffle furnace. Subsequently, the sample was maintained at 550°C for 4 h. The resulting powder was then ground, collected, and stored for further use.

9.2.2 Surface hydroxyl modification of g-C_3N_4

Hydroxyl modified g-C_3N_4 was prepared by a hydrothermal method. In a typical run, 0.3 g of g-C_3N_4 was dispersed into 35 mL of ammonia solution with a known concentration. In order to explore the influence of ammonia concentration on surface modification, the mass fraction of ammonia was varied between 0% (deionized distilled water, DDW), 1%, 5% and 20%. The suspension was ultrasonicated for 30 min, and then transferred into a 50 mL Teflon-lined stainless steel autoclave. The autoclave was heated up to 160°C and maintained at this temperature for 4 h. The resulting product was separated by centrifugation and dried at 60°C overnight. The sample treated with 1% ammonia was named OH-C_3N_4.

9.2.3 Characterizations

The morphologies of prepared samples were observed by a field-emission scanning electron microscope (FE-SEM, JEOL JSM-7500F) and a transmission electron microscope (TEM, JEM-2100F). X-ray diffraction (XRD) analysis was carried out by using a Rigaku Ultima IV Diffractometer with Cu Kα radiation (λ = 0.15418 nm) at 40 kV and 44 mA. XRD patterns were recorded at 2θ from 5° to 35°. Fourier transform infrared (FT-IR) spectroscopic analysis was performed using a Cary 630 FT-IR spectrometer (Agilent Technologies). The surface chemical composition and states were evaluated by a XSAM-800 X-ray Photoelectron Spectroscope (XPS). The optical properties of the samples were measured by the ultraviolet-visible diffuse reflectance spectra (DRS) using a Thermo Evolution 300 spectrophotometer. The zeta potentials of g-C_3N_4 samples were tested by using a Zetasizer (Malvern Panalytical). The hydrophilicity of prepared samples was evaluated by coating the powder samples on a non-woven fiber (NWF). As-prepared

samples (0.1 g) were dispersed in 5 mL anhydrous *N,N*-dimethylacetamide (DMAc) with a purity of 99.8% that was purchased from Sigma-Aldrich Inc. (St. Louis, MO) and the resulting suspension was cast by a casting bar (250 μm thickness) onto the NWF material by using a uniform-speed automatic film applicator (model AFA-II, Beijing, China). The cast film was immersed in distilled water at 25 °C along with the backing material to induce the phase inversion process after exposure to air for approximately 1 min. Thereafter, the membranes were kept in the water bath for 24 h while the water was replaced every 6 h to make sure the solvent DMAc was removed [22]. The coated membranes were then dried at room temperature for 24 h in preparation for testing. The water contact angle was measured using a VCA Optima Surface Analysis System (AST Product, Inc. Billerica, MA) to evaluate the membrane surface hydrophobicity. Basicity measurements were performed by CO_2-TPD using 200 mg samples with a Chemisorption Analyzer (Finesorb-3010). Electrochemical properties of the prepared samples were analyzed on a CHI 604E electrochemical analyzer (CH Instruments Inc., USA) using a platinum wire as the counter electrode, a calomel reference electrode and a working electrode. The working electrode was composed of indium tin oxide (ITO, 75 × 25 × 1.1 mm, 15 - 25 Ω, Sigma-Aldrich Canada Co.), glass-coated with the prepared samples. Electrochemical impedance spectroscopy (EIS) was performed with frequencies in the range of 0 – 1,000,000 Hz and a sinusoidal wave of 5 mV. The photocurrent was also measured with an on-off lamp. The electrolyte used was Na_2SO_4 with a concentration of 0.05 mol/L.

9.2.4 Electronic structure calculation

DFT simulations were performed using the Vienna *ab initio* simulation package (VASP) [23, 24]. The ion-electron interaction is described by the projector augmented wave (PAW)

method [25]. The electron exchange-correlation is represented by the Perdew, Burke, and Ernzerhof (PBE) function of generalized gradient approximation (GGA) [26]. A cut-off energy of 450 eV was used for the plane-wave basis set. The calculations were done on periodical supercells of C_3N_4 monolayer with 3 × 3 × 1 Monkhorst Pack k-point sampling. The charge density distribution and the distance between bonds were analyzed using VESTA [27]. The convergence tolerance for the geometry optimization was set to be 1.0 × 10^{-5} eV/atom for energy and 0.02 eV/Å for maximum force. The optimized structures of g-C_3N_4 and OH-C_3N_4 are shown in Fig. 9.1. After geometry optimization, the average potential profile was calculated to obtain the work functions of g-C_3N_4 and OH-C_3N_4. The work function (Φ) can be calculated by Equation 1 [28]:

$$\Phi = E_{vac} - E_f \qquad \textbf{Equation 1}$$

where E_{vac} and E_f are the vacuum energy and the Fermi energy, respectively. Water and phenol adsorption on the surface of g-C_3N_4 and OH-C_3N_4 was investigated by the calculation of the adsorption energy using Equation 2:

$$E_{ads} = E_{slab} + E_{adsorbate} - E_{slab+adsorbate} \qquad \textbf{Equation 2}$$

where E_{ads} is adsorption energy (eV), $E_{slab+adsorbate}$, E_{slab} and $E_{adsorbate}$ represent the total energies of the system, the slab (g-C_3N_4 or OH-C_3N_4) and the isolated adsorbate molecules (water or phenol), respectively.

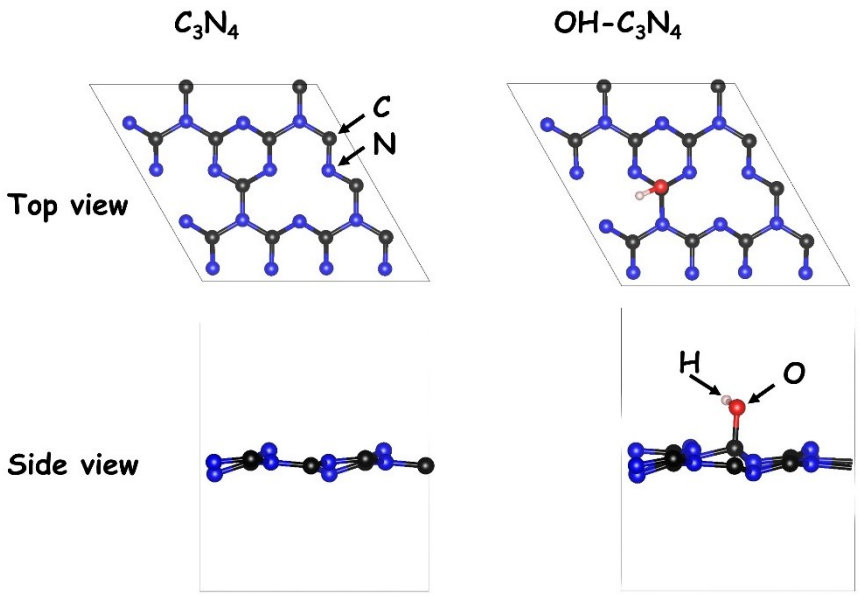

Figure 9.1. Optimized structures of g-C_3N_4 and OH-C_3N_4.

9.2.5 Photocatalytic activity testing

The photocatalytic activities of prepared samples were evaluated by the degradation of phenolic compounds (phenol, 2-chlorophenol and catechol) under visible light. The light source was provided by a 300 W halogen tungsten projector lamp (Ushio) equipped with a UV cut-off ($\lambda > 410$ nm) and the reaction temperature was maintained at 20°C. For each batch, 0.05 g of photocatalyst was mixed with 100 mL of phenol solution (10 ppm) in a 500 mL beaker. Before illumination, the reaction mixture was magnetically stirred for 30 min to reach the adsorption/desorption equilibrium. After that, aliquots were collected every 1 h and the concentration of the supernatant was analyzed by a high-performance liquid chromatograph (HPLC, Agilent 1100 series) equipped with a UV–vis detector. A ZORBAX Eclipse Plus C18 column (4.6 × 250 mm) was used at a temperature of 60°C. The detecting wavelength was fixed at 270 nm for the detection of phenol and possible intermediates. The flow phase was composed of methanol (55%, V/V) and water (45%,

V/V) at a flow rate of 0.6 mL/min. The injection volume was set to 25 μL. Meanwhile, the total organic carbon (TOC) of the samples collected at 0 h, 2 h, 4 h, and 6 h was measured by an Apollo 9000 TOC analyzer equipped with a Non-Dispersive Infra-Red (NDIR) detector at a combustion temperature of 750 °C. The reusability of OH-C_3N_4 was evaluated by separating the catalysts out from the suspension following a single run. The catalysts were then mixed with fresh model wastewater (phenol dissolved in water with an initial concentration of 10 mg/L) to start another run. In total, five runs were performed with the separated catalysts.

The concentration of OH radicals produced during photocatalysis was determined using *p*-chlorobenzoic acid (pCBA) as a probe. The initial concentration of pCBA was 10 mg/L, the catalyst dosage amount was 1 g/L and the solution volume was 100 mL. Photocatalytic degradation of pCBA was carried out for 90 min. Aliquots were taken and centrifuged and the supernatant was analyzed using HPLC with a detecting wavelength of 254 nm. All the other parameters were kept the same for the detection of the aforementioned phenol. For comparison, TiO_2 (anatase powder, Fisher Scientific Canada, ACS certified) was also tested.

9.2.6 Temporal course of inactivation

Non-pathogenic wild-type *Escherichia coli* K-12 (TG1 strain) was used as the target microorganism for bacterial inactivation studies. Before the inactivation experiment, *E. coli* K-12 strains were aerobically cultured overnight at 37 °C in a Luria-Bertani medium (Difco LB broth, Miller; containing 10 g/L tryptone, 5 g/L yeast extract, and 10 g/L NaCl) on a rotary shaker at 250 rpm until the stationary phase was reached. After serial dilution with 0.9% saline, an initial bacterial suspension with a concentration of 10^6 CFU (colony

forming units)/mL was obtained. Afterwards, 0.05 g photocatalyst was mixed with 100 mL of the bacterial suspension and magnetically stirred for 30 min in the dark. Upon illumination, aliquots were collected every 20 min and serially diluted using saline. Then, diluted samples were spread onto an LB agar plate and incubated at 37 °C for 18 hr. The bacteria were quantified using a standard plate count method (for viable and cultivable bacteria) in units of CFU/mL [29]. All experiments were performed in triplicate, and all materials were sterilized before use.

9.3 Results and discussion

9.3.1 Morphologies and chemical compositions

The morphology and structure of prepared samples were investigated using SEM and TEM, as illustrated in Fig. 9.2. It can be observed that the pure g-C_3N_4 exhibited a typical layered and plate-like structure (Fig. 9.2a and 9.2c). Due to the ultrathin structure, the edge of the prepared C_3N_4 is partially curly, which is intended to decrease the surface tension. This is typical in the construction of exfoliated carbon scrolls by peeling graphite [30]. After ammonia treatment as shown in Fig. 9.2b and 9.2d, no evident difference in morphology can be observed in the TEM image (Fig. 9.2d). To further explore the corrosion observed in the TEM image, XRD and FTIR were employed to identify the stability of the crystal structure and the modification of chemical functional groups on g-C_3N_4 layers, respectively, and the results were illustrated in Fig. 9.3. The crystal structure of pure C_3N_4 is shown in Fig. 9.3a, where two peaks can be observed at a 2θ of 13.0° and 27.5°. These peaks may be ascribed to the (100) plane and (002) plane, respectively, which agree well with the hexagonal phase of graphitic C_3N_4 (JCPDS 87-1526) [10]. The (002) peak was attributed

to a characteristic interlayer stacking peak of aromatic systems for graphitic materials. The calculated interplanar distance of aromatic units (d = 0.326 nm for g-C_3N_4 and 0.323 nm for OH-C_3N_4, respectively) is significantly lower than that of the crystalline g-C_3N_4 (d = 0.336 nm). The dense structure can be attributed to the localization of electrons and stronger binding between the layers. The interplanar distance for the (100) crystal plane, calculated as 0.650 nm for g-C_3N_4 and 0.671 nm for OH-C_3N_4, respectively, were slightly lower than the size of one tris-*s*-triazine unit (*ca.* 0.672 nm), which was probably due to the presence of a small tilt angularity in the structure [31]. Comparing the interplanar distances for these two peaks (*i.e.* peaks located at 13.0° and 27.5°), it can be deduced that the binding between C_3N_4 layers was negligibly influenced, but the tilt angularity was slightly reduced after the hydrothermal treatment. The lattice parameters for g-C_3N_4 were negligibly affected after the hydrothermal treatment, indicating that the primary crystal structure of C_3N_4 was also negligibly influenced. Furthermore, for the FTIR spectra for both pure g-C_3N_4 and modified g-C_3N_4 samples (Fig. 9.3b), the peaks located at 798 cm^{-1} may have originated from the out-of-plane bending modes of the triazine units [32]. The peaks located in the range of approximately 1100 to 1650 cm^{-1} may be ascribed to the aromatic C-N stretching associated with the skeletal stretching vibrations of the *s*-triazine ring system [32, 33]. Besides that, the wide peaks located between 3000 to 3400 cm^{-1} may have resulted from both –NH stretching vibration modes and surface hydroxyl groups [32, 34]. It should be noted that the shoulder peaks at 3164 cm^{-1}, which were mainly due to hydroxyl functional groups, became stronger with the hydrothermal treatment. This phenomenon indicates that additional hydroxyl groups were added onto the surface of g-C_3N_4 after the ammonia treatment [21, 35].

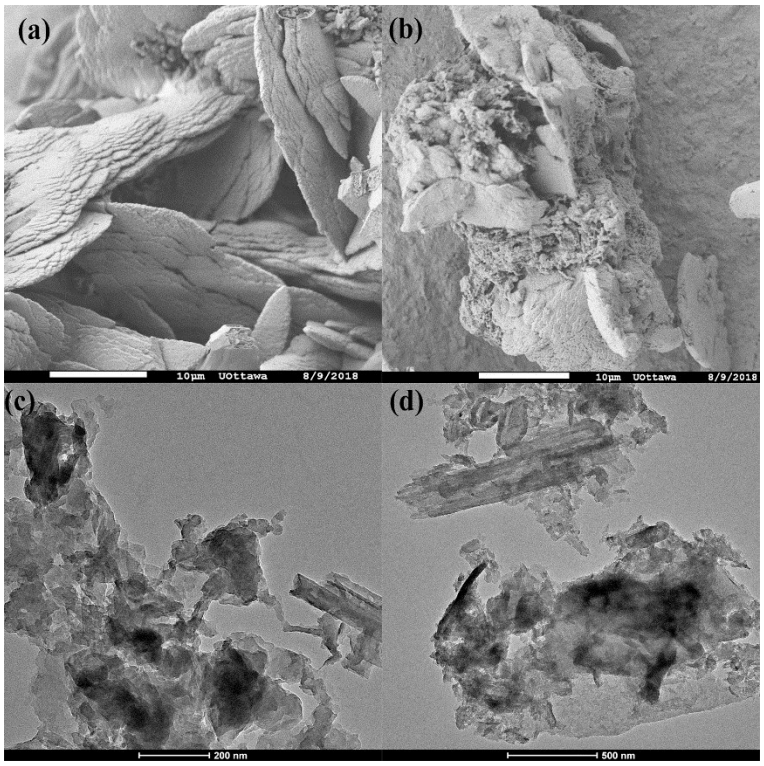

Figure 9.2. SEM images of (a) pure g-C_3N_4 and (b) OH-C_3N_4; and TEM images of (c) pure g-C_3N_4 and (d) OH-C_3N_4.

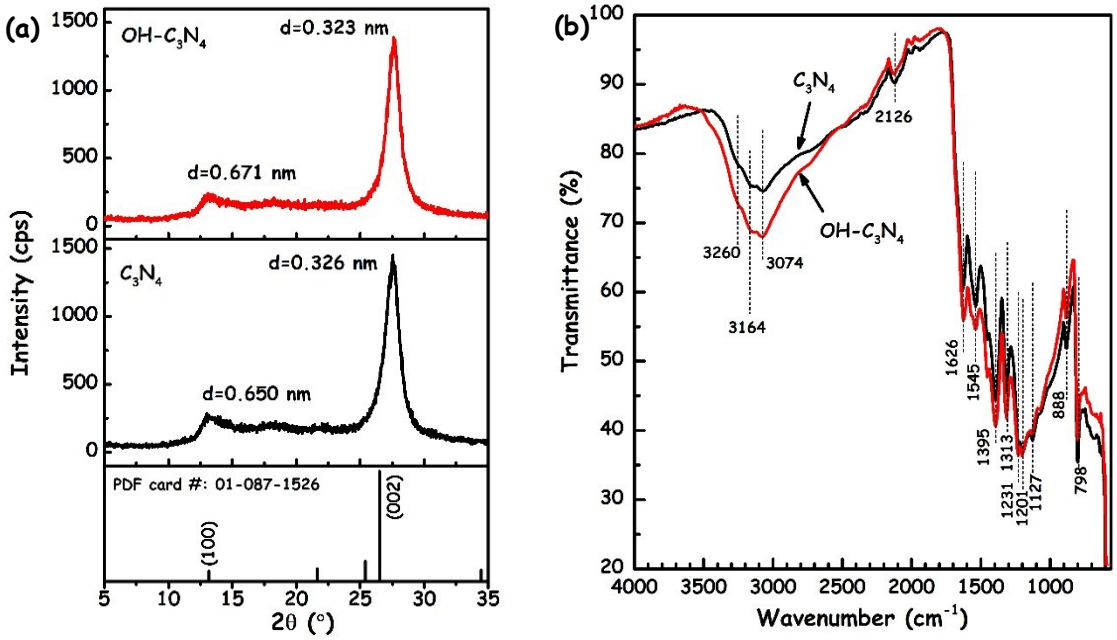

Figure 9.3. (a) XRD patterns and (b) FTIR spectra of pure g-C_3N_4 and OH-C_3N_4.

Surface compositions for prepared samples were further investigated using XPS. The XPS survey spectra for prepared samples are shown in Fig. 9.4 and demonstrate the existence

of C, N and O elements in both samples. The elemental ratios for both samples were calculated from the survey spectra, and the results are summarized in Table 9.1. For pure C_3N_4, the elemental ratio between carbon and nitrogen was 3:4.10, which was close to the stoichiometric amount of 3:4. The slight increase of nitrogen in the composites may be due to incomplete deamination of melamine during the preparation of g-C_3N_4. It can be found theoxygen content in the composites increased by a factor of almost 2 when compared to the oxygen content in the original g-C_3N_4. This significant increase may have resulted from hydroxyl surface modification during the hydrothermal treatment. To further explore the chemical states and bonds in theprepared samples, high-resolution (HR) XPS orbital scans for carbon, nitrogen and oxygen were performed and the spectra were plotted in Fig. 9.5. In the HR XPS scan for C 1s scan shown in Fig. 9.5a, three peaks located at 281.13, 284.6 and 290.13 eV were observed for g-C_3N_4. The peak located at 284.6 eV was attributed to the C-C coordination of adventitious hydrocarbons from the XPS instrument itself, and was used for calibration. The other two peaks, located at 281.13 and 290.13 eV, may be attributed to sp^2-hybridized carbon (C-C) atoms and sp^3-carbons of the N-C=N coordination present in g-C_3N_4 [15, 36]. After surface modification, the peak for N-C=N was slightly shifted, whereas the other peak for C-C was shifted by 0.24 eV. This phenomenon indicates that hydroxyls may be bonded with carbon, instead of nitrogen in g-C_3N_4. This experimental result agreed well with the simulation result that OH bonded to carbon was more stable compared to OH bonded to nitrogen in g-C_3N_4. In the HR XPS scan for N 1s, shown in Fig. 9.5b, the spectrum can be fitted into three peaks for g-C_3N_4, which may be ascribed to C=N-C, N-(C)3 and C-N-H, respectively. It should be noted that when g-C_3N_4 was hydrothermally treated by ammonia, all three peaks were negligibly

shifted. This phenomenon further confirmed that hydroxyl was not bonded with nitrogen in g-C_3N_4, and the slight shift between peaks may have resulted from the change in tilt angularity as observed from the XRD patterns. The O 1s HR spectra in Fig. 9.5c can be fitted with a single peak located at 529.44 eV for g-C_3N_4, corresponding to the O-H bond. After hydrothermal treatment, the peak was shifted by 0.66 eV, which may have resulted from the hydroxyl group being bonded with g-C_3N_4. All the above discussion suggests that hydroxyl functional groups may have bonded with g-C_3N_4, and -OH tended to chemically bond with carbon instead of nitrogen in g-C_3N_4, during the hydrothermal treatment.

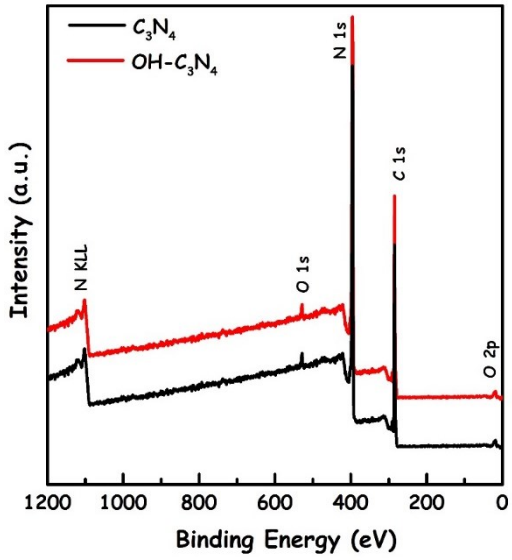

Figure 9.4. XPS survey spectra of pure C_3N_4 and OH-C_3N_4.

Table 9.1. Elemental ratios on the surface of prepared samples, calculated from the XPS survey spectra.

Elemental ratio	C:N:O
C_3N_4	3:4.10:0.073
OH-C_3N_4	3:4.13:0.130

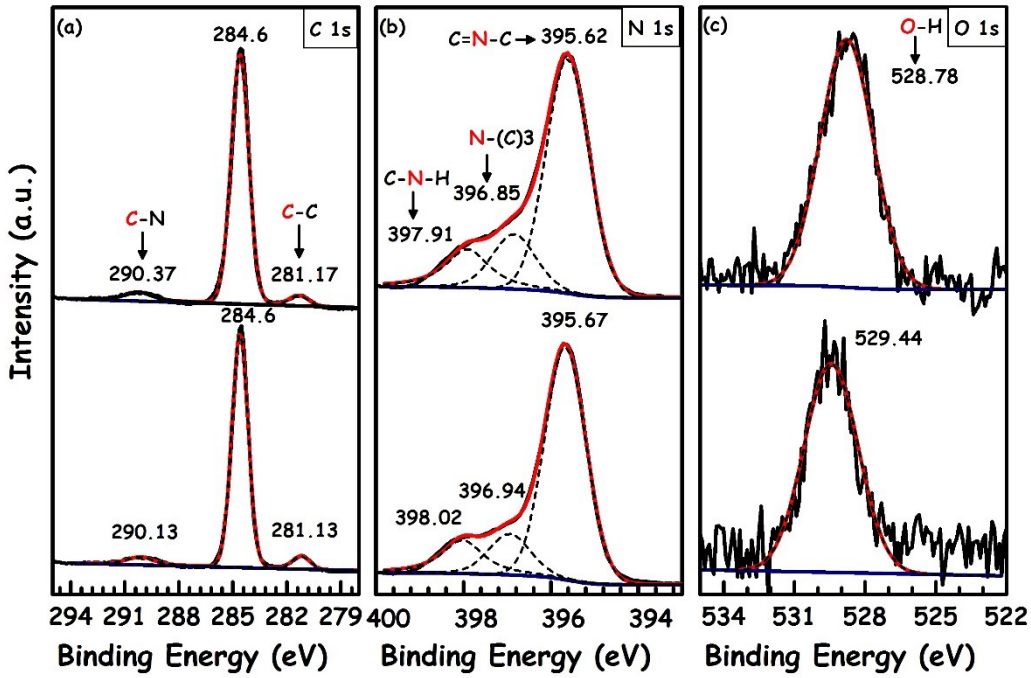

Figure 9.5. XPS spectra of (a) C 1s, (b) N 1s and (c) O 1s

9.3.2 Optical properties and electrical band structure

Optical properties are critical for a photocatalyst. To explore the optical properties for g-C_3N_4 before and after the surface hydroxyl modification, UV-Vis DRS were recorded as shown in Fig. 9.6. The DRS measurements indicated that both pure C_3N_4 and OH-C_3N_4 were visible light-responsive and that the band gap absorption edges for both samples were located at approximately 500 nm. The steep increase of absorption intensity with a decrease in irradiation wavelength below the absorption edge (*i.e.* 500 nm) may have resulted from the band transition. Although the surface hydroxyl modification had no significant influence on the bandgap energy of the photocatalyst, the visible light absorption intensity was boosted, suggesting enhanced light harvesting capacity and photocatalytic activity after hydroxyl modification. The electrical band structure of g-C_3N_4 was simulated through the computation of density of states using DFT, as shown in Fig. 9.7. It found that the

valence band maximum (VBM) and the conduction band minimum (CBM) of g-C_3N_4 were both primarily composed of C 2p and N 2p orbitals. With hydroxyl modification, the band gap of OH-C_3N_4 was narrowed by 0.31 eV, even though the compositions for both VBM and CBM remained the same compared to g-C_3N_4. A semiconductor with a narrower band gap can capture more visible light photons, which may favor an improvement in quantum efficiency. It should be noted that the simulated band gap values are narrower than experimental results, which may have resulted from the well-known limitations of GGA [37]. To further explore the band gaps, as well as CBM and VBM potentials, Tauc's plot (Equation 3) was used as follows:

$$\alpha E_{photon} = K\left(E_{photon} - E_g\right)^{\frac{n}{2}} \quad \textbf{\textit{Equation 3}}$$

where $E_{photon} = hv$, α is the absorption coefficient, K is a semiconductor constant (usually equal to 1), E_g is the bandgap energy, h is Planck's constant, v is the irradiation frequency, and n is a semiconductor bandgap transition constant (direct transition: n = 1; indirect transition: n = 4), respectively [38]. Based on the abovementioned DFT results and the previous report, the value of n for C_3N_4 is equal to 4 [39]. The calculated results were plotted in the inset of Fig. 9.6. The bandgap energies of both g-C_3N_4 and OH-C_3N_4 were estimated to be about 2.60 eV. The flat-band potentials of the semiconductors can be calculated by applying the Mulliken electronegativity theory for atoms as follows (Equation 4 and 5) [40, 41],

$$E_{CB} = \chi_p - E^e - \frac{1}{2}E_g \qquad \textbf{Equation 4}$$

$$E_{VB} = E_{CB} + E_g \qquad \textbf{Equation 5}$$

where E_{CB} and E_{VB} are the energies of the bottom position of the conduction band and the top position of the valence band respectively; χ_p is the electronegativity of the semiconductor, which can be estimated by the geometric mean of the electronegativity of its constituent atoms (~4.64 eV) [42-44]; E^e is the energy of free electrons on the hydrogen scale (~ 4.5 eV) and E_g is the band gap energy. Based on Equations 4 and 5, the calculated results for g-C_3N_4 were E_{CB} = -1.16 eV and E_{VB} = 1.44 eV.

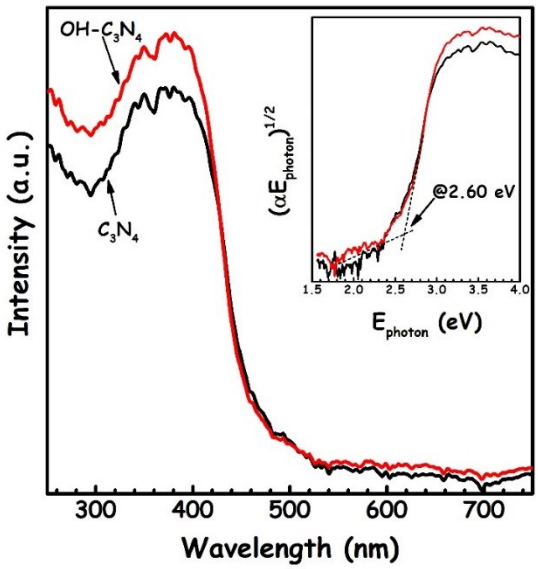

Figure 9.6. DRS and the plots of $(\alpha \times E_{photon})^{1/2}$ vs. E_{photon} (inset) of pure C_3N_4 and OH-C_3N_4.

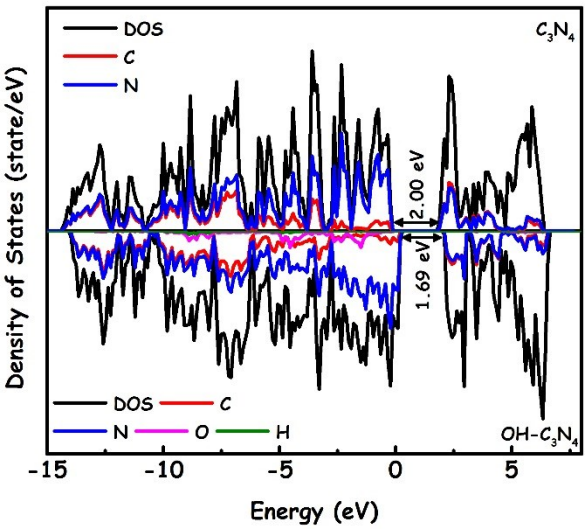

Figure 9.7. Density of states (DOS) and partial density of states (PDOS) for g-C_3N_4 and OH-C_3N_4.

9.3.3 Hydrophilic property

The effect of ammonia treatment on the hydrophilicity of prepared samples was evaluated using the water contact angle. As shown in Fig. 9.8, the contact angle for pure g-C_3N_4 was measured to be 118.00º. This may be due to the less hydrophilic groups on g-C_3N_4, and an applied hydrophobic support (*i.e.* NWF). After ammonia treatment, the measured contact angle was reduced to 75.40º for g-C_3N_4.. This phenomenon may have resulted from the surface hydroxyl modification during hydrothermal treatment. The increase in surface hydrophilicity further confirms successful surface hydroxyl modification via ammonia treatment [45, 46]. The adsorption energy for water adsorbed onto g-C_3N_4 and OH-C_3N_4 was calculated to be 0.67 eV and 0.89 eV per H_2O atom adsorbed, respectively. The increased adsorption energy indicated that water more readily adsorbed onto g-C_3N_4 after surface hydroxyl modification. To investigate the surface charges of prepared samples in aqueous suspensions, zeta potentials were measured; the results are shown in Fig. 9.9. The suspension with pH 5.5 was applied for both tests. The average zeta potentials for g-C_3N_4

and OH-C_3N_4 were estimated to be -38.5 mV and -47.3mV, respectively. The isoelectric point (IEP), defined as the pH value that results in a zero net surface charge, was measured as 5.0 for g-C_3N_4 prepared from melamine, which consists with values previously reported in the literature [47]. Since the pH in the testing solution in this work was above the IEP, all zeta potentials were negative. Similar to all the other compounds, when dispersed in water, protonation and deprotonation processes may occur at the interface between the water and g-C_3N_4. As indicated from the XPS analysis, -NH_2 may be present on g-C_3N_4 due to the incomplete condensation of amino groups. These amino groups on the surface may react with the hydroxyl groups in the aqueous suspension to create a negatively charged surface of g-C_3N_4, as shown in Equation 6 and 7. As for the hydrothermal treatment, hydroxyl groups may bond with the carbon, and the hydroxyl groups can react with hydroxyl ions in the suspension to produce additional negative ions on the surface, as shown in Equation 8. As a result, with surface hydroxyl modification, the surface of g-C_3N_4 became more negative, potentially causing the negative shift in the zeta potential, as shown in Fig. 9.9.

$$\equiv C\text{-}NH_2 + OH^- \rightarrow \equiv C\text{-}NH^- + H_2O \qquad \textbf{\textit{Equation 15}}$$

$$(\equiv C)_2 NH + OH^- \rightarrow (\equiv C)_2 N^- + H_2O \qquad \textbf{\textit{Equation 7}}$$

$$\equiv C - OH + OH^- \rightarrow \equiv C - O^- + H_2O \qquad \textbf{\textit{Equation 8}}$$

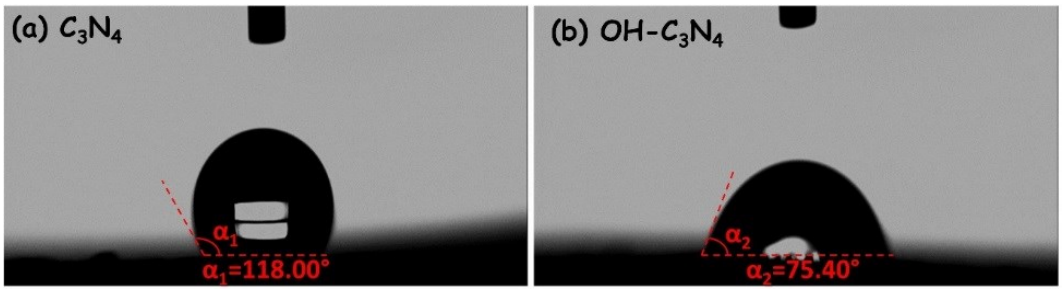

Figure 9.8. Water contact angles for prepared samples cast onto NWF material.

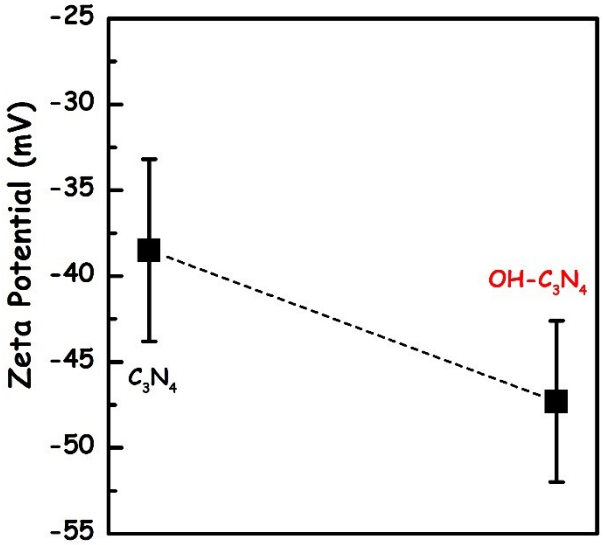

Figure 9.9. Zeta potentials for prepared samples dispersed in water (pH 5.5).

9.3.4 Photocatalytic activity test

9.3.4.1 Photocatalytic degradation of phenolic compounds

The photocatalytic activities of prepared samples were evaluated by the degradation of phenol and phenolic compounds under visible light irradiation. The Langmuir-Hinshelwood (L-H) kinetic model (Equation 9) is applicable to many photocatalytic processes:

$$r = -\frac{dc}{dt} = k\theta = \frac{kKc}{1+Kc} \qquad \textit{Equation 9}$$

where *r* is the reaction rate, *c* is the concentration of the phenolic compound, *t* is time, *k* is the reaction rate constant, θ is the surface coverage (a dimensionless quantity), and *K* is the adsorption constant. For all tests in this work, the initial concentration of the pollutant was 10 mg/L. There was no measurable adsorption of phenolic compounds during any experimental run, indicating that the adsorption constant (*K*) was negligible for both C_3N_4 and surface-modified C_3N_4 composites. Therefore, the *1 + Kc* term may be assumed to be equal to 1, and Equation 9 can be then expressed as Equation 10:

$$-\frac{dc}{dt} = kKc = k'c \qquad \textbf{Equation 10}$$

where *k'* is the pseudo first-order reaction constant. Equation 11 can be obtained by integrating Equation 10 from c_o at a time of 0 to c_t at time *t*:

$$\ln(\frac{c_o}{c_t}) = k't \qquad \textbf{Equation 11}$$

The value of *k'* for each photocatalytic process can be determined by plotting $\ln(c_o/c_t)$ *vs t* and calculating the slope of the line of best fit. For phenol degradation, it was found that the photocatalytic activity of g-C_3N_4 was significantly improved after hydrothermal treatment, as shown in Fig. 9.10a. Specifically, only 24% of phenol was degraded after 5 h in the presence of pure g-C_3N_4, while the removal fraction increased to 35% and 60% for g-C_3N_4 hydrothermally treated with DDW and ammonia treatment, respectively. However, as shown in Fig. 9.10a, no significant improvement in photocatalytic activity was observed between the three samples with increasing concentrations of ammonia. This result indicates

that low concentrations of ammonia (i.e. 1%) are sufficient for successful surface modification and improvement in photocatalytic activity of C_3N_4 [48].

The kinetic constant for the photocatalytic degradation process with C_3N_4 was 0.0524 h^{-1} (Table 9.2). The kinetic constant increased by up to a factor of 1.5 to 3 times when treated with DDW or ammonia. This improvement in photocatalytic activity may be attributed to the inhibition effect of the alkali treatment on charge recombination [33, 49]. Furthermore, the ammonia treatment may lead to a more positive valance band potential of as-prepared samples, which can generate holes with a higher oxidative capacity and improved photocatalytic activity [33]. The corresponding total organic carbon (TOC) concentration was also monitored and indicated in Fig. 9.10b. It can be observed that the relative TOC concentrations (TOC/TOC_0) within 2 h were rapidly reduced to 94.5%, 88.6%, and 80.3% in the presence of TiO_2, g-C_3N_4, and OH-C_3N_4, respectively. Afterwards, the relative TOC concentrations for TiO_2 and g-C_3N_4 were negligibly changed during the photocatalytic process while the TOC concentrations for OH-C_3N_4 was further reduced to 67.6% after 6 h. The lower TOC reduction rate at the second stage may be due to the formation of more refractory degradation intermediates (*e.g.* organic acids) [50], which suggests that a prolonged reaction time is required to achieve the complete mineralization of phenol.

Table 9.2. Kinetic constants for systems in the presence of different photocatalysts.

Degradation of phenol					
Photocatalyst	C_3N_4	C_3N_4-DDW	C_3N_4-1% NH_4OH	C_3N_4-5% NH_4OH	C_3N_4-20% NH_4OH
k' (h^{-1})	0.0524	0.0792	0.179	0.168	0.170
Degradation of 2-chlorophenol					
Photocatalyst		C_3N_4		OH-C_3N_4	
k' (h^{-1})		0.380		0.622	
Degradation of catechol					
Photocatalyst		C_3N_4		OH-C_3N_4	
k' (h^{-1})		0.090		0.137	

As discussed previously, the adsorption of water on g-C_3N_4 is enhanced by hydroxyl surface modification. Since photocatalysis occurs at the interface between the catalyst surface and the bulk liquid phase, this improved water adsorption may also contribute to an improvement in photocatalytic oxidation processes. The adsorption energy and charge distributions of phenol adsorbed on g-C_3N_4 and OH-C_3N_4 were determined and the results are shown in Fig. 9.10c. It can be seen that the adsorption energy increased from 0.32 eV to 0.45 eV per phenol molecule adsorbed. The adsorption energy of phenol is lower than that of water for the prepared sample, indicating that phenol adsorption may be more difficult in this degradation process and that the adsorption energies of both phenol and water increased for g-C_3N_4 modified by surface hydroxyl modification [48]. The charge distributions in the adsorption system for phenol-g-C_3N_4 are shown in Fig. 9.10c, where the non-electrostatic interaction between phenol and g-C_3N_4 is mainly attributed to the

donor-acceptor interaction; the surface of g-C_3N_4 is negatively charged, while the phenol is positively charged. Comparatively, for phenol-OH-C_3N_4, the electron donors are composed of hydroxyl groups, which may enhance the interaction between phenol and g-C_3N_4 in order to improve the adsorption energy. To further confirm the enhancement of photocatalytic activity for g-C_3N_4 modified by surface hydroxyls in the decomposition of phenolic compounds, other phenolic compounds, including 2-chlorophenol and catechol, were applied as probe molecules, and the testing results are shown in Fig. 9.10d. These photocatalytic degradation processes were also modeled using L-H kinetics, and the results of the kinetic models are included in Table 9.2. After surface modification with hydroxyl functional groups, the photocatalytic kinetic rate constants increased by a factors of 1.5 to 1.6. The results demonstrate that the photocatalytic oxidation of phenolic compounds for g-C_3N_4 is promoted after surface hydroxyl modification.

The reusability of the photocatalysts was evaluated by recycling OH-C_3N_4 for five runs during the decomposition of phenol under visible light (Fig. 9.10e). The difference among these concentration profiles was negligible, indicating the high stability of OH- C_3N_4 in the photocatalytic degradation of organic pollutants in water. A slight reduction in the removal fraction in subsequent runs may be due to either the refractory intermediates adsorbed on the surface of catalysts or the loss of catalyst during the recycling tests. These results suggest that OH-modified C_3N_4 exhibited high reusability, which makes them an attractive candidate for application as visible-light-driven photocatalysts.

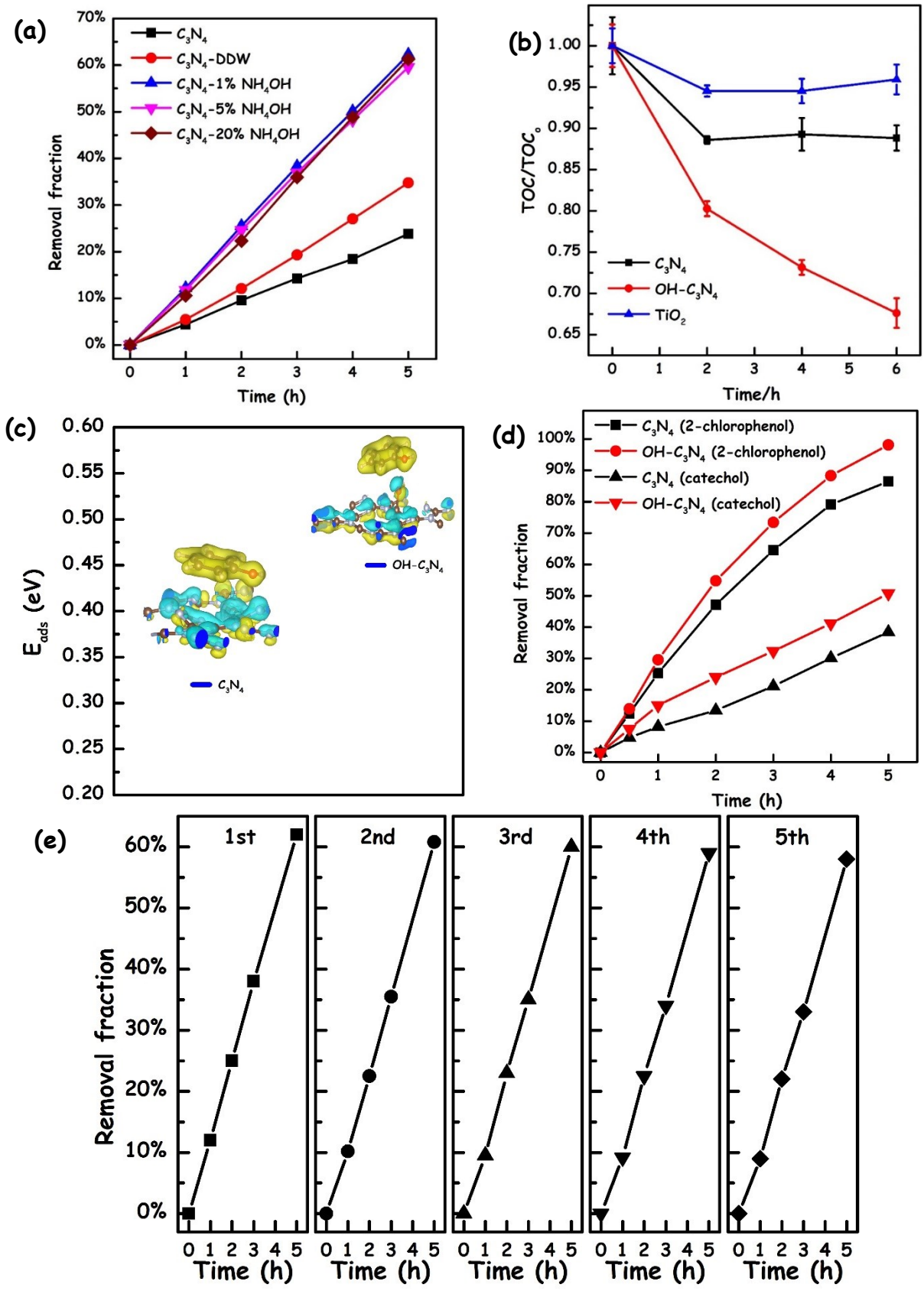
(a)
Removal fraction
Time (h)
C_3N_4
C_3N_4-DDW
C_3N_4-1% NH_4OH
C_3N_4-5% NH_4OH
C_3N_4-20% NH_4OH
(b)
TOC/TOC_o
Time/h
C_3N_4
OH-C_3N_4
TiO_2
(c)
E_{ads} (eV)
OH-C_3N_4
C_3N_4
(d)
Removal fraction
Time (h)
C_3N_4 (2-chlorophenol)
OH-C_3N_4 (2-chlorophenol)
C_3N_4 (catechol)
OH-C_3N_4 (catechol)
(e)
Removal fraction
Time (h)
1st
2nd
3rd
4th
5th

Figure 9.10. (a) Concentration profiles of phenol during photocatalytic degradation under visible light with pure and modified g-C_3N_4; (b) TOC removal ratios of different photocatalytic systems during phenol decomposition; (c) adsorption energy of phenol on g-C_3N_4 and OH-C_3N_4, calculated by DFT (yellow: positive charges; blue: negative charges), (d) photocatalytic degradation under visible light of 2-chlorophenol and catechol using pure and modified g-C_3N_4 and OH-C_3N_4, and (e) OH-C_3N_4 recycling tests during photocatalytic degradation of phenol under visible light.

9.3.4.2 Active species

It was determined that the flat-band position of the valence band for g-C_3N_4 (*ca.* +1.44 eV) was lower than the redox potential of •OH/H_2O (2.27 eV at pH 7 and 2.73 eV at pH 0 (vs SHE)) [51]. This may cause the photogenerated holes on the valence band to be incapable of oxidizing adsorbed water to produce •OH [52, 53]. To confirm the minimal contribution from •OH in the g-C_3N_4-based photocatalysis system, the concentration of •OH was measured indirectly through probe compounds (i.e. *p*-chlorobenzoic acid, pCBA) [50, 54, 55]. The rate of reaction between pCBA and •OH can be expressed as shown in Equations 12 and 13. The reaction rate constant ($k_{\bullet OH\text{-}pCBA}$) was estimated to be 5×10^9 M^{-1} s^{-1} (3.12×10^{11} M^{-1} min^{-1}). This high reaction rate constant indicates that pCBA selectively reacts with OH radicals. By integrating Equation 13 with the boundary conditions: $t = 0$, $c = c^0_{p\text{-}CBA}$, and $t = t$, $c = c^t_{p\text{-}CBA}$, Equation 14 can be derived. $\int_0^t c_{\bullet OH} dt$ on the right side of Equation 14 is defined as OH radicals exposure, which indirectly determines the accumulated concentration of photogenerated OH radicals in the system. Profiles for the photocatalytic degradation of pCBA, as well as the computed OH radicals exposure in the presence of TiO_2, g-C_3N_4 and OH-C_3N_4 composites, are separately depicted in Fig. 9.11. From these results, it is apparent that pCBA was rapidly degraded over 90 min with TiO_2 under UV light irradiation. In contrast, a negligible amount of pCBA was removed from the system

using either g-C_3N_4 or OH-C_3N_4. These results indicate that a large amount of OH radicals were generated in the TiO_2-based photocatalytic system, whereas a negligible amount of OH radicals were detected in the presence of either g-C_3N_4 or OH-C_3N_4 composites. This demonstrates that •OH may not have played a determining role in the decomposition of phenol. Instead, photogenerated holes on the valence band may play the most significant role in directly reacting with adsorbed organic pollutants in water.

$$p-CBA+\bullet OH \rightarrow p-CBA^{*} \qquad \textit{Equation 12}$$

$$\frac{dc_{p-CBA}}{dt} = -k_{\bullet OH-pCBA} \times c_{p-CBA} \times c_{\bullet OH} \qquad \textit{Equation 13}$$

$$\ln\left(\frac{c^{0}_{p-CBA}}{c^{t}_{p-CBA}}\right) = k_{\bullet OH-pCBA}\int_{0}^{t} c_{\bullet OH}\,dt \qquad \textit{Equation 14}$$

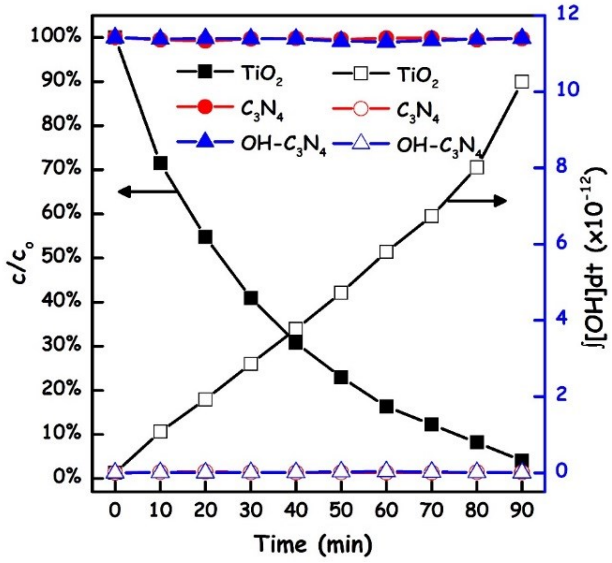

Figure 9.11. Photocatalytic degradation of pCBA with TiO_2 (UV light irradiation) and g-C_3N_4 and OH-C_3N_4 composites (visible light irradiation)

9.3.4.3 Pathways of the degradation of phenol

HPLC was employed to explore the concentrations of primary intermediates during photodegradation [56-58]. The pathways of the photocatalytic degradation of phenol were explored by recording the concentrations of potentially-produced intermediates, including benzoquinone (BQ), hydroquinone (HQ) and catechol (CA). Measured concentrations of phenol, as well as that of possible intermediates for photocatalysis in the presence of either OH-C_3N_4 under visible light or TiO_2 under UV light, were calculated and are illustrated in Fig. 9.12. It was determined that phenol was completely removed in the system with TiO_2, and 60% of phenol was removed in the system with OH-C_3N_4. However, more intermediates accumulated for photocatalysis with TiO_2 compared to that with OH-C_3N_4. Additionally, the three primary intermediates, BQ, HQ, and CA, were completely removed at the end of both photocatalytic processes. Notably, negligible amounts of intermediates were detected during the 300 min degradation of phenol using OH-C_3N_4. When compared to the TiO_2 process, the rapid reduction and elimination of intermediates may be responsible for the higher TOC removal ratio observed in Fig. 9.10b for the OH-C_3N_4 process.. The possible pathways in the degradation of phenol are proposed in Fig. 9.13. For the TiO_2-based photocatalytic process, OH radicals play a significant role and may react with phenol to form a large quantity of dihydroxycyclohexadienyl radical adducts (Route 1). These adducts may evolve further to form phenoxy radicals by the elimination of H_2O (Route 2); however this was shown in the literature to be a very slow process [59]. It is more likely that these adducts may react with dissolved oxygen (Route 3), followed by an elimination of HO_2 to form dihydroxy intermediates (Route 4). By contrast, in the absence of OH radicals for the OH-C_3N_4 system, phenol may react with oxygen (Route 5) followed

by the formation of phenoxy radicals with the elimination of HO_2 (Route 6) [60]. In the presence of O_2, phenoxy radicals are most likely to slowly form benzoquinone (Route 7). Due to the low reaction rate of the BQ formation process, a low concentration of BQ is expected. In our$OH\text{-}C_3N_4$ system, a low amount of intermediates was detected [61]. When these three phenolic intermediates are formed, OH radicals and dissolved oxygen, as well as holes may lead to ring cleavage and fragmentation, respectively, for the TiO_2 and $OH\text{-}C_3N_4$ systems. Once the ring is broken, different organic acids such as maleic, succinic, malonic, oxalic and acetic acids are the products of these phenolic compounds (Routes 8 and 9) [62]. Furthermore, these organic acids are most likely further degraded into CO_2 and H_2O (Route 10) [50, 63].

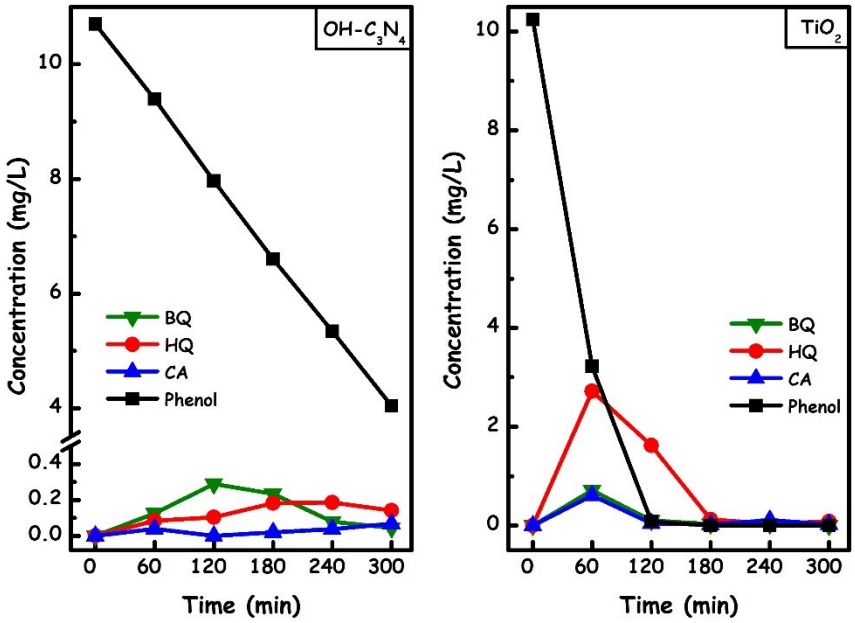

Figure 9.12. Concentrations of benzoquinone (BQ), hydroquinone (HQ), catechol (CA) and phenol during the photocatalytic processes in the presence of $OH\text{-}C_3N_4$ under visible light irradiation and TiO_2 under UV irradiation.

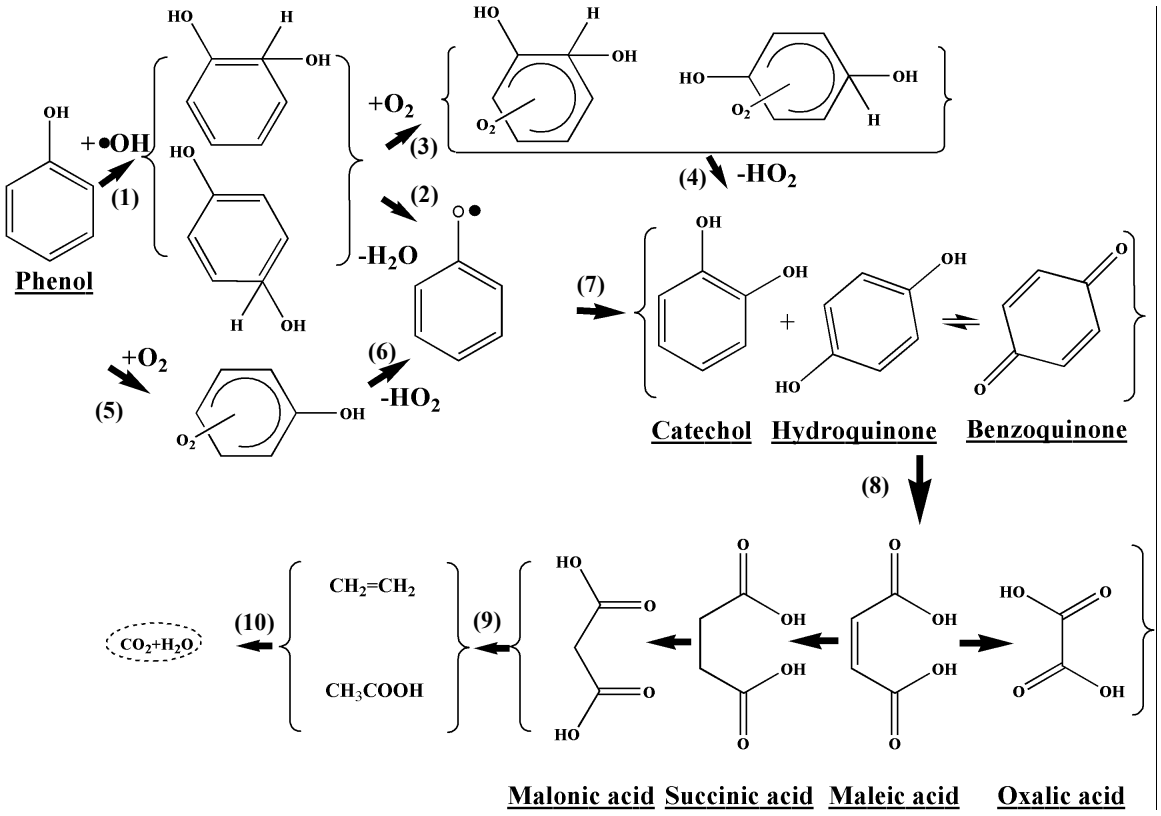

Figure 9.13. Proposed pathways for the photocatalytic degradation of phenol (adapted from [50]).

9.3.4.4 Photocatalytic inactivation of bacteria

The photocatalytic inactivation of bacteria under visible light has been studied in the presence of g-C_3N_4 and OH-C_3N_4 (Fig. 9.14). It is evident that the bactericidal activity for g-C_3N_4 is significantly improved after surface hydroxyl modification, which agrees well with the previous photocatalytic degradation results for phenolic compounds. Over 60 min of irradiation, the survival fractions in g-C_3N_4 and OH-C_3N_4 systems are 55.1% and 29.5%, respectively. It is generally accepted that photogenerated reactive oxidative species (ROS), such as h^+, •OH, and $•O_2^-$, are responsible for bacterial inactivation. These results suggest that more oxidative species are produced in the photocatalytic system of g-C_3N_4 modified

by surface hydroxyl groups. Beyond that, an enhancement of the interaction between the bacteria cell wall and the surface of g-C_3N_4 after hydroxyl modification may also contribute to the improvement in bacteria inactivation. When the bacteria interacts with the photocatalysts, the cell envelope integrity may be damaged by alteration of the outer membrane permeability to allow the penetration of deleterious substances. In addition, the main components of the cell wall of *E. Coli* (Gram-negative bacteria), such as lipo-polysaccharide, phosphatidylethanolcholine, and peptidoglycan are photocatalytically degraded at the bacteria-photocatalyst interface. As a result, the loss of the cell wall structure, as well as its functions, is directly linked to bacterial inactivation in photocatalytic processes [64]. It should be noted that the outer membrane for Gram-negative bacteria acts as a selective barrier to prevent the entry of toxic molecules into the cell [65], [67]. As the hydroxyl functional groups on the surface of g-C_3N_4 may favor an improvement in the interaction between the bacteria and the photocatalyst surface, photogenerated oxidative species can easily react with the outer wall of the bacteria, so as to further inactivate the bacteria by breaking the cell envelope's integrity.

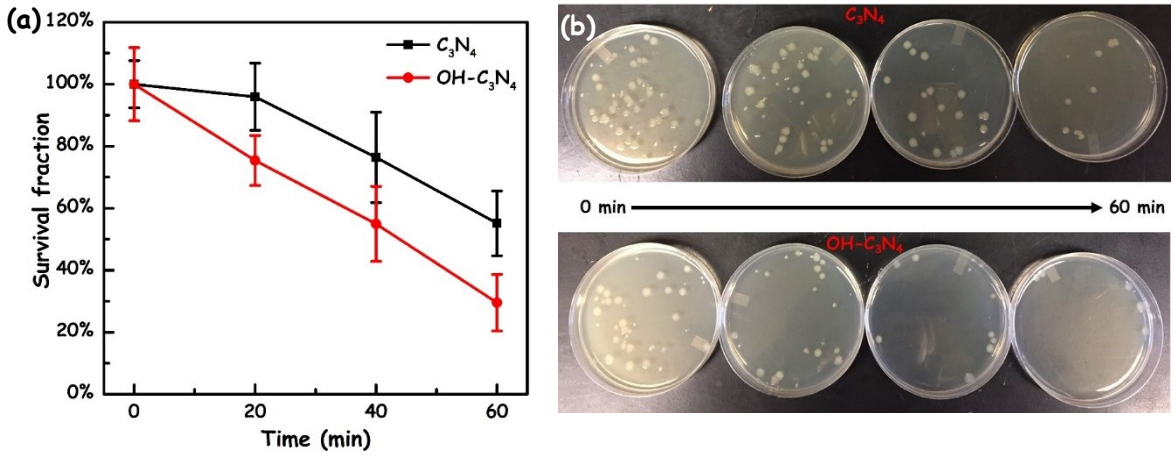

Figure 9.14. (a) Photocatalytic disinfection performance of various samples; (b) photos of E.

coli colonies which are cultured by the samples collected at different times during the photocatalytic disinfection process.

9.3.5 Mechanisms

CO_2-TPD was applied to investigate the basicity of C_3N_4 as well as OH-C_3N_4 (Fig. 9.15). Both materials exhibited desorption peaks in the temperature range of 50-450°C, which were attributed to the basic sites associated with chemical or physical adsorption of acidic CO_2 molecules [66]. Notably, two peaks were observed for each profile, which may be due to CO_2 desorbed from two different sites on the surface of C_3N_4. As reported by Yang et al., the peak at lower temperature may be attributed to the desorption of CO_2 adsorbed on the nitrogen site of C-N-C rings, while the one at higher temperature may be attributed to the amino groups on the surface edge [67]. The amount of basic sites is proportional to the integrated area of the desorption peaks in the profile. Therefore, the amount of basic sites was greatly increased with the surface hydroxyl modification. An increase in basic sites on the surface of C_3N_4 favoured the adsorption of acidic compounds, including phenolic compounds and acidic intermediates (e.g. carboxylic acid). Furthermore, increasing the basicity of the C_3N_4 surface also improved its photocatalytic activity during the decomposition of phenolic compounds.

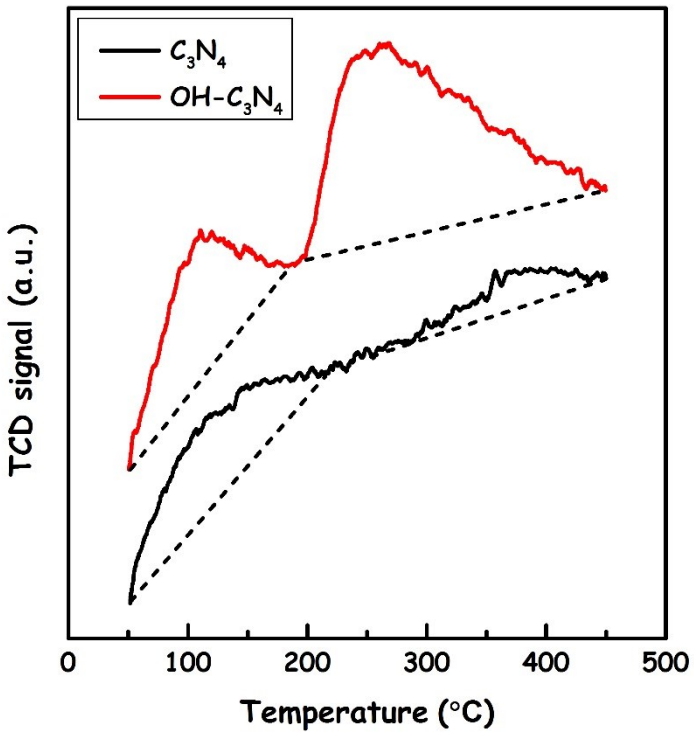

Figure 9.15. CO_2-TPD profiles of C_3N_4 and OH-C_3N_4.

Electrochemical impedance spectra (EIS) and transient photocurrent responses were applied to evaluate the charge separation on C_3N_4 and OH-C_3N_4 (Fig. 9.16) The EIS Nyquist plots (Fig. 9.16a) suggest that these photocatalytic processes were a simple electrode reaction. The diameter of the arcs in Fig. 9.16a are in direct proportion to the resistance values of the electron transfer on the electrode [68] Overall, this means that a wider diameter corresponds to a higher recombination rate of photogenerated charge carriers. It can be found that the charge separation on OH-C_3N_4 was significantly improved, as a smaller diameter was found for the EIS Nyquist plot. Furthermore, the photocurrent on these two electrodes was also recorded with an on/off switch for the lamp (Fig. 9.16b). It can be found that the traces of both tests were reproducible, indicating the high stability of these two electrodes. Moreover, the photocurrent intensity of the OH-C_3N_4 electrode when the lamp was on was approximately 2 times higher compared to that for the C_3N_4

electrode. This result further proved that with surface hydroxyl modification, the charge separation on C_3N_4 was significantly improved, which contributed to its enhanced photocatalytic activity.

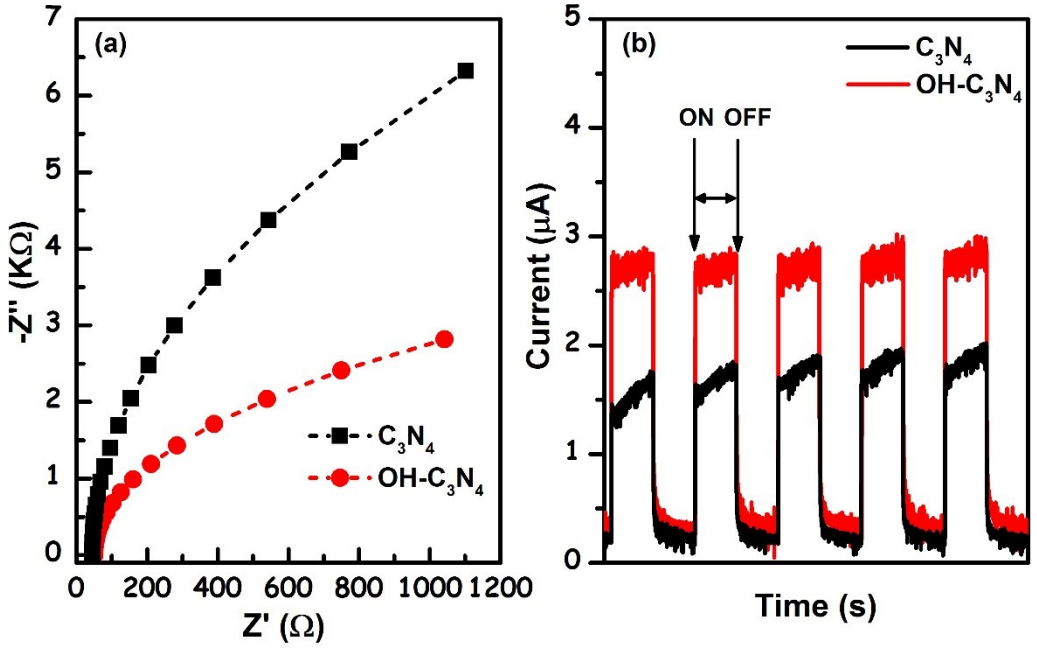

Figure 9.16. (a) EIS Nyquist plots and (b) transient photocurrent responses of C_3N_4 and OH-C_3N_4 electrodes under visible light irradiation.

Electrostatic potentials for g-C_3N_4 and OH-C_3N_4 are plotted in Fig. 9.17. Based on these results, the work functions for g-C_3N_4 and OH-C_3N_4 were estimated to be 4.84 eV and 5.41 eV (vs. vacuum), respectively. The difference in work functions between g-C_3N_4 and OH-C_3N_4 may drive electron transfer from g-C_3N_4 to OH-C_3N_4, due to the higher work function for g-C_3N_4 when modified with hydroxyl functional groups [9, 69]. Notably, hydroxyl groups are adsorption sites for organic compounds in water. An accumulation of electrons on surface hydroxyl groups favor an improvement in the photocatalytic decomposition efficiency of organics in water. In addition, the Fermi level for g-C_3N_4 was shifted from -3.46 eV to -3.94 eV (vs. vacuum) after surface hydroxyl modification. With this shift, a

heterostructure may be fabricated, as shown in Fig. 9.18. As a type-II heterojunction [70-75], photogenerated electrons and holes will move in opposing directions. More specifically, electrons will accumulate on the conduction band of OH-C_3N_4, while the holes will accumulate on the valence band of g-C_3N_4. With this opposite charge transfer, the separation efficiency of photogenerated charge carriers may be improved. Also, due to the positive shift of the valence band of hydroxyl-modified g-C_3N_4, the oxidizability of photogenerated holes on the valence band is improved, which may accelerate the decomposition of organics and bacterial inactivation in water. It should be noted that, even though the valence band is positively shifted after surface modification, the holes are still incapable of converting water to hydroxyl-free radicals, as the flat-band potential (2.01 eV *vs* NHE) was still lower than the redox potential of •OH/H_2O (2.73 eV *vs* NHE). The improved separation of photogenerated charge carriers, as well as a positively-shifted valance band after surface hydroxyl modification on g-C_3N_4, may therefore increase the photocatalytic oxidation activity.

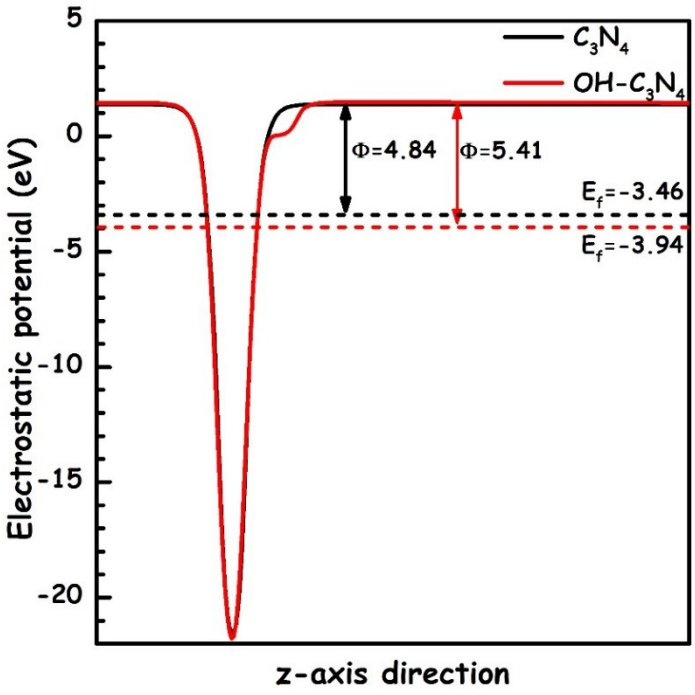

Figure 9.17. Work functions of g-C_3N_4 and OH-C_3N_4.

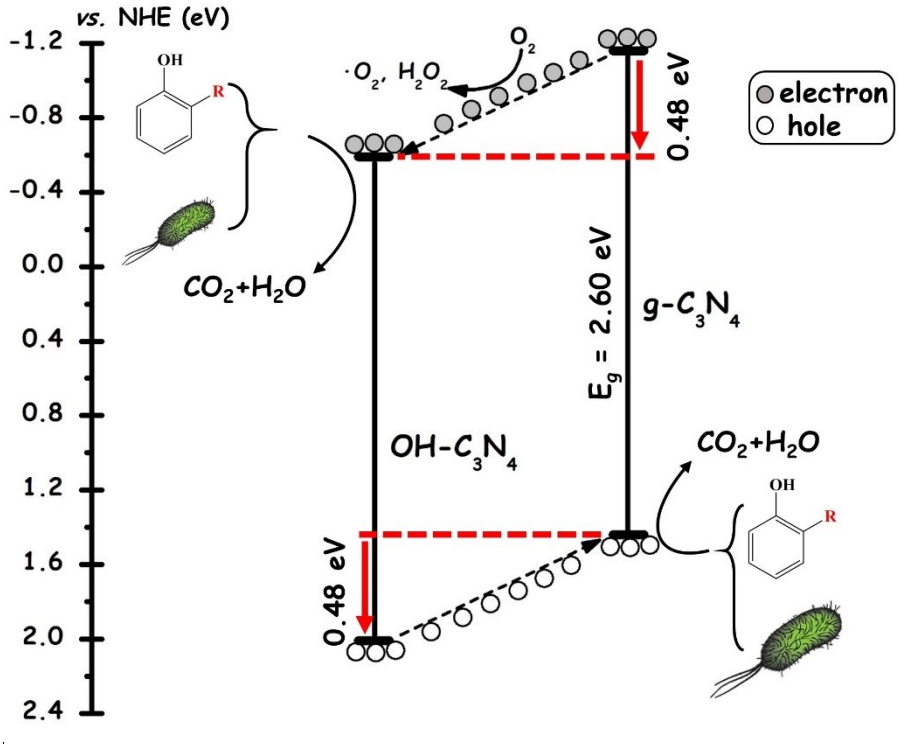

Figure 9.18. Proposed mechanism of photogenerated electrons and holes transfer for OH-C_3N_4 composite under visible light irradiation.

9.4 Conclusions

A hydrothermal synthesis method using ammonia solution was successfully applied to surface modify g-C_3N_4 with hydroxyl functional groups. . Upon introduction of hydroxyl groups, the adsorption energies for water and phenol on g-C_3N_4 were both increased, and the surface of g-C_3N_4 was tuned from hydrophobic to hydrophilic. In addition, the difference in work functions between g-C_3N_4 and OH-C_3N_4 drove charge transfer between each other. This effective transfer increased the separation of photogenerated charge carriers. Also, the position of the valence band may be positively shifted when the hydroxyl groups are bonded onto the surface of g-C_3N_4, which favored an improvement in the oxidizability of g-C_3N_4. All the above-mentioned benefits contributed to the enhancement of photocatalytic oxidization activity in both organics decomposition and bacteria inactivation.

References

[1] X. Chen, S. Shen, L. Guo, S.S. Mao, Semiconductor-based Photocatalytic Hydrogen Generation, Chem Rev, 110 (2010) 6503-6570.

[2] O. Ola, M.M. Maroto-Valer, Review of material design and reactor engineering on TiO_2 photocatalysis for CO_2 reduction, Journal of Photochemistry and Photobiology C: Photochemistry Reviews, 24 (2015) 16-42.

[3] X. Chen, N. Li, Z. Kong, W.-J. Ong, X. Zhao, Photocatalytic fixation of nitrogen to ammonia: state-of-the-art advancements and future prospects, Materials Horizons, 5 (2018) 9-27.

[4] A. Kudo, Photocatalyst Materials for Water Splitting, Catal Surv Asia, 7 (2003) 31-38.

[5] A. Fujishima, K. Honda, Electrochemical photolysis of water at a semiconductor electrode, Nature, 238 (1972) 37-38.

[6] D.F. Ollis, H. Al-Ekabi, TiO_2 Photocatalytic Purification and Treatment of Water and Air, Elsevier Science Ltd, Photocatalytic purification and treatment of water and air: proceedings of the 1st International Conference, 1993.

[7] L. Zhang, T. Kanki, N. Sano, A. Toyoda, Development of TiO_2 photocatalyst reaction for water purification, Sep Purif Technol, 31 (2003) 105-110.

[8] M. Ni, M.K. Leung, D.Y. Leung, K. Sumathy, A review and recent developments in photocatalytic water-splitting using TiO_2 for hydrogen production, Renewable and Sustainable Energy Reviews, 11 (2007) 401-425.

[9] W.-J. Ong, L.-L. Tan, Y.H. Ng, S.-T. Yong, S.-P. Chai, Graphitic Carbon Nitride (g-C_3N_4)-Based Photocatalysts for Artificial Photosynthesis and Environmental Remediation: Are We a Step Closer To Achieving Sustainability?, Chem Rev, 116 (2016) 7159-7329.

[10] X. Wang, K. Maeda, A. Thomas, K. Takanabe, G. Xin, J.M. Carlsson, K. Domen, M. Antonietti, A metal-free polymeric photocatalyst for hydrogen production from water under visible light, Nature Materials, 8 (2008) 76.

[11] X. Wang, S. Blechert, M. Antonietti, Polymeric Graphitic Carbon Nitride for Heterogeneous Photocatalysis, ACS Catalysis, 2 (2012) 1596-1606.

[12] S. Cao, J. Yu, g-C_3N_4-Based Photocatalysts for Hydrogen Generation, The Journal of Physical Chemistry Letters, 5 (2014) 2101-2107.

[13] H. Zhang, X. Zuo, H. Tang, G. Li, Z. Zhou, Origin of photoactivity in graphitic carbon nitride and strategies for enhancement of photocatalytic efficiency: insights from first-

principles computations, Phys Chem Chem Phys, 17 (2015) 6280-6288.

[14] C. Butchosa, P. Guiglion, M.A. Zwijnenburg, Carbon Nitride Photocatalysts for Water Splitting: A Computational Perspective, The Journal of Physical Chemistry C, 118 (2014) 24833-24842.

[15] Y. Zheng, Z. Zhang, C. Li, A comparison of graphitic carbon nitrides synthesized from different precursors through pyrolysis, Journal of Photochemistry and Photobiology A: Chemistry, 332 (2017) 32-44.

[16] L. Yang, J. Huang, L. Shi, L. Cao, Q. Yu, Y. Jie, J. Fei, H. Ouyang, J. Ye, A surface modification resultant thermally oxidized porous g-C3N4 with enhanced photocatalytic hydrogen production, Applied Catalysis B: Environmental, 204 (2017) 335-345.

[17] G. Liu, P. Niu, C. Sun, S.C. Smith, Z. Chen, G.Q. Lu, H.-M. Cheng, Unique Electronic Structure Induced High Photoreactivity of Sulfur-Doped Graphitic C3N4, J Am Chem Soc, 132 (2010) 11642-11648.

[18] J. Lei, Y. Chen, F. Shen, L. Wang, Y. Liu, J. Zhang, Surface modification of TiO2 with g-C3N4 for enhanced UV and visible photocatalytic activity, Journal of Alloys and Compounds, 631 (2015) 328-334.

[19] S. Cao, Y. Li, B. Zhu, M. Jaroniec, J. Yu, Facet effect of Pd cocatalyst on photocatalytic CO2 reduction over g-C3N4, Journal of Catalysis, 349 (2017) 208-217.

[20] Y. Zheng, Z. Zhang, C. Li, S. Proulx, Surface hydroxylation of graphitic carbon nitride: Enhanced visible light photocatalytic activity, Mater Res Bull, 84 (2016) 46-56.

[21] F.-t. Li, Y. Zhao, Q. Wang, X.-j. Wang, Y.-j. Hao, R.-h. Liu, D. Zhao, Enhanced visible-light photocatalytic activity of active Al2O3/g-C3N4 heterojunctions synthesized via

surface hydroxyl modification, J Hazard Mater, 283 (2015) 371-381.

[22] Z. Li, D. Rana, T. Matsuura, C.Q. Lan, The performance of polyvinylidene fluoride - polytetrafluoroethylene nanocomposite distillation membranes: An experimental and numerical study, Sep Purif Technol, 226 (2019) 192-208.

[23] G. Kresse, J. Hafner, Ab initio, Phys Rev B, 47 (1993) 558-561.

[24] G. Kresse, J. Furthmüller, Efficient iterative schemes for ab initio total-energy calculations using a plane-wave basis set, Phys Rev B, 54 (1996) 11169-11186.

[25] P.E. Blöchl, Projector augmented-wave method, Phys Rev B, 50 (1994) 17953-17979.

[26] J.P. Perdew, K. Burke, M. Ernzerhof, Generalized Gradient Approximation Made Simple, Phys Rev Lett, 77 (1996) 3865-3868.

[27] K. Momma, F. Izumi, VESTA 3 for three-dimensional visualization of crystal, volumetric and morphology data, J Appl Crystallogr, 44 (2011) 1272-1276.

[28] T. Di, B. Zhu, B. Cheng, J. Yu, J. Xu, A direct Z-scheme g-C_3N_4/SnS_2 photocatalyst with superior visible-light CO_2 reduction performance, Journal of Catalysis, 352 (2017) 532-541.

[29] J. Gamage McEvoy, D.A. Bilodeau, W. Cui, Z. Zhang, Visible-light-driven inactivation of Escherichia coli K-12 using an Ag/AgCl–activated carbon composite photocatalyst, J. Photochem. Photobiol. A: Chem., 267 (2013) 25-34.

[30] Z. Lin, X. Wang, Nanostructure Engineering and Doping of Conjugated Carbon Nitride Semiconductors for Hydrogen Photosynthesis, Angew Chem-Ger Edit, 125 (2013) 1779-1782.

[31] S.C. Yan, Z.S. Li, Z.G. Zou, Photodegradation Performance of g-C_3N_4 Fabricated by Directly Heating Melamine, Langmuir, 25 (2009) 10397-10401.

[32] Y. Zhao, D. Yu, H. Zhou, Y. Tian, O. Yanagisawa, Turbostratic carbon nitride prepared by pyrolysis of melamine, Journal of materials science, 40 (2005) 2645-2647.

[33] X.L. Wang, W.Q. Fang, H.F. Wang, H. Zhang, H. Zhao, Y. Yao, H.G. Yang, Surface hydrogen bonding can enhance photocatalytic H_2 evolution efficiency, Journal of Materials Chemistry A, 1 (2013) 14089-14096.

[34] P. Wang, C. Guo, S. Hou, X. Zhao, L. Wu, Y. Pei, Y. Zhang, J. Gao, J. Xu, Template-free synthesis of bubble-like phosphorus-doped carbon nitride with enhanced visible-light photocatalytic activity, J. Alloys Compd., 769 (2018) 503-511.

[35] Y.-N. Li, Z.-Y. Chen, M.-Q. Wang, L.-z. Zhang, S.-J. Bao, Interface engineered construction of porous g-C_3N_4/TiO_2 heterostructure for enhanced photocatalysis of organic pollutants, Appl. Surf. Sci., 440 (2018) 229-236.

[36] Y. Chen, W. Huang, D. He, Y. Situ, H. Huang, Construction of Heterostructured g-C_3N_4/Ag/TiO_2 Microspheres with Enhanced Photocatalysis Performance under Visible-Light Irradiation, ACS Applied Materials & Interfaces, 6 (2014) 14405-14414.

[37] K. Lai, W. Wei, Y. Dai, R. Zhang, B. Huang, DFT calculations on structural and electronic properties of Bi_2MO_6 (M = Cr, Mo, W), Rare Metals, 30 (2011) 166-172.

[38] X. Meng, Z. Zhang, Facile synthesis of BiOBr/Bi_2WO_6 heterojunction semiconductors with high visible-light-driven photocatalytic activity, J. Photochem. Photobiol. A: Chem., 310 (2015) 33-44.

[39] F.-J. Zhang, F.-Z. Xie, S.-F. Zhu, J. Liu, J. Zhang, S.-F. Mei, W. Zhao, A novel

photofunctional g-C_3N_4/Ag_3PO_4 bulk heterojunction for decolorization of Rh.B, Chem. Eng. J., 228 (2013) 435-441.

[40] Y. Xu, M.A.A. Schoonen, The absolute energy positions of conduction and valence bands of selected semiconducting minerals, Am Mineral, 85 (2000) 543-556.

[41] X. Meng, Z. Zhang, Bismuth-based Photocatalytic Semiconductors: Introduction, Challenges and Possible Approaches, Journal of Molecular Catalysis A: Chemical, 423 (2016) 533-549.

[42] R.T. Sanderson, Chemical periodicity, Reinhold, New York, US, 1961.

[43] R.S. Mulliken, A New Electroaffinity Scale; Together with Data on Valence States and on Valence Ionization Potentials and Electron Affinities, The Journal of Chemical Physics, 2 (1934) 782-793.

[44] R.S. Mulliken, Electronic Structures of Molecules XI. Electroaffinity, Molecular Orbitals and Dipole Moments, The Journal of Chemical Physics, 3 (1935) 573-585.

[45] J. Yu, X. Zhao, Effect of surface treatment on the photocatalytic activity and hydrophilic property of the sol-gel derived TiO_2 thin films, Mater. Res. Bull., 36 (2001) 97-107.

[46] H. Tada, M. Tanaka, Dependence of TiO_2 Photocatalytic Activity upon Its Film Thickness, Langmuir, 13 (1997) 360-364.

[47] B. Zhu, P. Xia, W. Ho, J. Yu, Isoelectric point and adsorption activity of porous g-C_3N_4, Appl Surf Sci, 344 (2015) 188-195.

[48] Z. Li, X. Meng, Z. Zhang, An Effective Approach to Improve the Photocatalytic Activity of Graphitic Carbon Nitride via Hydroxyl Surface Modification, Catalysts, 9

(2018) 17.

[49] A. Sattler, S. Pagano, M. Zeuner, A. Zurawski, D. Gunzelmann, J. Senker, K. Müller-Buschbaum, W. Schnick, Melamine–Melem Adduct Phases: Investigating the Thermal Condensation of Melamine, Chemistry – A European Journal, 15 (2009) 13161-13170.

[50] X. Meng, Z. Li, Z. Zhang, Pd-nanoparticle-decorated peanut-shaped $BiVO_4$ with improved visible light-driven photocatalytic activity comparable to that of TiO_2 under UV light, Journal of Catalysis, 356 (2017) 53-64.

[51] A. Fujishima, T.N. Rao, D.A. Tryk, Titanium dioxide photocatalysis, Journal of Photochemistry and Photobiology C: Photochemistry Reviews, 1 (2000) 1-21.

[52] L. Ye, J. Liu, Z. Jiang, T. Peng, L. Zan, Facets coupling of BiOBr-g-C_3N_4 composite photocatalyst for enhanced visible-light-driven photocatalytic activity, Applied Catalysis B: Environmental, 142-143 (2013) 1-7.

[53] S. Zhou, Y. Liu, J. Li, Y. Wang, G. Jiang, Z. Zhao, D. Wang, A. Duan, J. Liu, Y. Wei, Facile in situ synthesis of graphitic carbon nitride (g-C_3N_4)-N-TiO_2 heterojunction as an efficient photocatalyst for the selective photoreduction of CO2 to CO, Applied Catalysis B: Environmental, 158-159 (2014) 20-29.

[54] M.S. Elovitz, U. von Gunten, Hydroxyl Radical/Ozone Ratios During Ozonation Processes. I. The Rct Concept, Ozone: Science & Engineering, 21 (1999) 239-260.

[55] S.-K. Han, S.-N. Nam, J.-W. Kang, OH radical monitoring technologies for AOP advanced oxidation process, Water Sci Technol, 46 (2002) 7-12.

[56] C. Li, S. Yu, H. Dong, C. Liu, H. Wu, H. Che, G. Chen, Z-scheme mesoporous photocatalyst constructed by modification of Sn_3O_4 nanoclusters on g-C_3N_4 nanosheets

with improved photocatalytic performance and mechanism insight, Applied Catalysis B: Environmental, 238 (2018) 284-293.

[57] C. Li, S. Yu, H. Dong, Y. Wang, H. Wu, X. Zhang, G. Chen, C. Liu, Mesoporous ferriferrous oxide nanoreactors modified on graphitic carbon nitride towards improvement of physical, photoelectrochemical properties and photocatalytic performance, J Colloid Interf Sci, 531 (2018) 331-342.

[58] C. Li, S. Yu, H. Che, X. Zhang, J. Han, Y. Mao, Y. Wang, C. Liu, H. Dong, Fabrication of Z-Scheme Heterojunction by Anchoring Mesoporous γ-Fe_2O_3 Nanospheres on g-C_3N_4 for Degrading Tetracycline Hydrochloride in Water, ACS Sustainable Chemistry & Engineering, 6 (2018) 16437-16447.

[59] M.J. Lundqvist, L.A. Eriksson, Hydroxyl Radical Reactions with Phenol as a Model for Generation of Biologically Reactive Tyrosyl Radicals, The Journal of Physical Chemistry B, 104 (2000) 848-855.

[60] C. Wu, X. Liu, D. Wei, J. Fan, L. Wang, Photosonochemical degradation of Phenol in water, Water Res, 35 (2001) 3927-3933.

[61] F. Jin, J. Leitich, C. von Sonntag, The superoxide radical reacts with tyrosine-derived phenoxyl radicals by addition rather than by electron transfer, Journal of the Chemical Society, Perkin Transactions 2, (1993) 1583-1588.

[62] X.-y. Li, Y.-h. Cui, Y.-j. Feng, Z.-m. Xie, J.-D. Gu, Reaction pathways and mechanisms of the electrochemical degradation of phenol on different electrodes, Water Res, 39 (2005) 1972-1981.

[63] X. Meng, Z. Zhang, Bi_2MoO_6 co-modified by reduced graphene oxide and palladium

(Pd^{2+} and Pd^{0}) with enhanced photocatalytic decomposition of phenol, Applied Catalysis B: Environmental, 209 (2017) 383-393.

[64] J. Kiwi, V. Nadtochenko, Evidence for the Mechanism of Photocatalytic Degradation of the Bacterial Wall Membrane at the TiO_2 Interface by ATR-FTIR and Laser Kinetic Spectroscopy, Langmuir, 21 (2005) 4631-4641.

[65] M. Vaara, Agents that increase the permeability of the outer membrane, Microbiol Rev, 56 (1992) 395-411.

[66] J. Xu, K.-Z. Long, Y. Wang, B. Xue, Y.-X. Li, Fast and facile preparation of metal-doped g-C_3N_4 composites for catalytic synthesis of dimethyl carbonate, Applied Catalysis A: General, 496 (2015) 1-8.

[67] Q. Yang, W. Wang, Y. Zhao, J. Zhu, Y. Zhu, L. Wang, Metal-free mesoporous carbon nitride catalyze the Friedel–Crafts reaction by activation of benzene, RSC Advances, 5 (2015) 54978-54984.

[68] X. Meng, Z. Li, Z. Zhang, Palladium nanoparticles and rGO co-modified $BiVO_4$ with greatly improved visible light-induced photocatalytic activity, Chemosphere, 198 (2018) 1-12.

[69] B. Zhu, J. Zhang, C. Jiang, B. Cheng, J. Yu, First principle investigation of halogen-doped monolayer g-C_3N_4 photocatalyst, Applied Catalysis B: Environmental, 207 (2017) 27-34.

[70] X. Meng, Z. Zhang, Synthesis, Analysis, and Testing of BiOBr-Bi_2WO_6 Photocatalytic Heterojunction Semiconductors, International Journal of Photoenergy, 2015 (2015) 12.

[71] X. Meng, Z. Zhang, Facile synthesis of BiOBr/Bi_2WO_6 heterojunction semiconductors

with high visible-light-driven photocatalytic activity, Journal of Photochemistry and Photobiology A: Chemistry, 310 (2015) 33-44.

[72] X. Meng, Z. Li, H. Zeng, J. Chen, Z. Zhang, MoS_2 quantum dots-interspersed Bi_2WO_6 heterostructures for visible light-induced detoxification and disinfection, Applied Catalysis B: Environmental, 210 (2017) 160-172.

[73] X. Meng, Z. Zhang, Plasmonic Z-scheme Ag_2O-Bi_2MoO_6 p-n heterojunction photocatalysts with greatly enhanced visible-light responsive activities, Mater Lett, 189 (2017) 267-270.

[74] H. Che, C. Liu, W. Hu, H. Hu, J. Li, J. Dou, W. Shi, C. Li, H. Dong, NGQD active sites as effective collectors of charge carriers for improving the photocatalytic performance of Z-scheme g-C_3N_4/Bi_2WO_6 heterojunctions, Catalysis Science & Technology, 8 (2018) 622-631.

[75] H. Che, G. Che, H. Dong, W. Hu, H. Hu, C. Liu, C. Li, Fabrication of Z-scheme Bi_3O_4Cl/g-C_3N_4 2D/2D heterojunctions with enhanced interfacial charge separation and photocatalytic degradation various organic pollutants activity, Appl Surf Sci, 455 (2018) 705-716.

SECTION VI: CONCLUSIONS

Chapter 10 General Discussion and Conclusions

10.1 General discussion

In this thesis, three different two dimensional materials, namely MoS_2, SnS and BN have been studied as cocatalysts to enhance the photocatalytic activity of bismuth-based semiconductors. And g-C_3N_4 has been investigated as a photocatalytic substrate, and its photocatalytic activity was enhanced by surface modification with hydroxyl functional groups. The advancements of two dimensional materials in enhanced photocatalytic activity can be summarized thus:

1) It was found that layered two dimensional materials such as BN were excellent electron acceptors, for their high conductivity. With this property, photogenerated charge carriers were effectively transferred from the substrate to the two dimensional materials. This phenomenon was in favor of suppressing the recombination of charge carriers, so as to improve the photocatalytic activity;

2) Two dimensional materials with suitable band gap can be combined with another semiconductor to form heterojunctions. With the formation of heterostructure, an internal electrical force was formed, and drive the transfer of electrons and holes.

The transfer may facilitate the separation of charge carriers, so as to improve the photocatalytic activity;

3) Two dimensional materials generally have with highly specific surface areas, which provided more adsorption sites and increase the adsorption capacity of organic molecules on the catalysts surface. The large specific surface area also provided more reactive sites in photocatalysis and further improved the photocatalytic activity;

4) With two dimensional materials loaded on the surface, the adsorption capacity of the substrate may be improved, not only because of the high specific surface area of the two dimensional materials, but also the modified surface properties, such as zeta potentials;

5) Some two dimensional materials such as C_3N_4 exhibited suitable band gaps and can be applied as photocatalysts themselves;

6) For C_3N_4, the photocatalytic activity can be improved by various methods. In this thesis, a hydroxyl surface modification method was developed. And it was found that with the modification of hydroxyl on C_3N_4, the photocatalytic activity was greatly improved, which may be due to improved charge separation as well as improved hydrophility of the C_3N_4 surface.

10.2 Publications

The work undertaken was shared with academic peers internationally and resulted in seven publications in peer-reviewed journals and six conference presentations. Details were listed below:

Refereed journal articles (published or accepted)

1. **Z. Li**, X. Meng and Z. Zhang, "Fewer-layer BN nanosheets-deposited on Bi_2MoO_6 microspheres with enhanced visible light-driven photocatalytic activity", ***Applied Surface Science*** 483, 572-580 (2019).
2. **Z. Li**, X. Meng and Z. Zhang, "Fabrication of surface hydroxyl modified g-C_3N_4 with enhanced photocatalytic oxidation activity", ***Catalysis Science and Technology*** 9, 3979-3993 (2019).
3. **Z. Li**, X. Meng and Z. Zhang, "An effective approach to improve the photocatalytic activity of graphitic carbon nitride via hydroxyl surface modification", ***Catalysts***, 9 (1), 17 (2019).
4. **Z. Li**, X. Meng and Z. Zhang, "Hexagonal SnS nanoplates assembled onto hierarchical Bi_2WO_6 with enhanced photocatalytic activity in detoxification and disinfection", ***Journal of Colloid and Interface Science*** 537, 345-357 (2019).

5. **Z. Li**, X. Meng and Z. Zhang, "Equilibrium and kinetic modelling of adsorption of Rhodamine B on MoS_2", ***Materials Research Bulletin*** 111, 238-244 (2019).

6. **Z. Li**, X. Meng and Z. Zhang, "Few-layer MoS_2 nanosheets-deposited on Bi_2MoO_6 microspheres: A Z-scheme visible-light photocatalyst with enhanced activity", ***Catalysis Today***, 315 67-78 (2018).

7. **Z. Li**, X. Meng, Z. Zhang, "Recent development on MoS_2-based photocatalysis: A review", ***Journal of Photochemistry and Photobiology C: Photochemistry Reviews*** 35 39–55 (2018).

Conference presentations

8. **Z. Li**, X. Meng and Z. Zhang, "Few-layer MoS_2 nanosheets enhanced Photocatalysis under Visible light", ***25th Canadian Symposium on Catalysis***, Saskatoon, SK, Canada, May 9-11, 2018.

9. **Z. Li**, X. Meng and Z. Zhang, "MoS_2 Quantum dots implemented in improving visible light-induced detoxification and disinfection", ***5th Nano Today Conference***, Hawaii, USA, Dec. 6-10, 2017.

10. X. Meng, **Z. Li** and Z. Zhang, "Plasmonic ternary composites with enhanced visible light-driven photocatalytic activity", ***25th North American Meeting of the North American Catalysis Society***, Denver, AB, USA, June 4-9, 2017.

11. **Z. Li**, X. Meng and Z. Zhang, "MoS2 QDs as a co-catalyst for visible light-induced photocatalysis", ***25th North American Meeting of the North American Catalysis Society***, Denver, AB, USA, June 4-9, 2017.
12. X. Meng, **Z. Li** and Z. Zhang, "Photo-depositing NPs on the surface to improve its visible light driven photocatalytic activity", ***Surface Canada Conference***, Montreal, QC, Canada, May 10-12, 2017.
13. X. Meng, **Z. Li** and Z. Zhang. "Synthesis and characterization of plasmonic and magnetically separable core-shell composites for visible light-induced detoxification" ***66th Canadian Chemical Engineering Conference***, Quebec City, QC, Canada, Oct. 16-19, 2016.

10.3 Recommendation for future work

Recommendations for future work are as follows:

- From the aspect of practical use with solar light as the light source, stability of as-prepared materials under UV light should be studied, as UV accounts for 5% of sunlight;
- This process should be scaled up with photoreactor design as well as process engineering development;
- More two dimensional materials should be studied and compared, so as to find a photocatalyst with the highest activity;

- ❖ Tests under real/ simulated solar light should be conducted, to provide evidence of the advancements of this process in practical use;
- ❖ Integration with other techniques such as electrochemistry, membrane techniques and biotechnology can widen the application area and promote further development;
- ❖ Application of these materials should be extended from the environmental remediation to other fields such as water splitting, CO_2 reduction and N_2 fixation;
- ❖ It is necessary to develop an evaluation system for the comparison of different photocatalysts.

Even though many two dimensional materials modified bismuth-based semiconductors with high photocatalytic performances under visible light irradiation have been reported, they are still in the early stages of implementation for the commercialization of this advanced process. The excellent and promising properties of as-prepared compounds suggest a bright future.